

**Electron Transport  
in Quantum Dot Devices**  
**Kondo Physics and Coupled Quantum Dots**

Dissertation  
zur Erlangung des Grades eines Doktors  
der Naturwissenschaften  
der Mathematisch-Naturwissenschaftlichen Fakultät  
der Eberhard-Karls-Universität zu Tübingen

vorgelegt von  
Kittipong Tantisantisom  
aus Rayong, Thailand

2011

Tag der mündlichen Prüfung: 14.02.2011

Dekan: Prof. Dr. Wolfgang Rosenstiel

1. Berichtstatter: Prof. Dr. David A. Wharam
2. Berichtstatter: Prof. Dr. Dieter Kern

# Abstract

In this thesis measurements of electronic transport through quantum point-contacts (QPCs) and quantum dots (QDs) defined in GaAs-AlGaAs heterostructures are presented. The nanostructures are fabricated using electron beam lithography and the measurements are performed in He<sup>3</sup>/He<sup>4</sup> dilution refrigerator with a base temperature of approximately 60 mK.

The quantization of differential conductance in units of  $2e^2/h$  is observed in several quantum point-contacts. Furthermore, additional structure which may be explained in terms of the Coulomb blockade oscillations of a single quantum dot appears in the differential conductance of the QPC. This is interpreted as the accidental coupling of the quantum point-contact to an unexpected quantum dot. This unexpected dot is presumably located exactly underneath one of the metallic gates of the point-contact and results from either the inhomogeneous two-dimensional electron gas beneath or from the inhomogeneous vertical depletion of the gate. With strong coupling between the unexpected dot and reservoirs, the enhancement of conductance that results from the Kondo resonance in the density of states at the Fermi level of the reservoirs occurs, and a zero-bias anomaly is observed in the nonlinear measurements. This quantum dot is symmetrically coupled to the leads.

Electron transport measurements are also performed in single quantum dots in both the weak and strong coupling regimes. For weak tunnel coupling, clear patterns of Coulomb blockade diamonds are obtained and the capacitance parameters of the system are extracted from the pattern geometry. The extracted charging energy is in good agreement with the expectation for the size of the quantum dot structure defined by lithography. For strong tunnel coupling, an enhanced conductance is observed at a non-zero bias. This unexpected Kondo behaviour has been considered in the context of an asymmetrically coupled quantum dot structure. The Kondo resonance in the density of states is then pinned to the potential level of the reservoir with stronger coupling.

The characteristic of the coupling of the electron spin in the dot to the reservoirs is defined by a single parameter, the Kondo temperature, which is extracted from the measured linewidth of the Kondo conductance peak at base temperature. According to the Anderson impurity model, the temperature dependence of the Kondo effect may be compared to theoretical predictions quantitatively. The universal scaling of the Kondo data is studied by comparing the observed behaviour with the prediction of a numerical renormalization group calculation. The influence of the magnetic field on the Kondo effect in the dot is investigated and it is found that the Kondo resonance disappears when the magnetic field reaches about 0.5 Tesla. Furthermore a magnetic field improves the symmetry of the coupling of the dot to the reservoirs. This improvement may result from the formation of edge states both in the reservoirs and in the dot under an applied magnetic field. The coupling of the dot either to the source or to the drain reservoirs is then symmetric.

Electronic transport through double quantum dots coupled in series is studied in the transition regime from weak to strong interdot tunnel coupling. The crossover from two isolated dots to one single large dot can be obtained from the evolution of the stability charging diagram with increasing interdot coupling. The capacitive parameters for double dots are extracted from the geometry of the honeycomb pattern in the charging diagram. Not only the influence of interdot coupling, but also the coupling between dots and reservoirs is investigated for the electron transport.

# Zusammenfassung

In dieser Arbeit werden Messungen zum elektronischen Transport durch Quantenpunktkontakte (QPCs) und Quantenpunkte (QDs) in GaAs-AlGaAs-Heterostrukturen vorgestellt. Diese Nanostrukturen werden mittels Elektronenstrahlithographie hergestellt, und in einem He<sup>3</sup>/He<sup>4</sup>-Entmischungskryostat mit einer Basistemperatur von etwa 60 mK vermessen.

Eine Quantisierung des differentiellen Leitwerts in Einheiten von  $2e^2/h$  wird in mehreren Quantenpunktkontakten beobachtet. Des Weiteren wird im differentiellen Leitwert eines einzelnen Quantenpunktkontakts zusätzliche Strukturen beobachtet, die durch Coulomb-Blockade-Oszillationen eines Quantenpunktes erklärt werden können. Diese Struktur wird durch zufällige Kopplung des Quantenpunktkontaktes mit einem unerwarteten Quantenpunkt gedeutet. Der Quantenpunkt liegt vermutlich in unmittelbarer Nähe zu den metallischen Gates des Punktkontakts und entsteht entweder durch die Inhomogenität des zwei-dimensionalen Elektronengases oder die inhomogene Verarmung unterhalb des Gates. Bei starker Kopplung zwischen Quantenpunkt und den Reservoirien wird eine Erhöhung des Leitwerts beobachtet, die in einer Kondoresonanz der Zustandsdichte bei der Fermienergie der Reservoirie begründet liegt. Es wird dabei eine so genannte "Zero-Bias"-Anomalie in den nichtlinearen Messungen beobachtet. Dieser Quantenpunkt koppelt symmetrisch an die beiden Reservoirie.

Elektronische Transportmessungen werden auch für einzelne Quantenpunkte im Bereich schwacher und starker Kopplung durchgeführt. Bei schwacher Tunnel-Kopplung werden die für die Coulomb-Blockade charakteristischen Rautenstrukturen beobachtet, die eine Bestimmung der im System vorliegenden Kapazitäten ermöglichen. Die dadurch bestimmte Ladeenergie stimmt gut mit dem aufgrund der Lithographie erwarteten Wert überein, der durch die Abmessungen des Quantenpunkts gegeben ist. Bei starker Tunnel-Kopplung wird ein erhöhter Leitwert bei endlicher Source-Drain-Spannung beobachtet. Dieses unerwartete Kondoverhalten wird im Rahmen einer asymmetrischen Kopplung des Quantenpunkts betrachtet. In diesem Fall wird die Kondoresonanz der Zustandsdichte bei der Fermienergie des Reservoirs mit der stärkeren Kopplung zum Quantenpunkt gefunden.

Die Kopplung des Elektronenspin-Zustands im Quantenpunkt mit den Reservoirien wird durch einen einzigen Parameter, gegeben durch die Kondo-Temperatur, charakterisiert, die aus der Linienbreite der Kondoresonanz bei Basistemperatur bestimmt wird. Nach dem Anderson-Störstellen-Modell skaliert die Temperaturabhängigkeit des Kondo-Effekts mit der Kondo-Temperatur und ermöglicht daher einen quantitativen Vergleich mit den theoretischen Vorhersagen. In dieser Arbeit wird die universelle Skalierung des Kondo-Effekts durch den Vergleich der gemessenen Daten mit den Ergebnissen einer Berechnung auf Grundlage der Renormierungs-Gruppen-Theorie verglichen. Der Einfluss eines Magnetfeldes auf den Kondo-Effekt in Quantenpunkten wird untersucht, und das Verschwinden der Kondoresonanz bei Feldstärken um 0,5 Tesla beobachtet. Des Weiteren bewirkt das Magnetfeld eine Verbesserung der Symmetrie der Ankopplung des Quantenpunkts an die Reservoirie. Vermutlich basiert dies auf der Entstehung von Randzuständen im Quantenpunkt und in den Reservoirien. Die resultierende Ankopplung des Quantenpunkts sowohl zum Source- als auch zum Drain-Reservoir ist dann symmetrisch.

Weiter wird der elektronische Transport durch zwei in Serie gekoppelte Quantenpunkte im Übergangsbereich zwischen schwacher und starker Kopplung untersucht. Der Übergang von zwei getrennten Quantenpunkten bis zu einem einzelnen großen Quantenpunkt kann durch die Entwicklung des Ladediagramms mit zunehmender Kopplung beobachtet werden. Aus der Honigwabenstruktur des Ladediagramms werden die Kapazitäten der beiden QD berechnet. Nicht nur die Kopplung der beiden Punkte, sondern auch die Kopplung der einzelnen Quantenpunkte mit dem entsprechenden Reservoir wird systematisch untersucht.

# Contents

<b>Abstract</b>	<b>i</b>
<b>Zusammenfassung</b>	<b>ii</b>
<b>List of Figures</b>	<b>vi</b>
<b>List of Tables</b>	<b>xiii</b>
<b>1. Introduction</b>	<b>1</b>
<b>2. Theoretical Background</b>	<b>3</b>
2.1. Mesoscopic Physics . . . . .	3
2.1.1. Length Scales in Mesoscopic System . . . . .	3
2.1.2. Two-Dimensional Electron Gas . . . . .	4
2.1.3. Quantum Point Contact . . . . .	8
2.2. Electron Transport through Quantum Dots . . . . .	12
2.2.1. Coulomb Blockade Oscillations in Quantum Dots . . . . .	12
2.2.2. Non-linear Transport Regime . . . . .	18
2.3. The Kondo Effect in Quantum Dot System . . . . .	21
2.4. Electron Transport through Double Quantum Dots . . . . .	24
2.4.1. Charge Stability Diagram . . . . .	25
Linear Transport Regime . . . . .	29
2.4.2. Conductance Peak Splitting in Double Quantum Dots . . . . .	33
<b>3. Sample Fabrication</b>	<b>39</b>
3.1. Heterostructure . . . . .	39
3.2. Optical lithography . . . . .	40
3.2.1. Hallbar . . . . .	40
3.2.2. Ohmic Contacts . . . . .	42
3.2.3. Gate Leads and Bondpads . . . . .	43
3.3. Electron Lithography . . . . .	44
3.4. Wire Bonding . . . . .	45
<b>4. Measurement Techniques</b>	<b>47</b>
4.1. Cryostat . . . . .	47
4.1.1. $^3\text{He}/^4\text{He}$ Dilution Refrigerators . . . . .	47
4.2. Measuring Techniques . . . . .	49
4.2.1. 4-Point Measurement . . . . .	49
4.2.2. 2-Point Measurement . . . . .	50
4.2.3. Linear Measurement . . . . .	50
4.2.4. Nonlinear Measurement . . . . .	52
4.3. Characterization of 2DEG by Quantum Hall Effect . . . . .	53

<b>5. Quantum Point Contacts in Linear Transport</b>	<b>57</b>
5.1. Quantum Point Contacts in a Different Design	57
5.1.1. QPCs in the Sample PR1:d2	57
QPC F	57
QPC C and QPC E	58
5.1.2. QPCs in the Sample PR1:d1	60
5.2. Conductance Oscillation in Quantum Point Contacts	61
5.2.1. QPC C in the sample PR1:d2	61
5.2.2. QPC E in the sample PR1:d2	66
5.2.3. QPC A in the Sample PR1:d4	66
<b>6. Single Quantum Dots with Weak Coupling</b>	<b>71</b>
6.1. Linear Transport of the Quantum Dots in Weak Coupling Regime	71
6.1.1. Coulomb Oscillation of the dotII in the sample PR1:d2	71
6.1.2. Coulomb Oscillation of the dotI in the sample PR1:d2	76
6.1.3. Coulomb Oscillation of the dot structure in the sample PR1:d1	78
6.2. Nonlinear Transport of Quantum Dots in the Sample PR1:d2	84
6.2.1. The dotII Structure	84
Excited States	87
6.2.2. The dotI Structure	88
Excited States	89
6.3. Nonlinear Transport of Quantum Dots in the Sample PR1:d1	90
The dotIII Structure	90
The dotIV Structure	90
The dotI Structure	90
6.3.1. After Illumination	92
6.4. Temperature Dependence of Coulomb Oscillations	92
6.5. Nonlinear Transport in a Quantum Point Contact coupled with a Single Quantum Dot	98
6.5.1. Excited States	99
6.5.2. Temperature Dependence	99
<b>7. Kondo Physics in a Single Quantum dot</b>	<b>103</b>
7.1. Coulomb Oscillations in Strong Coupling	103
7.2. Analysis of the Kondo Resonance	107
7.3. Temperature dependence of the Kondo Resonance	112
7.4. Kondo resonance in the Magnetic field	118
7.5. Kondo Effect in a Quantum Point Contact coupled with a Single Quantum dot	123
7.5.1. Temperature dependence	126
<b>8. Electron transport in Double Quantum Dots</b>	<b>131</b>
8.1. Characterization of the Double Dot System	131
8.1.1. Honeycomb diagram in the sample PR1:d1	147
8.2. Conductance Peak Splitting in Double Quantum dots	151
8.2.1. Conductance peak splitting in the sample PR1:d1	159
<b>9. Conclusions</b>	<b>161</b>
<b>A. Parameters of Sample Fabrication</b>	<b>163</b>

<b>References</b>	<b>167</b>
<b>Acknowledgements</b>	<b>171</b>
<b>Curriculum Vitae</b>	<b>173</b>





# List of Figures

2.1. The density of states plotted against the energy for various dimensional systems and quasi-dimensional systems . . . . .	4
2.2. Structure of GaAs-AlGaAs heterostructure and the conduction band and electron density profile . . . . .	5
2.3. Schematic of a quantum point contact, defined in a high-mobility 2DEG at the interface of a GaAs-AlGaAs heterojunction . . . . .	8
2.4. The differential conductance quantization of a quantum point contact . . . . .	9
2.5. Dispersion relation, $E(k)$ vs. $k$ for the subbands arising from transverse confinement in zero magnetic field . . . . .	9
2.6. Dispersion relations for the difference subbands at the narrow conductor . . . . .	10
2.7. Schematic and circuit diagram of a quantum dot . . . . .	13
2.8. Energy level structure of the quantum dot system and position of the energy levels	15
2.9. Schematic comparison between $G$ , $\mu_{dot}$ , and $\varphi$ . . . . .	16
2.10. Schematic Coulomb blockade diamonds . . . . .	19
2.11. Schematic representation of a quantum dot at finite source-drain voltage and schematic Coulomb blockade diamonds with the excited states . . . . .	20
2.12. Schematic energy diagram of a quantum dot for Kondo effect . . . . .	22
2.13. Tunneling density of states for Kondo effect . . . . .	23
2.14. Double dot structure fabricated by electron beam lithography on the heterostructure containing a 2DEG . . . . .	25
2.15. Diagram of the resistors and capacitors representing two quantum dots coupled in series . . . . .	26
2.16. Total electrostatic energy of the double dot system . . . . .	28
2.17. Honeycomb pattern representing the charge stability diagram of a double dot system in the capacitance model . . . . .	30
2.18. Part of a charge stability diagram in Fig. 2.17 . . . . .	31
2.19. Charge stability diagram of the double dot system in weak and strong tunneling coupling regime . . . . .	32
2.20. Conductance of the double dots in series as a function of gate voltages $V_{g1}$ and $V_{g2}$	33
2.21. Coulomb peak spacings in a honeycomb cell of the charge stability diagram . . .	34
2.22. Double dot total energy vs gate voltage and double dot conductance $G_{dd}$ vs gate voltage for increasing interdot coupling . . . . .	35
2.23. The fractional Coulomb-blockade peak splitting $F$ data from [45, 46] . . . . .	36
3.1. The process of sample fabrication . . . . .	39
3.2. Designed structures on chromium plated glass mask . . . . .	40
3.3. The fabrication process of the Hallbar sample by using the optical lithography and chemical or wet etching method. . . . .	41
3.4. The pattern of a designed Hallbar in our work . . . . .	41
3.5. The preparation process of the ohmic contacts, gate leads, and bondpads . . . .	42
3.6. The pattern and position of ohmic contact at the parts of a Hallbar . . . . .	43
3.7. The pattern and position of gate leads and bondpads deposited on a Hallbar . .	44

List of Figures

3.8.	The pattern of designed nanostructures is in the alignment with the gate leads . . . . .	45
3.9.	The sample in a 18-pin chip carrier and the pattern of wire bonding between the bondpads of the device and chip carrier pads . . . . .	46
4.1.	Phase diagram of $^3\text{He}/^4\text{He}$ mixtures . . . . .	47
4.2.	Schematic diagram of a $^3\text{He}/^4\text{He}$ dilution refrigerator . . . . .	48
4.3.	The configuration of the (a) 4-point and (b) 2-point measurements for a Hallbar sample. . . . .	49
4.4.	Circuit diagram of a 4-point ac current bias measurement . . . . .	51
4.5.	Circuit diagram of a 2-point ac voltage bias measurement . . . . .	51
4.6.	Circuit diagram of a nonlinear measurement based on the 2-point voltage bias measurement . . . . .	52
4.7.	The voltage sources for gate voltage $V_g$ which can be swept in a smaller increment than the limit . . . . .	53
4.8.	Measured longitudinal and Hall resistance for a Hallbar sample <b>PR1:d2</b> at $T \approx 65$ mK . . . . .	54
4.9.	Landau quantization of 2DEG and plot of the longitudinal resistance versus inverse of the magnetic field . . . . .	54
5.1.	Schematic drawing of the nanostructures fabricated on the sample <b>PR1:d2</b> . . . . .	57
5.2.	Conductance quantization of QPC F of the sample <b>PR1:d2</b> . . . . .	58
5.3.	The comparison of the differential conductance of QPC C with grounded and ungrounded gate A2 . . . . .	59
5.4.	Conductance quantization of QPC C and QPC E of the sample <b>PR1:d2</b> . . . . .	59
5.5.	The differential conductance quantization of QPC C at the 1 <sup>st</sup> and the 2 <sup>nd</sup> cooling in the $\text{He}^3/\text{He}^4$ dilution refrigerator . . . . .	60
5.6.	Schematic structure of two different size of double quantum dot systems in series of the sample <b>PR1:d1</b> . . . . .	61
5.7.	The differential conductance $G(V_g)$ of the (a) QPC A, (b) QPC A1C2, (c) QPC D, (d) QPC D1F2, and (e) QPC F . . . . .	62
5.8.	The differential conductance $G$ of QPC C as a function of $V_{C2}$ while the $V_{C1}$ is fixed at a constant value . . . . .	63
5.9.	The differential conductance of QPC C as a function of $V_{C1}$ at three values of $V_{C2}$ . . . . .	65
5.10.	The differential conductance of QPC E as a function of $V_g$ . . . . .	65
5.11.	The electron micrograph of the quantum dots system and a standalone quantum point contact in the sample <b>PR1:d4</b> . . . . .	66
5.12.	Oscillation in the differential conductance of QPC A measured by the 2-point measurement. The $G$ is measured as a function of $V_g = V_{A1} = V_{A2}$ . . . . .	68
5.13.	The differential conductance of QPC A in the sample <b>PR1:d4</b> as a function of the $V_{A1}$ . . . . .	68
5.14.	The differential conductance of QPC A as a function of $V_{A1}$ . . . . .	69
5.15.	The conductance oscillation in QPC A as function of $V_{A1}$ when $V_{A2}$ is fixed at $-0.4$ V and $V_{B1,B2,C1}$ is biased with positive voltage . . . . .	70
6.1.	SEM image and schematic pattern of the double dots structure in the sample <b>PR1:d2</b> . . . . .	71
6.2.	Differential conductance of QPC C and QPC E in the sample <b>PR1:d2</b> . . . . .	72
6.3.	Coulomb blockade oscillations in dotII at different conditions of tuned gates . . . . .	73
6.4.	Coulomb blockade oscillations in differential conductance of dotII . . . . .	74

6.5. Coulomb oscillation of dotII in the sample <b>PR1:d2</b> at $V_{C1C2} = -0.345$ V and $V_{E1E2} = -0.24$ V . . . . .	75
6.6. The data in Fig. 6.5 fit very well to the sum of thermally broadened conductance peak centered at each peak . . . . .	75
6.7. Schematic structure of the double dots in sample <b>PR1:d2</b> . . . . .	76
6.8. Coulomb oscillation of dotI in the sample <b>PR1:d2</b> . . . . .	77
6.9. Coulomb oscillation of dotI at $V_{A1} = -0.5$ V, $V_{QPC\ c} = -0.534$ V and $V_{B2} = -1.3$ V. The center gate voltage $V_g = V_{B1}$ is swept in steps of $100\ \mu\text{V}$ . . . . .	77
6.10. SEM image and schematic pattern of the double dots structure in the sample <b>PR1:d1</b> . . . . .	78
6.11. Schematic of the double dots structure in the sample <b>PR1:d1</b> . . . . .	79
6.12. Coulomb oscillation in differential conductance of dotIII in the sample <b>PR1:d1</b> .	80
6.13. The Coulomb blockade oscillation of dotIII . . . . .	80
6.14. The schematic of the dots system in the sample <b>PR1:d1</b> . . . . .	81
6.15. The Coulomb blockade oscillation in dotIV . . . . .	81
6.16. Non-stable conductance peaks of dotIII after illuminated . . . . .	82
6.17. The differential conductance of dotI in the sample <b>PR1:d1</b> as a function of $V_{B2}$	83
6.18. Coulomb blockade diamonds measured on a quantum dot named dotII with $V_{C1C2} = -345$ mV and $V_{E1E2} = -240$ mV . . . . .	84
6.19. Comparison between the first, the second, and the third non-linear measurement	86
6.20. The expansion of the second Coulomb blockade diamond in Fig. 6.19(b) . . . . .	88
6.21. Measured Coulomb blockade diamonds on the dotI in the sample <b>PR1:d2</b> . . . . .	89
6.22. Grey-scale plot of differential conductance $G$ as a function of $V_g$ and $V_{sd}$ in the dot structures in the sample <b>PR1:d1</b> . . . . .	91
6.23. Non-stable Coulomb blockade diamonds after illumination . . . . .	92
6.24. Conductance $G$ as a function of gate voltage $V_g$ at various temperatures for dotII structure in the sample <b>PR1:d2</b> . . . . .	94
6.25. Plot of full width at half maximum or line width of peak A and B in 6.24 as a function of temperature . . . . .	94
6.26. Inverse of maximum conductance $1/G_{Max}$ of the conductance peak <b>B</b> versus temperature for dotII structure . . . . .	95
6.27. Conductance versus the center gate voltage $V_g$ of dotI in the sample <b>PR1:d2</b> at various temperatures. . . . .	96
6.28. Temperature dependence of line width of peak (a) no.1 and (b) no.2 in Fig. 6.27	96
6.29. Conductance as a function of gate voltage $V_g$ of dotIII in the sample <b>PR1:d1</b> for various temperatures. . . . .	97
6.30. The Coulomb oscillation in conductance at $T = 500$ mK and Temperature dependence of line width of peak . . . . .	97
6.31. Scanning electron micrograph of the quantum point contact A in the sample <b>PR1:d4</b> . . . . .	98
6.32. Differential conductance as a function gate voltage $V_{A1}$ while $V_{A2}$ is fixed at $-0.4$ V	100
6.33. Expansion of an indicated Coulomb blockade diamond in Fig. 6.32(b) with identified number of electrons in each diamond . . . . .	101
6.34. Coulomb oscillations in the differential conductance versus gate voltage $V_{A1}$ for different temperatures . . . . .	102
6.35. Temperature dependence of line width of the conductance peak which is fit to the thermally broadened resonance peak as shown as solid line shape in the inset . .	102
7.1. The comparison of Coulomb oscillation in three different gate voltage conditions	104

List of Figures

7.2. The differential conductance of the dotII in the nonlinear measurement with strong coupling, which corresponds to Fig. 7.1(b) . . . . .	104
7.3. Equilibrium and Non-equilibrium of Kondo resonance in DOS . . . . .	105
7.4. The density of states of a quantum dot in non-equilibrium Kondo situation with asymmetric barriers . . . . .	105
7.5. The evolution of an asymmetric of the Kondo conductance resonance by varying gate voltage $V_{E1E2}$ . . . . .	106
7.6. The differential conductance $G$ versus bias voltage $V_{sd}$ with $V_{C1C2} = -325$ mV and $V_{E1E2} = -220$ mV, as referred to Fig.7.5(d) . . . . .	108
7.7. The fit of hyperbolic cosine superposed with Lorentzian to one of data trace at $V_g = -1.148$ V in figure above . . . . .	108
7.8. The dependence of the (a) width, (b) amplitude, and (c) the peak position of the Kondo resonance on gate voltage ( $V_g$ or $V_{D1D2}$ ) at different $V_{E1E2}$ . . . . .	109
7.9. Plot of differential conductance as a function of $V_{sd}$ and $V_g$ at $V_{C1C2} = -326$ mV, $V_{E1E2} = -218$ mV . . . . .	111
7.10. (a) Kondo peak position, (b) maxima and amplitude of Kondo peak in differential conductance, (c) the width and depending Kondo temperature $T_K$ , and (d) the value of $\ln T_K$ . . . . .	111
7.11. Differential conductance $G \equiv dI/dV_{sd}$ versus dc bias voltage between source and drain contacts $V_{sd}$ for temperature ranging from 64 mK up to 600 mK . . . . .	113
7.12. Width ((a) and (b))and maximum point ((c) and (d)) of Kondo peak at $V_{C1C2} = -0.326$ V and $V_{E1E2} = -0.218$ V . . . . .	114
7.13. Electronic temperature dependence of the width of Kondo peaks . . . . .	114
7.14. Coulomb oscillations in $G$ versus $V_g$ with the Coulomb peak fitting at $V_{C1C2} = -326$ mV and $V_{E1E2} = -218$ mV . . . . .	116
7.15. The normalized conductance $G/G_0$ versus normalized temperature $T/T_K$ scales to a single data trace for different $V_g$ . . . . .	117
7.16. Grey-scale plot of $G = dI/dV_{sd}$ for a quantum dot at $V_{C1C2} = -327$ mV and $V_{E1E2} = -220$ mV for $B = 0$ to 200 mT, respectively . . . . .	119
7.17. Maximum conductance $G_{Max}$ and the width of Kondo peak versus $V_g$ for various applied magnetic field $B$ . . . . .	120
7.18. For $V_{C1C2} = -328$ mV and $V_{E1E2} = -215$ mV, differential conductance on a grey scale as functions of both $V_g$ and $V_{sd}$ at $T \sim 70$ mK for $B = 0$ and 250 mT, respectively . . . . .	121
7.19. Grey-scale plot of $dI/dV_{sd}$ as functions of $V_g$ and $V_{sd}$ for (a) $B = 0$ mT and (b) $B = 500$ mT . . . . .	122
7.20. At $V_{A2} = -230$ mV, Grey-scale plot of differential conductance $G \equiv dI/dV_{sd}$ as a function of $V_{A1}$ and $V_{sd}$ shows the Kondo resonance peak in both top and bottom Coulomb diamonds . . . . .	124
7.21. At $V_{A2} = -240$ mV, Grey-scale plot of differential conductance $G \equiv dI/dV_{sd}$ as a function of $V_{A1}$ and $V_{sd}$ shows the Kondo resonance peak in both top and bottom Coulomb diamonds . . . . .	125
7.22. Differential conductance versus $V_{sd}$ for different temperature, at (a) $V_{A2} = -230$ mV and (b) -240 mV . . . . .	127
7.23. Temperature dependence of Kondo peak width at setting $V_{A1}$ and $V_{A2}$ . . . . .	128
7.24. Coulomb oscillation in differential conductance at $V_{A2} = -230$ mV for $T$ ranging from 58 to 900 mK . . . . .	129
8.1. Differential conductance of the double dots (dotI-dotII) system coupled in series in the sample <b>PR1:d2</b> as a function of $V_g \equiv V_{B1D1D2}$ . . . . .	131

8.2. Double dot (dotI-dotII) conductance as a function of $V_{B1} = V_{gateB}$ and $V_{D1D2} = V_{gateD}$ . . . . .	132
8.3. Conductance of (a) dotI and (b) dotII as a function of their own center gate voltage $V_g$ . . . . .	132
8.4. Double dot conductance as a function of $V_g \equiv V_{B1D1}$ . . . . .	134
8.4. (cont.) Double dot conductance as a function of $V_g \equiv V_{B1D1}$ . . . . .	135
8.5. Charge stability diagram of dotI-dotII system at $V_{A1} \equiv V_{gateA} = -480$ mV and $V_{E1E2} \equiv V_{gateE} = -440$ mV . . . . .	136
8.6. Charge stability diagram of double dot system at $V_{A1} \equiv V_{gateA} = -480$ mV and $V_{E1E2} \equiv V_{gateE} = -440$ mV . . . . .	137
8.6. (cont.) Charge stability diagram of double dot system at $V_{A1} \equiv V_{gateA} = -480$ mV and $V_{E1E2} \equiv V_{gateE} = -440$ mV . . . . .	138
8.7. Equivalent electronic circuit for double dot system in the sample <b>PR1:d2</b> . . . . .	139
8.8. Extracting the cross capacitance out of the honeycomb pattern in the charge stability diagram of the double dot system. . . . .	140
8.9. Coulomb peak spacings in the honeycomb pattern of the charge stability diagram, which is modified from Fig. 2.21. . . . .	141
8.10. (a) The gate capacitances, $C_{B1}$ and $C_{D1}$ , and (b) The ratio between interdot and total capacitances of dotI and dotII, $C_{int}/C_{dI(II)}$ . . . . .	142
8.11. (a) The interdot capacitances $C_{int}$ and (b) total capacitances of dotI and dotII $C_{dI(II)}$ are extracted at various interdot gate voltage $V_{C1C2}$ . . . . .	143
8.12. Charge stability diagram of double dot system at $V_{A1} \equiv V_{gateA} = -520$ mV and $V_{E1E2} \equiv V_{gateE} = -440$ mV. The $V_{C1C2} \equiv V_{gateC}$ is varied from (a) -480 mV to (d) -460 mV . . . . .	143
8.13. Comparison of charge stability diagram of double dot system when $V_{E1E2} \equiv V_{gateE}$ is set at (a) -440 mV and (b) -445 mV . . . . .	144
8.14. Comparison between (a) the experimental data and (b) simulation of the charge stability diagram of double dot system . . . . .	145
8.15. The charging diagram of couple dot system. Measured conductance as a function of $V_{B1} \equiv V_{gateB}$ and $V_{D1} \equiv V_{gateD}$ . . . . .	146
8.16. Equivalent electronic circuit for double dot (dotIII-IV) system in the sample <b>PR1:d1</b> . . . . .	147
8.17. Charge stability diagram of double dot (dotIII-dotIV) system in the sample <b>PR1:d1</b> . . . . .	148
8.18. Charge stability diagram of double dot (dotIII-dotIV) system. Conductance is measured as function of $V_{E1}$ and $V_{E2}$ . . . . .	149
8.19. Charge stability diagram of double dot system with interdot gate voltage $V_{D1F2} = -230$ mV . . . . .	150
8.20. Charge stability diagram as a function of $V_{E1}$ and $V_{E2}$ . The interdot gate voltage $V_{D1F2}$ is increased from (a) -240 to (d) -205 mV . . . . .	151
8.21. Conductance peaks of double dots (dotI-dotII) in the sample <b>PR1:d2</b> at (a) $V_{E1E2} \equiv V_{gateE} = -435$ mV and (b) $V_{E1E2} = -440$ mV . . . . .	153
8.22. Double dot fractional peak splitting (F) vs interdot gate voltage $V_{C1C2} \equiv V_{gateC}$ of double dot (dotI-dotII) system. . . . .	154
8.23. Double-dot fractional peak splitting $F = 2\Delta V_s/\Delta V_p$ and measured interdot barrier conductance $G_{int}$ (Curve) vs gate voltage $V_{C1C2} \equiv V_{gateC}$ . . . . .	155
8.24. Gray scale plot of double dot differential conductance vs center gate voltage $V_g \equiv V_{B1D1}$ and source-drain voltage $V_{sd}$ for interdot gate voltage $V_{C1C2} \equiv V_{gateC}$ increased from (a) to (f) . . . . .	156

List of Figures

8.25. Conductance peaks of double dot vs interdot gate voltage, $V_{C1C2} \equiv V_{gateC}$ , for $V_{A1} \equiv V_{gateA}$ of -480 mV at $V_{B2D2} = -1.3$ V and $V_{gateE} = -435$ mV . . . . .	157
8.26. Gray scale of differential conductance of double dots as a function of interdot gate voltage $V_{C1C2} \equiv V_{gateC}$ at $V_{gateA} = -480$ mV, $V_{B1D1} = -470$ mV, $V_{B2D2} = -1.3$ V and $V_{gateE} = -435$ mV . . . . .	158
8.27. Differential conductance of double dot (dotIII-dotIV) system in the sample <b>PR1:d1</b> as a function of tied center gate voltage $V_{E1E2}$ . . . . .	160
8.28. Gray scale plot of differential conductance of double dot (dotIII-dotIV) system vs $V_{E1E2}$ and $V_{sd}$ . . . . .	160

## List of Tables

A.1. Parameters of the Hallbar fabrication. . . . .	163
A.2. Parameters of the ohmic contacts fabrication. . . . .	164
A.3. Parameters of the gate leads and bondpads fabrication. . . . .	164
A.4. Parameters of the nanostructures fabrication. . . . .	165





# 1. Introduction

Semiconductor quantum dots have been studied for more than 20 years, both experimentally and theoretically. The mesoscopic physics of such nanostructures has become increasingly more accessible due to two major technological developments which are the advances in nanometer scale fabrication and the attainment of very low temperatures in dilution refrigerators. In order to study quantum dots, there are many designs of such artificial atoms. The design structure that we are interested in and has been used in this thesis is the lateral quantum dot which is formed by depleting a two-dimensional system in a GaAs/AlGaAs heterostructure via metallic split gates. This gives us opportunities to study the physics of electrons in the dot by tuning the coupling of the dot to the electron reservoirs.

An important physical effect in quantum dots is the quantization of charge in the dots. This leads to Coulomb gaps in the energy spectrum of the islands and to a blockade of transport. This behaviour is known as the Coulomb blockade. The work we have done in this thesis is related to the investigation of confined electron systems - quantum point contacts and quantum dots - in the regime where the coupling plays an important role for both classical and quantum mechanical effects.

A quantum dot may be regarded as a small puddle of electrons. Electrons can enter and exit the dot through narrow constrictions which are connected to large electron reservoirs. These constrictions are known as quantum point contacts (QPCs). The theoretical background of the effects involving to electron transport through these structures is described in Chapter 2.

The fabrication of our samples by optical lithography and the different designs of the geometry of nanostructures with electron beam lithographic techniques is explained in Chapter 3. We describe how to study the effects in such quantum systems in Chapter 4. The sample measurement techniques at low temperatures, linear and nonlinear, and the cryogenic physics bringing the temperature of the system down to  $\sim 60$  mK are included in this chapter. The two-dimensional electron gas is also characterized by the quantum Hall effect in order to obtain the properties of electron system which is used for studying the system of QPCs or quantum dots.

Because the tunable quantum dots are formed and coupled with the reservoirs by tuning the gate voltage of QPCs, the characterization of these QPCs is therefore necessary. When a QPC is squeezed by tuning the gate voltage, the conductance of a QPC is quantized in units of  $2e^2/h$  which is a fundamental characteristic of quantum point contacts. In our work, Coulomb blockade oscillations in a single QPC have been observed. This surprising and interesting behaviour has been investigated and compared with more conventional quantum dots. Our quantum point contacts are characterized and studied in linear regime, and the quantum behaviour in conductance, quantization and oscillations, are discussed in Chapter 5.

In order to study the Coulomb blockade oscillations of electron transport in our quantum dot systems, the differential conductance of the dot with weak tunnel coupling to the electron reservoirs has been carefully measured. It is also interesting to understand the correlation between the electronic temperature and bath temperature; in this context experiments of the temperature dependence of Coulomb oscillations has been performed. We are also interested in the transport in the nonlinear regime where the DC-bias is applied to the electron reservoirs. In this regime, the transport via excited states in the dot is expected to be observed. These characterizations of single quantum dots with weak coupling in linear and nonlinear regime are

## 1. Introduction

described in Chapter 6.

Increasing the tunnel coupling between the quantum dot and the electron reservoirs to the strong coupling regime, the Kondo physics can be observed and studied in the dot system. A resonance in the differential conductance at zero bias source-drain voltage within the Coulomb blockade region is shown and is the so called zero-bias anomaly which is the signature of the Kondo effect in the dot system. Our aim of this study is to investigate the tunable Kondo effect, which is affected by the influence of the coupling symmetry of our quantum dot, and to compare our Kondo experimental data with the Anderson impurity model which is a simple model of a localized electron spin coupled to the reservoir of electrons. One of the unexpected places the Kondo effect seems to occur is in the quantum point contact device showing dot characteristics. The Kondo effect is thus not only studied in quantum dots, but also in the single QPC. The experiments described in Chapter 7 address the Kondo effect, first in a quantum dot and second in a quantum point contact. The temperature dependence of the Kondo resonance is investigated because we are motivated to study the Kondo physics of our quantum dot system with various temperatures and compare the evolution of Kondo peak with the theoretical prediction. To study the influence of a magnetic field on the Kondo resonance peak, experiments of the magnetic field dependence were performed and are also presented in this chapter.

The next step after studying individual quantum dots is to study systems of more than one dot. Where single quantum dots are regarded as artificial atoms, two quantum dots can be coupled to form an artificial molecule. Depending on the strength of the interdot coupling, two dots can form ionic-like (weak tunnel coupling) or covalent-like (strong tunnel coupling). With weak interdot coupling, the electrons are localized on the individual dot, whereas they are delocalized over two dots with strong interdot coupling. In this thesis we concentrate on electron transport through double quantum dots coupled in series. Not only the influence of interdot coupling, but also the coupling between dots and the reservoirs is investigated in the electron transport. The electron transport in series double quantum dot systems for various interdot coupling regimes is investigated and discussed in Chapter 8.

## 2. Theoretical Background

### 2.1. Mesoscopic Physics

Small conductors or semiconductor with dimensions that are intermediate between the microscopic and the macroscopic are called mesoscopic. When the size or dimension of the material is reduced from macroscopic size to a very small size, the properties of material are continuously changed [1, 2]. However when the size drops in the order of nanometer, dramatic changes in properties can occur. If we consider the system confined into a box with side  $L_x, L_y$  and  $L_z$  ( $L_x < L_y < L_z$ ), and assume that there is zero potential energy inside and an infinite potential outside. Deriving from the one-electron Schrödinger equation, the energy of this system is then given by

$$E(n_x, n_y, n_z) = \frac{\hbar^2 \pi^2}{2m} \left[ \left( \frac{n_x}{L_x} \right)^2 + \left( \frac{n_y}{L_y} \right)^2 + \left( \frac{n_z}{L_z} \right)^2 \right] \quad (2.1)$$

When the dimension of the system is reduced by the partial confinement in a particular direction, the conduction electrons remain delocalized in the remaining dimensions and distribute themselves in the levels below the Fermi level in the corresponding potential well along the confinement direction [2, 3]. The important length scale for low-dimensional system is the Fermi wavelength  $\lambda_F = 2\pi/k_F$ , where  $k_F$  is the Fermi wave number. At zero temperature, the electrons occupy the states specified by the wave vector  $\mathbf{k}$  with  $|\mathbf{k}| \leq k_F$  in the reciprocal space or k-space. The system can roughly be categorized as follows depending on the relative magnitude of  $L_x, L_y, L_z$  and  $k_F$ .

$$\begin{aligned} 3D & : \lambda_F \ll L_x, L_y, L_z \\ \text{quasi-2D} & : L_x \sim \lambda_F \ll L_y, L_z \\ 2D & : L_x < \lambda_F \ll L_y, L_z \\ \text{quasi-1D} & : L_x < L_y \sim \lambda_F \ll L_z \\ 1D & : L_x, L_y < \lambda_F \ll L_z \\ \text{quasi-0D} & : L_x, L_y < L_z \sim \lambda_F \\ 0D & : L_x, L_y, L_z < \lambda_F \end{aligned}$$

Figure 2.1 shows the density of states in energy in system of various dimensions. The density of states  $D(E)$  is the delta function of energy for zero-dimension,  $D(E) \propto 1/\sqrt{E}$ , for one-dimension, is constant for two-dimensions, and increases with increasing energy,  $D(E) \propto \sqrt{E}$ , for three-dimensions. In the quasi-dimensional systems, we can see above that there are some dimensions which are comparable to the Fermi wavelength. For example,  $L_x < L_y \sim k_F$  in a quasi-one-dimensional system (Q1D), while  $L_x < L_y < k_F$ , or  $L_x$  and  $L_y$  tend to zero in one-dimensional system (1D). In a Q1D system, there will be a quasi-continuum of states in the one dimension, but separated and discrete sets of energy levels in the other two dimensions.

#### 2.1.1. Length Scales in Mesoscopic System

At low temperatures the current is mainly carried by the electrons with energies close to the Fermi energy,  $E_F = \hbar^2 k_F^2 / 2m = 2\hbar^2 \pi^2 / m \lambda_F$ . This is the de Broglie wavelength of the electrons

## 2. Theoretical Background

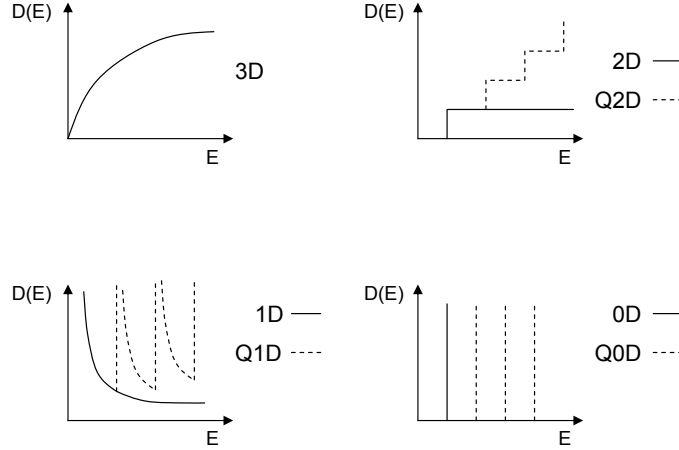


Figure 2.1.: The density of states  $D(E)$  plotted against the energy for various dimensional systems (3D, 2D, 1D, and 0D) and quasi-dimensional systems (Q2D, Q1D, and Q0D).

at the Fermi edge. Another important length scale is the mean free path. The mean free path  $L_m$  is the distance that an electron travels before they are colliding with the impurities, and change its initial momentum. The mean free path is given by

$$L_m = v_F \tau_m, \quad (2.2)$$

where  $v_F$  is the Fermi velocity and  $\tau_m$  is the momentum relaxation time. Both length scales will be discussed again in more details for the two-dimensional system in next section. The phase relaxation length or phase coherence length  $L_\phi$  is another important length scale as well [4]. It is the distance that an electron travels before its initial phase memory is destroyed by inelastic scattering events, such as electron-electron scattering and electron-phonon scattering, both of which depend strongly on temperature. In the diffusive regime,  $\tau_\phi \gg \tau_m$ , the phase relaxation length is given by

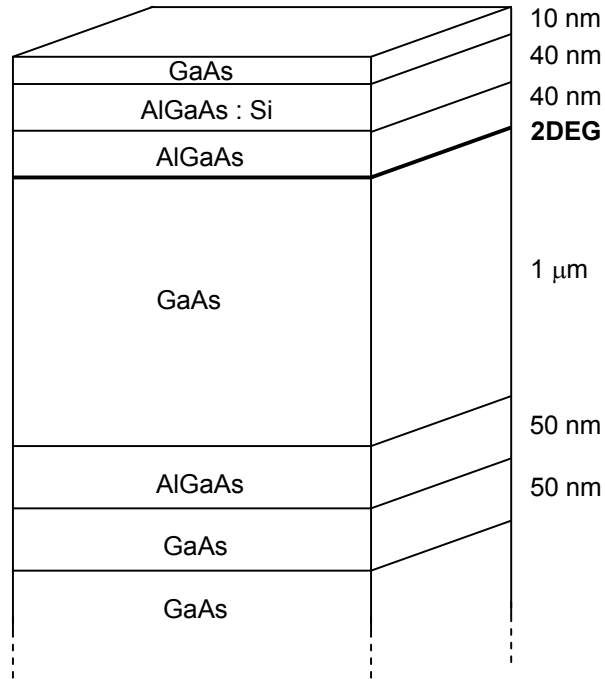
$$L_\phi = \sqrt{D\tau_\phi}, \quad (2.3)$$

where  $D = v_F^2 \tau_m / d$  is the diffusive coefficient,  $d$  is a dimension, and  $\tau_\phi$  is the phase-relaxation time determined by inelastic scattering. The scattering of electrons decreases at low temperatures. Then the  $L_\phi$  increases with decreasing temperature. In the ballistic regime,  $\tau_\phi \sim \tau_m$ , we have  $L_\phi \sim v_F \tau_\phi$ , which is often the case with high-mobility semiconductors.

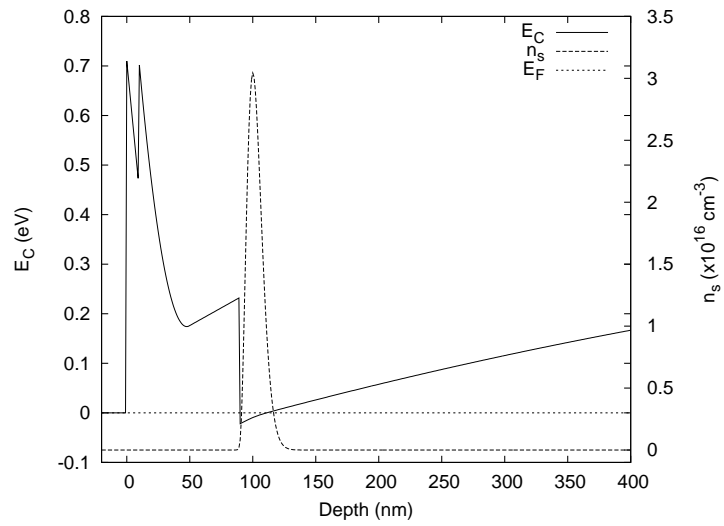
### 2.1.2. Two-Dimensional Electron Gas

Many experiments on mesoscopic conductors are based on GaAs-AlGaAs heterojunctions as shown in Fig. 2.2(a). A thin two-dimension electron gas (2DEG) is formed at the interface between GaAs and AlGaAs. We can use this heterostructure to fabricate a Hallbar sample, which is the base structure for supporting the additional nanostructure, for example, the quantum point contacts, the quantum dot system, etc. The AlGaAs has a higher energy gap than GaAs and is doped to be n-type. In this case the AlGaAs is doped with Si which can give excess electrons to the material if it replaces Al or Ga in the lattice.

When the materials are joined together, the electrons transfer from n-doped AlGaAs leaving behind positively charged donors. This space charge gives rise to an electrostatic potential that causes the conduction band bending as shown in Fig. 2.2(b), and the electron density ( $n_s$ ) is sharply peaked near the GaAs-AlGaAs interface forming a thin conducting layer of 2DEG. In



(a)



(b)

Figure 2.2.: (a) Structure of GaAs-AlGaAs heterostructure. (b) The conduction band and electron density profile in a direction perpendicular to wafer surface.

## 2. Theoretical Background

this figure we set the Fermi energy at the zero level. In equilibrium the Fermi level is always constant. The energy states in the quantum well below the Fermi level are all occupied by electrons. Therefore the electrons are trapped in the well at the interface. For the thin layer of 2DEG, the electrons are confined in the direction perpendicular to the wafer surface, but still able to move freely in the plane parallel to the wafer surface.

The GaAs-AlGaAs heterostructure is fabricated by Molecular Beam Epitaxy (MBE). In our work, we use a heterostructure from the Cavendish laboratory Cambridge for the sample preparation. For AlGaAs layer the ratio between Al and Ga can be defined by  $x = [\text{Al}]/([\text{Al}] + [\text{Ga}])$ , and  $x = 0.33$  for the heterostructure we use. The 2DEG is formed at 90 nm depth and is around 10 nm thick. The cap layer of GaAs protects the material from oxidation. The layer of n-doped AlGaAs provides a quadratic solution of the Poisson equation for the potential, and therefore a curvature as shown in Fig. 2.2(b), which is generated from the *1D Poisson/Schroedinger: A Band Diagram Calculator* program of G. Snider [5]. There are heterojunction steps at the depth of 90 nm and within the cap layer, otherwise the  $E_C$  is linear within the cap and spacer GaAs layer. The heterojunction may also need a superlattice buffer layer of GaAs/AlGaAs in order to smooth out the short-length roughness on the surface of a substrate [1].

At low temperature the mobility provides a direct measure of the momentum relaxation time as limited by impurities and defects. The mobility for 2DEG can be defined by

$$\mu \equiv \frac{|e|\tau_m}{m}, \quad (2.4)$$

where  $\tau_m$  is the momentum relaxation time,  $m$  is the effective mass, and  $e$  is the electron charge. We can find the mobility by measuring the Hall effect, which is a basic characterization measurement for semiconducting thin films. In a 2DEG the mobility found can be over  $10^3$  times of that in bulk semiconductor with the same order of equivalent concentration [4]. The scattering due to impurities is reduced because of the spatial separation between the donor atoms in AlGaAs layer and the conduction electrons in the GaAs layer. The undoped-AlGaAs spacer layer in Fig. 2.2(a) is introduced between the GaAs and the n-doped AlGaAs in order to increase the separation between the 2DEG in the GaAs and the ionized donors in the AlGaAs.

If we consider the 2DEG that the electrons are confined by some potential in the z-direction and free to move in xy plane, the wave function with no applied magnetic field can be written as

$$\Psi(\mathbf{r}) = \exp(ik_x x) \exp(ik_y y) \phi_n(z). \quad (2.5)$$

The  $\phi_n(z)$  exponentially decays in the spacer layer where the scattering by ionized donors in the n-AlGaAs is reduced. The dispersion relation is

$$E = \frac{\hbar^2}{2m} (k_x^2 + k_y^2) + E_c + \varepsilon_n, \quad (2.6)$$

where  $\varepsilon_n$  is a cut-off energy and  $n$  is the index number of the subband which corresponds to the  $\phi_n(z)$  in the z-direction. At low temperature and low carrier concentration, only the lowest subband with  $n = 1$  is occupied. Hence we can write the Schroedinger equation usually called the single-band effective mass equation [4, 6] by neglecting the z-dimension and only consider a two-dimensional system in the x-y plane:

$$\left[ \frac{(i\hbar\nabla + e\mathbf{A})^2}{2m} + U(x, y) + E_s \right] \Psi(x, y) = E\Psi(x, y), \quad (2.7)$$

where  $U(x, y)$  is the potential energy in the x-y plane,  $\mathbf{A}$  is the vector potential, and  $E_s = E_c + \varepsilon_1$ . Let  $U(x, y) = 0$  and  $\mathbf{A} = 0$ , The form of the eigenfunction normalized to an area  $S$  is

$$\Psi(x, y) = \frac{1}{\sqrt{S}} \exp(i(k_x x + k_y y)) \quad (2.8)$$

and the eigenenergies is given by

$$E = \frac{\hbar^2}{2m} (k_x^2 + k_y^2) + E_s. \quad (2.9)$$

We can find the density of states for 2DEG from the calculation of total number of states  $N_{tot}(E)$ . From Eq. 2.9, we determine the k-space for two-dimensional system and can get  $k^2 = k_x^2 + k_y^2$ . Therefore, the states having an energy less than  $E$  is contained within a circle of radius  $k$  in k-space. The area occupied by an individual state is given by  $4\pi^2/S$ , while the area enclosed by the circle is  $\pi k^2$ . Consider the spin of electron and  $k^2 = 2m(E - E_s)/\hbar^2$  from Eq. 2.9, thus the total number of states can be derived by

$$N_{tot}(E) = 2 \frac{\pi k^2}{4\pi^2/S} = \frac{k^2}{2\pi} S = \frac{mS}{\pi\hbar^2} (E - E_s). \quad (2.10)$$

Therefore the density of states per unit area per unit energy is given by

$$D(E) = \frac{1}{S} \frac{d}{dE} N_{tot}(E) = \frac{m}{\pi\hbar^2} \Theta(E - E_s), \quad (2.11)$$

where  $\Theta(E - E_s)$  is the step function. Then the density of states for 2DEG is constant for all energies exceeding the subband energy  $E_s$ . At low temperature, the equilibrium electron density  $n_s$  is given by

$$n_s = \frac{m}{\pi\hbar^2} (E_F - E_s), \quad (2.12)$$

The conductance is determined by electrons with energy close to the Fermi energy. The Fermi wave number  $k_F$  is then given by

$$k_F = \frac{1}{\hbar} \sqrt{2m(E_F - E_s)}. \quad (2.13)$$

By using Eq. 2.12, the Fermi wave number can be expressed as

$$k_F = \sqrt{2\pi n_s}. \quad (2.14)$$

Therefore the Fermi wavelength decreases as the electron density increase and is given by

$$\lambda_F = \sqrt{\frac{2\pi}{n_s}}. \quad (2.15)$$

Thus we can obtain the Fermi wavelength from the electron density, which is determined by the measurement of the Quantum Hall Effect (QHE). The Fermi wavelength in 2DEG that we use to be the substrate for fabricating the sample is typically of the order of 50 nm. From Eq. 2.14, the Fermi velocity is given by

$$v_F = \frac{\hbar k_F}{m} = \frac{\hbar}{m} \sqrt{2\pi n_s}. \quad (2.16)$$

The mean free path can be calculate from Eq. 2.2 and Eq. 2.4, and then obtained as

$$L_m = \frac{\hbar\mu}{|e|} \sqrt{2\pi n_s}. \quad (2.17)$$

The characteristic parameters in the 2DEG of our work will be discussed below in the discussion of the quantum Hall effect (QHE).

## 2. Theoretical Background

### 2.1.3. Quantum Point Contact

A quantum point contact consists of a short, narrow constriction connecting two conducting reservoirs, which is the two-dimensional electron system. To fabricate the quantum point contact, the dimension of devices must be comparable to the mean free path of the electrons. The lateral extent of the contact perpendicular to the direction of the current ( $W$ ) must be of the order of the Fermi wavelength  $\lambda_F$  and the length of contact ( $L$ ) should be shorter than the electronic mean free path  $l_m$ . Therefore the electron transport through the quantum point contact is the ballistic.

Figure 2.3 shows a metal electrode gate fabricated on the top of a GaAs-AlGaAs heterojunction. When the gate is biased with a negative voltage to deplete the electron gas beneath them, the 2DEG is squeezed and forms a one-dimensional narrow constriction. The electron transport can be investigated by measuring the current flowing through the point contact from one reservoir to another. The conductance decreases when the width  $W$  is reduced by increasing the negative voltage on the gates. The measured conductance does not decrease gradually but there is a sequence of steps in the conductance, as shown in Fig. 2.4. The conductance is quantized in units of the natural constant  $2e^2/h$ , where  $e$  is the absolute value of the electric charge and  $h$  is the Planck constant. This effect was discovered in 1988 by D. A. Wharam et al. in Cambridge [7] and B. J. van Wees et al. from the Delft-Philips group [8].

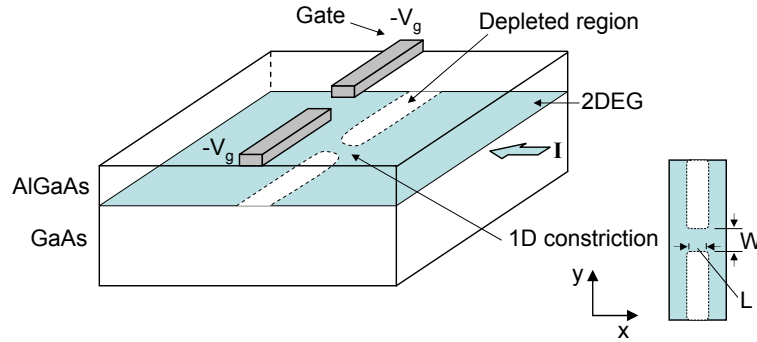


Figure 2.3.: Schematic of a quantum point contact, defined in a high-mobility 2DEG at the interface of a GaAs-AlGaAs heterojunction. The point contact is formed when a negative voltage is applied to the gate electrodes on the top of the AlGaAs layer. The transport measurement can be performed by measuring the current flowing through the 1D constriction from a reservoir in one side to another.

Assuming that the area of 2DEG at the constriction has a transverse parabolic confining potential  $U(y) = (1/2)m\omega_0^2 y^2$  and with no applied magnetic field, the motion of electrons can be described by the effective mass equation in Eq. 2.7, which is rewritten as

$$\left[ \frac{p_x^2 + p_y^2}{2m} + \frac{1}{2}m\omega_0^2 y^2 + E_s \right] \Psi(x, y) = E\Psi(x, y). \quad (2.18)$$

The solution to equation above can be expressed in the form of plane waves in the x-direction as

$$\Psi(x, y) = \frac{1}{\sqrt{L}} \exp(ikx)\chi(y), \quad (2.19)$$

where  $k$  is the wavenumber in the x-direction referred to  $p_x = \hbar k$  and the transverse function



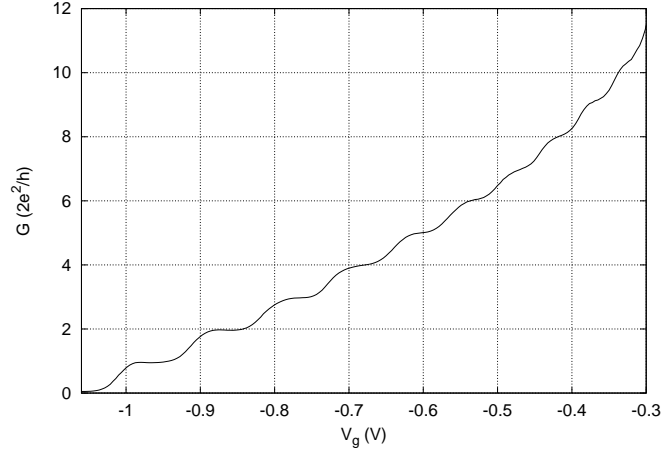


Figure 2.4.: The differential conductance quantization of a quantum point contact. The conductance is quantized in steps of  $2e^2/h$ . This shown conductance is the measured result from one of our QPCs.

$\chi(y)$  in the  $y$ -direction satisfies the equation

$$\left[ \frac{(\hbar^2 k^2 + p_y^2)}{2m} + \frac{1}{2} m \omega_0^2 y^2 + E_s \right] \chi(y) = E \chi(y). \quad (2.20)$$

Therefore the eigenenergies are given by

$$E(n, k) = \frac{\hbar^2 k^2}{2m} + \left(n + \frac{1}{2}\right) \hbar \omega_0 + E_s, \quad (2.21)$$

where  $n = 0, 1, 2, \dots$ . The dispersion relation is drawn in Fig 2.5. The  $\omega_0$  corresponds to the transverse confinement. Thus the spacing between two subbands  $\hbar\omega_0$  increases when the confinement is tighter. These subbands are also called transverse modes in the one-dimensional system.

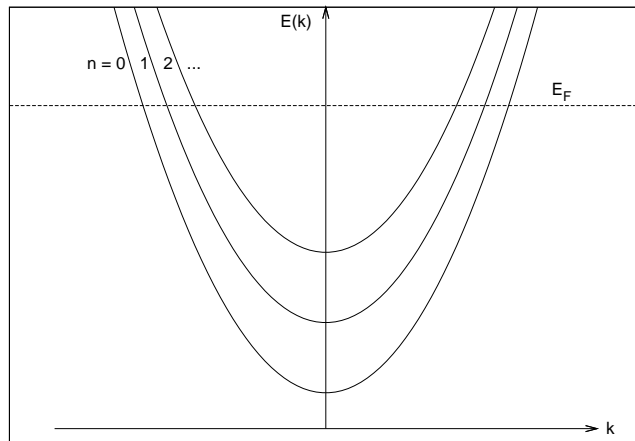


Figure 2.5.: Dispersion relation,  $E(k)$  vs.  $k$  for the subbands arising from transverse confinement in zero magnetic field. Different subbands are indexed by  $n$ .

Figure 2.6 shows the dispersion relation for the narrow conductor with applied voltage at the contacts as shown in the inset. The conductor with width  $W$  and length  $L$  is connected to the

## 2. Theoretical Background

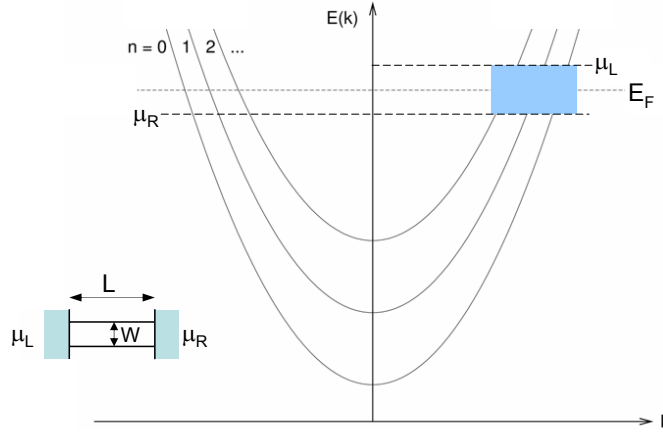


Figure 2.6.: Dispersion relations for the difference subbands at the narrow conductor. The shade area on the subbands in the  $+k$  states refers to the states carrying the net current through the conductor. Inset: a conductor is sandwiched between two contacts connected to the reservoirs which the bias is applied.

left and right contacts with applied voltage  $(\mu_L - \mu_R)/e$ . If the mean free path  $L_m$  is smaller than the dimensions of the conductor ( $L_m < W, L$ ), the electron transport is in the diffusive regime. In the quasi-ballistic transport regime, it can be obtained by  $W < L_m < L$ . When the dimensions of the conductance is smaller than the mean free path  $W, L < L_m$ , the ballistic transport regime is obtained and the conductor is also called the ballistic conductor. This means clearly that the ballistic electron transport can be found in the point contact.

From the dispersion relation in Fig.2.6, the  $+k$  states are occupied only by electrons originated in the left contact while the  $-k$  states are occupied only by electrons originated in the right contact. At low temperature, the current is carried by the  $+k$  states between  $\mu_L$  and  $\mu_R$ , as shown by the shaded area. Let us define that  $N(E)$  is the number of transverse modes at an energy  $E$  of the one-dimensional system:  $N(E) \equiv \sum \Theta(E - E_n)$ , where  $E_n$  is the cut off energy at  $k = 0$ . The net current can be given by [4, 6]

$$I = \frac{2e}{h} \int_{-\infty}^{+\infty} [f_L(E) - f_R(E)] N(E) dE, \quad (2.22)$$

where  $f_L(E) = f(E, \mu_L)$  and  $f_R(E) = f(E, \mu_R)$ . It is the Fermi-Dirac distribution function of the left and right reservoir respectively. In the linear regime the applied voltage difference  $V_{sd}$  is very small,  $\mu_L - \mu_R = eV_{sd} \ll k_B T$ . We can expand the difference in Fermi functions at the lowest order in a Taylor series [6]:

$$f_L(E) - f_R(E) \approx (\mu_L - \mu_R) \frac{\partial f(E, \mu)}{\partial \mu} = -eV_{sd} \frac{\partial f(E, \mu)}{\partial E}, \quad (2.23)$$

where  $\mu$  is the Fermi level at equilibrium. Assuming that the number of occupied modes  $N$  is constant over the energy range  $\mu_R < E < \mu_L$ . The  $N$  is also related to the Fermi wavelength  $\lambda_F$  of the 2DEG and the width  $W$  of the constriction via  $N \approx \text{Int}(2W/\lambda_F)$  [4]. The current can be obtained as

$$I = \frac{2e^2}{h} N \frac{(\mu_L - \mu_R)}{e} = \frac{2e^2}{h} N V_{sd}. \quad (2.24)$$

Therefore the conductance for the ballistic electron transport is given by

$$G = \frac{2e^2}{h} N, \quad (2.25)$$

where  $N$  is the number of occupied modes. It can be seen that the conductance does not decrease linearly with the width  $W$ . It depends on the number of occupied transverse modes in the conductor and decreases in discrete steps. This is called the quantization of the conductance, as seen in Fig. 2.4. Increasing the negative voltage on the gate makes the channel narrower and decreases the number of energy subbands or transverse modes below the Fermi energy and hence reduces the number of modes that are free for the electrons to occupy. The separation between each plateau of the conductance in Fig. 2.4 is constant of  $2e^2/h$ .

At zero temperature, the Fermi-Dirac distribution function in Eq. 2.22 can be determined and rewritten in the form of step function as  $f_L(E) = \Theta(\mu_L - E)$  and  $f_R = \Theta(\mu_R - E)$ . In the energy range  $\mu_R < E < \mu_L$ , we can determine the current and then obtain

$$\begin{aligned} I &= \frac{2e}{h} N \int_{\mu_R}^{\mu_L} [f_L(E) - f_R(E)] dE \\ &= \frac{2e}{h} N \int_{\mu_R}^{\mu_L} [\Theta(\mu_L - E) - \Theta(\mu_R - E)] dE \\ &= \frac{2e}{h} N (\mu_L - \mu_R). \end{aligned} \quad (2.26)$$

Hence the conductance is obtained and equal to  $(2e^2/h)N$  as found in Eq. 2.25. The relationship of the quantization of the conductance above can also determined and understood by using the Landauer-Buttiker formalism. First, we consider that the current carried per transverse mode is

$$I = e \int D(E) v(E) T(E) dE, \quad (2.27)$$

where  $D(E)$  is the density of state,  $v(E)$  is the velocity of the electrons, and  $T$  is the transmission function that represents the transmission probability of an electron transferring from one end to another end of the conductor. In one-dimensional system,  $D(E) = (1/\pi) dk/dE$  and  $v(E) = (1/\hbar) dE/dk$ , then the current can be rewritten in the same electrochemical potential range as above as

$$I = e \int_{\mu_R}^{\mu_L} T(E) \frac{1}{\pi} \frac{dk}{dE} \frac{1}{\hbar} \frac{dE}{dk} dE = \frac{2e}{h} \int_{\mu_R}^{\mu_L} T(E) dE. \quad (2.28)$$

For the linear regime and zero temperature, the total current can be expressed as

$$I_{tot} = \sum_{n=1}^N \frac{2e}{h} \int_{\mu_R}^{\mu_L} T_n(E) dE, \quad (2.29)$$

where  $N$  is the number of occupied subbands. The conductance can be given by

$$G = \frac{e}{\mu_L - \mu_R} \sum_{n=1}^N \frac{2e}{h} \int_{\mu_R}^{\mu_L} T_n(E) dE. \quad (2.30)$$

According to Landauer-Buettiker formalism [1, 6], the transmission is expressed in the term of transmission coefficient  $t_{ij}$  that is the transmission amplitude between mode  $i$  and  $j$ . For the ballistic conductor, the perfect transmission is determined for every modes and the transmission probability can be written as  $T_n = |t_{nn}|^2 = 1$ , and  $t_{ij} = 0$  for  $i \neq j$ . The Eq. 2.30 can be rewritten as

$$\begin{aligned} G &= \frac{2e^2}{h} \frac{1}{\mu_L - \mu_R} \sum_{n=1}^N \int_{\mu_R}^{\mu_L} |t_{nn}|^2 dE = \frac{2e^2}{h} \frac{\mu_L - \mu_R}{\mu_L - \mu_R} \sum_{n=1}^N |t_{nn}|^2 \\ &= \frac{2e^2}{h} N \end{aligned} \quad (2.31)$$

## 2. Theoretical Background

The conductance is the same as Eq. 2.25 and quantized in the unit of  $2e^2/h$ , as shown in Fig. 2.4. It also turns out that each energy subband has a resistance of  $h/2e^2 \approx 12.9 \text{ k}\Omega$ .

Many interesting effects of quantum point contacts have been studied and investigated widely for over twenty years. The effect of a finite temperature on the conductance of a quantum point contact has been determined by the temperature dependence of the Fermi distribution and the occupation of the states at the Fermi level. For increasing temperature the conductance quantization of point contacts broadens and disappears at high temperatures. This is because the electron states of the higher subbands become occupied, and not all states of the low subbands are fully occupied anymore [9].

The application of a magnetic field leads to the magnetic depopulation of the subbands in the quantum point contact. The quantization of the conductance in high magnetic field has also been studied [9]. When a perpendicular magnetic field is applied, the quantization is modified, and hybrid magneto-electric subbands evolve. This results in a reduction of the number of subbands within the channel width [7]. The number of conductance plateaus observed in a given gate voltage range decreases, the plateaus are more pronounced, and the plateaus width measured as a function of gate voltage increase with increasing magnetic field [9, 10]. The magnetic field can lift the spin degeneracy of the subbands, and then the additional quantized plateaus in the linear regime can be observed [11]. The 0.7 structure,  $0.7 \times 2e^2/h$ , which is an interesting anomaly structure in conductance quantization evolves to  $0.5 \times 2e^2/h$  when magnetic field increases. This is half of the value that one would normally expect because of the effect of spin splitting [12].

Nonlinear effects have been observed in the quantum point contact devices. In the nonlinear regime, the finite bias voltage  $V_{sd}$  is applied to the reservoirs, this shifts the electrochemical potential as  $\mu_s - \mu_d = eV_{sd}$ . Additional plateaus can be observed with quantized conductance  $G = (n + 1/2)2e^2/h$ . This leads to the broadening between the conductance plateaus at finite bias and the disappearance of the plateaus when the energy spacing between quantized levels become comparable with the applied bias voltage. The observed differential conductance for the lowest conductance plateaus is given by  $G = \beta 2e^2/h$  and  $(1 - \beta)2e^2/h$  where  $\beta$  is the fraction of the potential dropped at the entrance to the ballistic channel of quantum point contact [13]. A more investigation of the non-linear properties over a wide range of gate voltage where several subbands are occupied has also been considered under the influence of a perpendicular magnetic field, the additional conductance plateaus can appear and all plateaus become more pronounced [14]. The evolution of 0.7 structure along the source-drain voltage direction can also be observed as a zero-bias anomaly in the nonlinear regime [15, 16].

Quantum point contacts may also be used to define nanostructures of reduced dimensionality. If we arrange the quantum point contacts in series, electrons are confined in a dot or an island in the 2DEG at the interface of the heterojunction and can be considered to be a quantum dot. The characteristics and physics phenomena in quantum dot systems will be discussed in the next section.

## 2.2. Electron Transport through Quantum Dots

### 2.2.1. Coulomb Blockade Oscillations in Quantum Dots

In a typical quantum dot arrangement there are the source and drain contacts and a plunger gate. The structure is depicted in Fig. 2.7(a) which is coupled to these three terminals. Tunneling junctions connect the dot to source and drain while the gate provides an electrostatic or capacitive coupling and can be use as a gate electrode. The source and drain terminals connect the dot to macroscopic current and voltage reservoirs. Electron transport can occur with these two terminals, as indicated by the arrows. If there is no coupling to the source and drain con-

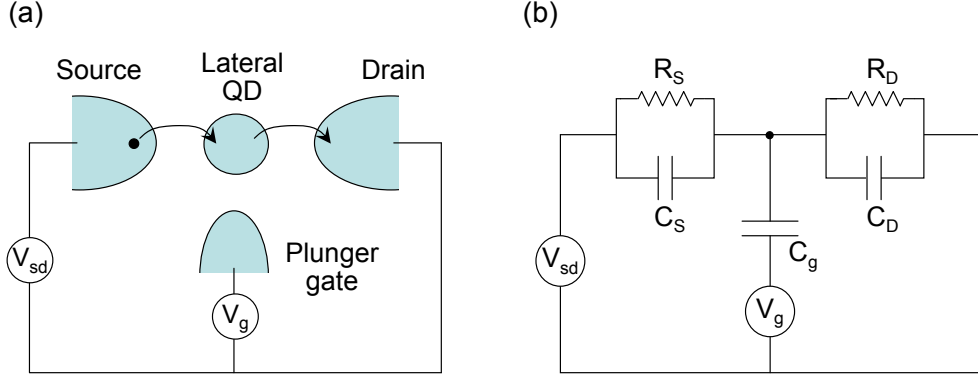


Figure 2.7.: (a) Schematic of a quantum dot connecting to the source and drain contacted by the tunnel junctions and to a plunger gate. (b) Circuit diagram in which the tunnel barriers are represented as a parallel resistance and capacitor. A quantum dot connects to a gate by capacitance  $C_g$

tacts, then the quantum dot acts as an island for electrons. The number of electrons on the island is an integer  $N$ . Therefore the charge on the island is quantized and equal to  $-Ne$ . If there is tunneling to the source and drain electrodes, the number of electrons  $N$  adjusts itself until the energy of the whole circuit is minimized. For the measurement of electron transport through quantum dots, many experiments have been performed in samples with lateral quantum dots which are defined by metallic gates on the 2DEG of a GaAs/AlGaAs heterostructure.

The single quantum dot can be modeled as a circuit diagram shown in Fig. 2.7(b). The quantum dot is coupled to source and drain through a tunneling barrier represented by a tunnel resistor  $R_{s(d)}$  and a capacitor  $C_{s(d)}$  connected in parallel. The dot is capacitively coupled to a gate voltage  $V_g$  through a capacitor  $C_g$ . The bias voltage  $V_{sd}$  is applied to the source contact with the drain contact grounded.

A theory of transport through quantum dots that incorporates both single electron charging and energy level quantization will be presented in this section. Fig. 2.8(a) shows the potential structure of a quantum dot. The states in the leads are filled up to the electrochemical potentials  $\mu_s$  and  $\mu_d$  which are defined via the externally applied source-drain voltage  $V_{sd} = (\mu_s - \mu_d)/e$ . At zero temperature, the electron transport can be observed when there are electron states on the dot aligned in the energy window between  $\mu_s$  and  $\mu_d$ , and the current will be zero when no states are in the energy window. The number of available states follows from calculating the electrochemical potential energy  $\mu_{dot}(N)$ . By definition, this is the minimum energy for adding the  $N$ th electron to the dot.

$$\mu_{dot}(N) \equiv U(N) - U(N - 1), \quad (2.32)$$

where  $U(N)$  is the total ground state energy for  $N$  electrons on the dot at zero temperature.

To be able to calculate  $U(N)$  first and explain electronic states and electron transport through a quantum dot, the model for this system has been introduced and called as Constant-Interaction (CI) model [17, 18, 19]. The CI model is based on two important assumptions. First, the quantum levels are calculated independently of the number of electron on the dot. This means that the discrete single particle energy spectrum is unaffected by any interactions. Second, the Coulomb interaction of an electron on the dot with all other electrons, in and outside the dot, are parameterized by a constant total capacitance  $C_\Sigma$  which is assumed independent of the number of electron on the dot. According to Fig. 2.7(b), the total capacitance  $C_\Sigma = C_s + C_g + C_d$  consists of capacitances across the tunnel barriers,  $C_s$  and  $C_d$ , and a capacitance between the dot and

## 2. Theoretical Background

gate,  $C_g$ . The voltage for source and drain contact can be defined as  $V_s$  and  $V_d$  respectively, and the applied source-drain voltage is then  $V_{sd} = V_s - V_d$ . According to the capacitance model [20] the total charge on a single dot is the sum of the charges on all of the capacitors connected to the dot. Therefore the total charge on the dot,  $Q_{dot}$ , is

$$Q_{dot} = C_s(V_{dot} - V_s) + C_g(V_{dot} - V_g) + C_d(V_{dot} - V_d), \quad (2.33)$$

where  $V_{dot}$  is the voltage defined at the node of the single dot and can be expressed as

$$V_{dot} = \frac{1}{C_\Sigma} (Q_{dot} + C_s V_s + C_g V_g + C_d V_d), \quad (2.34)$$

where  $C_\Sigma$  is the total capacitance coupled to the dot. The electrostatic energy of the system,  $E_{elstat}$ , needed to add  $N$  additional electrons to the dot is given by

$$\begin{aligned} E_{elstat} &= \frac{1}{2} V_{dot} \cdot C_\Sigma V_{dot} \\ &= \frac{1}{2C_\Sigma} (Q_{dot} + C_s V_s + C_g V_g + C_d V_d)^2. \end{aligned} \quad (2.35)$$

Substituting  $Q_{dot} = -(N - N_0)e$ , we obtain

$$E_{elstat} = \frac{1}{2C_\Sigma} (-(N - N_0)e + C_s V_s + C_g V_g + C_d V_d)^2, \quad (2.36)$$

where  $N_0$  is the number of electrons on the dot when all voltage source is zero, which compensates the positive background charge originating from donors in the heterostructure [20]. In the linear regime,  $V_{sd} \ll \Delta E/e, e/C_\Sigma$ , we assume  $V_s = V_d = 0$ , hence Eq. 2.36 can be re-written as

$$E_{elstat} = \frac{1}{2C_\Sigma} ((N - N_0)e - C_g V_g)^2. \quad (2.37)$$

Including a sum over the quantized energy levels, the total energy of the dot with  $N$  additional electrons is

$$U(N) = \frac{1}{2C_\Sigma} ((N - N_0)e - C_g V_g)^2 + \sum_{i=1}^N E_n. \quad (2.38)$$

According to Eq. 2.32 above, the electrochemical potential  $\mu_{dot}(N)$  for  $N$  electrons on the dot is

$$\mu_{dot}(N) = E_N + \frac{(N - N_0 - 1/2)e^2}{C_\Sigma} - e \frac{C_g}{C_\Sigma} V_g, \quad (2.39)$$

where  $N_0$  is the number of electrons on the dot at zero gate voltage and  $E_N$  is the topmost occupied single particle state for an  $N$  electron dot. Generally, the electrochemical potential can also be expressed as the form of the summation of the chemical and the electrostatic potential as

$$\mu_{dot}(N) = \mu_{ch}(N) + e\varphi_N, \quad (2.40)$$

where  $\mu_{ch}(N) = E_N$  is the chemical potential and  $e\varphi_N$  is the electrostatic potential. According to Fig. 2.8 the single-particle state  $E_N$  for the  $N$ th electron on the dot depends on the characteristics of the confinement potential and is measured from the bottom of the conduction band. From Eq. 2.39 and 2.40 the electrostatic potential  $e\varphi_N$  contains two terms, a discrete and a continuous part, respectively. In the discrete term the integer number of electrons  $N$  at a fixed gate voltage can be changed by one and be the largest integer for which  $\mu_{dot}(N) < \mu_s \cong \mu_d$  in linear regime. The continuous term of  $e\varphi_N$  is clearly proportional to the gate voltage  $V_g$ .

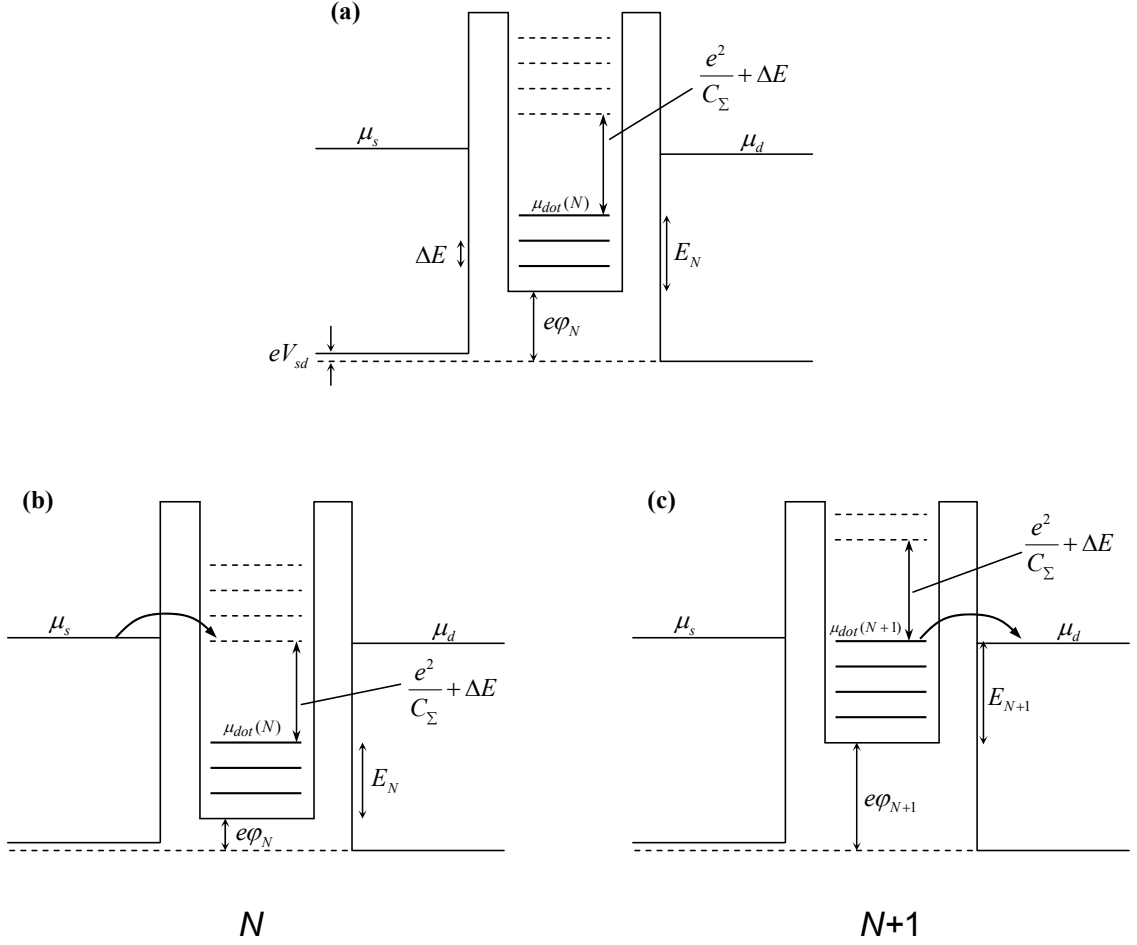


Figure 2.8.: (a) Energy level structure of the quantum dot system in the Coulomb blockade. (b) and (c) Position of the energy levels that allows an electron to tunnel through the dot from source to drain with a very small applied bias voltage at the same gate voltage. There are  $N$  and  $N + 1$  electrons in the dot in the situation of (b) and (c), respectively.

When the number of electrons on the dot is changed by one at the fixed gate voltage, the resulting change in electrochemical potential called the *addition energy* is given by

$$\mu_{dot}(N + 1) - \mu_{dot}(N) = \Delta E + \frac{e^2}{C_\Sigma}, \quad (2.41)$$

where  $\Delta E$  is the energy level spacing and  $e^2/C_\Sigma$  can be defined as the charging energy. The gate voltage  $V_g$  linearly changes the electrochemical potential in Eq. 2.39 with proportionality factor  $C_g/C_\Sigma$  relating the peak spacing in the gate voltages to the addition energy:  $\Delta\mu_{dot}(N) = e\alpha(V_g^{N+1} - V_g^N)$  where  $\alpha = C_g/C_\Sigma$ , and  $V_g^N$  and  $V_g^{N+1}$  are the gate voltage of the  $N$ th and  $(N+1)$ th Coulomb peak, respectively. The addition energy is large for a small total capacitance. The energy states below  $\mu_{dot}(N)$  are separated by the single particle energy difference  $\Delta E$  and the  $N$  electrons are localized on the dot as depicted in Fig. 2.8(a). The  $N + 1$ th electron cannot tunnel into the dot because the  $\mu_{dot}(N + 1)$  is higher than the potentials of source and drain. The electron transport is blocked for  $\mu_{dot}(N) < \mu_s, \mu_d < \mu_{dot}(N + 1)$ . This situation is called the *Coulomb blockade*.

The addition energy can lead a blockade to the tunneling of electrons on and off the dot.

## 2. Theoretical Background

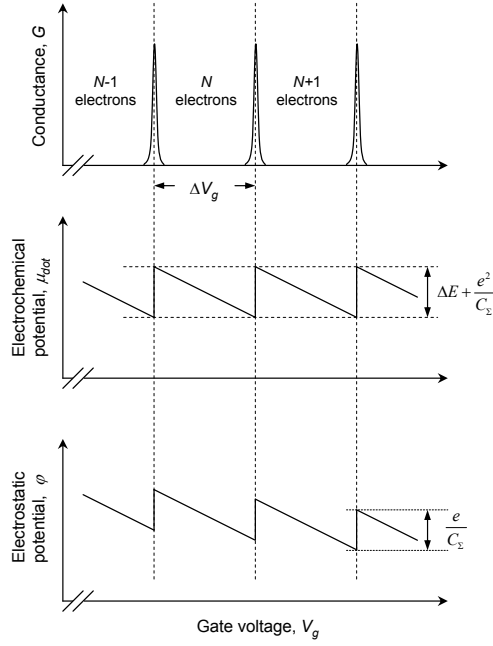


Figure 2.9.: Schematic comparison, as a function of gate voltage, between the Coulomb oscillation in the conductance  $G$ , the electrochemical potential  $\mu_{dot}$ , and the electrostatic potential  $\varphi$

Hence the Coulomb blockade can be removed by changing the gate voltage  $V_g$ . Figure 2.8(b) and (c) shows the electrochemical potential in the dot  $\mu_{dot}(N+1)$  is aligned within the small window of source-drain voltage. In this situation an electron can transfer from the source to the dot since  $\mu_s > \mu_{dot}(N+1)$ . The electrostatic increase  $e\varphi(N+1) - e\varphi(N) = e^2/C_\Sigma$  is seen as a change in the bottom of the conduction band. An electron can tunnel off the dot to drain since  $\mu_{dot}(N+1) > \mu_d$ . This causes the electrochemical potential to drop back to  $\mu_{dot}(N)$ . Now a new electron can tunnel on the dot and repeat the cycle  $N \rightarrow (N+1) \rightarrow N$  and the electron current can be carried from one side of reservoir to another side. This process is known as *single electron tunneling*.

By sweeping the gate voltage, we obtain the Coulomb oscillations showing that the conductance oscillates between zero to non-zero (or Coulomb peak) as shown in Fig. 2.9. When the conductance is zero, the number of electron  $N$  on the dot is fixed. At the maximum of a Coulomb peak,  $N$  changes by one, the electrochemical potential  $\mu_{dot}$  shifts by  $\Delta E + e^2/C_\Sigma$ , and the electrostatic potential  $\varphi$  shifts by  $e^2/C_\Sigma$ . In order to derive the separation between Coulomb oscillation in gate voltage  $\Delta V_g$ , Eq. 2.39 and the condition  $\mu_{dot}(N, V_g) = \mu_{dot}(N+1, V_g + \Delta V)$  can be used. Then we get  $\Delta V_g$  between two neighbouring Coulomb peaks as

$$\begin{aligned} \Delta V_g &= V_g(N+1) - V_g(N) \\ &= \frac{1}{e\alpha} \left( \Delta E + \frac{e^2}{C_\Sigma} \right). \end{aligned} \quad (2.42)$$

In the case that the single-particle energy level spacing vanish  $\Delta E \cong 0$ , the classical relationship between capacitance and voltage for a single electron charge is then

$$\Delta V_g = \frac{e}{C_g}. \quad (2.43)$$

Periodic Coulomb oscillations are found in this so-called metallic regime. For non-vanishing energy spacing, the oscillations will be nearly periodic.



The temperature dependence of the line shape of the Coulomb oscillation is now considered. The tunneling coupling of the dot states to the leads is defined by  $\Gamma$ . In the case of  $\Gamma \ll k_B T$ , the conductance resonances will be thermally broadened. Otherwise, in the opposite case of  $\Gamma \gg k_B T$ , the resonances will be broadened by the tunneling coupling. Therefore, we assume the temperature is greater than the quantum broadening of the energy levels in the dot due to the coupling to the leads  $\Gamma \ll k_B T$ . To be able to observe the Coulomb blockade effect, the temperature must be small compared to the charging energy  $k_B T \ll e^2/C_\Sigma$ . Thus the size of the dot must be sufficiently small such that the total capacitance is small to fulfill this condition in the experiment.

In the high temperature limit,  $k_B T \gg e^2/C_\Sigma$ , the conductance is independent of the electron number and the size of the dot. We can completely characterize the conductance with the Ohmic sum of the barrier conductances

$$\frac{1}{G} = \frac{1}{G_\infty} = \frac{1}{G_{left}} + \frac{1}{G_{right}}. \quad (2.44)$$

In the classical or metallic Coulomb blockade regime,  $\Gamma, \Delta E \ll k_B T \ll e^2/C_\Sigma$ , the oscillation behaviour can be explained by orthodox Coulomb blockade theory. Many levels are excited by thermal fluctuations. We can consider the calculated temperature dependence of the Coulomb oscillations as a function of Fermi energy. The Coulomb oscillation peak is more pronounced when the ratio  $k_B T/(e^2/C_\Sigma)$  decrease. This means that the oscillation will be visible with decreasing temperature. For  $k_B T \ll e^2/C_\Sigma$ , the width of the peaks are linear in temperature. In this regime, the peak maximum  $G_{max}$  is independent of the temperature and equal to half the high temperature value  $G_{max} = G_\infty/2$ , because an electron must first tunnel off the dot before the next can tunnel on. The probability to tunnel through the dot hence decrease to one half. The line shape of an individual single conductance peak is given by [17, 19].

$$\frac{G}{G_{max}} = \frac{\delta/k_B T}{\sinh(\delta/k_B T)} \approx \cosh^{-2} \left( \frac{\delta}{2.5k_B T} \right), \quad (2.45)$$

where  $\delta$  is the measured distance to the center of the conductance peak in units of energy. This is able to express in gate voltage as  $\delta = e\alpha \cdot |V_g - V_{g, cen}|$  in which  $V_{g, cen}$  is the gate voltage at the center of the peak and  $\alpha = C_g/C_\Sigma$ .

In the quantum Coulomb blockade regime,  $\Gamma \ll k_B T \ll \Delta E, e^2/C_\Sigma$ , the temperature is small compared to the single-particle level spacing. An electron can tunnel through only one quantized energy level in the dot. This can be called the single-level transport regime. The temperature dependence is calculated with the assumption that  $\Delta E$  is independent of  $E$  and  $N$  [19]. The peak maximum  $G_{max} = G_\infty \cdot (\Delta E/4k_B T)$  decrease linearly when temperature increases in this regime. The line shape of the single conductance peak is given by

$$\frac{G}{G_{max}} = \cosh^{-2} \left( \frac{\delta}{2k_B T} \right). \quad (2.46)$$

The peak is thermally broadened and decays exponentially with increasing distance from the maximum.

Therefore we can use the temperature dependence of a single conductance peak to distinguish the classical from the quantum regime. On the classical regime, the peak maximum decreases down to half the Ohmic value with decreasing temperature. On entering the quantum regime, the peak maximum increase and start to exceed the Ohmic value. Furthermore, we can also consider the height of different peaks at a single temperature to distinguish classical from quantum regime. The height of all classical peaks are the same at  $G_{max} = G_\infty/2$ . On the other hand, in

## 2. Theoretical Background

the quantum regime, the peak height depends sensitively on the coupling between the energy levels in the dot and in the leads.

For both the classical and quantum Coulomb blockade regimes, the important assumption is that the quantum dot is weakly coupled to the reservoirs. This assumption implies that the barrier conductance is small,  $G_{left,right} \ll e^2/h$ , and the broadening  $\Gamma$  of the energy levels is much smaller than  $k_B T$  even at low temperatures. If the barrier conductance increases until  $\Gamma \sim k_B T$ , this regime is strongly coupling between the dot and the reservoirs. For non-interacting electrons and equal barriers, the Coulomb peaks in this regime have the Lorentzian line shape [21, 22]. This means that the electron tunneling through a discrete energy level is approximately Lorentzian. The measured conductance peak fitting in strongly coupling with thermally broadened Lorentzian is better than that with thermally broadened function in Eq. 2.46.

### 2.2.2. Non-linear Transport Regime

The details about relevant energy scales of the dot can be obtained by measuring the nonlinear dependence of the current on the source-drain voltage  $V_{sd}$ . We can combine the result in the measurement of the differential conductance  $dI/dV_{sd}$  as a function of gate voltage and as a function of the source-drain voltage  $V_{sd}$  in the measurement of the *Coulomb blockade diamonds* [23]. The measurement of Coulomb blockade diamonds corresponds to taking many gate voltage swept at various source-drain voltages. The finite source-drain voltage  $V_{sd}$  is applied to a quantum dot. The current depends on the number of available states in the bias window  $eV_{sd} = \mu_s - \mu_d$ . The number of available states can be changed by varying  $V_{sd}$ . We first consider the case that the applied source-drain is less than the energy level spacing  $eV_{sd} < \Delta E$ . Figure 2.10(a) shows the schematic of Coulomb diamond which corresponds to alignment of energy levels in the dot within bias window as shown in Fig. 2.10(b)-(d).

The differential conductance is represented by the gray triangular shaped regions in Fig. 2.10(a). Black lines indicate alignment between one of the electrochemical potentials in the leads with the electrochemical potential in the dot. The intersection of these black lines on axis of the gate voltage is the sequence of the conductance peaks at zero-bias voltage, which is also obtained in the linear measurement. Between these conductance peaks there are diamond shaped white regions in which electron transport is completely suppressed as a result of the Coulomb blockade effect. As long as  $\mu_s \geq \mu_{dot}(N) \geq \mu_d$  in Fig. 2.10(b)-(d), the electron can keep tunneling through the dot from source to drain. Consider the vertical dashed line in Fig. 2.10(a), with increasing gate voltage, the current increases from zero at point (b),  $\mu_s = \mu_{dot}(N, V_g)$ , to a finite value and then remains constant until point (d),  $\mu_d = \mu_{dot}(N, V_g + \Delta V_g)$ , where it drops again to zero. From Eq. 2.39, we can get  $\mu_d = \mu_{dot}(N, V_g) - e\alpha\Delta V_g$  and the separation between point (b) and (d) in gate voltage can be calculated

$$|\Delta V_g| = \frac{|V_{sd}|}{\alpha}. \quad (2.47)$$

If source-drain voltage keeps increasing, the boundary line of a Coulomb diamond will intersect, for example, at the encircled point in Fig. 2.10(a) where  $\mu_{dot}(N) = \mu_s$  and  $\mu_{dot}(N+1) = \mu_d$ . From Eq. 2.41, we can obtain

$$V_{sd} = \frac{1}{e} \left( \Delta E + \frac{e^2}{C_\Sigma} \right). \quad (2.48)$$

It can be seen that the bias voltage difference between current changes measures the addition energy.

So far we have determined the electrons tunnel through the dot involving the ground states, for example, the transitions  $(N-1, 0) \rightarrow (N, 0) \rightarrow (N-1, 0)$  where index 0 refers to the ground state.

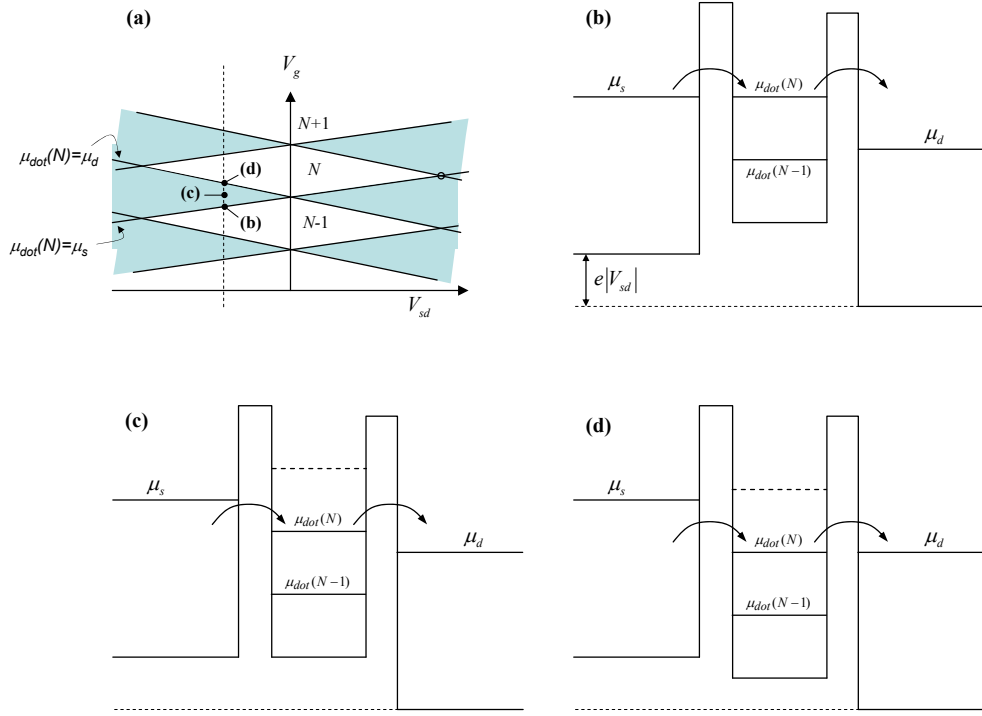


Figure 2.10.: (a) Schematic Coulomb blockade diamonds. Current can flow only in the gray shaped regions. The points labeled (b)-(d) refer to the situations schematically representing a quantum dot with finite bias source-drain for various gate voltage. The electron transport is indicated by arrows. Situations is shown with (b)  $\mu_s = \mu_{dot}(N)$ , (c)  $\mu_s > \mu_{dot}(N) > \mu_d$ , and (d)  $\mu_{dot}(N) = \mu_d$

When  $eV_{sd} > \Delta E$ , the tunneling through excited states of the dot leads to additional structure in the Coulomb blockade diamond. For example, the transport can be achieved starting from the dot in  $(N - 1)$  electron ground state into an  $N$  electron excited state back into the  $(N - 1)$  electron ground state:  $(N - 1, 0) \rightarrow (N, 1) \rightarrow (N - 1, 0)$  where index 1 refer to the first excited state. In more generally the transition can be written as  $(N - 1, m) \rightarrow (N, n) \rightarrow (N - 1, m)$ . The energy for adding an electron to the dot in this transition process is defined by  $\mu_{dot}^{n,m}(N)$ . All  $\mu_{dot}^{n,0}(N)$  with  $n > 0$  are larger than  $\mu_{dot}^{0,0}(N) = \mu_{dot}(N)$ , whereas all  $\mu_{dot}^{0,m}(N)$  with  $m > 0$  are smaller.

If the excited states and  $\mu_{dot}(N)$  are within the bias window, the excited states can contribute the electron tunneling through the dot as shown in Fig. 2.11(a). The electrons can tunnel into the dot not only to the ground state but also to the first excited state. These extra tunneling channels can be detected as an increase in the current in the Coulomb blockade diamond.

Figure 2.11(b) shows that the additional lines occur outside the Coulomb blockade diamond whereas no lines are found in the diamonds themselves. The dashed lines running parallel to the upper boundaries of the  $N - 1$  electron diamond indicate the energy of an  $N$  electron excited state. The dotted lines beneath the lower boundaries of the  $N - 1$  electron diamond indicate the  $N - 2$  electron excited state.

The dashed lines are shifted from the upper edges of the diamond by  $\Delta^*/(e\alpha)$ , where  $\Delta^*$  is the energy difference between the ground state and the first excited state or can be called the excitation energy of the  $N$  electrons system. The simplest estimate within the constant interaction model can identify this excitation energy with the single particle energy spacing  $\Delta E$ . Therefore, the Coulomb blockade measurement can be used for excited state spectroscopy.

## 2. Theoretical Background

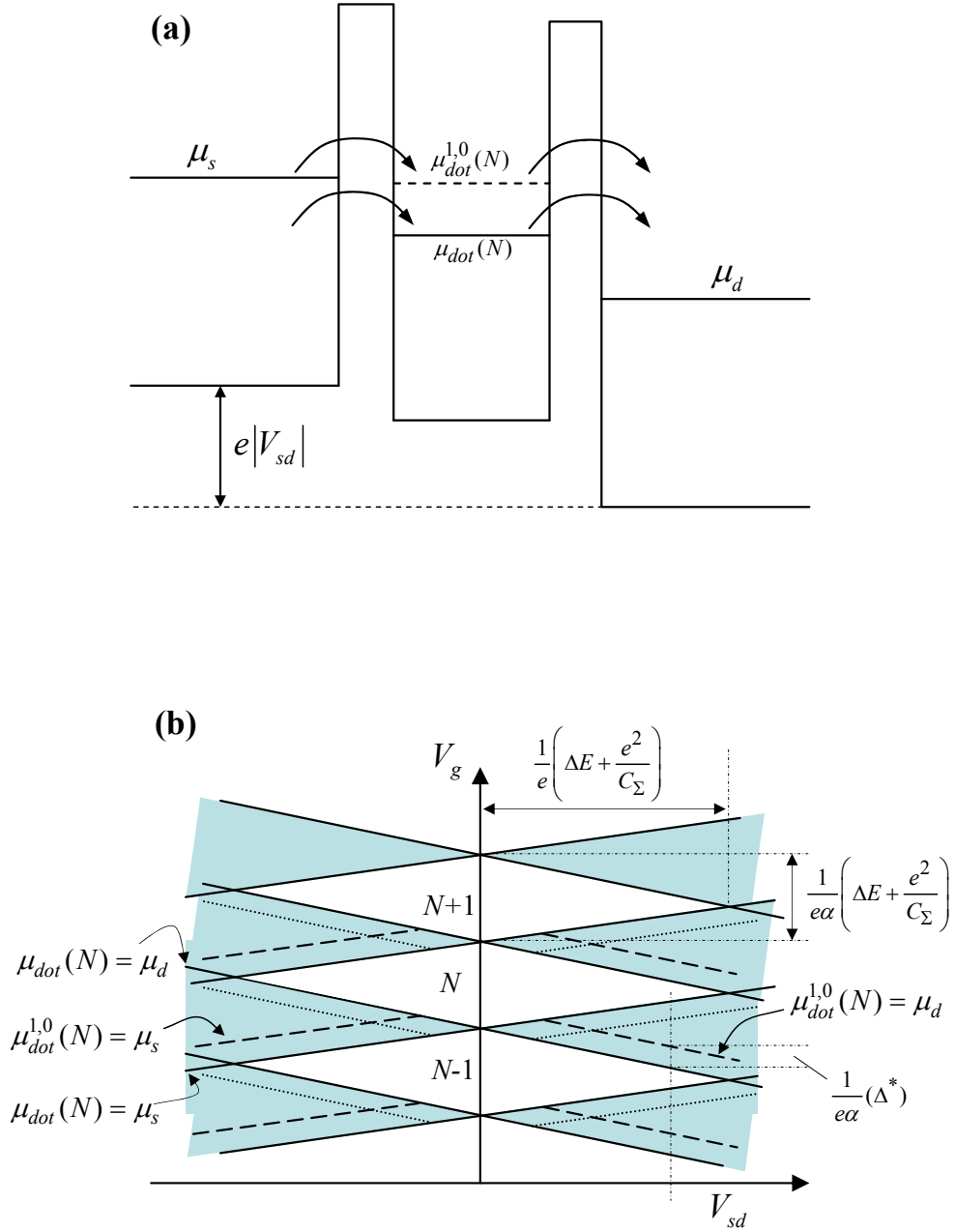


Figure 2.11.: (a) Schematic representation of a quantum dot at finite source-drain voltage. The excited state is indicated as dashed line. The  $\mu_{dot}^{1,0}(N)$  is in the bias window and therefore contributes to electron transport through the dot. (b) Schematic Coulomb blockade diamonds with the excited states. Current can flow in the gray shaped regions. The dashed lines indicate the excited states

## 2.3. The Kondo Effect in Quantum Dot System

The original Kondo effect is found in the conductance measurement of the metals containing a small concentration of magnetic impurities [24]. When the temperature is lowered, the electrical resistance of a pure metal, for example gold and copper, usually drops because the lattice vibrations decrease and electrons can travel through a metallic crystal more easily. The resistance, however, saturates at finite resistance as the temperature decrease below about 10 K because of static defects or nonmagnetic impurities in the material. Although more defects are added and increase the saturation resistance, the temperature dependence characteristic of the resistance remains the same. While the resistance of pure metals tends towards a saturated resistance, the resistance of metals with magnetic impurities, such as cobalt, shows a logarithmic increase as temperature is lowered further [25]. This is the Kondo effect and the temperature at which the resistance starts to increase again is called *Kondo temperature* ( $T_K$ ).

The effect is named after the Japanese theorist J. Kondo who developed the theory to explain the temperature dependence of this anomalous resistance. The important point of this effect is the exchange interaction between the localized magnetic moment and the spins of conduction band electrons known as Kondo cloud. In order to consider the scattering from these localized magnetic ions, the model of a magnetic impurity was introduced by Phil Anderson in 1961 [26]. The Anderson impurity model and his approach can be used to predict the properties of a system close to absolute zero temperature. According to the Kondo effect, at the temperature below  $T_K$ , the magnetic moment of the impurity ion is screened entirely by the spins of the electrons in the metal. The Kondo effect only occurs when the total spin of all electrons in the impurity atom is non-zero or unpaired. A spin singlet state is formed between the unpaired localized electron and delocalized electrons at the Fermi energy of the host metal at low temperature.

A quantum dot or a single electron transistor (SET) containing a small droplet of localized electrons and being strongly coupled to conducting lead is analogous to the localized magnetic impurity within the metal. Therefore it has been predicted that the Kondo effect should be able to occur in the quantum dot and be explained by Anderson impurity model [27]-[29]. In the metal, the Kondo cloud increases scattering which increases the resistivity, but the analogous event in a quantum dot is the mechanism for enhancing the the conductance in the Coulomb blockade at zero bias. This novel Kondo effect has been found and studied in various quantum dot systems, vertical and lateral quantum dots, which have odd number of electrons in the droplet and hence one electron is unpaired [30]-[32]. Also there are many experiments done in order to investigate the Kondo effect in the applied magnetic field [31, 33, 34].

Consider the Coulomb blockade regime for a quantum dot system occupied by an odd number of electrons. In the Anderson model, a quantum dot is approximated as a single localized state coupled by tunneling to two electron reservoirs. Hence the dot with energy levels in Fig. 2.12(a) is separated from the leads by tunnel barriers. The state  $\varepsilon_0$  in energy diagram is a single spin degenerate energy state and referenced to the Fermi level in the leads. The  $\varepsilon_0$  is occupied by one electron of either spin up or spin down. In this diagram we show a spin up electron occupies the state. In order to add another electron to the dot, the addition energy  $U$  is required. If we assume that  $\mu_L \simeq \mu_R \simeq \mu_F = 0$ ,  $\varepsilon_0 < 0$ , but  $\varepsilon_0 + U > 0$ . The electron tunneling is blocked at the initial state in Fig. 2.12(a). An electron cannot tunnel onto the dot because the energy level  $\varepsilon_0 + U$  is higher than the Fermi energies of the leads,  $\mu_L$  and  $\mu_R$ . The electron on the dot also cannot tunnel off because  $\varepsilon_0 < \mu_L, \mu_R$ .

However, the electron on the dot can tunnel into the right lead with rate  $\Gamma/h$ , which leads to Lorentzian broadening of the localized state energies with full width at half maximum (FWHM)  $\Gamma$  [35, 36]. This electron tunneling occurs in the virtual intermediate state as shown in Fig. 2.12(b) and then be replaced by an electron with the opposite spin from the left lead.

## 2. Theoretical Background

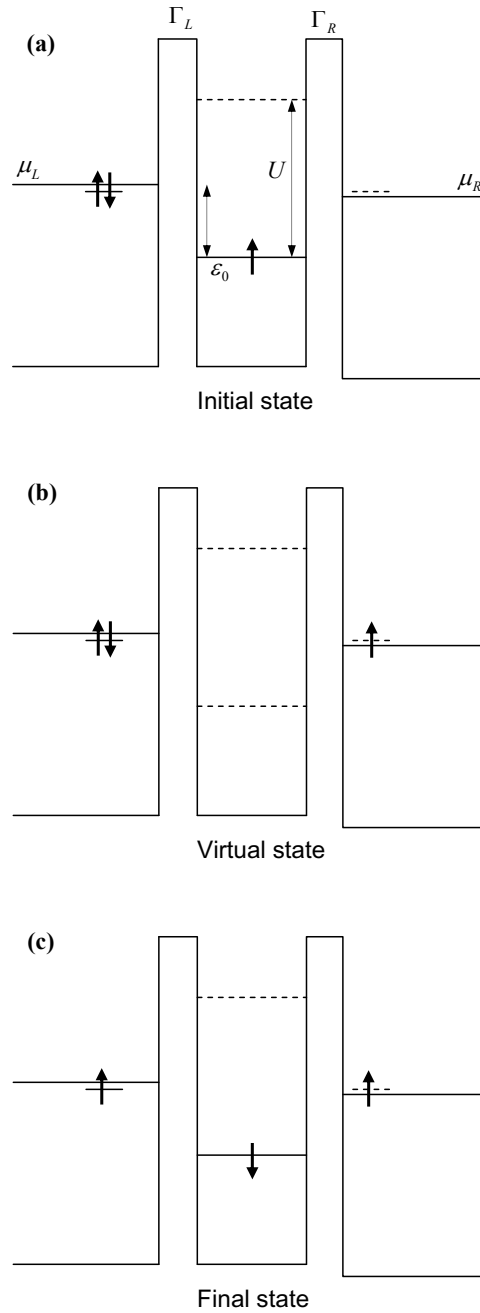


Figure 2.12.: Schematic energy diagram of a quantum dot for Kondo effect. (a) At the initial state, an unpaired spin electron is occupied the energy state  $\varepsilon_0$  on the dot. The  $U$  is the single electron charging energy, and  $\Gamma_L$  and  $\Gamma_R$  give the tunnel coupling to the left and right leads. (b) The virtual state can occur that converts the spin of electron. The spin up electron tunnels off the dot and the spin down tunnels on the dot in (c) at the final state. An electron then transfers from one side of the dot to the another.

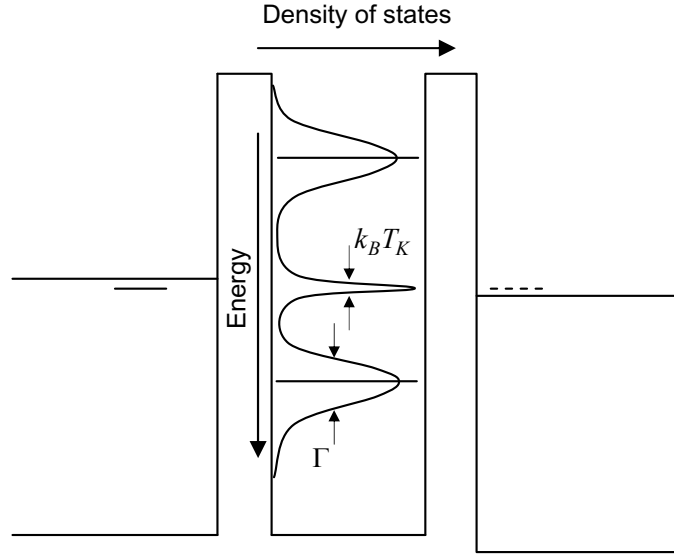


Figure 2.13.: Tunneling density of states for Kondo effect showing a sharp peak of width  $k_B T_K$  at Fermi energy level of the source and drain reservoirs in addition to the broadened level at  $\varepsilon_0$  of width  $\Gamma$ .

Therefore the quantum dot has reversed the direction of its unpaired spin in the final state of Fig. 2.12(c). The success of spin-flip process effectively screen the local spin on the dot such that the electrons in the leads and on the dot together form a spin-singlet state [31]. This is analogous to the singlet state formed by the magnetic impurity in the metal. Figure 2.13 shows that the narrow peak in the tunneling density of states is exactly at the Fermi energies of the leads,  $\mu_L \simeq \mu_R$ , leading to the enhanced conductance through the dot. This sharp resonance of the density of states has been known as the Kondo resonance, and the width of this resonance peak is defined by  $k_B T_K$ .

At the Kondo resonance peak, an enhanced current is exhibited in the Coulomb blockade at zero bias voltage. This effect shows a zero-bias anomaly in the Coulomb diamond of the nonlinear measurement for a quantum dot. When a bias voltage  $V_{sd}$  is applied between source and drain,  $eV_{sd} = \mu_L - \mu_R$ , the Kondo peak in the density of states splits into two peaks. One peak is located at each chemical potential [28, 31]. The energy  $\varepsilon_0$  and  $\Gamma = \Gamma_L + \Gamma_R$ , the energy broadening of the discrete states on the dot caused by the coupling to the left and right leads, can be tuned by adjusting the negative gate voltage of the dot system. The Kondo resonance with non-zero bias and asymmetric tunneling barrier has also been investigated that the resonance peak of the density of states is pinned to the the chemical potential of the thin barrier or strong coupling side [37, 38].

According to the Anderson model, the parameter  $\tilde{\varepsilon} \equiv \varepsilon_0/\Gamma$  has been defined to distinguish the Kondo regime from other regimes [35]. There are three interesting regimes, each of which has different transport properties, in this model: the Kondo regime  $\tilde{\varepsilon}_0 \ll -0.5$  which describes the system of dilute magnetic impurities in metals, the mixed-valence regime  $-0.5 \lesssim \tilde{\varepsilon} \lesssim 0$  which provides some understanding of heavy-fermion compounds [39], and the empty orbital regime  $\tilde{\varepsilon} \gtrsim 0$ . The Kondo effect only occurs when the temperature of the system is comparable to or lower than the Kondo temperature  $T_K$ , which is the characteristic temperature scale of the Kondo effect [35]. The Kondo temperature  $T_K$ , is given by

$$k_B T_K = \frac{\sqrt{\Gamma U}}{2} e^{\pi \varepsilon_0 (\varepsilon_0 + U) / \Gamma U}, \quad (2.49)$$

## 2. Theoretical Background

where  $\Gamma$  is the FWHM in the energy scale unit of the localized state in the dot, reflecting the tunneling coupling between the dot and the leads,  $\varepsilon_0$  is the energy of the localized state,  $U$  is the addition energy for the next electron, and  $k_B$  is the Boltzmann constant. Since  $\varepsilon_0 = \alpha V_g + \text{constant}$ , then we can obtain that  $U = \alpha \Delta V_g$ , where  $V_g$  is the gate voltage used to adjust the position of the energy state in the dot.

It is obvious that the Kondo temperature  $T_K$  is higher with larger tunneling coupling  $\Gamma$ . Therefore the Kondo effect can only be observed in the strongly coupling regime of the dot. Furthermore, the  $T_K$  increases as one of the energy state  $\varepsilon_0$  and  $\varepsilon_0 + U$  is tuned closer to the Fermi energies in the leads. A further condition for observing the Kondo effect is that the single-particle level spacing  $\Delta$  is larger than the tunneling coupling,  $\Delta \gtrsim \Gamma$ , and hence requires a small quantum dot.

According to the work about the scaling theory in [35, 40], the temperature dependence of the conductance  $G$  in the Kondo regime follows the empirical form

$$G(T) = G_0 \left( \frac{T_K'^2}{T^2 + T_K'^2} \right)^s \quad (2.50)$$

with  $T_K' = T_K / \sqrt{2^{1/s} - 1}$ , where  $G_0$  is the zero temperature extrapolation of the conductance,  $G_0 = 2e^2/h$  is the unitarity limit for symmetric tunneling to the two leads, and  $s$  is the fit parameter that is approximately 0.2 for spin 1/2 system in the Kondo regime, as obtained in [40]. The Kondo effect has given rise to a lot of research, both theoretical and experimental and is attractive for study further.

### 2.4. Electron Transport through Double Quantum Dots

Quantum dots in semiconductors are submicron islands of electrons that are influenced by the interplay of quantum mechanical and electrostatic effects [41, 42]. In low temperature tunneling measurements through double dot systems defined in a two-dimensional electron gas (2DEG) by tunable gates as in Fig 2.14. The confinement of the dots can be obtained by applying negative voltage to the lateral tunneling gates to deplete the electron in 2DEG beneath. The interdot tunneling can leads to a variety of phenomena not observed for single dots. Where single quantum dots are often referred to as "artificial atoms", double quantum dots can be coupled to form an "artificial molecule". They depend on the strength of the interdot coupling to be able to form ionic like (weakly tunnel coupling) or covalent like bonds (strongly tunnel coupling).

In the case of ionic like bonding the electrons are localized and well quantized on the individual dots. The binding is formed by a static redistribution of electrons leading to an attractive Coulomb interaction. Electrostatically coupled dots with negligible interdot tunnel conductance are covered by the orthodox Coulomb blockade theory. In the case of covalent bonding, the electron state in two dots are quantum mechanically coupled and an electron can tunnel many times between the two dots in a phase-coherent way which is delocalized over two dots. The binding state of a strongly coupled artificial molecule has a lower energy than the energies of the original states of the individual dots. This energy gain forms the binding force between the two dots [20]. This behaves like the real covalent molecules in which the bonding is weaker than that of ionic molecules.

In this section the electron transport through lateral double quantum dots coupled in series have been summarized. Tunnel coupling between the quantum dots can be continuously adjusted from the weakly coupling regime to the strongly coupling regime. In the weak tunnel coupling regime, the dots are well isolated and the numbers of electrons on each dot,  $n_1$  and  $n_2$ , are quantized. In this regime Coulomb blockade theory can apply to each dot individually. On the



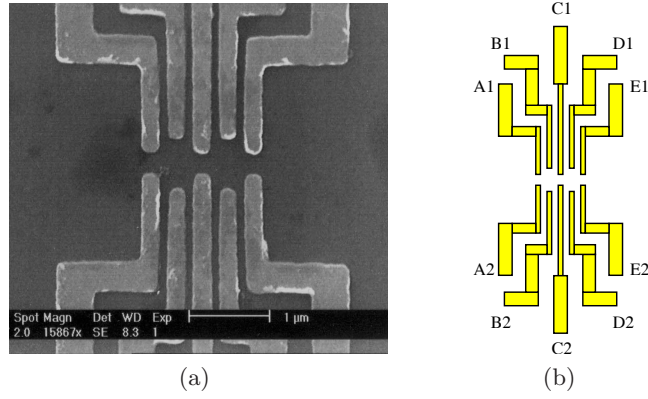


Figure 2.14.: Double dot structure fabricated by electron beam lithography on GaAs/ $\text{Al}_x\text{Ga}_{1-x}\text{As}$  heterostructure containing a 2DEG. (a) Scanning electron micrograph of the series double dot system compounded with five pairs of metallic gates. (b) Schematic drawing of the structure. The gates are energized with negative voltage to form the double dot.

other hand the two dots effectively are merged into one big dot in the strong tunnel coupling regime. The  $n_1$  and  $n_2$  are not individually well defined and the coupled dot system acts like an artificial molecule.

Transport through quantum dots depends strongly on the strength of tunnel coupling between the dot and its surroundings. When the coupled dot system is well isolated or tunnel conductance between a quantum dot and surroundings leads is weak ( $G_{dot-lead} \ll 2e^2/h$ ) and the total number of electrons  $n_{tot} = n_1 + n_2$  is quantized, the transport properties are well described by standard Coulomb blockade theory for the entire double dot system to probe its ground state energy. In order to understand double dot systems, the charge stability diagram has been studied [20].

### 2.4.1. Charge Stability Diagram

In this section the charge stability or *honeycomb* diagram is introduced; that is the visual diagram of the equilibrium charge states of two quantum dots coupled in series. Fig. 2.15 shows the network of tunnel resistors and capacitances representing two quantum dots coupled in series. The configuration of the number of electrons on dot1 and dot2 is  $(n_1, n_2)$ . Each dot is capacitively coupled to the electrode with gate voltage  $V_{g1(2)}$  through a capacitor  $C_{g1(2)}$  and to the source (S) or drain (D) contact through a tunnel barriers which is characterized by a tunnel resistor  $R_{L(R)}$  and a capacitor  $C_{L(R)}$  connected in parallel, as indicated in the inset. The interdot tunnel barrier is represented the coupling interaction between dots by a tunnel resistor  $R_{int}$  and a capacitor  $C_{int}$  in parallel. The bias voltage  $V$  is applied to the source contact with the drain contact grounded. we first consider the electron transport in the linear regime, then  $V \approx 0$ . For this model, we assume that the cross capacitances, other voltage sources, and stray capacitances are negligible. The gate voltage  $V_{g1(2)}$  changes the charge on dot1(2) only and has no effect on the charge of the other dot.

In order to study the structure of double dot system we determine the electrostatic coupling between the quantum dots by using the capacitance model [20, 43]. From this model we can represent the coupling between each dot and the electrodes by a capacitance matrix. The general

## 2. Theoretical Background

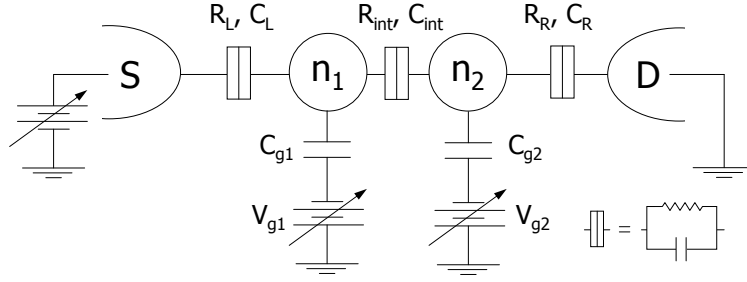


Figure 2.15.: Diagram of the resistors and capacitors representing two quantum dots coupled in series. The tunnel barrier are characterized by a tunnel resistor and a capacitor, as indicated in the inset.

expression for the charges on the individual dot are related to the electrostatic potential by

$$Q_i = \sum_{j=0}^n q_{ij} = \sum_{j=0}^n C_{ij}(V_i - V_j), \quad (2.51)$$

where  $i$  is the index denoting the electrodes and dots. The total charge on dot  $i$  is the sum of the charges on all of the capacitors connected to dot  $i$ . The voltage source in the network can be treated as a node with large capacitance to ground and large charge on it such that  $V = Q/C$ . Since the voltage on the voltage source is already known, only the voltages on the other nodes need to be determined. Here we define the electrostatic potential at left and right lead electrode by  $V_L$  and  $V_R$  respectively. The ground is defined to be zero potential and potential of dot1(2) is defined by  $V_1(2)$ . Therefore we can express the total charge  $Q_{1(2)}$  on dot1(2) as

$$\begin{aligned} Q_1 &= C_L(V_1 - V_L) + C_{g1}(V_1 - V_{g1}) + C_{int}(V_1 - V_2), \\ Q_2 &= C_R(V_2 - V_R) + C_{g2}(V_2 - V_{g2}) + C_{int}(V_2 - V_1). \end{aligned} \quad (2.52)$$

We can write this as

$$\begin{pmatrix} Q_1 + C_L V_L + C_{g1} V_{g1} \\ Q_2 + C_R V_R + C_{g2} V_{g2} \end{pmatrix} = \begin{pmatrix} C_1 & -C_{int} \\ -C_{int} & C_2 \end{pmatrix} \begin{pmatrix} V_1 \\ V_2 \end{pmatrix}, \quad (2.53)$$

where  $C_{1(2)} = C_{L(R)} + C_{g1(2)} + C_{int}$ .  $C_1$  and  $C_2$  are the sum of all capacitances coupled to the dot 1 and dot 2 respectively. We can invert the equation above to obtain

$$\begin{pmatrix} V_1 \\ V_2 \end{pmatrix} = \frac{1}{C_1 C_2 - C_{int}^2} \begin{pmatrix} C_2 & C_{int} \\ C_{int} & C_1 \end{pmatrix} \begin{pmatrix} Q_1 + C_L V_L + C_{g1} V_{g1} \\ Q_2 + C_R V_R + C_{g2} V_{g2} \end{pmatrix}. \quad (2.54)$$

The total electrostatic energy of the double dot system is expressed using the capacitance matrix and then given by

$$\begin{aligned} U &= \frac{1}{2} \vec{V}^T \cdot \mathbf{C} \vec{V} = \frac{1}{2} \vec{V}^T \cdot \vec{Q} \\ &= \frac{1}{2} \vec{Q}^T \begin{pmatrix} C_1 & -C_{int} \\ -C_{int} & C_2 \end{pmatrix}^{-1} \vec{Q}, \end{aligned} \quad (2.55)$$

where

$$\vec{Q} = \begin{pmatrix} Q_1 + C_L V_L + C_{g1} V_{g1} \\ Q_2 + C_R V_R + C_{g2} V_{g2} \end{pmatrix}. \quad (2.56)$$

## 2.4. Electron Transport through Double Quantum Dots

For linear transport regime we assume  $V_L = V_R = 0$  and the total charge on dot1(2) is  $Q_{1(2)} = -eN_{1(2)}$ . By using Eqs. 2.54 and 2.55 the double dot electrostatic energy  $U$  becomes

$$U(n_1, n_2) = \frac{1}{2}(n_1^2 E_{C1} + n_2^2 E_{C2}) + n_1 n_2 E_{Cint} + f(V_{g1}, V_{g2}), \quad (2.57)$$

$$f(V_{g1}, V_{g2}) = -\frac{1}{e} [C_{g1} V_{g1} (n_1 E_{C1} + n_2 E_{Cint}) + C_{g2} V_{g2} (n_1 E_{Cint} + n_2 E_{C2})] + \frac{1}{e^2} \left[ \frac{1}{2} C_{g1}^2 V_{g1}^2 E_{C1} + \frac{1}{2} C_{g2}^2 V_{g2}^2 E_{C2} + C_{g1} V_{g1} C_{g2} V_{g2} E_{Cint} \right], \quad (2.58)$$

where  $E_{C1}$  and  $E_{C2}$  can be interpreted as the charging energy of each dot,  $E_{Cint}$  is the electrostatic coupling energy and  $e$  is the electron charge. It can be seen that the total electrostatic potential is controlled by the two gate voltages  $V_{g1}$  and  $V_{g2}$ . The coupling energy  $E_{Cint}$  is the energy change of one dot when electron is added to the other dot. These energies can be expressed in terms of the capacitances as follows:

$$E_{C1} = \frac{e^2}{C_1} \left( \frac{1}{1 - \frac{C_{int}^2}{C_1 C_2}} \right), \quad (2.59)$$

$$E_{C2} = \frac{e^2}{C_2} \left( \frac{1}{1 - \frac{C_{int}^2}{C_1 C_2}} \right), \quad (2.60)$$

$$E_{Cint} = \frac{e^2}{C_{int}} \left( \frac{1}{\frac{C_1 C_2}{C_{int}^2} - 1} \right), \quad (2.61)$$

In the case of two dots with equal total capacitance,  $C_\Sigma = C_1 = C_2 = C_{L(R)} + C_{g1(2)} + C_{int}$  can be defined to be the total capacitance of each dot to ground. From the double dot electrostatic energy in Eqs. 2.57 and 2.58 the equation can be reduced and re-written as

$$U(n_1, n_2, V_{g1}, V_{g2}) = \frac{1}{2C_\Sigma(1 - \alpha^2)} [(C_{g1} V_{g1} - n_1 e)^2 + (C_{g2} V_{g2} - n_2 e)^2 + 2\alpha(C_{g1} V_{g1} - n_1 e)(C_{g2} V_{g2} - n_2 e)], \quad (2.62)$$

where  $\alpha = C_{int}/C_\Sigma$ . According to Eqs. 2.57, 2.58 and 2.62, the total electrostatic energy surface  $U(V_{g1}, V_{g2})$  is a paraboloid for the given values of  $n_1$  and  $n_2$ . For each pair of gate voltage values, there is a ground state of the double dot system. The charge state configuration is determined by the values of  $n_1$  and  $n_2$  that minimize the total electrostatic energy. The ground state of electrostatic energy is plotted in Fig. 2.16 which is the array of paraboloids corresponding to different charge configuration  $(n_1, n_2)$ . The electrostatic energy  $U$  also presents a barrier of tunneling as the Coulomb blockade. Therefore an electron can tunnel through double dot in series only when both  $n_1$  and  $n_2$  can change simultaneously at the intersections of three paraboloids.

When the interdot coupling is very weak,  $C_{int} = 0$ , and hence  $E_{Cint} = 0$ , Eq. 2.57 reduces to

$$U(n_1, n_2) = \frac{(C_{g1} V_{g1} - n_1 e)^2}{2C_1} + \frac{(C_{g2} V_{g2} - n_2 e)^2}{2C_2}. \quad (2.63)$$

This is the sum of the energies of two independent dots. In the case of strongly interdot coupling,  $C_{int}$  becomes the dominant capacitance ( $C_{int}/C_{1(2)} \rightarrow 1$ ), the total electrostatic energy is given by

$$U(n_1, n_2) = \frac{[C_{g1} V_{g1} + C_{g2} V_{g2} - (n_1 + n_2)e]^2}{2(C_1 + C_2 - 2C_{int})}. \quad (2.64)$$

## 2. Theoretical Background

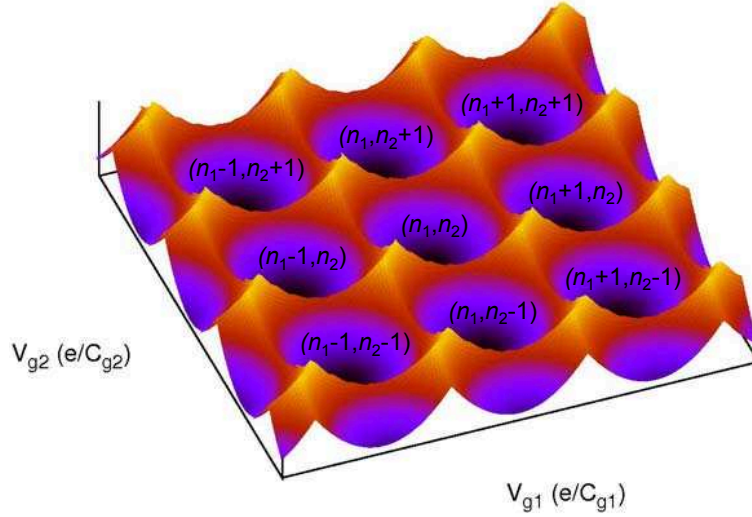


Figure 2.16.: Total electrostatic energy of the double dot system. Plot of the minimum energy surface as a function of center gate voltages calculated from the capacitance model. Dark regions are minima of the energy paraboloids for given occupation numbers, e.g.  $(n_1, n_2)$ . Bright regions are the intersections of paraboloids corresponding to different charge states. The Coulomb blockade is lifted and the current may flow at the intersection points of three paraboloids. This plot is generated from the simulation program written by D. Schefzyk.

This is the energy of a large single dot with a charge configuration of  $n_1 + n_2$  and a capacitance of the dot to the outside world:

$$C_1 + C_2 - 2C_{int} = C_L + C_{g1} + C_{g2} + C_R. \quad (2.65)$$

In order to obtain the energy needed to add a single  $n_{1(2)}$ th electron to dot1(2) while keeping the electrons in dot2(1) constant at  $n_{2(1)}$ , we use the total electrostatic energy expressed in Eqs. 2.57 and 2.58 to calculate for this quantity. This value can be called the electrochemical potential of the dot1(2) which is given by

$$\begin{aligned} \mu_1(n_1, n_2) &\equiv U(n_1, n_2) - U(n_1 - 1, n_2) \\ &= (n_1 - \frac{1}{2})E_{C1} + n_2 E_{Cint} - \frac{1}{e}(C_{g1}V_{g1}E_{C1} + C_{g2}V_{g2}E_{Cint}), \end{aligned} \quad (2.66)$$

$$\begin{aligned} \mu_2(n_1, n_2) &\equiv U(n_1, n_2) - U(n_1, n_2 - 1) \\ &= (n_2 - \frac{1}{2})E_{C2} + n_1 E_{Cint} - \frac{1}{e}(C_{g1}V_{g1}E_{Cint} + C_{g2}V_{g2}E_{C2}). \end{aligned} \quad (2.67)$$

At fixed gate voltage, if the number of electron in dot1(2)  $N_{1(2)}$  is changed by 1, the electrochemical potential  $\mu_{1(2)}(n_1, n_2)$  will be changed by  $E_{C1(2)}$ , as the followings

$$\begin{aligned} \mu_1(n_1 + 1, n_2) - \mu_1(n_1, n_2) &= E_{C1}, \\ \mu_2(n_1, n_2 + 1) - \mu_2(n_1, n_2) &= E_{C2}, \end{aligned} \quad (2.68)$$

and

$$\mu_1(n_1, n_2 + 1) - \mu_1(n_1, n_2) = \mu_2(n_1 + 1, n_2) - \mu_2(n_1, n_2) = E_{Cint}. \quad (2.69)$$

The  $E_{C1(2)}$  from above can be called the addition energy of the dot1(2) and equals the charging energy of dot1(2) in the classical regime, while the discrete energy level spacing is added and plays a role in the quantum regime.

In the quantum regime, the strong confinement of the electrons in the dots can form a discrete energy spectrum. For the quantized energy states in the dots, the electrochemical potential for adding an electron into energy level  $n$  of the dot  $i$  can be defined by  $\mu_{i,n}$ . With the constant interaction model,  $\mu_{i,n}$  is the sum of the classical electrochemical potential  $\mu_i^{class}$ , as discussed above in Eqs. 2.66 and 2.67, and the single-particle energy  $E_n$ :  $\mu_{i,n} = \mu_i^{class} + E_n$ . Therefore the addition energy for the  $(n_1 + 1)$ th electron occupying discrete energy level  $m$  of dot1 in which the energy level  $n$  has already been occupied by  $n_1$ th electron, is

$$\begin{aligned} \mu_{1,m}(n_1 + 1, n_2) - \mu_{1,n}(n_1, n_2) &= E_{C1} + (E_m - E_n) \\ &= E_{C1} + \Delta E. \end{aligned} \quad (2.70)$$

Similarly, we can find the addition energy for dot2 as

$$\mu_{2,m}(n_1, n_2 + 1) - \mu_{2,n}(n_1, n_2) = E_{C2} + \Delta E. \quad (2.71)$$

Note that for a spin degeneracy energy level  $\Delta E$  can be zero. The configuration of electron number in both dot  $(n_1, n_2)$  that give the lowest possible total energy in dot1 or dot2, is referred to the ground state of dot1 or dot2, respectively. The  $\mu_{1(2)}(n_1, n_2)$  at ground state is the electrochemical potential for adding the  $n_{1(2)}$ th electron to the lowest unoccupied energy level of the  $(n_{1(2)} - 1)$ -electron ground state. Any configuration with higher total energy is referred to the excited state.

### Linear Transport Regime

In the linear regime electron transport occurs via ground states. In the following discussion, we use  $\mu_{1(2)}(n_1, n_2)$  to denote the ground state of the dot1(2). Hence from the electrochemical potential in Eqs. 2.66 and 2.67 including the energy level at ground state, the charge stability diagram of the double dot system can be constructed and give the equilibrium electron numbers  $n_1$  and  $n_2$  at ground states as a function of gate voltage  $V_{g1}$  and  $V_{g2}$ . In each point of this gate voltage plane, a charge state  $(n_1, n_2)$  can be seen and is the ground state of the system. The region in the plane which belong to the same charge ground state is called charge stability region. Whenever the electrochemical potentials  $\mu_s = \mu_d$  in the source and drain leads are not resonant with one of the two electrochemical potential in the double dot, the charge in the double dot system is stable. On the other hand, if electrochemical potential in either dot1 or dot2 is aligned to  $\mu_s$  or  $\mu_d$ , including the condition of  $\mu_1(n_1 + 1, n_2) = \mu_2(n_1, n_2 + 1)$ , the boundaries of the charge stability region  $(n_1, n_2)$  will be reached. These conditions, plus the fact that  $n_1$  and  $n_2$  must be integers, create hexagonal areas in the two-dimension gate voltage plane in which the charge configuration  $(n_1, n_2)$  is stable as shown in Fig. 2.17.

The typical shape of such hexagons form a honeycomb pattern in the gate voltage plane which is called charge stability diagram. In this diagram, along the diagonal lines from bottom left to top right, only the total number of electrons  $n_1 + n_2$  is changed. If we follow the diagonal lines from top left to bottom right, the total charge  $n_1 + n_2$  of the double dot system remains constant. The six corners of each hexagon of the stable charge are called *triple points* because at these points, whenever three boundaries in the honeycomb diagram meet in one point, three charge states coexist and become degenerate. Triple points are important for double dots connected in series with weakly tunnel coupling, because these are the only points where an electron can tunnel from source to drain and a conductance resonance is then found.

## 2. Theoretical Background

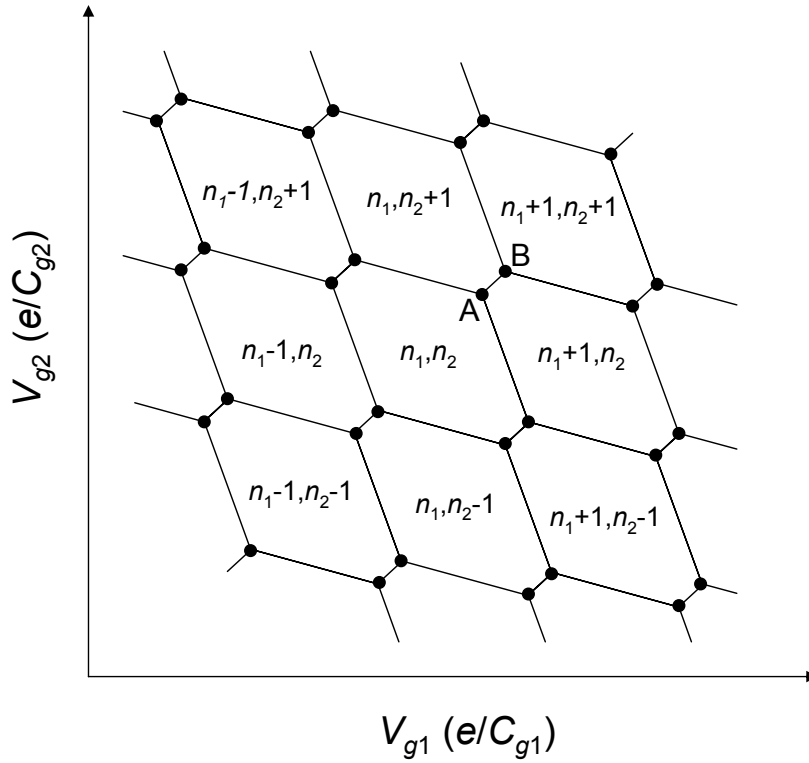


Figure 2.17.: Honeycomb pattern representing the charge stability diagram of a double dot system in the capacitance model. The vertices **A** and **B** have been discussed in the text.

We now consider the electron transport in the linear regime, which implies low source-drain bias voltage,  $\mu_{Left} - \mu_{Right} = \mu_s - \mu_d = eV_{sd} \approx 0$ . In Fig. 2.17 and 2.18 an electron can tunnel through both dots at triple points **A** and **B** in the charge stability diagram where the electrochemical potentials are aligned with each other and with the electrochemical potential of source and drain. **A** and **B** are two kind of triple points distinguished by different charge transfer process. At triple point **A**, the cycle of charge transition is

$$(n_1, n_2) \rightarrow (n_1 + 1, n_2) \rightarrow (n_1, n_2 + 1) \rightarrow (n_1, n_2),$$

which is the cycle of an electron transport through double dots from the left lead (source) to the right (drain). At the other triple point **B**, the cycle is

$$(n_1 + 1, n_2 + 1) \rightarrow (n_1 + 1, n_2) \rightarrow (n_1, n_2 + 1) \rightarrow (n_1 + 1, n_2 + 1),$$

corresponding to the transition of hole through double dots as shown in the configuration of energy level in Fig. 2.18 at point **B**. It is obvious that the direction for this cycle is opposite to the direction of electron transition [20, 44]. The situation is different at point **C** and **D**, where the electrochemical potential level in only one of the dots is aligned with the electrochemical potential of one lead, whereas another dot is in the Coulomb blockade. In this case electron transfer from source to drain is suppressed in weakly tunnel coupling between two dots and between dots and leads. The tunneling current, however, may flow and conductance is found when the interdot coupling of double dot system is increased.

The coupling between double dots can be continuously tuned via interdot tunnel conductance  $G_{int}$  from two isolated dots in the weak tunnel regime,  $G_{int} \cong 0$ , to one large dot in the strong

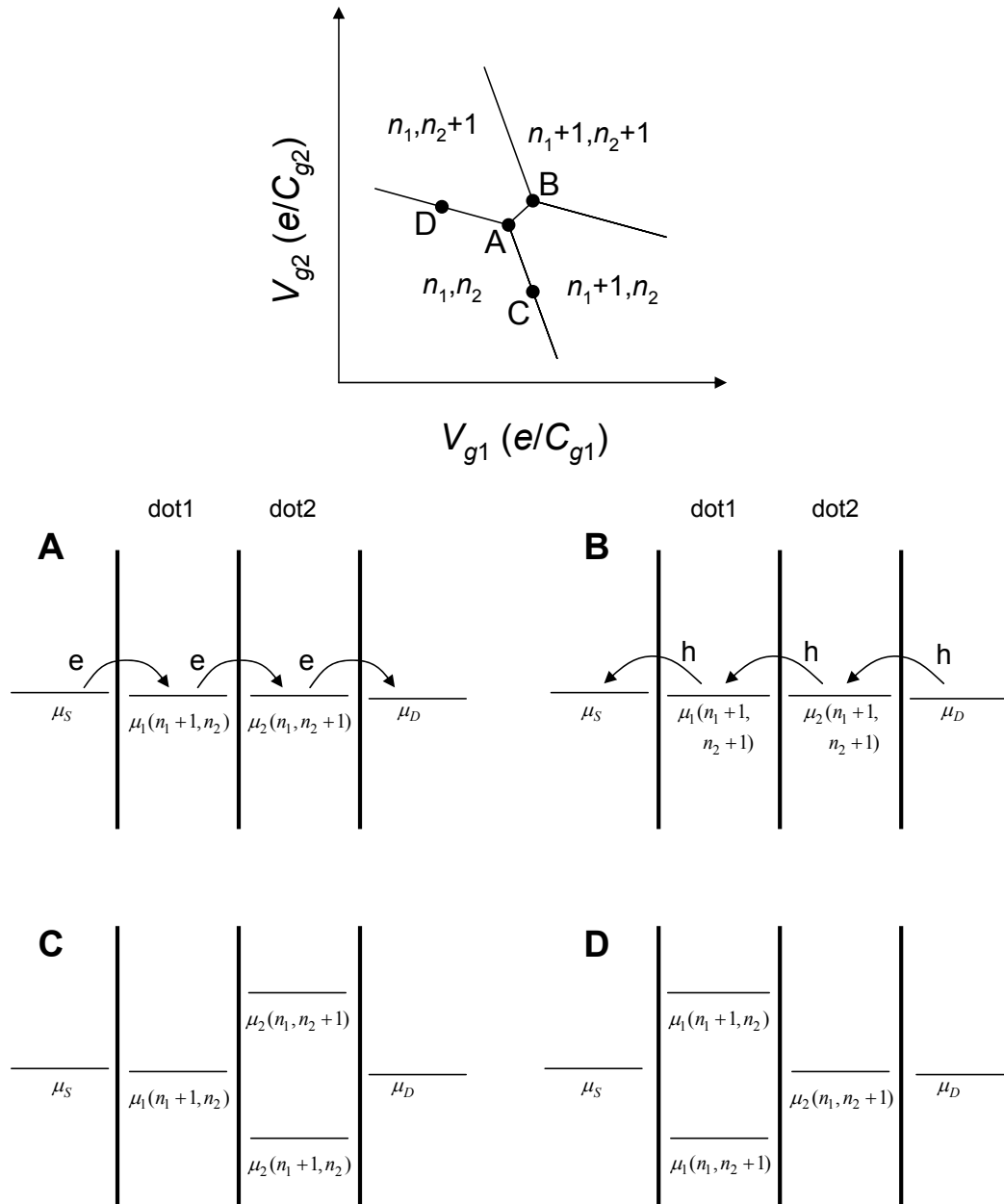


Figure 2.18.: Part of a charge stability diagram in Fig. 2.17. Schematic electrochemical potential energy levels of double dot system in four situations are shown and corresponding to four points marked with filled circles in honeycomb pattern. Four different charge states can be separated by solid lines. Two solid lines are connected at the triple point **A** and **B**. At the other solid lines, point **C** and **D**, the energy level of one dot equals the electrochemical potential of the leads.

## 2. Theoretical Background

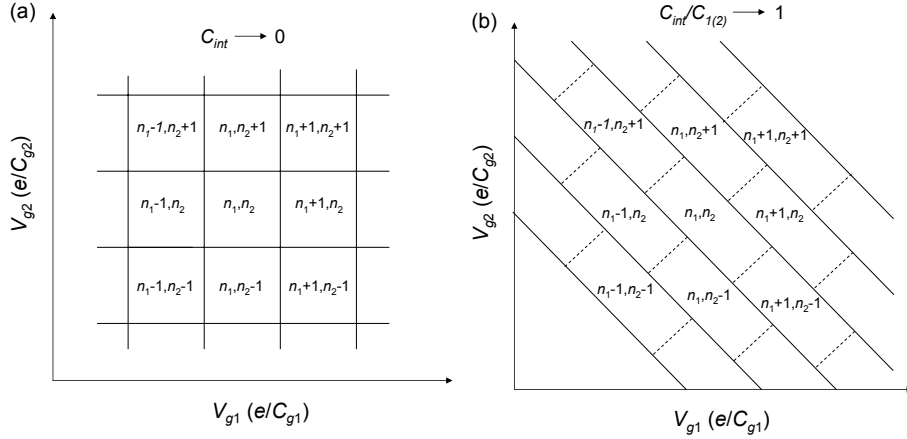


Figure 2.19.: Charge stability diagram of the double dot system in (a) weak and (b) strong tunneling coupling regime

tunnel regime,  $G_{int} \rightarrow 2e^2/h$ . This interdot conductance can be obtained by measuring the point contact conductance between dots with all other gates energized and the outer point contacts open. If double dots are decoupled completely according to the condition in Eq. 2.63,  $C_{int} \rightarrow 0$ , the pattern of charge stability diagram is shown in Fig. 2.19(a). When the interdot coupling is increased, the pattern changes to the honeycomb pattern as seen in Fig. 2.17. The vertices of the square have separated into triple points.

Figure 2.20 shows the measured double dot conductance as a function of the gate voltages. This shows the evolution of the measured conductance pattern for the double dot system from weakly coupling regime in Fig. 2.20(A) to strongly coupling regime in Fig. 2.20(F) when interdot coupling is increasing. An array of the points in Fig. 2.20(A) can be expressed by Coulomb blockade theory for capacitively coupled separate dots. These triple points are at the intersection of the hexagons defined by charge configuration  $(n_1, n_2)$ . When interdot conductance is increased, the splitting of the triple points increases because of interdot capacitance  $C_{int}$ . Figure 2.20(B) shows the arrays of triple points where the Coulomb blockade for both dots is lifted and electron can transfer through the system.

For larger interdot conductances, Fig. 2.20(C) to (F), the pattern is no longer described by the Coulomb blockade theory of individual dots. In Fig. 2.20(D) conductance can be seen clearly along the boundaries of the hexagons. The charge states are delocalized between the dots and electrons are shared by both dots in this regime. At  $G_{int} \approx 2e^2/h$  the conductance pattern becomes an array of lines corresponding to the Coulomb blockade for a single large dot. In this strongly interdot coupling,  $C_{int}/C_{1(2)} \rightarrow 1$ , the triple points can separate and reach their maximum. The pattern in charge stability diagram evolves from honeycomb to the pattern in Fig. 2.19(b) and 2.20(F). The double dot system behaves like one large dot with total charge  $n_1 + n_2$  corresponding to Eq. 2.64. We can see that the conductance grows out from the points in Fig. 2.20(A) along the boundaries between configuration with different total charge  $n_1 + n_2$ , and the shape of these boundaries changes from the zigzag pattern for weakly coupling to straight lines for strongly coupling in Fig. 2.20(F) [41]. The tunneling through double dot system is controlled by three parameters, the two gate voltages  $V_{g1}$  and  $V_{g2}$  and the interdot tunnel conductance  $G_{int}$ .

The dimensions of the honeycomb cell in Fig. 2.21 can be calculated from the capacitances



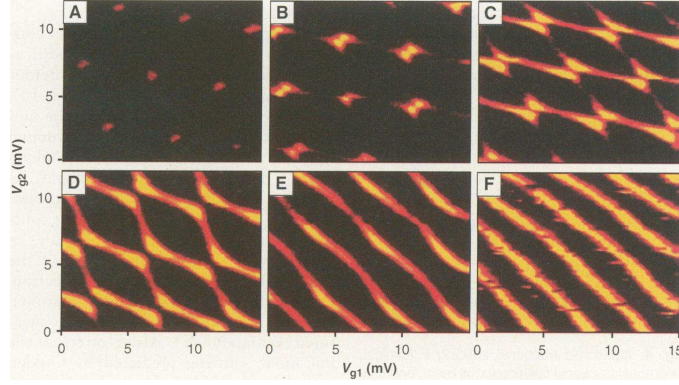


Figure 2.20.: Conductance of the double dots in series as a function of gate voltages  $V_{g1}$  and  $V_{g2}$ . The grey scale is logarithmic. Bright (dark) regions indicate high (low) conductance. Interdot conductance is given by (A)  $0.22G_0$ , (B)  $0.40G_0$ , (C)  $0.65G_0$ , (D)  $0.78G_0$ , (E)  $0.96G_0$ , and (F)  $0.98G_0$ , where  $G_0 = 2e^2/h$  [41].

by using Eqs. 2.66 and 2.67 .

$$\mu_1(n_1, n_2; V_{g1}, V_{g2}) = \mu_1(n_1 + 1, n_2; V_{g1} + \Delta V_{g1}, V_{g2})$$

We can derive

$$\Delta V_{g1} = \frac{e}{C_{g1}}. \quad (2.72)$$

Similarly, from

$$\mu_2(n_1, n_2; V_{g1}, V_{g2}) = \mu_2(n_1, n_2 + 1; V_{g1}, V_{g2} + \Delta V_{g2})$$

we obtain

$$\Delta V_{g2} = \frac{e}{C_{g2}}. \quad (2.73)$$

From

$$\mu_1(n_1, n_2; V_{g1}, V_{g2}) = \mu_1(n_1, n_2 + 1; V_{g1} + \Delta V_{g1}^{int}, V_{g2})$$

we can derive

$$\Delta V_{g1}^{int} = \frac{C_{int}}{C_2} \Delta V_{g1}. \quad (2.74)$$

Similarly, from

$$\mu_2(n_1, n_2; V_{g1}, V_{g2}) = \mu_2(n_1 + 1, n_2; V_{g1}, V_{g2} + \Delta V_{g2}^{int})$$

we obtain

$$\Delta V_{g2}^{int} = \frac{C_{int}}{C_1} \Delta V_{g2}. \quad (2.75)$$

We assume above that  $V_{g1}$  and  $V_{g2}$  only couple directly to dot1 and dot2, respectively. In practice, however, there are finite cross capacitances causing a change of the slope along the boundaries in the honeycomb diagram. With finite cross capacitances the positions of the triple points move to lower  $V_{g1(2)}$  when  $V_{g2(1)}$  is increased [20].

### 2.4.2. Conductance Peak Splitting in Double Quantum Dots

In this section we discuss the details of the electron transport through identical double dot system with a pair of center gates which are tuned simultaneously,  $V_{g1} - V_{g2} = \Delta V_g = 0$  [45, 46]. Increasing the interdot tunnel conductance  $G_{int}$  leads to a continuous transition from isolated

## 2. Theoretical Background

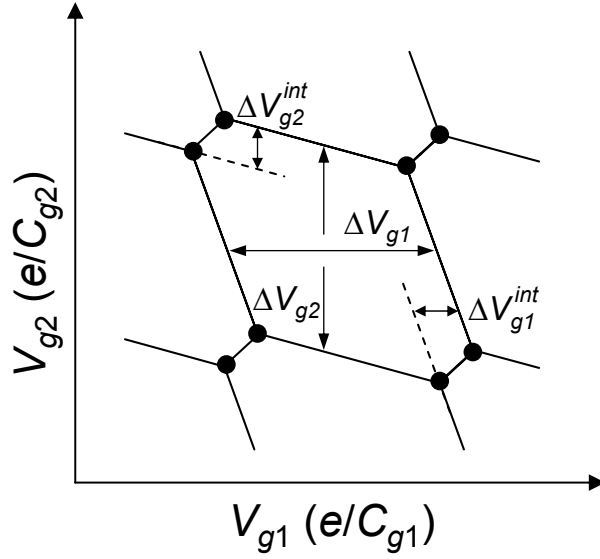


Figure 2.21.: Coulomb peak spacings in a honeycomb cell of the charge stability diagram. These spacings can be determined experimentally by connecting the triple points.

dots to one large dot as  $G_{int} \rightarrow 2e^2/h$ . Isolated dot arrays show strong Coulomb blockade conductance peaks vs gate voltage, which split into two peaks for double dots as the tunnel conductance increases. The splitting approaches zero for weak tunneling regime,  $G_{int} \ll 2e^2/h$ , and saturates as the dots merge for strong tunneling regime  $G_{int} \rightarrow 2e^2/h$ . For double dots system with unequal gate capacitances, conductance peaks show beating, quasiperiodicity and peak suppression for weak interdot tunneling. While the interdot tunneling for weakly coupled dots are consistent with classical capacitive charging, peak splitting for strongly coupled dots is a quantum phenomenon arising from interdot tunneling.

Peak splitting in double quantum dots coupled in series can be understood by considering single-dot capacitive charging models. Consider two identical dots weakly coupled to external leads, the total number of electrons  $n_{tot} = \sum n_i$  is a good quantum number, where  $n_i$  is the number of electrons on the dot  $i$ . In the case of weak coupling, the  $n_i$  for each dot are also good quantum numbers and the orthodox Coulomb blockade theory of single electron charging can be applied.

For the identical dots the total capacitance on both dots can be defined that  $C_\Sigma = C_1 = C_2$  and balanced gate voltages  $V_{g1} = V_{g2}$  gives the equal induced charges  $C_{g1}V_{g1} = C_{g2}V_{g2} = C_gV_g$ . From Eq. 2.63 in the weak tunneling coupling,  $C_{int} \approx 0$ , The total electrostatic energy of the double dot system can be re-written as

$$U = \sum_{i=1}^2 U_i = \sum_{i=1}^2 \frac{(C_g V_g - n_i e)^2}{2C_\Sigma}, \quad (2.76)$$

which is the sum of the single dot charging energies  $U_i$ , where  $C_g$ ,  $V_g$  and  $C_\Sigma$  are the gate capacitance, gate voltage, and total capacitance, assumed to be the same for both dots. In order to obtain the total energy the sum over quantized energy states  $E_n$  in the two dots is added to the electrostatic energy. From the definition above the double dots are first considered with negligible interdot tunnel conductance,  $G_{int} \rightarrow 0$ , and negligible interdot capacitances. Assuming  $E_F > U > \Delta E > k_B T$ , where  $E_F$  is the Fermi energy,  $U = e^2/C_\Sigma$  is the charging energy, and  $\Delta E \cong 2E_F/n$  is the average level spacing. At the low temperatures, the ground state for each dot charge configuration, which is determined by the value of  $n_1$  and  $n_2$ , dominates



## 2. Theoretical Background

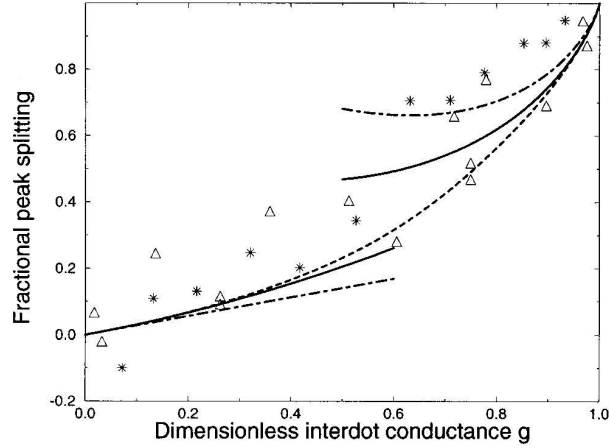


Figure 2.23.: The fractional Coulomb-blockade peak splitting  $F$  data from [45, 46] is plotted together with recent theory [49] (solid curves) and old theory [48] (dot-dashed curves) in the weak and strong tunneling limits, and the interpolation between these limits (dashed curve).

and unpolarized parabolas. In order to understand the relationship between peak splitting  $\Delta V_s$  and shifting energy  $\Delta$ , we consider the conditions of total energy at intersection of three parabolas as  $U(n_1, n_2, V_g) = U(n_1 + 1, n_2, V_g) - \Delta = U(n_1, n_2 + 1, V_g) - \Delta$  and  $U(n_1 + 1, n_2, V'_g) - \Delta = U(n_1, n_2 + 1, V'_g) - \Delta = U(n_1 + 1, n_2 + 1, V'_g)$  in which  $U(n_1 + 1, n_2)$  and  $U(n_1, n_2 + 1)$  are degenerate. We can derive

$$V_g = \frac{1}{eC_g} [(n_1 + 1/2)e^2 - C_\Sigma \Delta], \quad (2.77)$$

and

$$V'_g = \frac{1}{eC_g} [(n_2 + 1/2)e^2 + C_\Sigma \Delta]. \quad (2.78)$$

The conductance peak splitting  $\Delta V_s$  can be calculated by

$$\Delta V_s = V'_g - V_g = \frac{1}{eC_g} [2C_\Sigma \Delta + e^2(n_2 - n_1)]. \quad (2.79)$$

For  $n_1 = n_2$  the electronic configuration is an unpolarized parabola, a decrease  $\Delta$  in the energy of a polarized configuration leads to conductance peak splitting

$$\Delta V_s = \frac{2C_\Sigma}{eC_g} \Delta. \quad (2.80)$$

For strong interdot coupling, peak splitting saturates when two dots merge into one large dot. At saturation, the maximum value of a decrease in ground state energy of double dots reaches  $\Delta_{max} = e^2/4C_\Sigma$ . The fractional peak splitting  $F$  compares  $\Delta V_s$  to the peak separation  $\Delta V_p = e/C_g$  in the absence of splitting, and is defined that  $0 \leq F \leq 1$ :

$$F = \frac{\Delta}{\Delta_{max}} = \frac{2\Delta V_s}{\Delta V_p}. \quad (2.81)$$

The peak splitting is strongly correlated with the interdot tunnel conductance  $G_{int}$  which increase from a small value for  $G_{int} \cong 0$  to saturation for  $G_{int} \cong 2e^2/h$ . Conductance peak

splitting due to interdot tunneling coupling has been studied theoretically by using a variety of approaches. One of them, which has been developed by Matveev *et al.* [47] and Golden and Halperin [48, 49], is the many-body calculations of the double dot energy shifts with few tunneling modes and with  $\Delta E \ll e^2/C_\Sigma$ . The tunneling to the leads is assumed negligible compared to tunneling between two dots. These calculations predict a universal relationship between conductance peak splitting and tunnel conductance for double dots. This is found to be a function  $F(G_{int})$  of the interdot tunnel conductance that saturates exactly at  $F(2e^2/h) = 1$  for dots coupled by two tunneling modes. The fractional peak splitting is proportional to  $G_{int}$  for weak tunneling,  $G_{int} \ll 2e^2/h$ , and has a logarithmic form for strong tunneling,  $G_{int} \rightarrow 2e^2/h$ . In the weak tunneling limit the fractional peak splitting is

$$F \approx \frac{2\ln 2}{\pi^2} N_{ch} g + 0.1491 N_{ch} g^2 - 0.009798 N_{ch}^2 g^2 + \dots \quad (2.82)$$

where  $N_{ch}$  is the number of tunneling channels between the two dots,  $N_{ch} = 2$  for one spin degenerate mode, and  $g = G_{int}/(N_{ch}e^2/h)$  is the dimensionless interdot conductance per tunneling channel. In the strong tunneling limit, the fractional peak splitting for  $N_{ch} = 2$  becomes

$$F \approx 1 + \frac{16e^\gamma}{\pi^3} (1-g) \ln(1-g) - 0.425(1-g) + \dots \quad (2.83)$$

where  $\gamma \cong 0.577$ . The plot of the experimental measured fractional peak splitting  $F$  versus the dimensionless interdot conductance per channel  $g$  for  $N_{ch} = 2$  is shown in Fig. 2.23 [49], where  $F$  as a function of the dimensionless interdot conductance  $g$  in the weak and strong tunneling limits is shown. The recent theoretical curves in [49] give proper fitting to the data from Waugh *et al.* [45] and [46] for both limits. The old theoretical curves from [47] and [48] are dot-dashed lines. The dashed curve shows a possible interpolating function. As shown, the agreement between experimental data and theory is excellent, providing strong support for the charge quantization theory.



## 3. Sample Fabrication

### 3.1. Heterostructure

Our work on the mesoscopic conductors is based on GaAs/AlGaAs heterostructures as used for the substrate materials. The AlGaAs has a higher energy gap than GaAs and is doped to be n-type. When the materials are joined together, the electrons transfer from n-doped AlGaAs leaving behind positively charged donors. This space charge gives rise to an electrostatic potential that causes the band bending as a potential well in the energy band diagram of the junction, and the electrons are confined in the potential well near the GaAs/AlGaAs interface forming a thin conducting layer of two-dimensional electron gas (2DEG). We use the heterostructures prepared by molecular beam epitaxy at Cavendish laboratory, University of Cambridge to fabricate the Hallbar samples. The GaAs-AlGaAs heterojunctions used has been shown in Fig. 2.2 in the section 2.1.2.

The process of our sample fabrication can be presented in Fig. 3.1. The process starts from a heterostructure substrate with 2DEG etched to form Hallbar on the surface. The ohmic contacts, gate leads and bondpads are respectively grown on the Hallbar pattern by the metal evaporation method. Our nanostructures are written by electron beam, and metal deposited on the working area and also connected to the gate leads. Finally, the sample is bonded with current conducting wire to contact the measurement setup.

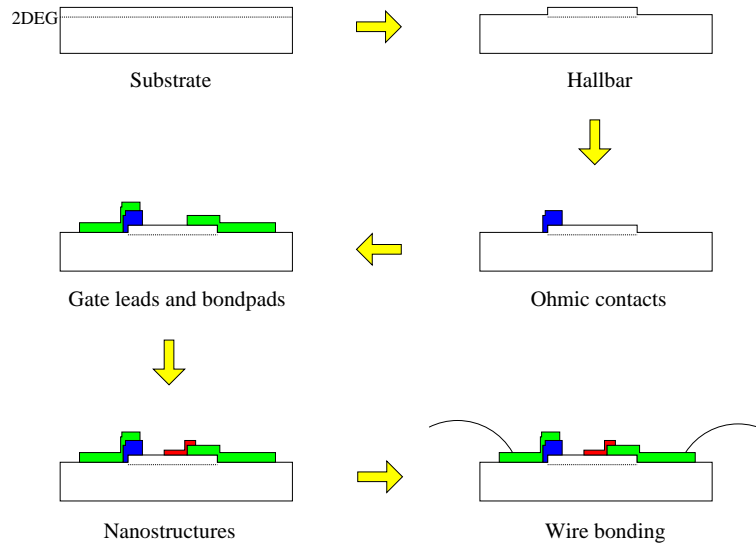


Figure 3.1.: The process of sample fabrication. The ohmic contacts (blue), gate leads, bondpads (green), and nanostructures (red) are metalized by the evaporation method, respectively. The sample is wire bonded to pads of a chip-carrier. This schematic pattern is not drawn in a correct ratio.

At the beginning of the sample fabrication, the heterostructure wafer is cleaved to define a small chip of  $5 \text{ mm} \times 6 \text{ mm}$ . Since the wafer is very brittle, it needs only gentle force to cut and break a small piece of the wafer. Four Hall bars can be prepared in this small chip. We clean

### 3. Sample Fabrication

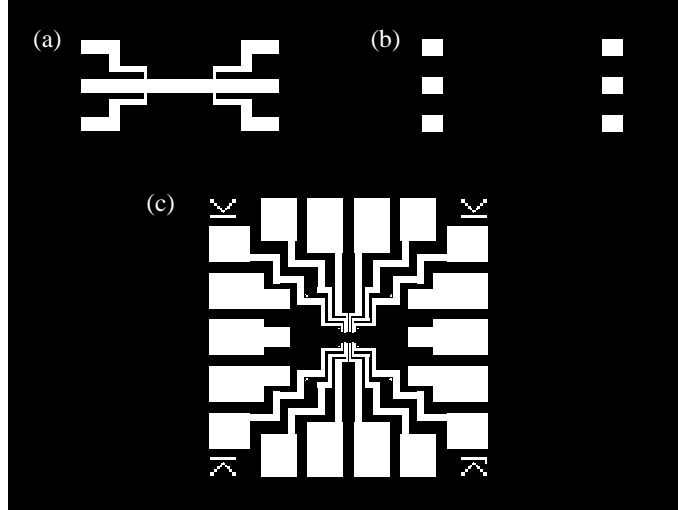


Figure 3.2.: Designed structures on chromium plated glass mask: (a) Hallbar, (b) Ohmic contacts, and (c) Gate leads and bondpads. The dark areas represent the regions of the mask cover in Cr which is opaque to UV-light, while the light can go through the white areas.

the surface of the chip with ultrasonics bath in acetone for few seconds, rinse with isopropanol (IPA), and blow-dry a chip surface with nitrogen gas. Then it is dried by hard baking in the oven.

## 3.2. Optical lithography

In order to microfabricate a Hallbar sample, we use the optical lithography process to selectively remove parts of the heterojunction substrate. It uses a UV-light to transfer a pattern from a photo mask, glass with a designed chromium pattern on one side, to a chemical photoresist on the substrate. The structures designed on our photo mask are Hallbars, ohmic contacts, gate leads, and bondpads as represented as the white areas in Fig. 3.2, whereas the dark area represents the regions of the glass covered with evaporated chromium blocking the UV-light from the lamp of the optical lithography machine. In our work, we use the exposure station of KSM-MJB 3 from Karl Süss KG. We use negative photoresist in the step of Hall bar fabrication, and positive photoresist in the step of Ohmic and bondpads contact preparation. A series of chemical treatments, developing and etching process, then transfers the exposure pattern into the material underneath the photoresist. The steps of our sample fabrication can be presented as the followings.

### 3.2.1. Hallbar

A Hallbar pattern in the heterostructure is prepared by optical lithography. The Hallbar is about  $900 \mu\text{m}$  long and  $100 \mu\text{m}$  wide. The pattern is designed with three legs on each side as shown on the photo mask in Fig. 3.2(a). These Hallbar legs are used in the measurement for either current contacts or voltage contacts. The process of optical lithography for Hallbar is summarized and presented in Fig. 3.3. The 2DEG level formed at the interface between GaAs and AlGaAs is identified by dashed line which is underneath the surface about  $100 \text{ nm}$ . At first step, we put the dry Heterostructure substrate on the middle of spinning table, and drop some amount of adhesion chemical HMDS covering all surface. We leave it for  $30 \text{ s}$ , and then spin



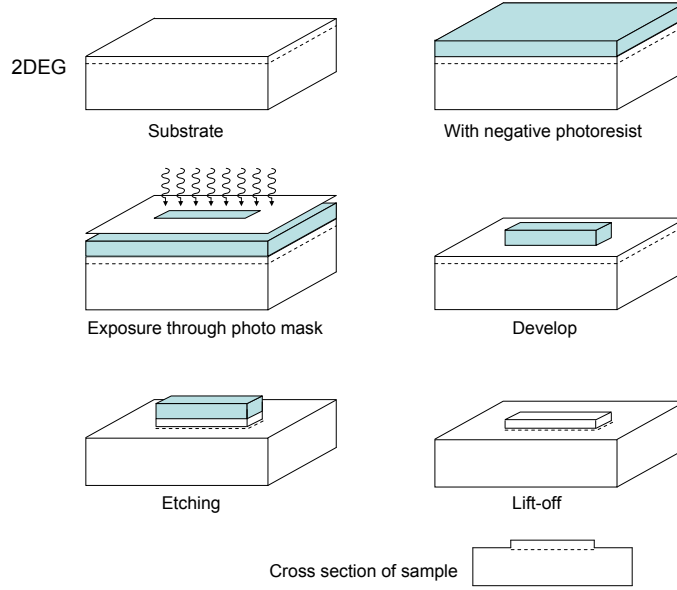


Figure 3.3.: The fabrication process of the Hallbar sample by using the optical lithography and chemical or wet etching method.

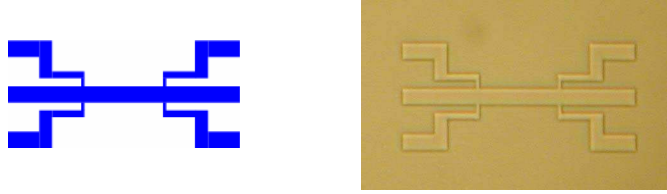


Figure 3.4.: (Left) The pattern of a designed Hallbar in our work. (Right) Optical micrograph of a Hallbar etched from the heterostructure substrate.

the substrate to spread HMDS all over the surface. The negative photoresist MaN 405, which is sensitive to the wavelength of 300-365 nm and has a resolution of  $0.4 \mu\text{m}$ , is put on the surface, and the substrate is spined to cover the surface with homogeneous resist. The sample is then baked on the hot plate.

Using the desired photo mask, the substrate is exposed by UV light generated from optical lithography machine. The direction of Hallbar axis is considered by depending on the plane orientation of III-IV compound semiconductor. The good direction for carrying the current through Hallbar is found to be parallel to the direction of  $[011]$ , which is perpendicular to plane  $(011)$  of the substrate. On the other hand, the bad direction is perpendicular to the good direction and parallel to  $[0\bar{1}\bar{1}]$  direction, which is perpendicular to plane  $(01\bar{1})$  of the substrate. After finishing the exposure, we make post baking on the hot plate.

We then develop the sample with exposed negative photoresist in the developer maD 333 depending on how long the Hallbar structure needs to begin appearing on the surface. In this step we need to stir the sample and monitor the changing of the resist simultaneously. The area of negative photoresist which is not exposed will dissolve in the developer, while only exposed resist defines the pattern of Hallbars on the surface. We stop the development process by using deionized water and blow dry the sample with  $N_2$  gas. To get rid of any unwanted remaining resist at the edge of the pattern, the sample is brought into an  $O_2$  plasma etching machine. We use an  $O_2$  plasma to remove any unwanted resist parts. Before we perform this step, we first need to pre-heat and clean the system in chamber by running the plasma for 5 min. The sample

### 3. Sample Fabrication

is then hard baked on the hot plate.

To transfer the pattern into the bulk of the material, the chemical etching is needed in this step. The sample is dipped into 37 % HCl before being dipped into the etching solution. The etching solution we used for our substrate is the mixture of  $H_2O : H_2SO_4 : H_2O_2$ . The depth of the etched surface can be controlled and monitored by DEKTAK 3030 ST surface texture profiler. The depth difference between before and after etching should be about 70-80 nm. The etching rate is approximately 1 nm/s. The 2DEG is still located underneath the Hallbar pattern. We can stop etching by rinsing with deionized water and blow dry with  $N_2$  gas. In a final step, the photoresist is lifted off with acetone and IPA. The Hallbar structure with thickness of 70-80 nm will be left on the surface of Heterojunction substrate, as shown in Fig 3.4.

#### 3.2.2. Ohmic Contacts

In this step ohmic contacts to the 2DEG are prepared. The pattern of ohmic contacts for a Hallbar is shown as six rectangular windows on the photo mask in Fig. 3.2(b). Optical lithography with a positive photoresist is used in this step. The ohmic contact fabrication is presented in Fig. 3.5. The substrate with Hallbars structure dried with acetone and IPA is put on the spin-coater. The positive photoresist maP 1215, which is sensitive to wavelengths between 300-460 nm and has a resolution of 1  $\mu m$ , is then coated on the surface by spinning method. The substrate with photoresist is baked on the hot plate. On the table of exposure machine, we align the ohmic contact windows in the photo mask on each legs of a Hallbar, and then expose with UV-light together.

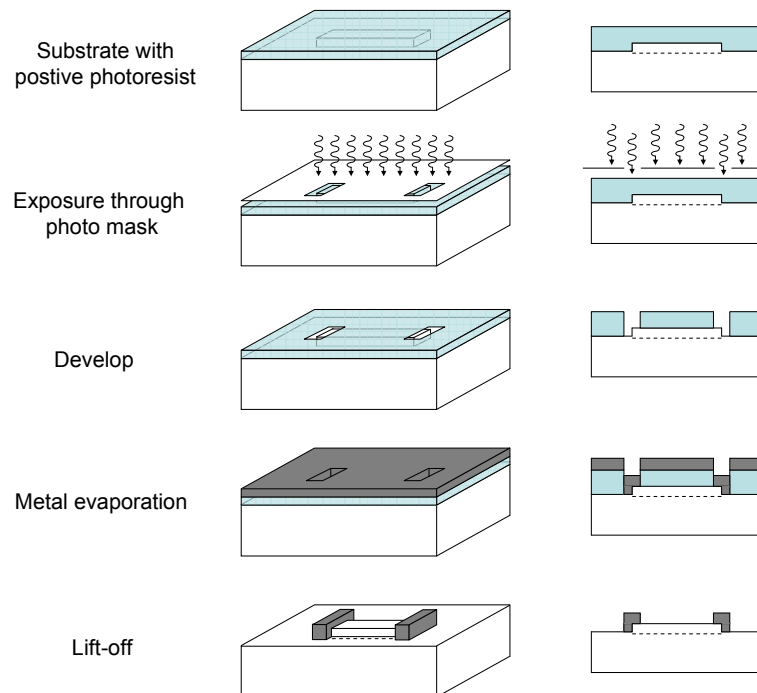


Figure 3.5.: The preparation process of the ohmic contacts, gate leads, and bondpads. Figures in right hand show the cross-section view.

After exposure, the sample is developed by using developer MF 26A or maD 331. Because of the positive photoresist, the exposed area will dissolve in the developer and left un-exposed photoresist on the sample. During developing the sample, we need to stir and monitor the pattern appearing on the sample. We stop developing with deionized water and blow dry with

$N_2$  gas. The  $O_2$  plasma etching is used to get rid of the unwanted remaining resist at edge of the contact windows. Before loading the sample in the evaporator, we prepare the surface for metal deposition by dipping the sample in 37% HCl and blow dry with  $N_2$  gas. This step removes the oxide that might form on the sample surface and could lead to metal adhesion problems.

Metal pads for ohmic contact are deposited on parts of the Hallbar by evaporating process. The metal for ohmic contact are also loaded in the heating sources inside the machine. For ohmic contacts, we deposit three layers from bottom to top of metals which are gold-germanium (AuGe), nickel (Ni), and gold (Au). The AuGe and gold is evaporated by using thermal evaporator, while the Ni is evaporated by using e-beam evaporator. After liftoff in acetone and rinsing with IPA, the AuGe/Ni/Au only sticks to the areas of ohmic contact windows. After liftoff, the ohmic metal must be annealed into the heterostructure to make the contact with the 2DEG.

The sample is heated in the annealing oven AZ500 from MBE Komponenten GmbH. The metal melts and is absorbed into the underlying Hallbar and forms an electrical contact between metal and the 2DEG. The sample is annealed under the atmosphere of forming gas 20%  $Ar/H_2$ . The position and pattern of ohmic contacts on each leg of a Hallbar is shown in Fig. 3.6. It can be noticed that there is some remaining photoresist from the Hallbar preparation, which cannot be dissolved. However, their resist did not cause any problems in the next step of sample preparation and also in the sample measurement.

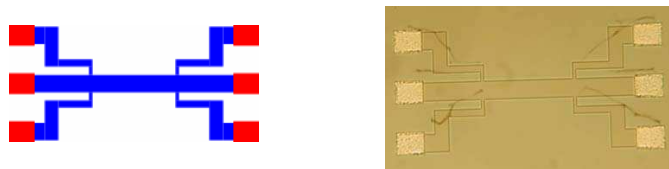


Figure 3.6.: (Left) The pattern and position of ohmic contact at the parts of a Hallbar. (Right) The optical micrograph of a Hallbar with deposited metal at ohmic contacts.

### 3.2.3. Gate Leads and Bondpads

In this step, we deposit the metal layers (Ni and Au) for bondpads and gate leads which connect designed nanostructure from electron beam lithography to their own bondpads. For our samples, we can prepare gate leads and bondpads simultaneously. There are six lead gates with bondpads designed at each side of the center of a Hallbar. Six bondpads are positioned on the ohmic contacts. All bondpads, which are large metallic areas, are prepared for wire bonding between the sample and chip carrier. This process of preparation is the same as ohmic contact as presented in Fig. 3.5, but evaporated metal and some details are different.

First, the dried sample is coated with positive photoresist maP 1215 with spinning technique. Then the sample is baked on the hot plate. The sample is aligned with the pattern of gate leads and bondpads on the photo mask, and exposed with UV-light. We develop the photoresist on the sample with the developer MF 26A or maD 331 until the pattern of gate leads and bondpads appear clearly, and then stop with deionized water and blow dry with  $N_2$  gas. We clean the unwanted remaining photoresist with  $O_2$  plasma. The surface of the sample is cleaned and prepared for metal adhesion with dipping in 37% HCl and then blow dry with  $N_2$  gas.

The sample is loaded into the evaporator as well as the metal sources which are chromium (Cr) and gold. We evaporate Cr as adhesion layer by using e-beam evaporating source, and then evaporate gold by using thermal evaporating source. Lift-off in acetone and rinse with IPA. The metals only stick to the area of the sample where there is no photoresist before evaporation. Ultrasonic can be used for short time if necessary to assist lift-off. The position and pattern

### 3. Sample Fabrication

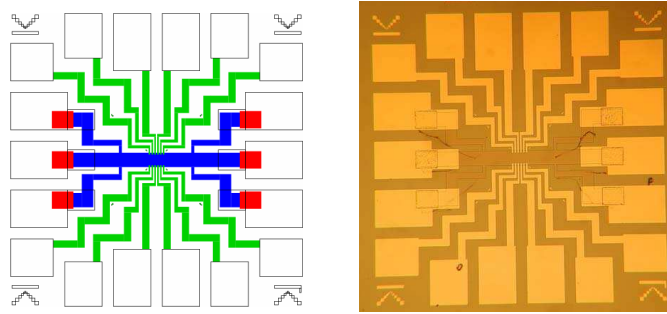


Figure 3.7.: (Left) The pattern and position of gate leads and bondpads deposited on a Hallbar. (Right) Optical micrograph of a Hallbar with ohmic contact, gate leads, and bondpads.

of gate leads and bondpads deposited on a Hallbar has been shown in Fig. 3.7. This distance between two big markers at the adjacent corners is  $920 \mu\text{m}$ .

### 3.3. Electron Lithography

Electron beam (e-beam) lithography is used to write the fine pattern of nanostructures that define the gates of the point contacts and quantum dots as well as the larger parts of these gates that connect out to the gate leads prepared by optical lithography as described above. The lithography process is similar to that used for optical lithography. In this process, an e-beam resist is coated on the surface of the sample, and the electron beam microscope is used to expose the desired pattern whose size is in the order of nanometer.

For the process of e-beam lithography, the sample is firstly dried by acetone and IPA. The sample is coated with a 2% solution of PMMA (polymethyl methacrylate) in MIBK (methyl isobutyl ketone) for positive e-beam resist by spinning technique. The sample is firstly baked on the hot plate and then hard baked in the oven. The sample is then loaded into the chamber of scanning electron microscope (SEM) to be written with e-beam. The SEM system that we use in our work is Philips XL 30. The pattern generator connected to the SEM system is used to control the e-beam to write the desired nanostructure.

The pattern of nanostructure can be designed in Xfig program and saved in a format of FIG file. The format of file is transformed to be PAT file. This file format will be used and read out by the pattern generator. When the pressure inside the chamber is less than  $10^{-5}$  mbar, we can turn on the e-beam with 30 kV. Before writing any pattern, the good resolution for e-beam of about 10 nm is needed. Then we adjust the focus and astigmatism of e-beam on the tin ball particles. The current of e-beam is measured by pointing to a Faraday cup at high magnification. We can change the position of the sample by controlling the stage, and also protect some PMMA areas without exposing with e-beam by using the beam blanker.

The sample is aligned with the markers in order to get the center of a writing field whose size is  $82 \times 82 \mu\text{m}^2$ . In this step, it is necessary to adjust the focus of e-beam again with the gold markers appearing underneath PMMA. For the pattern of nanostructure, we define the dose of e-beam in each part. The base dose is set at  $160 \mu\text{C}/\text{cm}^2$  defined in some big parts of nanostructure. At a magnification of  $976\times$ , the dose is set higher when the pattern parts are getting smaller. The smallest parts, for example the point contacts, is set at  $264 \mu\text{C}/\text{cm}^2$ . This value of the dose is obtained from the array of test pattern which is written with different dose in the dummy sample. After developing, metal evaporation, and checking the patterns with SEM, we therefore get the proper dose for the point contacts and dots structure in the real sample.

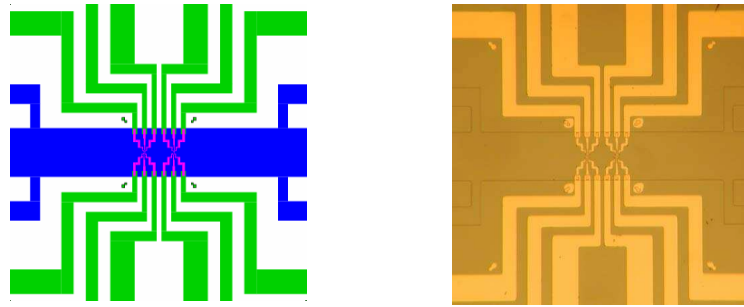


Figure 3.8.: (Left) The pattern of designed nanostructures is in the alignment with the gate leads. (Right) Optical micrograph of the nanostructures on the middle of a Hallbar.

The sample is exposed with e-beam at the dose determined during a test exposure array as discussed above. The pattern is written in the middle of the Hallbar, and each gate is connected to the lead deposited at the same step as the bondpads, as shown in Fig. 3.8(left). The additional pattern, which is a matrix of  $5 \times 5$  squares with different dose, is also written beside the bondpads where is covered with PMMA and no structures beneath. The dose for middle square is defined at  $160 \mu\text{C}/\text{cm}^2$ . This matrix is really needed to use for monitoring in the develop step. A solution of MIBK:IPA = 1:2 is used as a developer. We develop and check the developed pattern by optical microscope until the middle square of the additional matrix is clearly developed. We then stop developing with IPA and blow dry with  $N_2$  gas.

The developed sample is now ready to be loaded into the evaporator for gate metal deposition. For the gates of our nanostructures, we typically deposit Cr and Au at the same rates as bondpads preparation for both materials. We lift-off in acetone, rinse the sample with IPA, and blow dry with  $N_2$  gas. The optical micrograph of the metal deposited nanostructures after lift-off has been shown in Fig. 3.8(right).

### 3.4. Wire Bonding

We glue the sample into the chip carrier with silver epoxy, because the sample chip is needed to have good contact with high thermal conductivity and can be held and fixed inside the chip carrier when the epoxy hardens. Our samples are contained in the ceramic chip carriers with 18 pins, as shown in Fig. 3.9(a). We use an ultrasonic wedge bonder with gold wire to connect the bondpads on the sample and the chip carrier pads. During wire bonding, the sample is heated at  $120^\circ\text{C}$  to get rid of the moisture on the surface of bondpads. The schematic bonding is shown in 3.9(b), and the optical and SEM micrograph of the sample with wire bonding at bondpads are respectively shown in Fig. 3.9(c) and (d). The silver epoxy for gluing the sample in a chip carrier can also be seen in Fig. 3.9(d).

### 3. Sample Fabrication

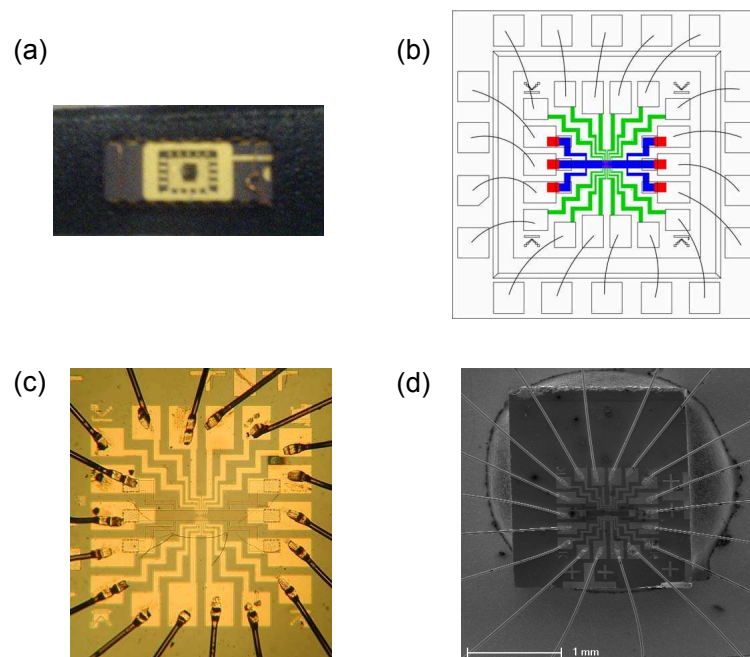


Figure 3.9.: (a) The sample in a 18-pin chip carrier. (b) The pattern of wire bonding between the bondpads of the device and chip carrier pads. (c) Optical and (d) SEM image of the sample with gold wire bonded at bondpads.

## 4. Measurement Techniques

### 4.1. Cryostat

In order to study the behaviour and physics of electron transport in nanostructures, e.g. quantum point contacts and dots, one needs to perform measurements of the samples at very low temperatures. Therefore, we use an Oxford Instruments Kelvinox 25  $^3\text{He}/^4\text{He}$  dilution refrigerator cryostat for our cryogenics system, which is able to operate at temperatures down to order of 100 millikelvin (mK).

#### 4.1.1. $^3\text{He}/^4\text{He}$ Dilution Refrigerators

The principle of operation of the dilution refrigerator was originally proposed by H. London in 1951 [50]. When a mixture of the two stable isotopes of helium ( $^3\text{He}/^4\text{He}$ ) is cooled below the critical temperature, it separates into two phases. The lighter *concentrated phase* is rich in  $^3\text{He}$  and the heavier *dilute phase* is rich in  $^4\text{He}$  [50], [51]. The phase diagram of  $^3\text{He}/^4\text{He}$  mixtures at saturated vapor pressure is shown in Fig. 4.1. The diagram shows the lambda line for superfluid transition of  $^4\text{He}$ . The phase separation line of the mixtures below separate into a  $^4\text{He}$ -rich and a  $^3\text{He}$ -rich phase. The concentration of  $^3\text{He}$  in each phase depends on the temperature. The cooling process can be obtained by evaporating the  $^3\text{He}$  from the concentrated phase into the dilute phase.

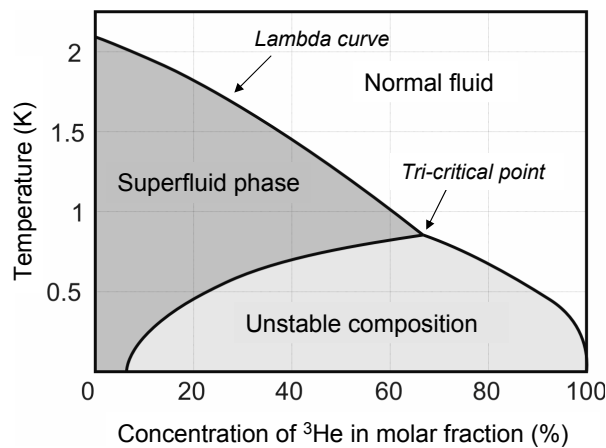


Figure 4.1.: Phase diagram of  $^3\text{He}/^4\text{He}$  mixtures

$^4\text{He}$  becomes superfluid at a temperature of 2.177 K. The temperature of the superfluid phase transition of  $^4\text{He}$  is depressed if it is diluted with liquid  $^3\text{He}$ . At  $^3\text{He}$  concentration of 67% and at a temperature of 0.87 K, the  $\lambda$ -line meets the phase separation line at the tri-critical point. The shaded phase separation region in the figure is a non-accessible range of temperatures and concentrations for Helium mixture. If the helium mixture, which has a  $^3\text{He}$  concentration in excess of 6.5%, is cooled to temperatures below 0.87 K, the liquid will separate into two phase, one rich in  $^4\text{He}$  (dilute phase) and the other rich in  $^3\text{He}$  (concentrated phase). Because of its lower density, the  $^3\text{He}$ -rich liquid floats on top of the  $^4\text{He}$ -rich liquid. If the temperature is

#### 4. Measurement Techniques

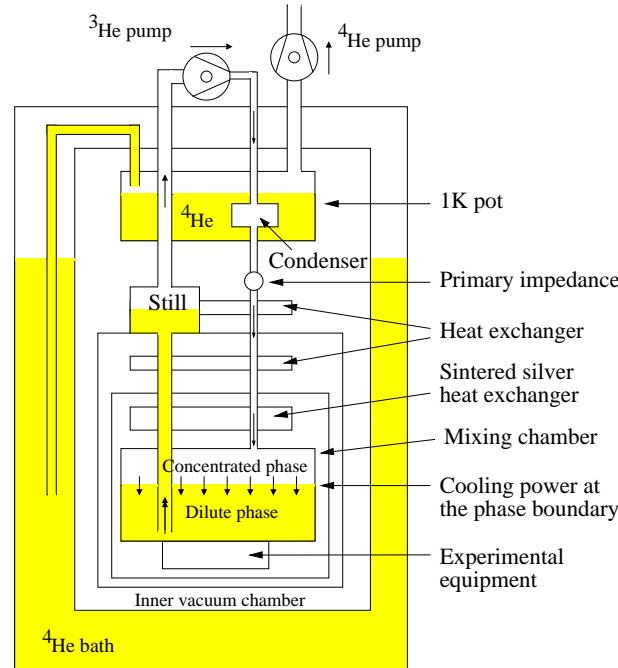


Figure 4.2.: Schematic diagram of a  $^3\text{He}/^4\text{He}$  dilution refrigerator

decreased to close to absolute zero, It can be seen that liquid in the concentrated phase becomes pure  $^3\text{He}$ . But the concentration of the  $^3\text{He}$  does not approach zero when the temperature approaches zero in the dilute phase and it instead reaches a constant concentration of 6.5%  $^3\text{He}$  in  $^4\text{He}$  at saturated vapor pressure even for  $T = 0$  K.

It is helpful to regard the concentrated phase of the mixture as  $^3\text{He}$  liquid and the dilute phase as  $^3\text{He}$  gas. The main components of a  $^3\text{He}/^4\text{He}$  dilution refrigerator and a flow diagram are shown in Fig. 4.2. First, the mixture, mostly  $^3\text{He}$  gas, coming from the pump at room temperature will be precooled by a liquid  $^4\text{He}$  bath at 4.2 K. Then, it will be condensed in 1 K pot. It is not intended to cool the mixture enough to set up the phase boundary but only to cool it to 1.2 K. To get phase separation, the temperature must be reduced to below the tri-critical point. The  $^3\text{He}$  liquid will flow through the primary impedance, which is used to maintain a high enough pressure in the 1 K pot region for condensing the gas, and enter the heat exchanger which is in thermal contact with the still.

The still is the first part to cool below 1.2 K. It cools the incoming  $^3\text{He}$  at a temperature of about 0.6 - 0.7 K before it enters the next heat exchangers and the mixing chamber. Below the still we have a secondary flow impedance to prevent reevaporation of  $^3\text{He}$ . After leaving this impedance, the liquid  $^3\text{He}$  will flow through several heat exchangers to precool it to a low enough temperature before entering the upper concentrated phase in the mixing chamber.

In the mixing chamber, the  $^4\text{He}$  which makes up the majority of the dilute phase is inert. Evaporating of  $^3\text{He}$  takes place of the phase-boundary and the  $^3\text{He}$  gas moves through the liquid  $^4\text{He}$  without interaction. This process continues to work even at the lowest temperature because the equilibrium concentration of  $^3\text{He}$  in the dilute phase is still finite, even as the temperature approaches absolute zero. However, the base temperature is limited by other factor, and in particular by the residual heat leak and exchanger performance. A wider tube for dilute phase in the mixing chamber leaves the lower dilute phase, and then goes through the series of heat exchangers to precool the incoming concentrated  $^3\text{He}$ . Then, the contact area has to be increased as far as possible, and so this can be done by using sintered silver heat exchanger being very efficient even at the lowest temperatures.



It enters the dilute liquid phase in the still where we have a liquid  $^3\text{He}$  concentration of less than 1%. Therefore the concentration of the  $^3\text{He}$  is lower than it is in the mixing chamber, and the flow of  $^3\text{He}$  can be driven into the still by the osmotic pressure difference. The vapor above the dilute liquid phase in the still has a concentration of typically 90 % of  $^3\text{He}$  because of the high vapor pressure of  $^3\text{He}$  at the temperature of the still. At this temperature the vapor pressure of the  $^3\text{He}$  is about 1000 times higher than that of  $^4\text{He}$ , so  $^3\text{He}$  evaporates preferentially. A small amount of heat can be supplied to the still to promote the required return flow. If  $^3\text{He}$  gas is pumped on the still and compressed to a pressure of a few hundred millibar, and resupply the condensation line continuously, we will get a closed  $^3\text{He}$  circuit. The gas is then passed through filters and Nitrogen cold traps to remove impurities and returned to the cryostat.

The experimental equipment is mounted on or inside the mixing chamber, ensuring that it is in good thermal contact with the dilute phase. The lowest possible base temperature can be obtained by reducing any heat load on the mixing chamber. For our dilution refrigerator, a sample in a chip-carrier is put in a socket on the cold finger which has a good thermal contact with the mixing chamber. To estimate the temperature of our sample, a ruthenium oxide ( $\text{RuO}_2$ ) resistance thermometer is also mounted on the cold finger. A 4-point measurement with a current of 10 nA is performed on the  $\text{RuO}_2$  thermometer to read out the electrical resistance, what can be calibrated to the electronic temperatures of the  $\text{RuO}_2$ .

## 4.2. Measuring Techniques

We usually use two different setups to measure the conductance through the nanostructures on a sample. We can feed a current and measure the voltage, or vice versa, via the ohmic contacts. The current through and voltage across the device have to be kept relatively small for our measurements. These two different measurement setups are 4-point and 2-point measurement. For the 4-point measurement, we feed a constant current,  $I = V_{sd}/R$ , through the device via two ohmic contacts (source and drain), and measure the voltage drop between two different ohmic contacts, as shown in Fig. 4.3(a). For the 2-point measurement, a constant bias voltage,  $V_{sd}$ , is applied and the current is measured through the sample, as shown as a configuration in Fig 4.3(b).

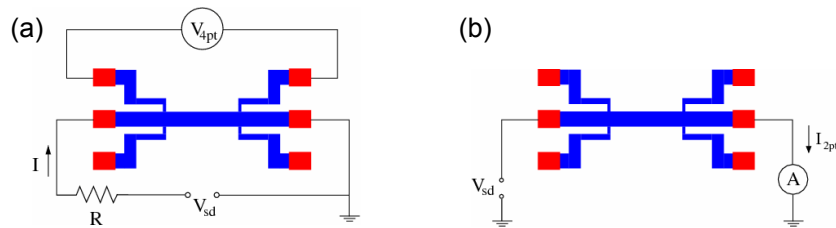


Figure 4.3.: The configuration of the (a) 4-point and (b) 2-point measurements for a Hallbar sample.

### 4.2.1. 4-Point Measurement

The 4-point current bias measurement requires two ohmic contacts in both of the source and drain reservoirs, and the voltage drop across the device is measured by using the other two ohmic contacts, as illustrated schematically in Fig. 4.4. In our measurement setup, the 4-point measurement is usually performed for measuring the conductance of quantum point contacts which are described in the chapter of characterization of quantum point contacts. We measure the differential resistance  $R = dV/dI$ , which can be converted to the differential conductance

## 4. Measurement Techniques

$G = dI/dV$ , by using standard ac lock-in techniques. In this setup, the constant bias current of 10 nA is fed into the sample. Because the output signal is comparable to the background noise, then a lock-in amplifier is used to read out the periodically modulated signal and hence eliminate the unwanted noise.

The small ac current  $I_{sd} = 10$  nA is generated from the current source by applying ac voltage of 1 V from a 7260 or 7265 EG&G lock-in amplifier through the large in-line resistor  $R = 100$  M $\Omega$ . The voltage drop across the device is fed back into the lock-in at channel A and B, and obtained as  $\Delta V_{AB} = V_A - V_B$ . The measured voltage drop is due only to the resistance of the sample including small series resistance because no current flows through the voltage probe leads, ohmic contacts and external wires. The conductance from  $I_{sd}/\Delta V_{AB}$  is therefore equal to the differential conductance because of the small source-drain current and voltage.

The depletion gates of the nanostructures are negatively biased with respect to the bondpad by using individual channels of a Keithley 213 quad voltage source with analog output connector. The applied voltage limit is  $\pm 10$  V. There are four channels of digital-to-analog converters (DACs) on a quad voltage source. The gate voltage  $V_g$  can be smoothly swept in a small step via the measurement program called *Measkern* based on the Linux operation system. This program was developed by U. Wilhelm at Max-Planck institute for solid state research in Stuttgart. All our measurements are running with the *Measkern* program via GPIB-Bus port interfacing the experimental instruments and the computer.

### 4.2.2. 2-Point Measurement

The 2-point voltage bias measurement are also usually used for characterizing our samples, for example the ohmic contact resistances. According to the simplest voltage bias setup for 2-point measurement in Fig. 4.3(b), the Keithley 236/237 Source Measure Units (SMU) can be used to bias the voltage and measure the current through the sample along the path bounded with two probe points in order to investigate the contact resistance at each ohmic contact of the sample. The voltage is varied from -10 mV to 10 mV, and then the relationship between voltage and current is linear according to Ohm's law. From this method at low temperature, we can extract the resistance of the ohmic contacts; average values of  $\sim 150$   $\Omega$  for sample **PR1:d2** and  $\sim 2$  k $\Omega$  for sample **PR1:d1** were found.

For investigation of the quantum point contacts and dots, the lock-in technique is used in this measurement. In this 2-point voltage bias setup, a constant ac voltage,  $V_{sd}$ , is applied across the source-drain reservoirs and the resulting current in the circuit is measured to determine the conductance, as shown schematically in Fig. 4.5. The sample resistances are measured in series with the ohmic contact resistances and wiring resistances.

As seen in Fig. 4.5, a voltage bias is applied across the sample using the output of the lock-in amplifier divided down to the source-drain voltage  $V_{sd}$  of 10  $\mu$ V with the  $10^4 : 1$  divider of resistors of 10 k $\Omega$  and 1  $\Omega$ . The high voltage is connected to an ohmic contact in the source reservoir. An ohmic contact in the drain reservoir is connected to a Stanford Research Systems model SR 570 low-noise current preamplifier which converts an ac current to ac voltage and feeds back into lock-in amplifier. The factor of 1  $\mu$ A/V is set for the current preamplifier. The gates are again negatively biased with the Keithley quad voltage sources connected to digital-to-analog converters as described above.

### 4.2.3. Linear Measurement

For the measurement in linear transport, the source-drain voltage  $V_{sd}$  is kept near 0 V. This applied voltage across the sample should not exceed the temperature of electron,  $T_e$ , that is

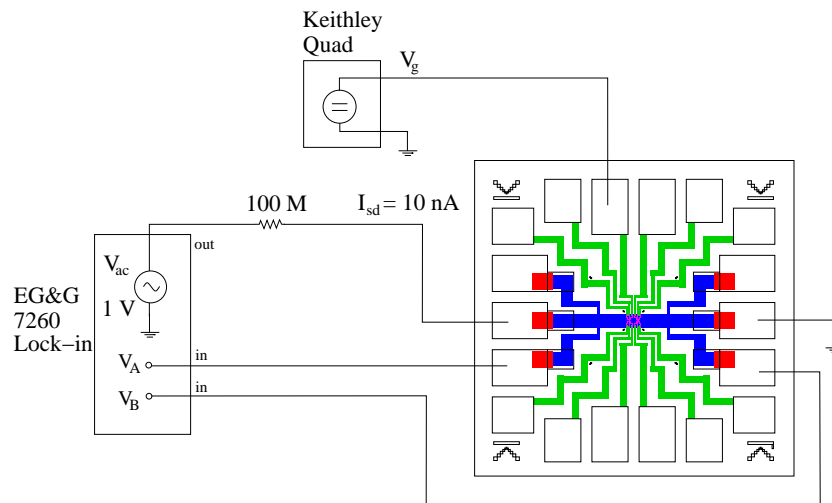


Figure 4.4.: Circuit diagram of a 4-point ac current bias measurement. The lock-in sources an ac voltage converted into a constant ac current source via a  $100\text{ M}\Omega$  resistor. Two ohmics are used for current path and two are used to measure the voltage drop  $\Delta V_{AB}$  across the sample. The gates are biased with negative voltages from the quad voltage sources connected with DACs.

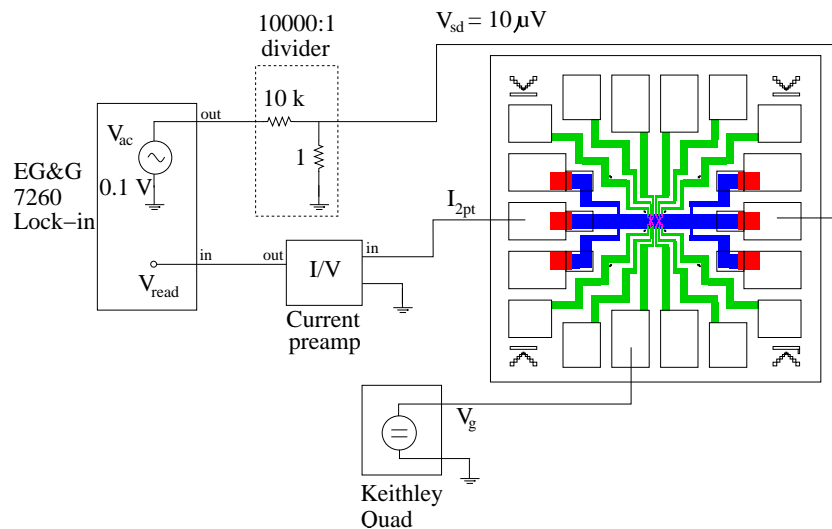


Figure 4.5.: Circuit diagram of a 2-point ac voltage bias measurement. The lock-in sources an ac voltage divided down to  $V_{sd} = 10\text{ }\mu\text{V}$ . The circuit is completed with a low-noise current preamplifier connected to an ohmic in the drain. The current  $I_{2pt}$  is converted to  $V_{read}$  and fed into the lock-in. The gates are biased with negative voltages from the quad voltage sources connected with DACs.

#### 4. Measurement Techniques

$eV_{sd} < k_B T_e$ , where  $k_B$  is Boltzman's constant. Both 4-point and 2-point measurement performed above are in the linear regime, because the voltage across the sample is very small. The 4-point measurement for low resistance samples is used where the conductance is greater than  $e^2/h$ , whereas the high resistance samples with conductance less than  $e^2/h$  are better suited to 2-point measurements [52]. The conductances in this case is usually defined as  $G = dI/dV_{sd}$  so called the differential conductance. In the 2-point measurement, the  $dV_{sd}$  can be approximately the voltage drop between two probe points of the sample  $\Delta V_{AB}$ , whereas  $dV_{sd}$  is equal to the bias ac voltage to the sample in the 4-point measurement. The differential conductances of quantum point contacts or quantum dots are usually presented as a function of gate voltage  $V_g$ , that is  $G(V_g)$ .

#### 4.2.4. Nonlinear Measurement

In the nonlinear measurement, an additional bias voltage  $V_{sd}$  is applied between source and drain. Therefore, we usually perform the measurement in nonlinear transport regime with 2-point voltage bias setup. The schematic drawing of the nonlinear measurement is shown in Fig. 4.6. The applied dc voltage from one DAC channel of the Keithley quad voltage source is added in series with the ac voltage generated from lock-in amplifier before they are connected to the  $10^3 : 1$  divider in order to obtain  $V_{sd}^{ac} = 10 \mu\text{V}$ . The dc source-drain voltage  $V_{sd}^{dc}$  is also divided with a factor of  $10^3$ . The dc voltage can then be adjusted for non-zero source-drain voltage. Therefore the voltage across the sample contains the dc and ac components for the applied source-drain bias voltage;  $V_{sd} = V_{sd}^{dc} + V_{sd}^{ac}$ .

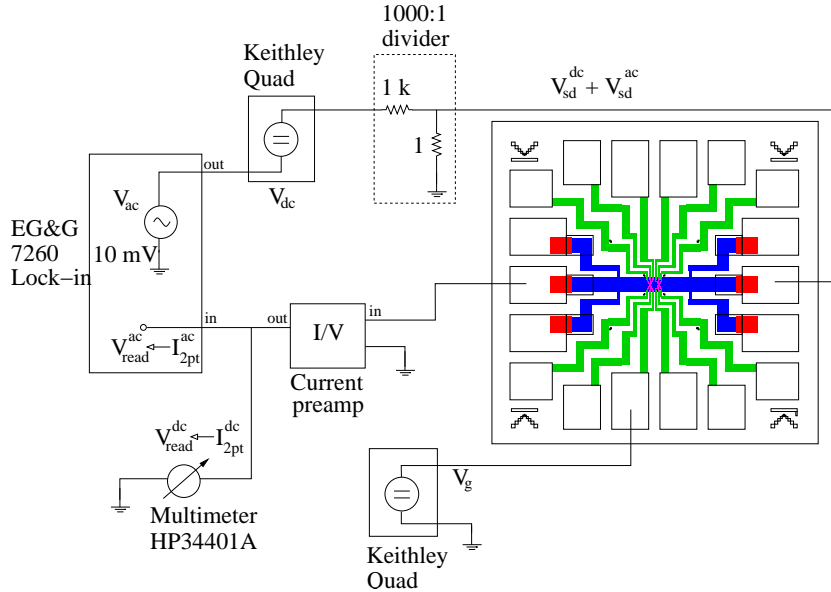


Figure 4.6.: Circuit diagram of a nonlinear measurement based on the 2-point voltage bias measurement. A finite  $V_{dc}$  from a DAC channel of voltage source is added in series to the  $V_{ac}$ . The voltage is divided with resistance divider to obtain dc+ac source-drain bias voltage. The current through a sample is converted to  $V_{read}$  by a low-noise current preamplifier, and fed back to the lock-in to read out the  $V_{read}^{ac}$ . The multimeter is used to measure the  $V_{read}^{dc}$ . The gates are biased with negative voltages from the quad voltage sources connected with DACs.

The current,  $I_{2pt}$ , through the sample is converted to a voltage value with the same factor of the low-noise current preamplifier that is used in the 2-point measurement setup. The dc read-

### 4.3. Characterization of 2DEG by Quantum Hall Effect

out voltage  $V_{read}^{dc}$  converted from the dc current,  $I_{2pt}^{dc}$ , can be measured by the HP34401A digital multimeter. The lock-in amplifier is fed back with the ac read-out voltage,  $V_{read}^{ac}$ , converted from the ac current,  $I_{2pt}^{ac}$ . The gates are negatively biased with the Keithley quad voltage sources. The differential conductance,  $G = dI/dV_{sd}$ , is generally measured as a function of gate voltage and dc source-drain voltage as  $G(V_g, V_{sd})$ .

The gate voltage  $V_g$  can be negatively biased with a DAC channel connected to the Keithley quad voltage source as described in the 2 and 4-point measurement setups. Nevertheless, the gate voltage is usually swept in very small steps in the nonlinear measurement for high resolution results. The sweeping limit for a DAC voltage source is an increment of 250  $\mu\text{V}$  for voltage varying range of -1 to 1 V, and 1.25 mV for varying range of 1 to 5 V or -1 to -5 V. In order to sweep gate voltage in a smaller step than the limit, we add a DAC voltage sources connecting to the resistance divider  $R_1 : R_2$  with another DAC voltage source in series. The schematic circuit diagram is show in Fig. 4.7.

According to this circuit,  $V_{DAC1}$  is divided by a factor of  $R_1/R_2$  and added in series with  $V_{DAC2}$  which is fixed at a constant. Therefore we can sweep the  $V_g$  in a very small step, for example, if  $R_1/R_2 = 100$  and  $V_{DAC1}$  is swept in the step of 1 mV which is far from the limit, then  $V_g = V_{DAC2} + V_{DAC1}(R_2/R_1)$  and is swept in the increment of 10  $\mu\text{V}$ , which gives a high resolution detail of the result as a function of gate voltage  $V_g$ .

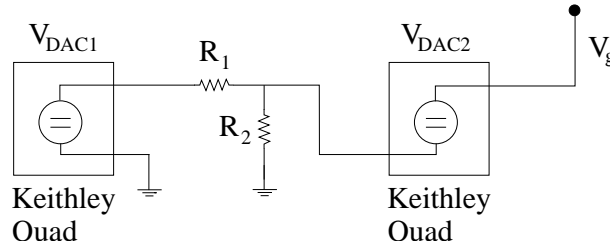


Figure 4.7.: The voltage sources for gate voltage  $V_g$  which can be swept in a smaller increment than the limit. It is compounded with two DAC channels of the quad voltage sources. One source with  $V_{DAC1}$  is connected to the resistance  $R_1/R_2$  divider, and in-line connected to another voltage source  $V_{DAC2}$ .

### 4.3. Characterization of 2DEG by Quantum Hall Effect

Without negative voltage bias to any gates of nanostructure, we can set up the 4-point measurement in applied magnetic field to study the quantum Hall effect of the Hallbar sample and obtain the characteristics of the 2DEG. The magnetic field is applied perpendicular to the plane of 2DEG in the sample. The 4-point measurement of the Hallbar sample is shown as the inset of Fig. 4.8, the longitudinal resistance and transverse or Hall resistance where of the sample temperature of  $\sim 65$  mK are shown. At low magnetic fields the longitudinal resistance is constant while the Hall resistance increases linearly. However, at high magnetic fields the longitudinal resistance shows pronounced oscillatory behaviour, which is referred to as Shubnikov-de Haas oscillations, while the Hall resistance shows plateaus corresponding to the minima in the longitudinal resistance [1, 4, 53].

The Hall resistance is quantized in units of  $h/e^2$  divided by an integer  $i$ ;  $R_{Hall} = h/(ie^2)$ . It can be noticed in Fig. 4.8 that the even indices with  $i \geq 4$  label show flat plateaus. At  $0.3 \text{ T} < B < 0.6 \text{ T}$ , the plateaus with even indices only appear and correspond to a spin degeneracy of the electrons. The minima of the oscillations are nearly zero at high magnetic field, and the kinks in the longitudinal resistance peaks are related to the lifting of the spin degeneracy by

#### 4. Measurement Techniques

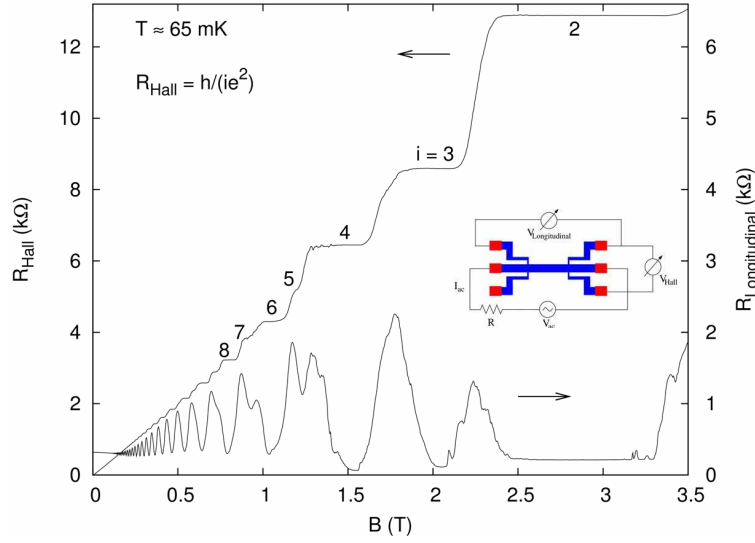


Figure 4.8.: Measured longitudinal and Hall resistance for a Hallbar sample **PR1:d2** at  $T \approx 65$  mK. The 4-point current bias measurement setup has been shown in the inset.

Zeeman effect and correspond to the Hall resistance's plateaus labeled with odd indices.

The plateaus appearing at 65 mK correspond to the Fermi energy lying in a gap between Landau levels in the density of states of 2-D electrons system with applied magnetic field. The energy of the electrons is quantized and the Landau levels are separated by the cyclotron energy  $\hbar\omega_c$ , where  $\omega_c$  is the cyclotron frequency and  $\omega_c = eB/m_e$ . The gaps between Landau levels become wider when the magnetic field increases as shown in Fig. 4.9(a). As the magnetic field is varied, the Landau levels move relative to the Fermi energy. The energy states underneath the Fermi level are occupied by electrons identified as the shaded areas. The longitudinal resistance goes through a maximum every time the Fermi level lies at the center of a Landau level.

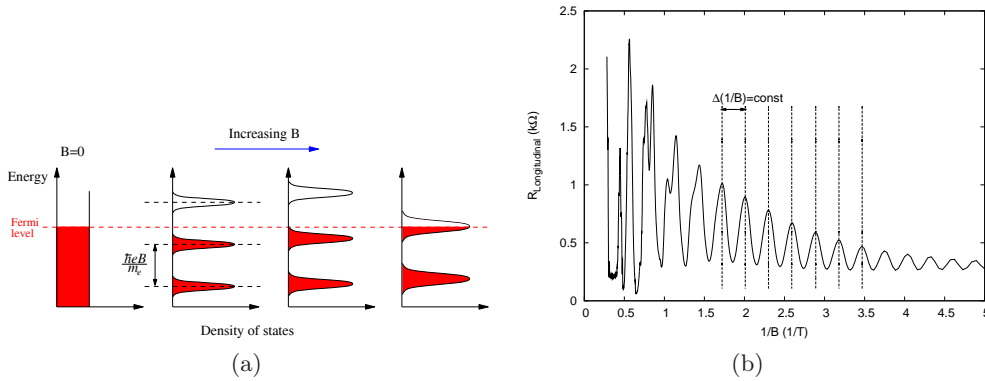


Figure 4.9.: (a) Landau quantization of 2DEG. (b) Plot of the longitudinal resistance versus inverse of the magnetic field. This shows the periodic oscillation with a constant  $\Delta(1/B)$ .

In Fig. 4.9(b), the periodic oscillation of longitudinal resistance as a function of the inverse of magnetic field has been plotted. The interval of  $1/B$  between two peaks is equal to the constant of  $2e/h$  divided by the electron density  $n_s$  of the 2DEG. The oscillations in longitudinal resistance therefore provide an alternative method to determine  $n_s$ . Since  $\Delta(1/B) = 0.29 \text{ T}^{-1}$

### 4.3. Characterization of 2DEG by Quantum Hall Effect

for the sample **PR1:d2** fabricated from the same heterostructures wafer as the other samples, the electron density is calculated as  $n_s = 2e/h(\Delta(1/B)) = 1.66 \times 10^{15} \text{ m}^{-2}$ , which is typical for our samples. The Fermi wavelength is given by  $\lambda_F = \sqrt{2\pi/n_s} \simeq 62 \text{ nm}$ .

The longitudinal resistance at zero magnetic field,  $R_{long}^{B=0}$ , is equal to  $316 \Omega$ , the sheet resistance,  $\rho_{\square}$ , is then given by  $\rho_{\square} = R_{long}^{B=0}/N_{4pt} \simeq 60 \Omega$ , where  $N_{4pt}$  is the number of squares of the Hallbar geometry between voltage probes in the 4-point measurement. From the electron density and sheet resistance, the mobility can be calculated as  $\mu = (en_s\rho_{\square})^{-1} = 6.3 \times 10^5 \text{ cm}^2/(\text{Vs})$ , and hence the mean free path given by  $L_m = (\hbar/e)\mu\sqrt{2\pi n_s} = 4.2 \mu\text{m}$ . This shows that the dimension of designed nanostructures of the order of  $10^2 \text{ nm}$  is smaller than the mean free path of electrons, and we can obtain ballistic transport through our nanostructures.





## 5. Quantum Point Contacts in Linear Transport

Quantum point contacts (QPCs) are short one dimensional (1D) channels connected adiabatically to large source and drain reservoirs. In this chapter, the electron transport through QPCs is measured with very small bias source-drain voltage. Therefore the investigated transport in this chapter is all in the linear regime.

### 5.1. Quantum Point Contacts in a Different Design

In our samples, we design dot structures which are formed an arrangement of point contacts, and we also define standalone point contacts in a different pattern. We can therefore study the interesting properties of electron transport in many designs of our quantum point contacts.

#### 5.1.1. QPCs in the Sample PR1:d2

Firstly, we consider the sample **PR1:d2** with nanostructures of the couple dots in series and a standalone quantum point-contact, as shown schematically in Fig. 5.1(a). The electron micrographs of designed patterns are shown in Fig. 5.1(b) and (c). The metal gates are labeled and tuned with negative voltages to deplete the 2DEG underneath at the interface of GaAs-AlGaAs heterojunction, and force the electrons to flow through a narrow constriction in the 2DEG. The metallic split-gates A1-A2, C1-C2 and E1-E2 have a geometry of 250 nm width and 200 nm length. The standalone split gate F1-F2 is bigger than the gates at quantum dots structure, and is 400 nm width and 250 nm length. The width of the constriction is controlled by the gate voltage and can be made comparable to the Fermi wavelength.

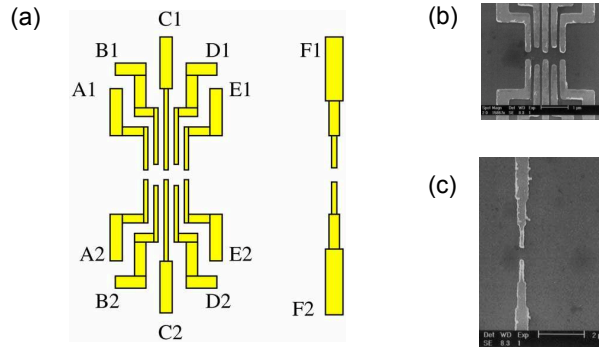


Figure 5.1.: (a) Schematic drawing of the nanostructures fabricated on the sample PR1:d2 and all metal gate are labeled as gate A to gate F. (b) and (c) The SEM images of the designed double dots and standalone QPC F.

#### QPC F

The conductance quantization of quantum point-contacts has been observed and investigated by 2-point and 4-point measurements with the lock-in technique. Figure 5.2 shows the differential conductance,  $G = dI/dV_{sd}$ , in QPC F as a function of applied gate voltage  $V_g = V_{F1} = V_{F2}$

## 5. Quantum Point Contacts in Linear Transport

at temperature of 70 mK with the 4-point measurement. In this case, the  $V_{sd}$  depends on the QPC resistance which is increased as more negative voltage biased to the gates of a QPC. The conductance is obtained from the measured resistance in QPC F after subtraction of a constant series resistance of  $370 \Omega$ , and is quantized in the unit of  $2e^2/h$ .

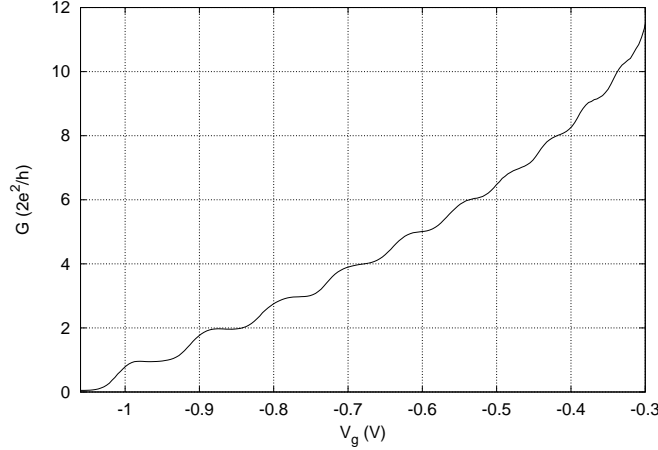


Figure 5.2.: Conductance quantization in the unit of  $2e^2/h$  in QPC F of the sample **PR1:d2**. The differential conductance is corrected with a series resistance of  $370 \Omega$ .

The series resistance used for the subtraction was chosen to match the plateaus with their corresponding quantized values. This resistance is in reasonable agreement with the series resistance based on the sheet resistance of the 2DEG. In this measurement, the other gates except gate F1, F2 and A2 are grounded. A negative voltage is applied to the gates F1 and F2, whereas the gate A2 must be not grounded because there is a short circuit between one terminal contact of the hall bar and gate A2 as discussed below.

The conductance of the QPC F shows a sequence of quantized plateaus with steps of  $2e^2/h$ . The conductance is pinched off at  $-1.06 \text{ V}$  and ten steps of quantization are observed. Several plateaus, in particular first three plateaus, are quite flat and well fit to the quantized value. The conductance is simply given by the conductance quantum  $2e^2/h$ , multiplied by the number of occupied 1-D subbands ( $N$ ) in the QPC:  $G = 2e^2/h(N)$ . Each occupied subband contributes  $2e^2/h$  to the conductance. The broadening between conductance plateaus is caused by the effect of finite temperature at which the quantization at zero temperature limit convolves with the derivative of Fermi-Dirac distribution. Some of plateaus deviate from the exact quantization. These deviations might come from the finite reflection probability of the current carried by a subband as discussed by B. J. Wees et al [9].

### QPC C and QPC E

We return to determine why we need to un-ground gate A2. Consider the quantization of conductance of QPC C observed from the resistance measured by the 2-point technique as shown in Fig. 5.3, the result is corrected with a sum of the contact resistance and series resistance of  $2.4 \text{ k}\Omega$ . The conductance of QPC C with ungrounded gate A2 is higher and more pronounced than that with grounded gate A2. This means that the current can leak via grounded gate A2, and thus a lower current through the sample is measured. To avoid any influence from this leaking current, the gate A2 is always ungrounded in every measurement.

Figure 5.4 shows the differential conductance of QPC C and QPC E of sample **PR1:d2** from (a) the 2-point and (b) the 4-point measurement. In the 2-point measurement, the conductance

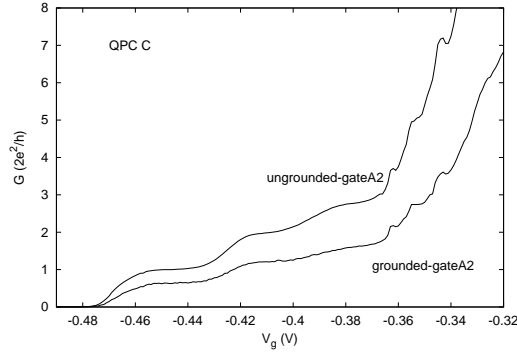


Figure 5.3.: The comparison of the differential conductance of QPC C with grounded and ungrounded gate A2. These results have been investigated by the 2-point measurement and corrected with a resistance of  $2.4 \text{ k}\Omega$ .

is corrected with a resistance of  $2.4 \text{ k}\Omega$ . The conductance in the 4-point measurement is corrected with a series resistance of  $470 \text{ }\Omega$ . This used series resistance is a bit higher than that used for QPC F. The differential conductance of QPC C and QPC E are respectively measured as a function of applied gate voltage  $V_g = V_{C1} = V_{C2}$  and  $V_g = V_{E1} = V_{E2}$ . There is the quantization in conductance for both point contacts. It can be seen from the comparison of the position of the kinks appeared in the conductance between (a) 2-point and (b) 4-point measurement. The kinks in (b) are lower than (a), clearly at  $V_g = -0.35 \text{ V}$  for QPC C. From both measurement techniques, the position of the plateaus is corrected by a series resistance for each techniques, but there is the difference of the kinks position in the region before quantization. Therefore the series resistance shows the dependence on applied gate voltage  $V_g$ .

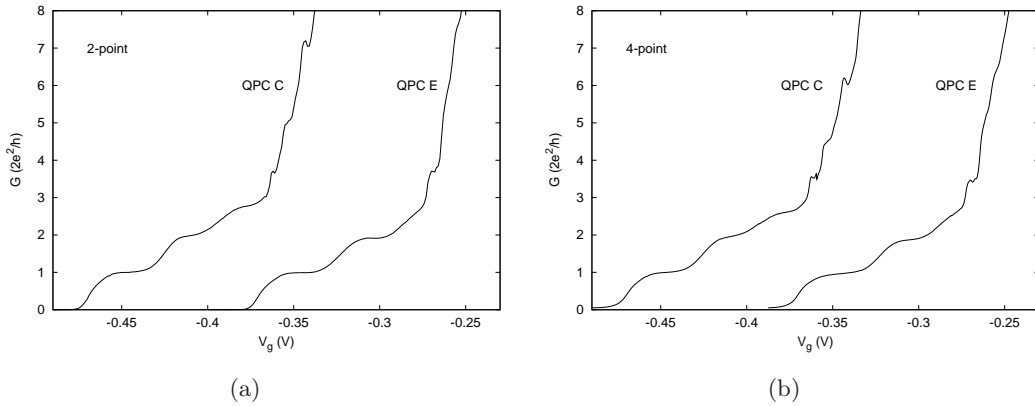


Figure 5.4.: Conductance quantization of QPC C and QPC E of the sample **PR1:d2**. (a) The differential conductance is obtained by the 2-point measurement and corrected with a resistance of  $2.4 \text{ k}\Omega$ . (b) The differential conductance is obtained by the 4-point measurement and corrected with a series resistance of  $470 \text{ }\Omega$ .

There are three plateaus in the conductance of QPC C and two plateaus in the conductance of QPC E. For QPC C three plateaus are observed in the gate voltage interval between  $-0.365 \text{ V}$  to  $-0.48 \text{ V}$  at pinch off. For QPC E there are two plateaus observed in the interval between  $-0.27 \text{ V}$  and  $-0.38 \text{ V}$  at pinch off. After correction with a series resistance, the curve of each QPCs in (a) and (b) is almost repeated in the same trace. For both measurements, the conductance of each QPC shows the quantization in the same range of the gate voltage. Comparing with

## 5. Quantum Point Contacts in Linear Transport

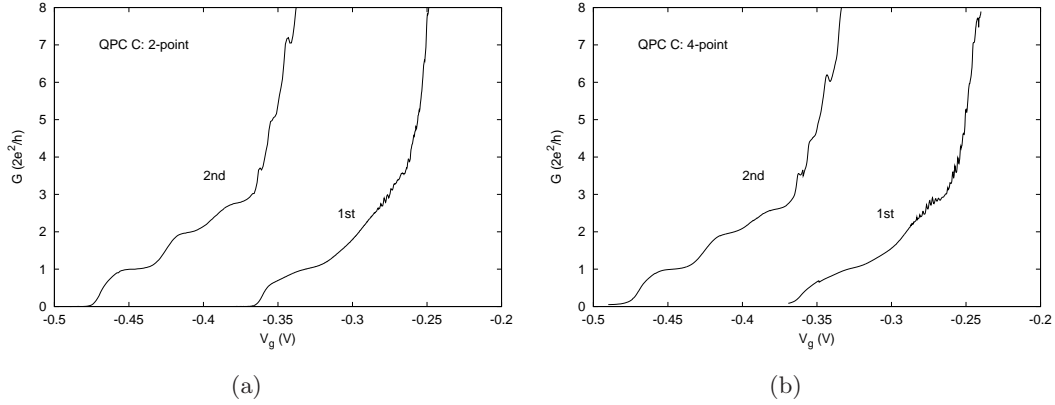


Figure 5.5.: The differential conductance quantization of QPC C at the 1<sup>st</sup> and the 2<sup>nd</sup> cooling in the He<sup>3</sup>/He<sup>4</sup> dilution refrigerator. The conductance is obtained by (a) 2-point measurement after correction for a resistance of 2.4 kΩ, and (b) 4-point measurement after correction for a series resistance of 470 Ω

the conductance of QPC F, the gate voltage interval of the formation of QPC C and QPC E is smaller than that of QPC F. This confirms that the width size of gate F1-F2 is wider than that of gate C1-C2 and E1-E2.

The comparison of the differential conductance of QPC C (C1-C2) between the cooling process at a different time, the 1<sup>st</sup> and the 2<sup>nd</sup> cooling, has been shown in Fig. 5.5. The conductance presented before is all obtained after the 2<sup>nd</sup> cooling. The differential conductance obtained by the 2-point and 4-point measurement setup is shown in Fig. 5.5(a) and Fig. 5.5(b), respectively. We can see clearly that there is an improvement of conductance quantization. The conductance quantization in the 2<sup>nd</sup> cooling process is observed in the region of a more negative gate voltage. The quantization is more pronounced, and shows more plateaus in conductance from one to three plateaus. The conductance is the inverse of measured resistance after subtraction of a series resistance of 2.4 kΩ for the 2-point measurement and 470 Ω for the 4-point measurement. We also notice the curve in the 1<sup>st</sup> cooling that there is an oscillation appearing in the differential conductance at the beginning of the quantization. For the details of this oscillation, we will discuss afterwards in the section 5.2

### 5.1.2. QPCs in the Sample PR1:d1

We studied the differential conductance quantization of the quantum point contacts in the sample **PR1:d1**, which has the structure of two systems of double quantum dots in series, as schematically shown in Fig. 5.6. The geometry of the QPC split gates for both systems is 250 nm width and 200 nm length. The pattern of gate A1, C2, D1, and F2 are designed as the finger gates in order to form each dot structure. The inset shows the electron micrograph of one of double dot systems. The size of the double dot is designed to be different for two systems.

Figure 5.7(a) to 5.7(e) show the comparison of differential conductance of QPCs in sample **PR1:d1** obtained by the 2-point measurement between before and after the sample illumination with IR-LED. The conductance for each QPC is measured as a function of corresponding split gate voltage. The illumination is used to change the properties of the 2DEG, for example, to increase electron density, to reduce the impurity scattering influencing the electron mobility, etc. The conductance  $G$  before illumination for all QPCs shows unclear quantization. After illuminating the sample, the quantization is improved and the traces are shifted to higher negative

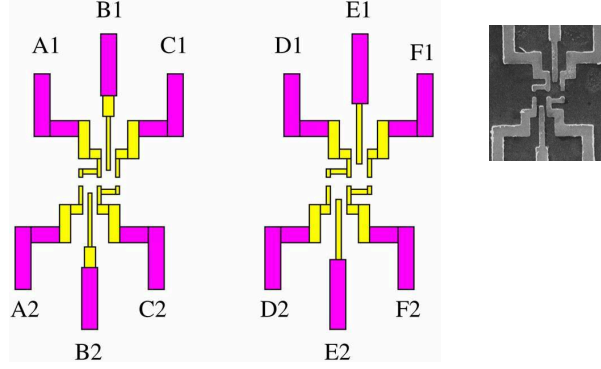


Figure 5.6.: Schematic structure of two different size of double quantum dot systems in series of the sample **PR1:d1**. The SEM image of such double dots has been shown in the inset.

gate voltages.

All conductance traces show pronounced plateaus in units of  $2e^2/h$ . Therefore, we can correct the conductance of each QPC with a series resistance by matching the plateaus to the reasonable value in the unit of  $2e^2/h$ . A series resistance of 2 k $\Omega$  is used to subtract from the resistance of QPC A and QPC A1C2. The measured resistance of QPC D, D1F2, and F is subtracted with the series resistance of 1.8 k $\Omega$ , 2.2 k $\Omega$ , and 2 k $\Omega$ , respectively. Thus, the well-defined eight conductance plateaus of QPC A and four plateaus of QPC A1C2 appear and have been respectively shown in Fig. 5.7(a) and 5.7(b), whereas, there are four plateaus appearing in the conductance of QPC D, QPC D1F2, and QPC F, as shown in Fig. 5.7(c)-5.7(e). Unfortunately, the conductance of QPC C is not presented here because the gate C1 is broken. We also tried to measure the conductance in QPC C but it needed too high a negative voltage, and it does not show any evidence of quantization.

The series resistance used to corrected the conductance for all QPCs is noticed to be in the range of 1.8 k $\Omega$ - 2.2 k $\Omega$ . This series resistance include the resistances at two contacts of the Hallbar terminal that are used for the 2-point measurement setup. It can be seen that the quality of quantization in all differential conductance traces is improved after sample illumination. These traces have been corrected with the corresponding series resistance, but the conductance traces before sample illumination are not corrected.

## 5.2. Conductance Oscillation in Quantum Point Contacts

In this section, we discuss the oscillatory behaviour appearing in the conductance of some quantum point contacts in our samples.

### 5.2.1. QPC C in the sample PR1:d2

From the the 1<sup>st</sup> cooling in Fig. 5.5, the conductance of QPC C decreases as the  $V_g$  increases negatively, and there is an additional structure; a sequence of conductance peaks before the quantization begins. This oscillatory behaviour can be observed in both measurement setups. However, after 2<sup>nd</sup> cooling these conductance oscillations disappears.

Figure 5.8(a) shows the differential conductance of QPC C as a function of the gate voltage  $V_{C2}$  when the gate voltage  $V_{C1}$  is fixed. The  $V_{C2}$  is swept in steps of 250  $\mu$ V, and the  $V_{C1}$  is varied in steps of 4 mV. We can observe that a sequence of conductance peaks exists in three regions: (i)  $-0.23$  V <  $V_{C2}$  <  $-0.22$  V, (ii)  $-0.27$  V <  $V_{C2}$  <  $-0.24$  V, and (iii)  $-0.29$  V

## 5. Quantum Point Contacts in Linear Transport

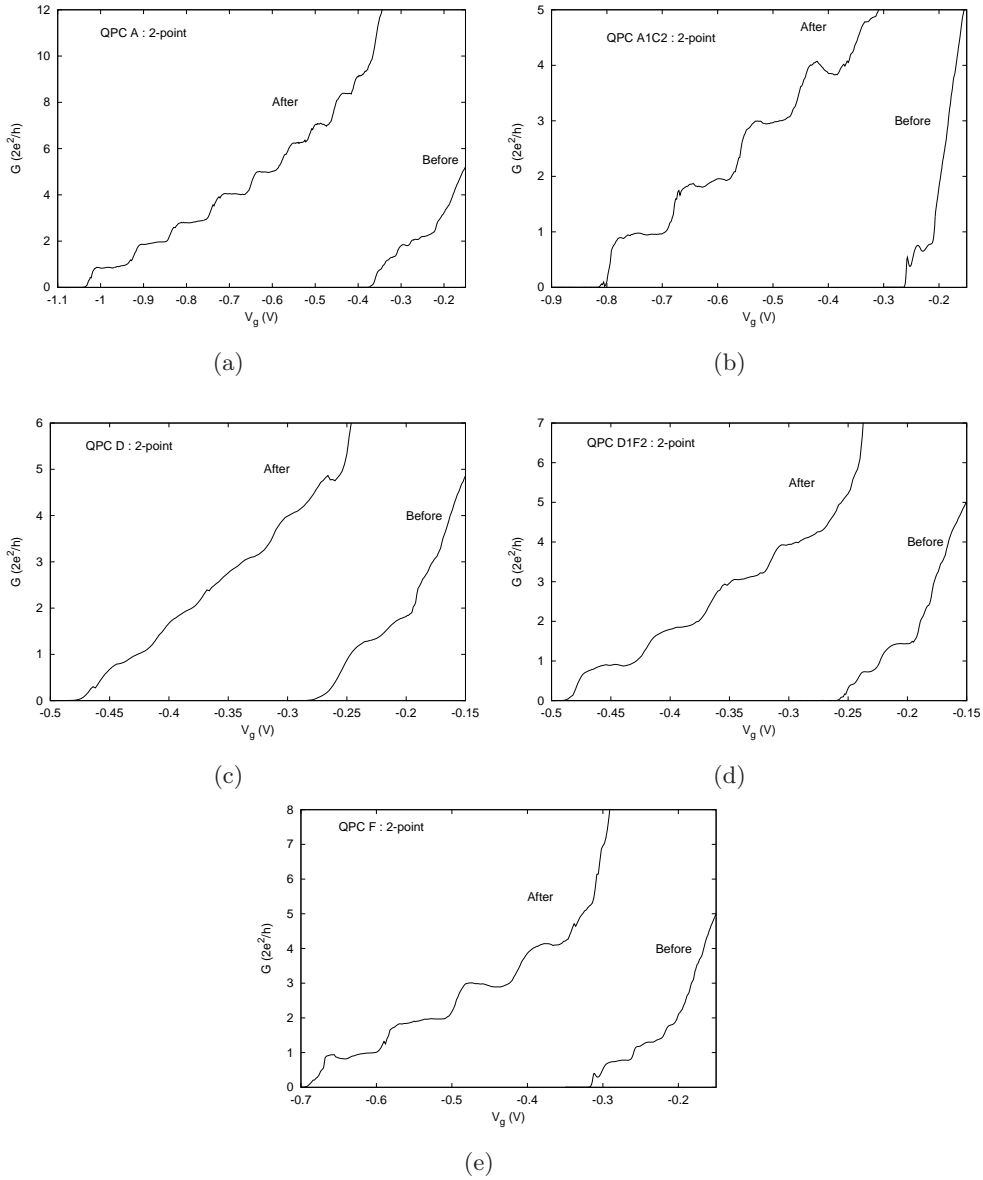


Figure 5.7.: The differential conductance  $G(V_g)$  of the (a) QPC A, (b) QPC A1C2, (c) QPC D, (d) QPC D1F2, and (e) QPC F of the sample **PR1:d1** before and after illuminating the sample. All traces are obtained by the 2-point measurement.

## 5.2. Conductance Oscillation in Quantum Point Contacts

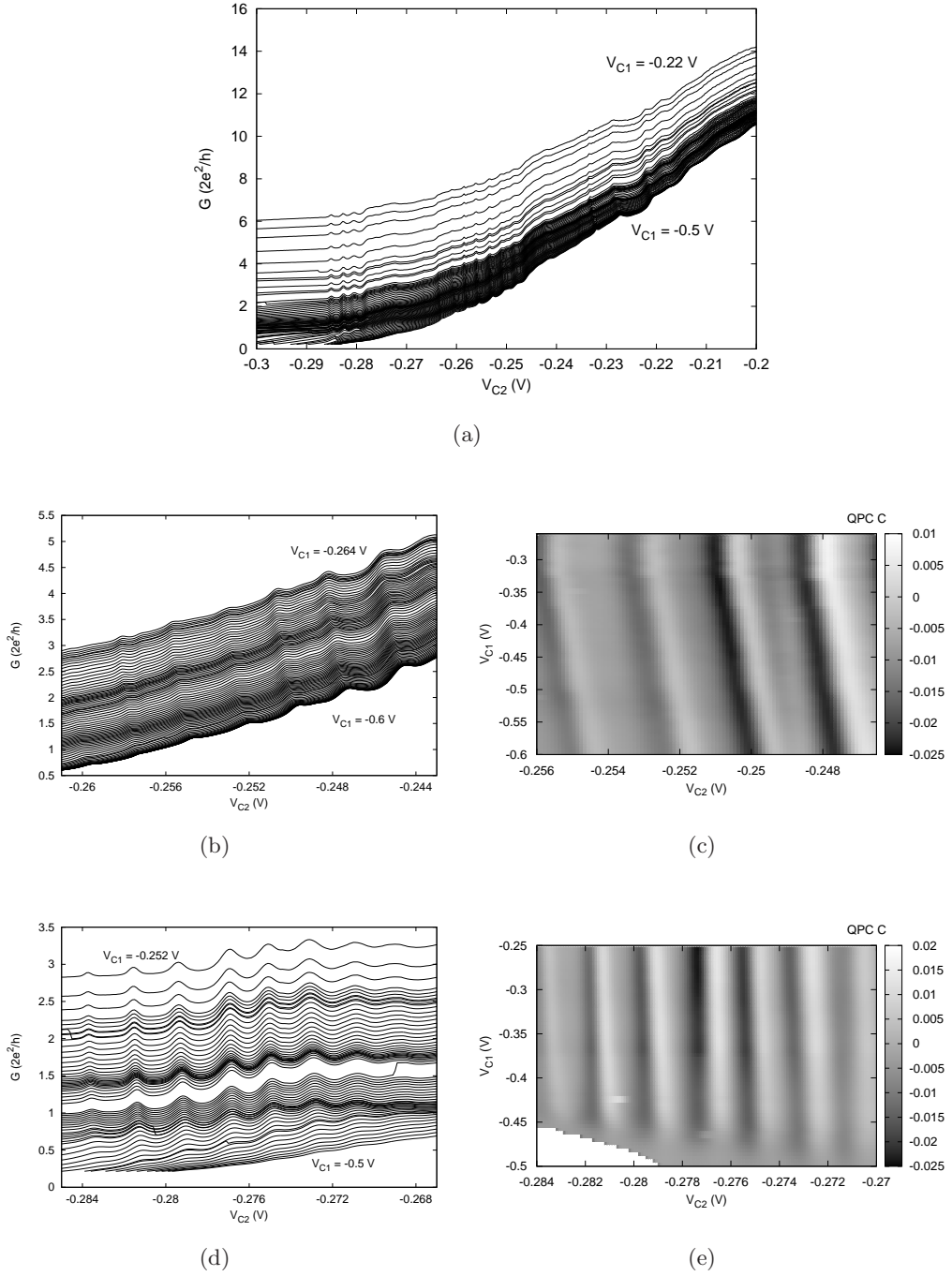


Figure 5.8.: (a) The differential conductance  $G$  of QPC C as a function of gate voltage  $V_{C2}$  while the  $V_{C1}$  is fixed at a constant value. The  $V_{C1}$  is varied from  $-0.22$  to  $-0.5$  V in steps of  $4$  mV. There are the sequences of conductance peaks appearing in each trace. (b) and (d) Conductance oscillation in (a) at two regions of  $V_{C2}$ . (c) and (f) Gray-scale plot of the transconductance  $dG/dV_{C2}$  respectively corresponding to (b) and (d) as a function of  $V_{C1}$  and  $V_{C2}$  for clarity of the peak position.

## 5. Quantum Point Contacts in Linear Transport

$< V_{C2} < -0.27$  V. These oscillations can be observed in every conductance trace in which the gate C1 voltage is varied from -0.22 V to -0.5 V in steps of 4 mV. Seven conductance peaks in the the middle region are shown in Fig. 5.8(b). To see the detail of this feature in the differential conductance, the  $V_{C2}$  is swept in steps of 100  $\mu$ V, which is smaller than that of the data in Fig. 5.8(a). The average separation between peaks is about 2.5 mV.

To display the feature in the conductance traces more clearly we show the transconductance  $dG/dV_{C2}$ , which is calculated by numerical differentiation from the measured differential conductance. The transconductance is zero on the conductance peaks or valleys, and shows maxima or minima in the transition regions between conductance peaks and valleys. Figure 5.8(c) shows the gray scale plot of the transconductance of the data in Fig. 5.8(b). The maxima are represented as the bright area and the minima are represented as the dark area. Four stripes are shown and their slope  $dV_{C1}/dV_{C2} \approx -4000$ , which is an almost vertical line, is clearly changed to be approximately -370 at  $V_{C1} = -328$  mV, and also slightly changed again around  $V_{C1} = -0.5$  V. For the sequence of the peaks in the middle, the position of the conductance peaks shifts to less negative of the  $V_{C2}$  as the  $V_{C1}$  is varied to more negative. This means that the position of conductance peaks in Fig. 5.8(c) is slightly shifted when  $V_{C1} > -328$  mV, and obviously shifted when  $V_{C1} < -328$  mV.

In order to see the detail of the oscillation in the region of  $-0.29$  V  $< V_{C2} < -0.27$  V, the  $V_{C2}$  is also swept in steps of 100  $\mu$ V and the data is shown in Fig. 5.8(d). The oscillations can be observed clearly in this region. The data gap shown in this figure is the jumping of the measured data at  $V_{C1} = -376$  mV, which is not significant and also not reproducible. The gray scale plot of transconductance,  $dG/dV_{C2}$ , of the data in Fig. 5.8(d) is shown in Fig. 5.8(e). The transconductance pattern is almost vertical stripes. The slope of each stripe is constant. This shows that the gate C1 voltage does not effect the position of conductance peaks when the gate C2 voltage is swept. The average spacing between peaks is about 2 mV.

The conductance oscillations might be Coulomb blockade oscillations due to the periodicity. It can be assumed that there is an unexpected quantum dot coupled to the quantum point contact. For the system with low density of electrons, the ionized donors in the doped layer of the heterostructure can generate the random impurity potential [54, 55]. Many electron puddles in the 2DEG are formed by wells in the random potential. Qualitatively, a electron puddle behaving like a quantum dot might be accidentally coupled with one of split gates of the quantum point contact; gate C2 for this QPC. Hence, when the  $V_{C2}$  is swept, the coupling of the dot is changed and the electron in the dot can tunnel through the barrier of the random potential. The conductance peak can therefore be observed as the superposition between the Coulomb blockade oscillations and the conductance of a QPC. This assumption could be confirmed by the cooling sample in another time that can change the properties of 2DEG and also the distribution of ionized donors providing the random potential. This can make more homogeneous in 2DEG and redistribute electron puddles, especially the one coupled with our QPC. The oscillation then disappears in the conductance of QPC C in the 2<sup>nd</sup> cooling as already shown in Fig. 5.5.

Figure 5.9 shows the differential conductance as a function of  $V_{C1}$  corresponding to the data in Fig. 5.8(d). We can see a big data jumping at  $V_{C1} = -376$  mV, which has been shown as a data gap in Fig. 5.8(d). The conductance at  $V_{C2} = -277$  mV which is a maximum of the conductance peak in Fig. 5.8(d) has been shown and compared to the conductance at two neighbouring minima:  $V_{C2} = -276$  mV and  $V_{C2} = -278$  mV. The conductance traces with  $V_{C2} = -276$  mV and -278 mV are obviously below the trace with  $V_{C2} = -277$  mV. The slight plateau at  $G \approx 1.5(2e^2/h)$  corresponds to the dark repeating conductance traces at  $G \approx 1.5(2e^2/h)$  in Fig. 5.8(d).



## 5.2. Conductance Oscillation in Quantum Point Contacts

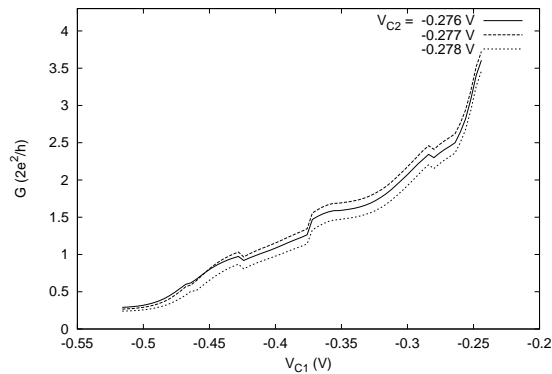
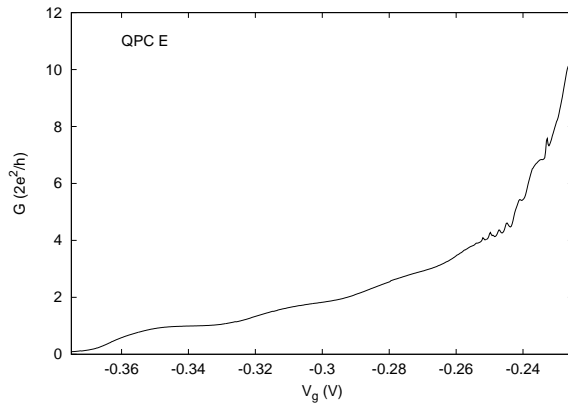
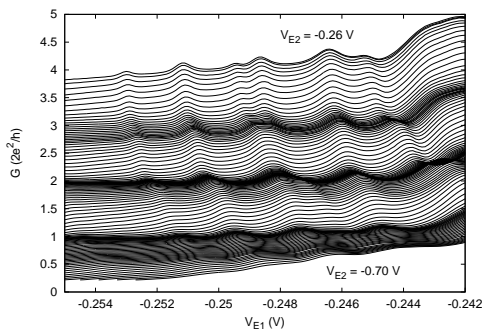


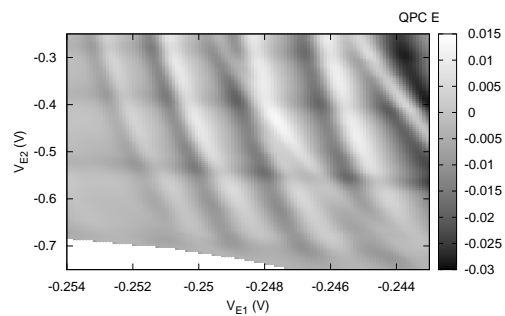
Figure 5.9.: The differential conductance of QPC C as a function of gate voltage  $V_{C1}$  at three values of gate voltage  $V_{C2}$ .



(a)



(b)



(c)

Figure 5.10.: (a) The differential conductance of QPC E as a function of gate voltage  $V_g$ . (b) The traces of  $G$  of QPC E as a function of the  $V_{E1}$ . Each trace is plotted at one fixed value of  $V_{E2}$ . The  $V_{E2}$  is varied from  $-0.25$  V to  $-0.7$  V. (c) Gray-scale plot of the transconductance  $dG/dV_{E1}$  corresponding to data in (b) as a function of  $V_{C1}$  and  $V_{C2}$  for clarity of the peak position.

### 5.2.2. QPC E in the sample PR1:d2

Oscillations in the conductance can also be observed in QPC E as well. These oscillations might also be due to the coupling of QPC E to an accidental quantum dot which is formed by the random impurity potential. The differential conductance with the 4-point measurement of QPC E is shown in Fig. 5.10(a). The conductance is corrected with a series resistance of 1 k $\Omega$  to match the 1<sup>st</sup> and the 2<sup>nd</sup> plateaus. The conductance of QPC E is measured as a function of gate voltage  $V_g = V_{E1} = V_{E2}$ . The oscillation is also found at the beginning of quantization. Hence, we keep the  $V_{E2}$  at a fixed value and measure the differential conductance as a function of the  $V_{E1}$ , as shown in Fig. 5.10(b).  $V_{E1}$  is swept in steps of 100  $\mu$ V and  $V_{E2}$  is varied with 4 mV per step from -0.25 V to -0.7 V. We can clearly see the dark repeating conductance traces at  $G \approx 2e^2/h$ ,  $2(2e^2/h)$ , and  $3(2e^2/h)$ . These repeating traces correspond to the first to the third plateaus if this conductance data is presented as a function of the  $V_{E2}$ .

Figure 5.10(c) shows the gray scale plot of transconductance  $dG/dV_{E1}$  of the data in Fig. 5.10(b) to see the pattern clearly. There are four pronounced peaks appearing in the conductance of QPC E. The position of the Coulomb peaks is shifted to less negative  $V_{E1}$  as the  $V_{E2}$  is negatively increased. It can also be seen that there is structure crossing the transconductance traces. They occur as slight dark lines along  $V_{E1}$  on the plane of the transconductance. This almost likes some double dot structure with weak interdot coupling. It can be inferred that the QPC E might couple with the system of two electron puddles from the inhomogeneous of electron density in the 2DEG, and these two dot are also weak coupled with each other. Thus, the structure like charging diagram of double dot system occurs when  $V_{E1}$  and  $V_{E2}$  are independently varied.

### 5.2.3. QPC A in the Sample PR1:d4

The oscillatory behaviour in the differential conductance of a QPC has also been observed in a third sample. The SEM image of the quantum dots system and a standalone point contact in the sample **PR1:d4** is shown in Fig. 5.11. One split gate of standalone QPC A, A1, is linked to the left gate (lead-to-dot) of a single dot structure in the quantum dots system. All metal gates are labeled from A to F. When a negative voltage is applied to the gate A1, one gate of a dot is also energized simultaneously. The split gates A1-A2 with 200 nm length are placed diagonally and separated with 250 nm in the vertical direction. Thus, the diagonal separation between gate A1 and A2 is about 320 nm. In this section, we are only interested in the QPC A in this sample.

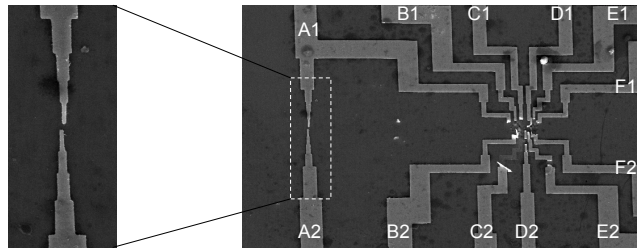


Figure 5.11.: The electron micrograph of the quantum dots system and a standalone quantum point contact in the sample **PR1:d4**. The left figure shows the closed-up of QPC A.

The negative voltage is applied to gate A1 and A2, and swept simultaneously. The sequence of the differential conductance peaks of QPC A can be observed, as shown in Fig. 5.12. The gate voltage  $V_g = V_{A1} = V_{A2}$  is swept in steps of 250  $\mu$ V. The measured resistance from QPC A is not subtracted by any series resistance because we cannot obtain and match any plateaus in

the conductance. This data is obtained by the 2-point measurement technique. The oscillatory behaviour in the conductance of QPC A can be seen more clearly when we keep the the gate A2 voltage fixed and sweep the gate A1 voltage. The result can be shown in Fig. 5.13.

Figure 5.13(a) shows that the gate voltage  $V_{A2}$  is varied from -160 mV to -400 mV in 2.5 mV per step, and the gate voltage  $V_{A1}$  is swept in steps of 250  $\mu$ V. This conductance is compounded with three sets of measured data. It can be seen the evolution of the peaks while the gate voltage is changing. When the  $V_{A2}$  increases negatively, the sequence of peaks shows more pronounced. There are five pronounced conductance peaks which occur as the conductance is decreasing. To be able to see the position and the pattern of the conductance peaks clearly, the gray scale plot of the differential conductance of QPC A has been shown in Fig. 5.13(b). The solid line indicates the position of the maximum of the peak and the slope,  $dV_{A2}/dV_{A1}$ , is approximately -450, which means that the conductance peak is just slightly shifted. The peak spacing  $\Delta V_{A1}$  is about 4.5 mV. Figure 5.13(c) shows the gray scale plot of the transconductance corresponding to the peaks pattern in 5.13(a) and 5.13(b). The solid line with the same slope is also used to indicate the peaks position changing.

Figure 5.14(a) shows the differential conductance of QPC A as a function of the  $V_{A2}$ . The conductance quantization of QPC A is observed when the  $V_{A1}$  is fixed and  $V_{A2}$  is swept. When  $V_{A1}$  is tuned to higher negative voltages, the first plateau of the quantization is clearly observed. The  $V_{A1}$  is varied in steps of 2.5 mV and the  $V_{A2}$  is swept in steps of 250  $\mu$ V. Figure 5.14(b) shows the re-plotted conductance in Fig. 5.14(a) as function of  $V_{A1}$  as well as the plotting in Fig. 5.13(a). This measured data corresponds to the data in Fig. 5.13 because the oscillatory behaviour also occurs in the range of  $-200 \text{ mV} < V_{A1} < -175 \text{ mV}$  in Fig. 5.14(b). We can clearly see the thick line of a few repeating conductance traces at  $-170.5 \text{ mV} < V_{A2} < -170 \text{ mV}$ . It shows that the conductance in this small range of  $V_{A2}$  is at the first plateau of the conductance quantization for all sweeping value of  $V_{A1}$ . As seen in Fig. 5.14(b), the conductance converges to  $2e^2/h$  when the  $V_{A1}$  is reduced, and  $G \approx 2e^2/h$  at  $V_{A1} < -240 \text{ mV}$ .

The periodic oscillation in the differential conductance of QPC A come from the superposition effect of the coupling system between a QPC and a single unexpected quantum dot as well as QPC C and QPC E of the sample **PR1:d2** described in two previous sections. The Coulomb blockade oscillation of a single dot then appears in the conductance of the QPC. The unexpected quantum dot might be formed by the random impurity potential contributed by ionized donors [54]. Another possibility, which can explain Coulomb blockade oscillations in this sample, might be the influence of the Ohmic contact of the metal gates on the surface of the Hallbar. Because of this influence, a single quantum dot in which the gate A1 is the one of the lead-to-dot gates may be formed and deplete the 2DEG underneath a dot structure. To compensate the influence forming the dot structure, therefore, we apply the positive voltage to the other split gates except gate A1 and A2. However, this also improves the properties of 2DEG by attracting the electron at the interface of heterojunction.

Firstly, the positive voltage is applied and varied from 0 to 0.5 V to the gate B1, B2, and C1, which are the metal gates of a dot structure having a lead-to-dot gate linked to the gate A1. While the  $V_{A2}$  is fixed at -0.4 V, the pattern of the conductance peaks does not change significantly, as shown in Fig 5.15(a). In Fig. 5.15(b) all split gates except gate A1 and A2 are applied with higher positive voltage  $V_{pos}$ , while  $V_{A2}$  is still fixed at -0.4 V. We can see the change of peaks pattern beginning at  $V_{pos} = 0.9$ . The applied positive voltage finally has some influence to the 2DEG.

Then, we ground all split gates except the gate A1 and A2 again. The split gates of QPC A are applied with the negative voltage, and the differential conductance is measured again after applying the positive voltage to other gates. It can be seen clearly that the quantization of conductance is improved and shows some well defined plateaus. Figure 5.15(c) shows the

## 5. Quantum Point Contacts in Linear Transport

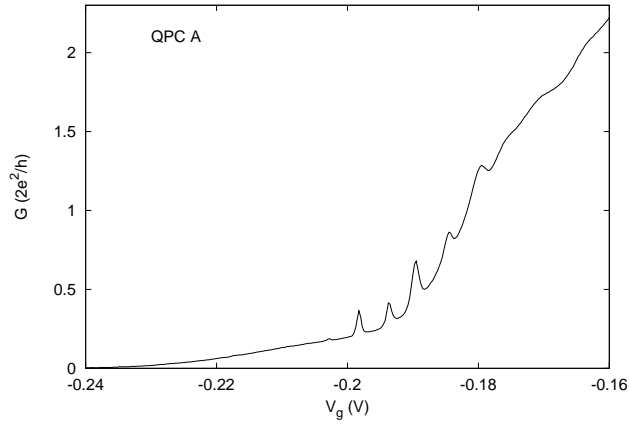
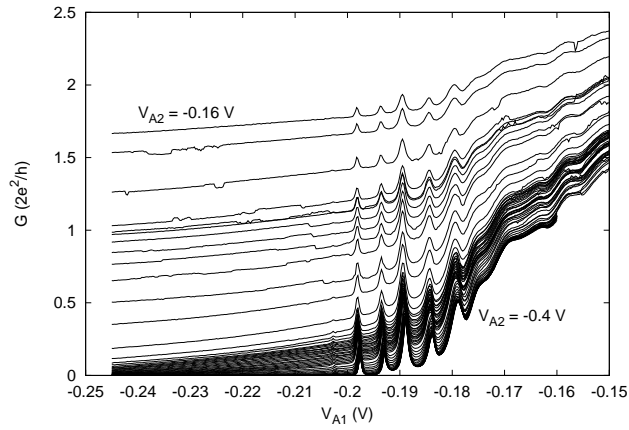
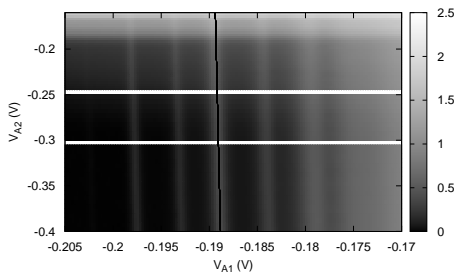


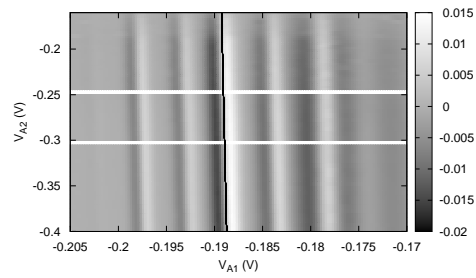
Figure 5.12.: Oscillation in the differential conductance of QPC A measured by the 2-point measurement. The  $G$  is measured as a function of  $V_g = V_{A1} = V_{A2}$ .



(a)



(b)



(c)

Figure 5.13.: (a) The differential conductance of QPC A in the sample **PR1:d4** as a function of the  $V_{A1}$ . Each trace is shown at a fixed value of  $V_{A2}$ . The  $V_{A2}$  is varied from -0.16 V to -0.4 V. Gray scale plot of (b) the conductance and (c) the transconductance of QPC A as a function of  $V_{A1}$  and  $V_{A2}$ . Solid line indicates the changing of the Coulomb peak position.

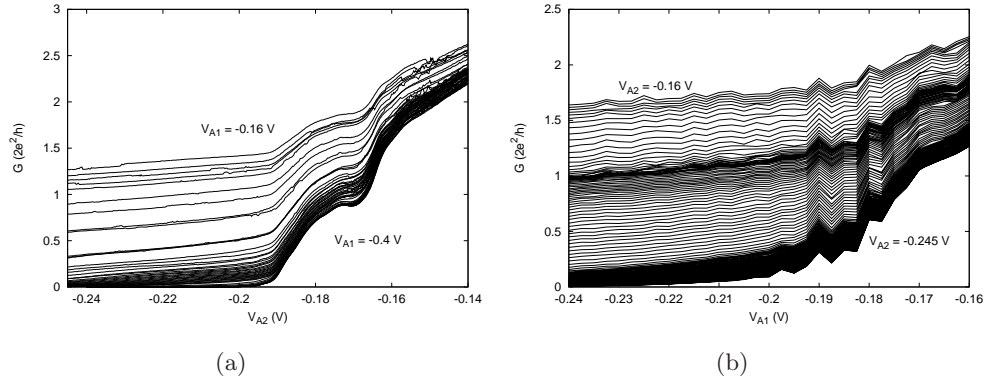


Figure 5.14.: (a) The differential conductance of QPC A as a function of  $V_{A1}$ . Each trace is shown at a fixed  $V_{A1}$ . The  $V_{A1}$  is varied from -0.16 V to -0.4 V. (b) The conductance data in (a) is re-plotted as a function of  $V_{A1}$ . The  $V_{A2}$  is varied from -0.16 V to -0.245 V. Oscillation in the conductance can be observed at the same region of  $V_{A1}$  as Fig. 5.13(a).

comparison of the differential conductance before and after applying the positive voltage. Figure 5.15(d) shows the differential conductance of QPC A after correction for a series resistance of 2.3 k $\Omega$ . The Coulomb blockade oscillation disappears and the quality of conductance of QPC A is much better and quantized in the unit of  $2e^2/h$ . There are seven plateaus in the differential conductance. It can be inferred that an unexpected single quantum dot disappears in the 2DEG and no longer couples to the QPC. For the interesting oscillatory behaviour in the conductance of the QPC A in the sample **PR1:d4**, it will be discussed again in the nonlinear measurement of a QPC coupled with an unexpected quantum dot in Coulomb regime in the section 6.5.

## 5. Quantum Point Contacts in Linear Transport

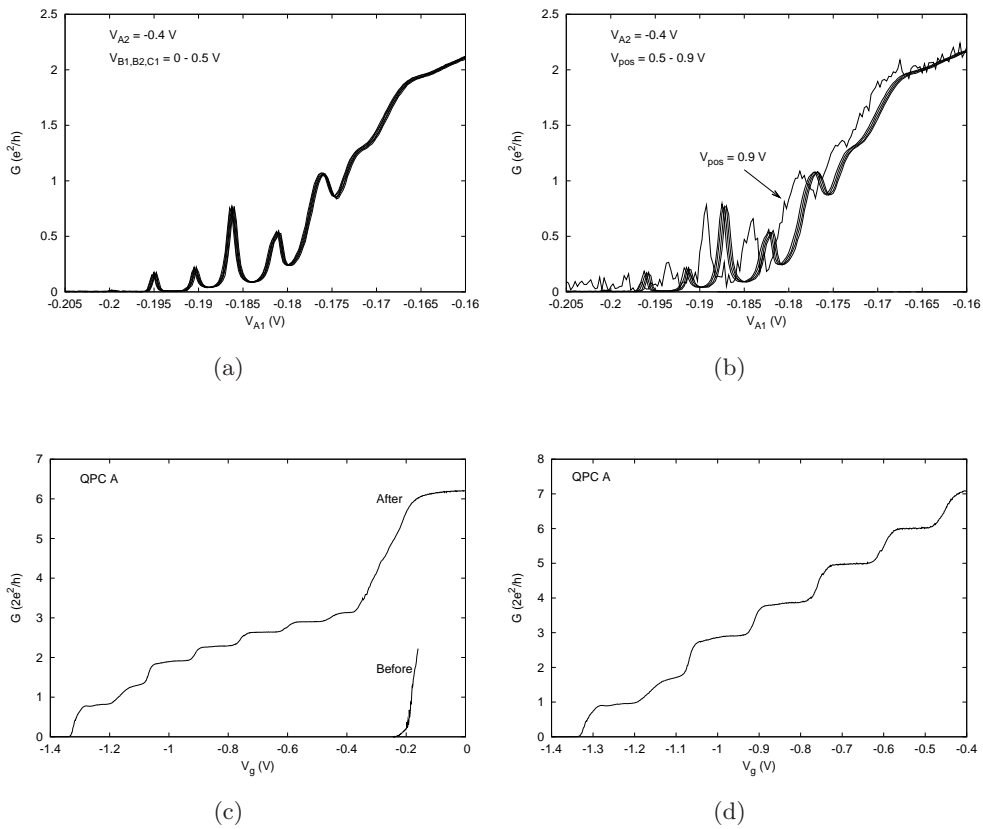


Figure 5.15.: (a) The conductance oscillation in QPC A as function of  $V_{A1}$  when  $V_{A2}$  is fixed at  $-0.4$  V and  $V_{B1,B2,C1}$  is biased with positive voltage. (b) The conductance of QPC A when other gates except gate A1 and A2 are applied by positive voltage  $V_{pos} = 0.5$  V to  $0.9$  V. (c) The comparison of  $G$  between before and after applying  $V_{pos}$ . (d) The quantization of  $G$  in QPC A after correction for a series resistance.

## 6. Single Quantum Dots with Weak Coupling

### 6.1. Linear Transport of the Quantum Dots in Weak Coupling Regime

To characterize all single quantum dots in our samples, we need to perform linear measurements in which a very small voltage is biased to source and drain contact of the sample;  $V_{sd} = 10 \mu\text{V}$  comparable to  $k_B T$  for our measurement at low temperature. Because the energy level spacing  $\Delta E$  is presumed to be greater than  $k_B T$ , only one quantized energy level within  $k_B T$  or small biased window contributes to the electron transport. The linear transport so called the single level transport is therefore obtained in this regime. There are five single dots in two samples to present in this part showing the investigation of the Coulomb blockade oscillations with weak coupling between the quantum dots and the reservoirs.

#### 6.1.1. Coulomb Oscillation of the dotII in the sample PR1:d2

Initially, we study the electron transport through the dotII structure in the sample **PR1:d2** in weak tunnel coupling regime. In order to obtain the Coulomb oscillations occurring in the differential conductance in this regime, we have tuned the voltage of the left gate ( $V_{C1C2} \equiv V_{\text{QPC } c}$ ) and the right gate ( $V_{E1E2} \equiv V_{\text{QPC } e}$ ) which are connected to the reservoirs, to obtain strong tunneling barriers.

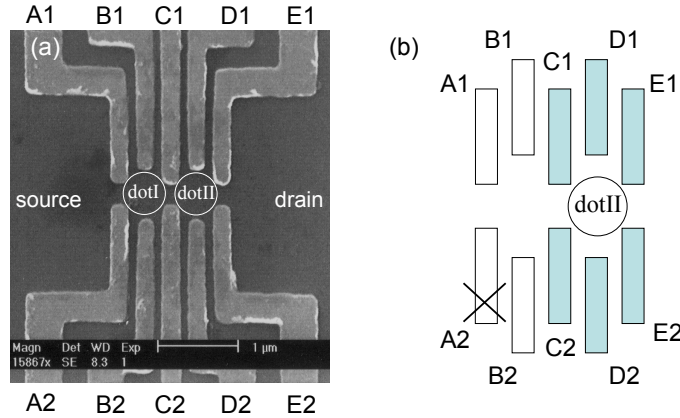


Figure 6.1.: (a) Scanning electron micrograph of the double dots structure in the sample **PR1:d2**. (b) Schematic of device and labels for each gates. Shaded gates are used to form the dotII. The gate A2 is ungrounded due to a shortcut to a contact of Hall bar sample.

The dots structure in the sample **PR1:d2** with identified gates and dots is shown in Fig. 6.1(a). The size of lithographic design for each dot is 400 nm by 600 nm. To form the dotII in Fig. 6.1(b), all shaded gates are tuned to define an electron puddle. The side gate voltage can be tuned by adjusting the voltage of gate C1(E1) and C2(E2) simultaneously. Similarly, the center or plunger gate is controlled by simultaneously tuning the voltage of gate D1 and D2. The gate A1 and

## 6. Single Quantum Dots with Weak Coupling

center gate B1B2 are not used. They are grounded and have no effect on the 2DEG. Additionally, the gate A2 has a short circuit to one contact of Hall bar, thus it is always ungrounded during the measurement performed.

We investigate the range of  $V_{C1C2}$  and  $V_{E1E2}$  to obtain the Coulomb blockade oscillation in the dotII structure. In Fig. 6.2, the differential conductance  $G$  of QPC C and QPC E is measured as a function of their own gate voltage at each applied voltage of QPC D ( $V_{D1D2} \equiv V_{\text{QPC D}}$ ), which is the center gate or plunger gate voltage for the quantum dot structure. Because the changing of the center gate voltage  $V_{D1D2}$  has an influence to the side gate voltage,  $V_{C1C2}$  and  $V_{E1E2}$ , and the measured differential conductance, we are then interested in the effect of center gate voltage to the side gate voltage.

The differential conductance of QPC C in Fig. 6.2(a) and QPC E in Fig. 6.2(b) with fixed  $V_{D1D2}$  and no applied other gate voltages show the quantization of the conductance for each curve. The  $V_{D1D2}$  has been varied from -0.9 to -1.3 V in order to observe the effect of center gate voltage to side gate voltage. The differential conductance is presented in the unit of  $2e^2/h$ . We can barely see the first plateau of the conductance quantization of QPC C and QPC E with  $V_{D1D2}$  of -0.9 to -1.2 V, whereas the conductance of both QPCs with  $V_{D1D2} = -1.3$  show the losing of conductance quantization. In order to obtain the Coulomb blockade oscillation in a single quantum dot, the conductance of side gates are focused on about  $e^2/h$  or below. Therefore, the range of side gate voltages for observing the Coulomb oscillation are selected as  $V_{C1C2} = -0.32$  to  $-0.35$  V and  $V_{E1E2} = -0.21$  to  $-0.25$  V.

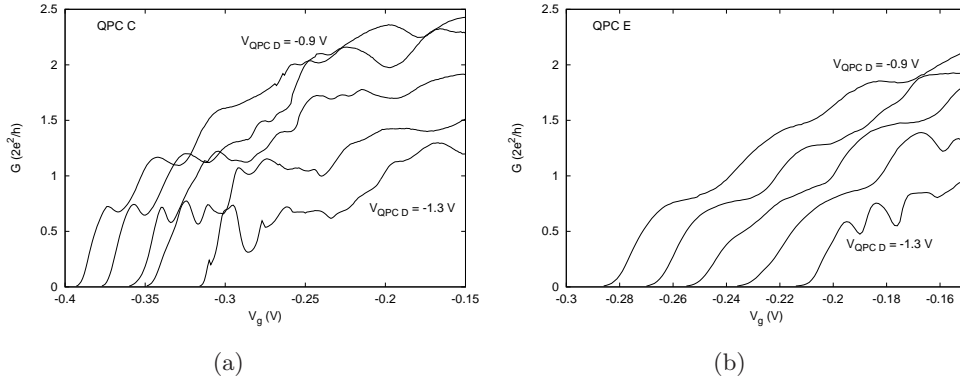


Figure 6.2.: Differential conductance of QPC C and QPC E in the sample **PR1:d2** with applied QPC D from -0.9 V to -1.3 V in steps of 0.1 V

Figure 6.3 shows the observation of Coulomb blockade oscillation as a function of center gate voltage  $V_g$  at various values of  $V_{C1C2}$  and  $V_{E1E2}$ . The  $V_g$  is swept in the increment of  $250 \mu\text{V}$ . Each subfigure shows the differential conductance with fixed  $V_{C1C2}$ , and  $V_{E1E2}$  is varied from -0.21 to -0.25 V. The  $V_{C1C2}$  is changed from (a) -0.32 V to (d) -0.35 V. The curves have been offset by  $0.5e^2/h$  for clarity. In (a), we can observe the periodic oscillation in the differential conductance, especially in the range of  $-1.15\text{V} \lesssim V_g \lesssim -1\text{V}$ , but the valleys do not touch zero. When  $V_{E1E2}$  is decreased, the pinch off of conductance is clearly shifted to higher value of  $V_g$ .

When  $V_{C1C2}$  is lowered to (b) -0.33 V, it can be seen that the valleys of the conductance peaks are closer to zero conductance at  $V_g < -1.15$  V, however, the amplitude of these peaks are quite low. For  $V_{C1C2} = -0.34$  V and  $V_{C1C2} = -0.35$  V, we can clearly see the sequence of pronounced conductance peaks at  $V_{E1E2} = -0.23$  V and  $V_{E1E2} = -0.24$  V respectively, while the conductance peaks do not appear clearly with the other values of  $V_{E1E2}$ . Therefore, we can locate the condition for the side gate voltage to obtain a good pronounced Coulomb blockade oscillation as  $-0.35 \text{ V} \leq V_{C1C2} \leq -0.34 \text{ V}$  and  $-0.24 \text{ V} \leq V_{E1E2} \leq -0.23 \text{ V}$ . The objective of this



## 6.1. Linear Transport of the Quantum Dots in Weak Coupling Regime

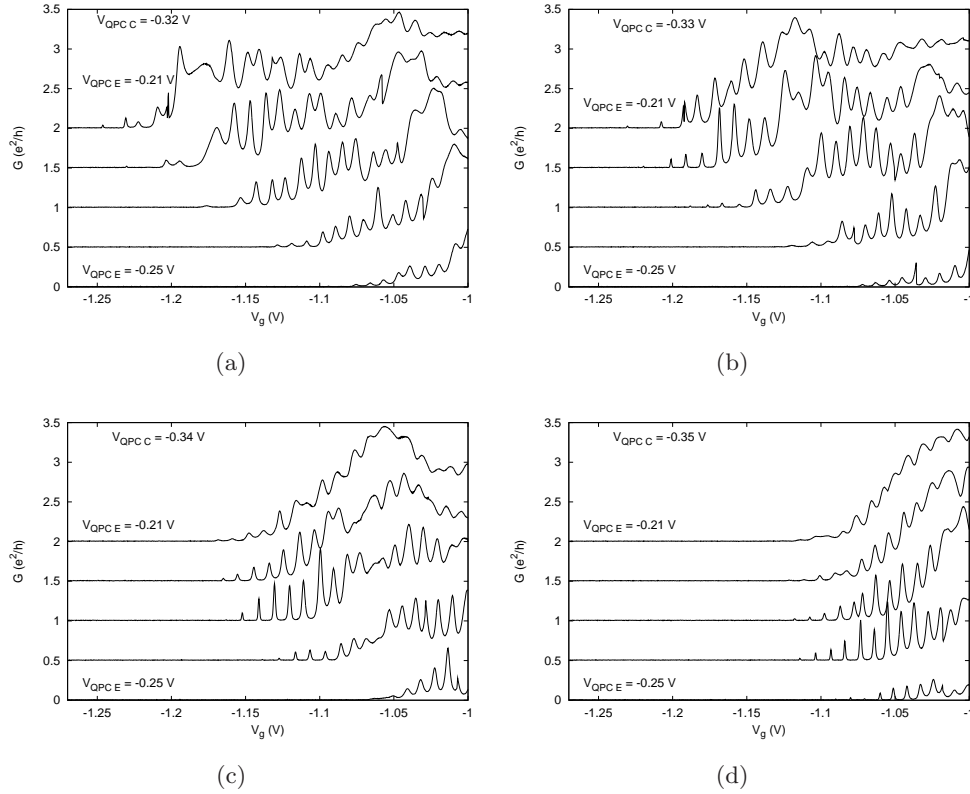


Figure 6.3.: Coulomb blockade oscillations in dotII at different conditions of tuned gates. Each curve is measured as a function of  $V_g$ . The  $V_{C1C2}$  is varied from (a)  $-0.32$  V to (d)  $-0.35$  V. The curves have been offset for clarity.

initial characterization is to obtain pronounced Coulomb oscillations with well-defined minima in between.

Thus, we can obtain more nice Coulomb blockade periodic oscillations with varying the  $-0.355$   $V \leq V_{C1C2} \leq -0.34$  V and  $-0.245$   $V \leq V_{E1E2} \leq -0.23$  V in the step of 5 mV, as shown in Fig. 6.4(a) to (d). In (a) and (b), it can be noticed that the sequence of conductance peaks is shifted to higher value of  $V_g$  when  $V_{E1E2}$  is reduced. With  $V_{C1C2} = -0.34$  V, the pronounced conductance peaks are exhibited at  $V_{E1E2} = -0.235$  V, while they are shown at lower  $V_{E1E2}$  of  $-0.24$  V with  $V_{C1C2} = -0.345$  V as well. The valleys of this sequence of peaks is flat on the zero conductance. The conductance peak spacing  $\Delta V_g$  is approximately 10 mV.

When  $V_{C1C2}$  is reduced to (c)  $-0.35$  V, the Coulomb oscillation still appears along decreasing conductance curve, the most pronounced conductance peaks are shown at  $V_{E1E2} = -0.245$  V, but the amplitude of the peaks with flat valleys is relatively low. The Coulomb oscillation is clearly shifted to higher  $V_g$  when  $V_{C1C2}$  is reduced to  $-0.355$  V, as shown in (d). This confirms the center gate voltage affecting to the tunneling coupling of the dot to the reservoirs. The amplitude of oscillation increases when  $V_{E1E2}$  decreases, however, the conductance peaks with flat valleys at zero conductance disappear. For all Coulomb oscillations in the strong tunnel coupling regime in Fig. 6.4, especially in the range of high value of  $V_g$ , the peaks are so broadened due to the tails of adjacent peaks overlapping. Therefore, we select the sequence of the most pronounced and sharp conductance peaks at  $V_{C1C2} = -0.345$  V and  $V_{E1E2} = -0.24$  V in the range of  $-1.13$   $V \leq V_g \leq -1.07$  V to study the detail of the Coulomb blockade oscillation in the weak tunnel coupling regime.

## 6. Single Quantum Dots with Weak Coupling

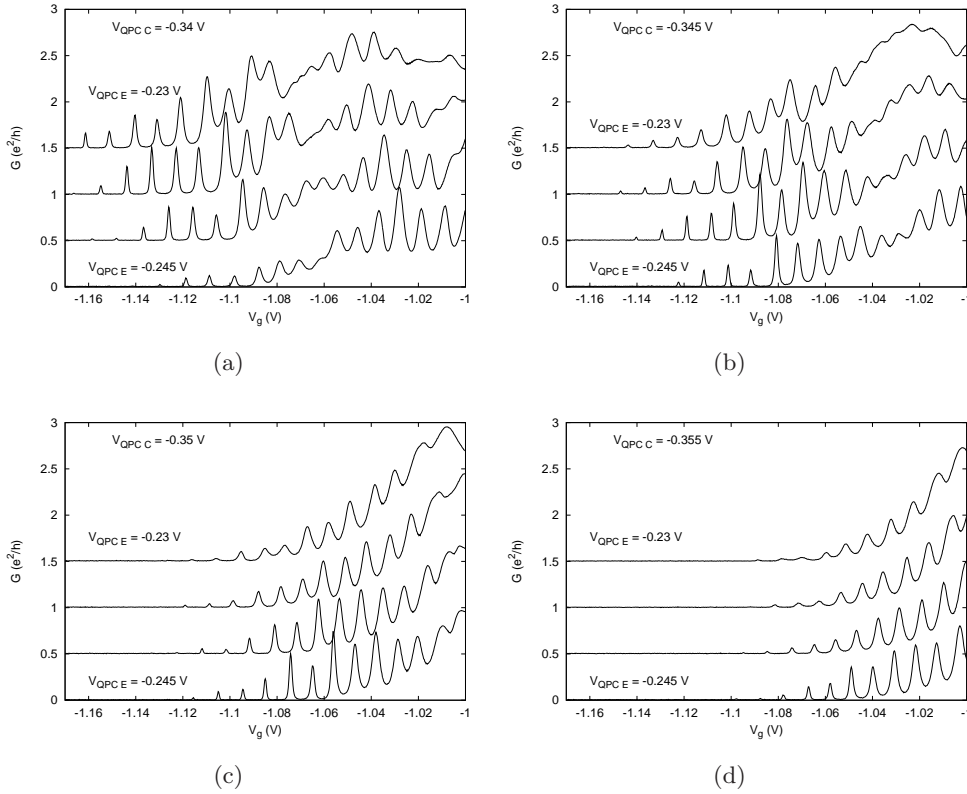


Figure 6.4.: Coulomb blockade oscillations in differential conductance of dotII. The  $V_{C1C2}$  is varied from (a)  $-0.34$  V to (d)  $-0.355$  V. Each subfigure,  $V_{E1E2}$  is varied from  $-0.23$  V to  $-0.245$  V. Both side gates are tuned in the increment of  $5$  mV. The curves have been offset for clarity.

The Coulomb blockade oscillations in the dotII structure at  $V_{C1C2} = -0.345$  V and  $V_{E1E2} = -0.24$  V with sweeping  $V_{D1D2}$  in the fine increment of  $50$   $\mu$ V has been shown in Fig. 6.5. There are six well pronounced and sharp conductance peaks with spacing between neighbouring peaks of  $\sim 10$  mV presented. The gate capacitance  $C_g = e/\Delta V_g$  is approximately  $16$  aF. This measurement was performed at bath temperature of  $65$  mK. The valleys between peaks fall down and touch almost zero conductance, which means no electron tunneling through the dot in the region. However, at  $V_g \gtrsim -1.09$ , the valleys are not so flat because the coupling become stronger with increasing  $V_g$ .

The line shape of an individual conductance peak is given by

$$G(V_g) = A \cdot \cosh^{-2} [B(V_g - V_{res})] + \text{offset}, \quad (6.1)$$

where  $A$  is the amplitude of the conductance peak,  $V_{res}$  is the gate voltage at the center of a resonance peak. The factor  $B = e\alpha/2k_B T$  in the quantum Coulomb blockade regime ( $\Gamma \ll k_B T \ll \Delta E \ll U$ ), whereas  $B = e\alpha/2.5k_B T$  in the classical Coulomb blockade or metallic regime ( $\Gamma \ll \Delta E \ll k_B T \ll U$ ), where  $\Gamma$  is the tunnel coupling of the dot to the reservoirs,  $\Delta E$  is the energy level spacing, and  $U = e^2/C_\Sigma$  is the charging energy. This equation is corrected with the background offset. The amplitude of conductance peaks is inversely proportional to the temperature in the quantum regime, whereas it is temperature independent in the metallic regime.

Eq. 6.1 give us the line shape of a thermally broadened resonance peak. This line shape is determined by the derivative of the Fermi-Dirac distribution function of the electrons in the

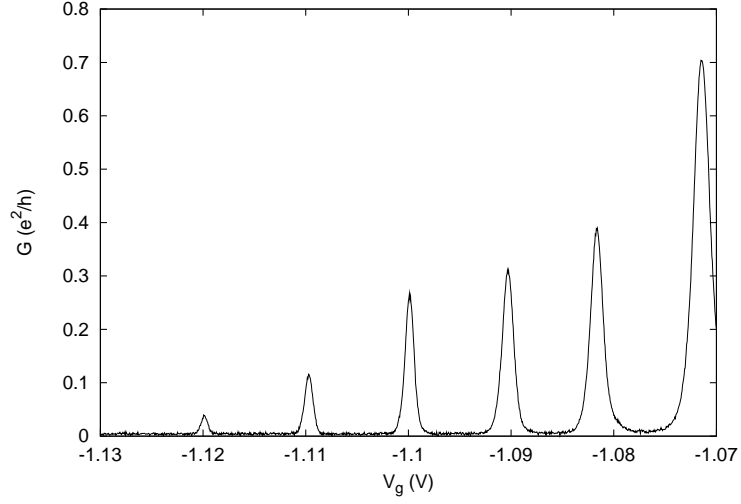


Figure 6.5.: Coulomb oscillation of dotII in the sample **PR1:d2** at  $V_{C1C2} = -0.345$  V and  $V_{E1E2} = -0.24$  V. The center gate D1D2 is swept in steps of  $50 \mu\text{V}$ .

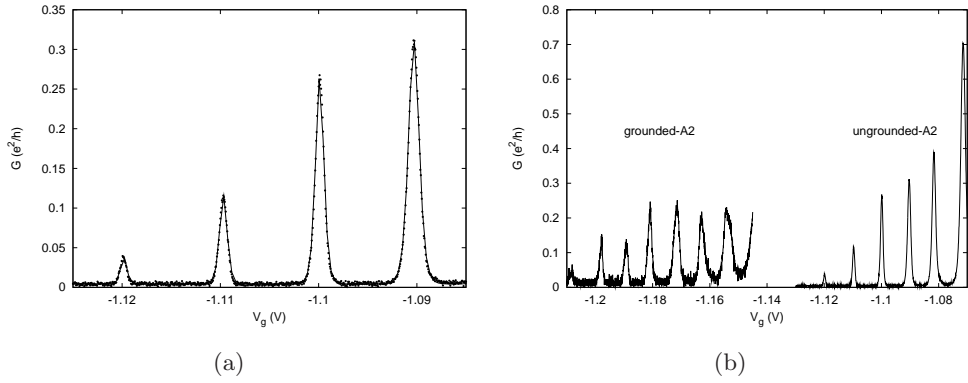


Figure 6.6.: (a) The data in Fig. 6.5 fit very well to the sum of thermally broadened conductance peak centered at each peak. (b) Comparison of coulomb oscillation of dotII in the sample **PR1:d2** between grounded and ungrounded gate A2. The center gate D1D2 in both data is swept in the same steps of  $50 \mu\text{V}$ .

## 6. Single Quantum Dots with Weak Coupling

reservoirs [56]. The conductance peak data in Fig. 6.5 fits excellently, at valleys as well as peaks, to sum of Eq. 6.1 centered at each peak at base temperature, as shown in Fig. 6.6(a). The line width or full-width at half maximum (FWHM) of the peaks slightly increases with  $V_g$  due to the increasing tunnel coupling influenced by center gate voltage.

Since there is a shortcut between gate A2 and one terminal contact of the Hall bar, if the gate A2 is grounded to the earth, the current might be able to leak out of the sample. The Coulomb oscillations shows a noisy background and peaks is measured when the gate A2 is grounded to the earth. It is compared to the nice oscillation with un-grounded gate A2 in Fig. 6.6(b).

### 6.1.2. Coulomb Oscillation of the dotI in the sample PR1:d2

Due to the shortcut between gate A2 and a terminal contact of Hall bar sample, we lost one gate to form a quantum dot in the dotI pattern. However, we tried to form the dotI with the remaining gates as indicated with the shaded gates in Fig. 6.7(a). Firstly, we use the gate A1 and B2 to form a quantum point contact so called QPC A1B2. The gate B2 is applied and fixed at a high negative voltage of -1.3 V. The differential conductance as a function of gate voltage  $V_g \equiv V_{A1}$  has been shown in Fig. 6.7(b). The conductance decreases with  $V_g$ , until  $V_g < -0.3$ , the conductance quantization can be observed, and the first three plateaus appear slightly. This means that the gate A1 and B2 can be used for coupling the dot to the reservoir.

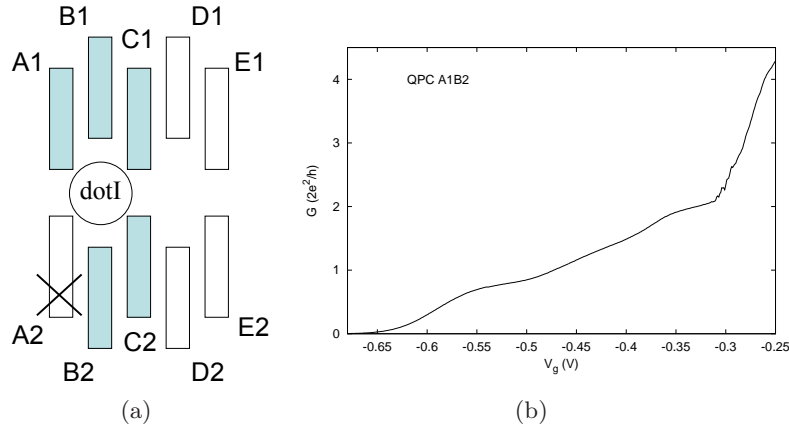


Figure 6.7.: (a) Schematic structure of the double dots in sample **PR1:d2**. The shaded gates are used to form a quantum dot in dotI structure. (b) The differential conductance,  $G$ , of QPC A1B2 as a function of gate voltage of both gates, which are swept simultaneously. The quantization in  $G$  can be observed.

To observe the condition for a good Coulomb blockade oscillation in the dotI, the gate voltage  $V_{A1}$  is varied from -0.45 to -0.53 V in the increment of 20 mV at a fixed  $V_{C1C2}$ , and the gate voltage  $V_{C1C2}$  is also varied from -0.534 to -0.546 V in the increment of 4 mV. The gate B2 is always fixed at -1.3 V. The center gate B1 is then swept in the step of 250  $\mu$ V. Each subfigure in Fig. 6.8, the  $V_{C1C2}$  is kept at the fixed value. The curves of each value of  $V_{A1}$  have been offset for clarity. The periodic Coulomb oscillation in differential conductance can be observed in these range of gate voltages.

When  $V_{A1}$  is reduced, the peak height decreases and pattern of oscillation is slightly changed. The conductance pinch off is clearly shifted to higher center gate voltage when  $V_{C1C2}$  decreases. This shows that the changing of  $V_{C1C2}$  has more influence on the oscillation than  $V_{A1}$  changing. The valleys of the conductance peaks reach to zero and become flat with decreasing  $V_g$ . This means that the center gate voltage  $V_g \equiv V_{B1}$  also has an effect on the coupling of the dot to reservoirs.

## 6.1. Linear Transport of the Quantum Dots in Weak Coupling Regime

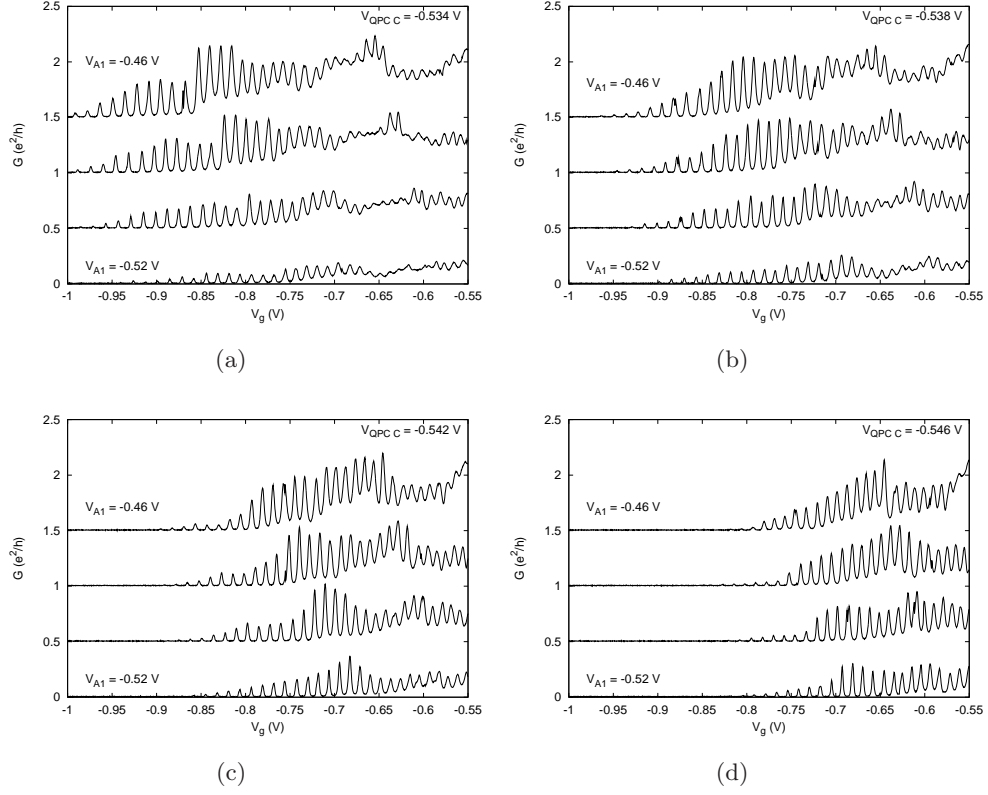


Figure 6.8.: Coulomb oscillation of dotI in the sample **PR1:d2**. The  $V_{\text{QPC C}}$  is varied from (a)  $-0.534$  V to (d)  $-0.546$  V. Each figure the  $V_{\text{QPC C}}$  is fixed and the  $V_{A1}$  is varied from  $-0.46$  V to  $-0.52$ . The gate B2 is always fixed at  $-1.3$  V. The center gate voltage  $V_g = V_{B1}$  is swept in steps of  $250 \mu\text{V}$ . The graphs have been offset with  $0.5e^2/h$  for clarity.

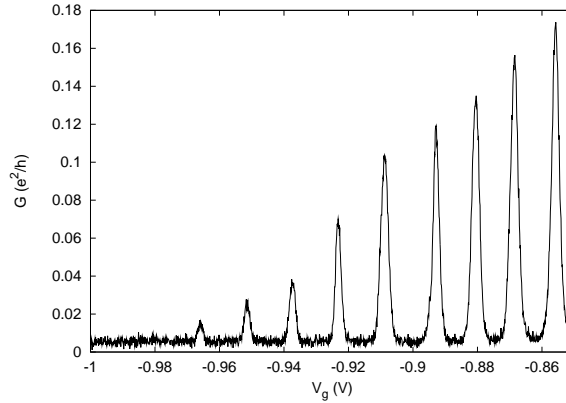


Figure 6.9.: Coulomb oscillation of dotI at  $V_{A1} = -0.5$  V,  $V_{\text{QPC C}} = -0.534$  V and  $V_{B2} = -1.3$  V. The center gate voltage  $V_g = V_{B1}$  is swept in steps of  $100 \mu\text{V}$ .

## 6. Single Quantum Dots with Weak Coupling

We determine the Coulomb blockade oscillation in weak tunnel coupling regime at  $V_{C1C2} = -0.534$  V,  $V_{A1} = -0.5$  V,  $V_{B2} = -1.3$  V, and  $-1$  V  $< V_g < -0.85$  V, because there are the sharp pronounced conductance peaks and flat valleys at the background, which is almost zero conductance. The Coulomb blockade oscillation is measured by sweeping the center gate voltage  $V_g$  in the small step of  $100 \mu\text{V}$ . In Fig. 6.9, it shows the sequence of pronounced conductance peaks which compound with nine sharp dominant peaks and low noise at background. The line shape of this data can be fit very well to the thermally broadened resonance peak in Eq. 6.1 for each single peak.

It is noticeable that the conductance peak spacing  $\Delta V_g$  is not same in all region. The  $\Delta V_g$  can be approximately 14 mV for  $-0.97$  V  $< V_g < -0.9$  V, while  $\Delta V_g$  is approximately 12 mV for  $-0.9$  V  $< V_g < -0.85$  V. The gate capacitance for  $-0.97$  V  $< V_g < -0.9$  V can then be calculated as  $C_g = e/\Delta V_g \simeq 11$  aF which is less than  $C_g \simeq 13$  aF for  $-0.9$  V  $< V_g < -0.85$  V. It can be confirmed that the increasing center gate voltage  $V_g$  has an influence to the tunnel coupling of the dot by increasing the coupling to reservoirs. This results in the valleys between peaks in the right part being lifted up and no longer going to zero due to the tail of adjacent peaks overlapping.

### 6.1.3. Coulomb Oscillation of the dot structure in the sample PR1:d1

In this section, we characterize each quantum dot in the double dots system in the the sample **PR1:d1**. The lithographic designed pattern of this double dots system is shown in Fig. 6.10(a). The size of each dot is 500 nm by 800 nm. Only three pairs of gate contact are required to be able to form the coupled dots. Figure 6.10(b) shows the schematic drawing of the double dots with labeling for each gate. Each dot can be formed by applying negative voltage to four gates. One gate behaves like a finger gate and is usually fixed at constant applied voltage, for example, gate D1 for the dotIII structure and gate F2 for the dotIV structure.

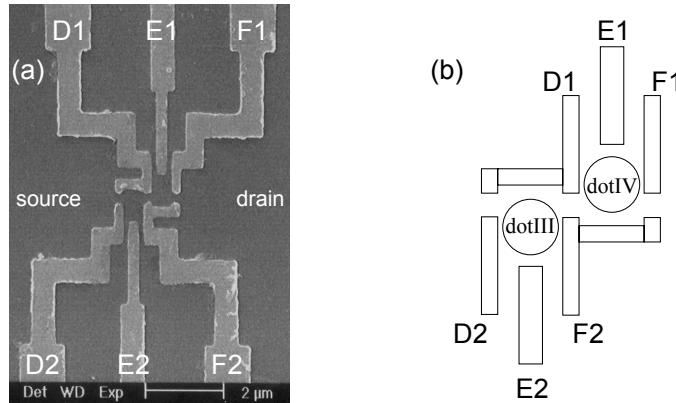


Figure 6.10.: (a) Scanning electron micrograph of the double dots structure in the sample **PR1:d1**. (b) Schematic of device and labels for each gates. The dots are identified as dotIII and dotIV. This pattern is decided to be able to form double dots by using only three pairs of gates.

**dotIII:** A quantum dot in the dotIII structure can be formed by applying negative voltage to the shaded gates as identified in Fig. 6.11. The gates D2 and F2 are used with gate D1 to make the tunneling barrier of the dot. Figure 6.12 shows the Coulomb oscillation in the differential conductance as a function of center gate voltage  $V_{E2}$ . The gate voltages  $V_{D1}$  and  $V_{F2}$  are varied independently between  $-0.24$  V and  $-0.25$  V. The  $V_{D2}$  is varied from  $-0.3$  V to  $-0.34$  V in

increments of 20 mV at fixed  $V_{D1}$  and  $V_{F2}$ . In each data curve, the center gate voltage  $V_{E2}$  is swept in steps of 1 mV. The curves have been offset with  $0.05e^2/h$  for clarity. When the  $V_{D1}$  is changed, the coupling of the dot to reservoirs via gate D2 and F2 both change.

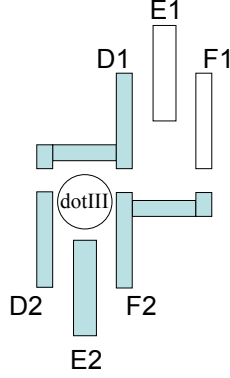


Figure 6.11.: Schematic of the double dots structure in the sample **PR1:d1**. A quantum dot identified as dotIII can be formed by applying negative voltage to four shaded gates.

In Fig. 6.12(a), The gate D1 and F2 are applied with the same voltage of -0.24 V. At  $V_{D2} = -0.3$  V, the oscillations appear with decreasing conductance as a function of  $V_{E2}$ . It can be seen that the conductance decreases with  $V_{D2}$  presumably due to increasing tunneling barrier via gate D2. In this range of  $-0.6$  V  $< V_{E2} < -0.3$  V, the small oscillation in the differential conductance and the pinch-off can be found, when  $V_{D2}$  is reduced to -0.34 V. The tunneling barrier of the dot is increased by decreasing the voltage of gate F2, which is another side gate of the dot structure. The conductance oscillations after reduced  $V_{F2}$  to -0.26 V are shown in Fig. 6.12(b). The pronounced oscillation still appears along the decreasing conductance curve. In Fig. 6.12(c),  $V_{D1}$  is reduced to -0.25 V, while  $V_{F2}$  is set at -0.24 V. In this case, we change the voltage of the finger gate affecting to the tunneling barrier at both side gates. Comparing to voltage condition in (a), the coupling of the dot to the leads is getting weaker. The pronounced sequence of conductance peaks shown at  $V_{D2} = -0.3$  V in (c), while the peaks in the oscillations are much lower at  $V_{D2} = -0.32$  V and disappear or pinch-off at  $V_{D2} = -0.34$  V. Figure 6.12(d) shows the Coulomb oscillations when the gate D1 and F2 are applied at the same value of -0.25 V. The valleys of the oscillations can almost reach to zero in this range of  $V_{E2}$ . The oscillation disappears when  $V_{D2}$  is decreased to -0.34 V in the pinch-off region.

From the Coulomb oscillations in Fig. 6.12, it can be interpreted that the increasing coupling of the dot to the reservoirs results in broadened, overlapping peaks with minima which do not go to zero. We can calculate that the  $\frac{\langle \delta(\Delta V_{E2}) \rangle}{\langle \Delta V_{E2} \rangle} \sim 0.02 - 0.03$ , where  $\delta(\Delta V_{E2})$  is the difference of two neighbouring Coulomb gaps. This fraction relates to the comparison of the energy level spacing  $\Delta E$  and the charging energy  $e^2/C_{\Sigma}$ , where  $C_{\Sigma}$  is the total capacitance of the dot. Thus, we can infer that the level spacing in this dot is relatively small compared with its own charging energy. Figure 6.13(a) shows the Coulomb oscillations close to pinch-off for  $V_{D1} = -0.25$  V,  $V_{F2} = -0.24$  V and  $V_{D2} = -0.3$  V. There are a few pronounced peaks appearing with flat valleys on a background of nearly zero conductance. This region is measured again by sweeping  $V_{E2}$  with smaller step of 250  $\mu$ V, and the conductance is then shown in Fig. 6.13(b). The estimated peak spacing  $\Delta V_{E2}$  is approximately 10 mV. The peaks in this region are broad and their amplitude is quite low, but the valleys reach nearly zero. We then use this condition of gate voltages to perform the nonlinear measurement of this dot system. The nonlinear result will be presented later in the section of nonlinear transport in weak coupling regime.

## 6. Single Quantum Dots with Weak Coupling

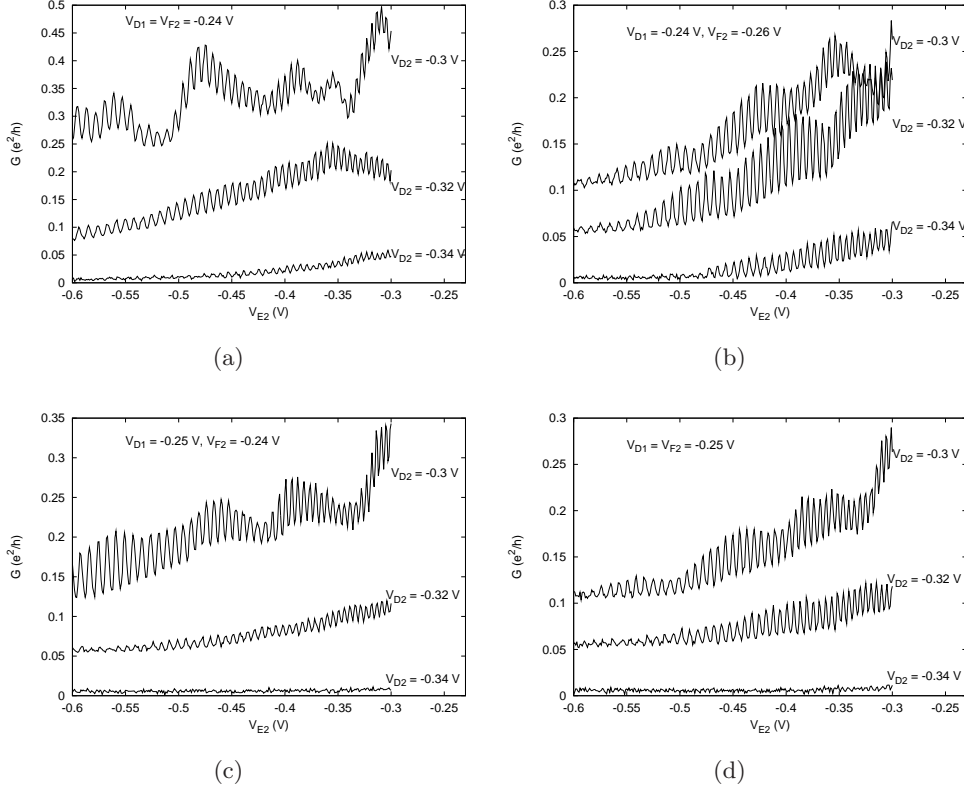


Figure 6.12.: Coulomb oscillation in differential conductance of dotIII in the sample **PR1:d1**. The  $V_{D1}$  and  $V_{F2}$  is varied separately. Each pair of  $V_{D1}$  and  $V_{F2}$  in (a) to (d),  $V_{D2}$  is varied from  $-0.3$  V to  $-0.34$  V. The curves have been offset by  $0.05e^2/h$  for clarity.

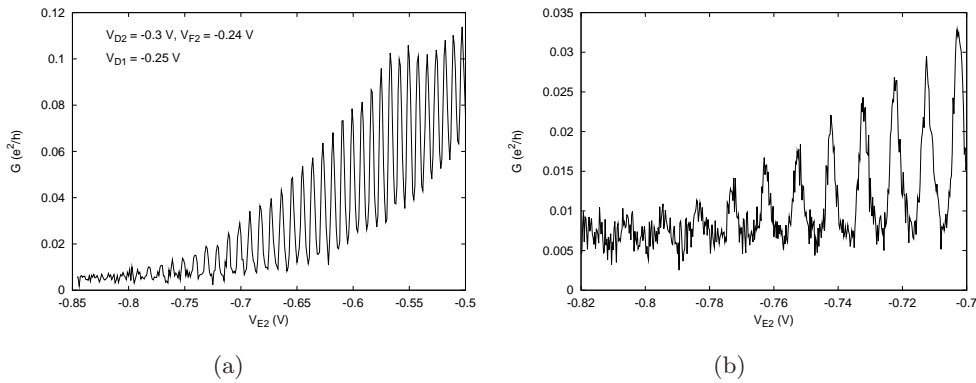


Figure 6.13.: The Coulomb blockade oscillation of dotIII. The differential conductance is measured as a function of  $V_{E2}$  in steps of (a) 1 mV and (b) 250  $\mu$ V. Both are measured at the same set of gate voltage parameters.



### 6.1. Linear Transport of the Quantum Dots in Weak Coupling Regime

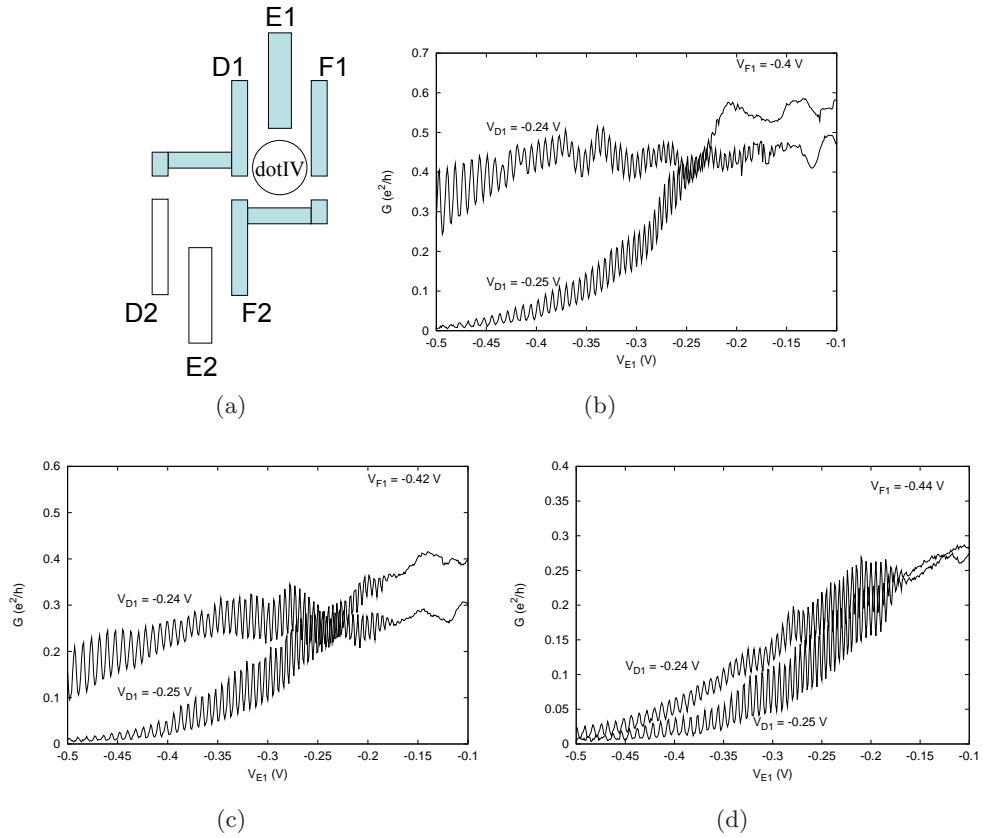


Figure 6.14.: (a) The schematic of the dots system in the sample **PR1:d1**. The shade gates are used to form a quantum dot named as dotIV. The Coulomb oscillation appears in the decreasing differential conductance. The  $V_{F1}$  is varied from (b) -0.4 V to (d) -0.44 V. The  $V_{E1}$  is swept in steps of 1 mV.

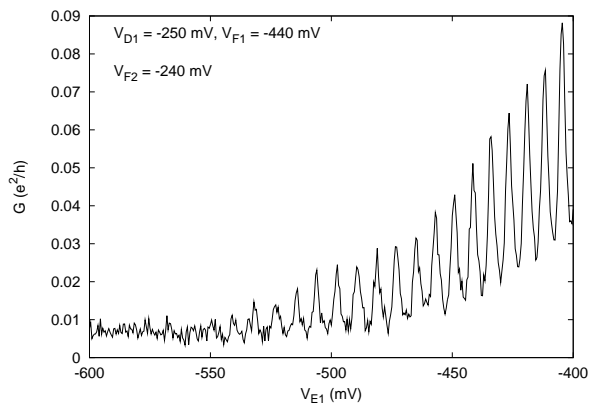


Figure 6.15.: The Coulomb blockade oscillation in dotIV at  $V_{D1} = -0.25$  V,  $V_{F2} = -0.24$  V, and  $V_{F1} = -0.44$  V. The  $V_{E1}$  is swept in steps of 500  $\mu$ V

## 6. Single Quantum Dots with Weak Coupling

**dotIV:** A quantum dot in the dotIV structure can be formed by applying negative voltages to the shaded gates as identified in Fig. 6.14(a). The gates D1 and F1 are used with gate F2 to form the tunneling barriers of the dot to the reservoirs. Figure 6.14(b)-(d) show the differential conductance as a function of center gate voltage  $V_{E1}$ . The Coulomb oscillations appear in each conductance curve. The gate F2 is fixed at  $-0.24$  V for all data curves. The  $V_{F1}$  is varied from (b)  $-0.4$  to (d)  $-0.44$  V. The conductance decreases when  $V_{E1}$  is swept to more negative voltages, and the oscillations then occur as the conductance decreases. The Coulomb oscillations appear in every curve with two different values of  $V_{D1}$ , which are  $-0.24$  and  $-0.25$  V.

It can be seen that the conductance clearly decreases when either  $V_{D1}$  or  $V_{F1}$  is reduced, because reducing this voltage increases the tunneling barrier between the dot and the reservoirs. In this our interesting range of  $V_{E1}$ , the Coulomb blockade oscillations with minima close to zero appear at  $V_{D1} = -0.25$  V. Therefore, we sweep the  $V_{E1}$  in steps of  $500 \mu$  V, which is small as a half of step swept in Fig. 6.14. The periodic oscillations are measured again at  $V_{D1} = -0.25$  V,  $V_{F1} = -0.44$  V, and  $V_{F2} = -0.24$  V. The sequence of conductance peaks is shown in Fig. 6.15. The estimated conductance peak spacing is approximately  $8.3$  mV. The gate capacitance is therefore about  $19$  aF. There are about 7-8 peaks with the valleys nearly zero before they disappears as decreasing  $V_{E1}$ . These peaks are quite low and broad. However, we use this condition of gate voltages to measure nonlinear transport of dotIV structure as presented later.

**After illumination:** We illuminated the sample **PR1:d1** with IR-LED to increase the carrier concentration in 2DEG, and then measured the differential conductance of both dots in the weak coupling regime again. Figure 6.16 shows the Coulomb blockade oscillation in (a) dotIII and (b) dotIV in the sample after illuminated. For both dots, the gate D1 and F2 are tied and applied by the same voltage of  $-0.45$  V. In order to determine the Coulomb oscillation in weak coupling regime,  $V_{D1}$  is set at  $-0.42$  V for dotIII, whereas  $V_{F1}$  is set at  $-0.95$  V for dotIV.

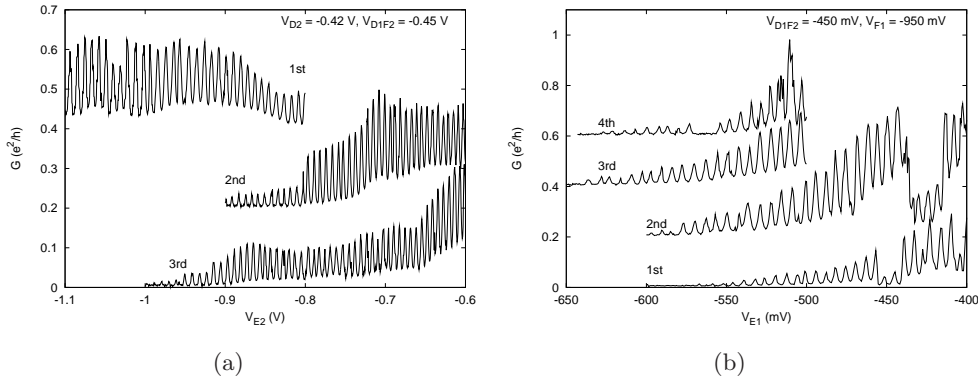


Figure 6.16.: (a) Non-stable conductance peaks of dotIII after illuminated.  $V_{D2} = -0.42$  V, and  $V_{D1F2} = -0.45$  V. Three repeat measurements have been done with the same gate voltage parameters. (b) Non-stable conductance peaks of dotIV in the same sample at  $V_{D1F2} = -0.45$  V, and  $V_{F1} = -0.95$  V. All curves have been offset with  $0.2e^2/h$  for clarity.

In Fig. 6.16(a), three repeat measurements are performed with the same side gate voltages. They clearly show that the results are not reproducible as well as the results of dotIV shown in Fig. 6.16(b). According to the result from both dots, the quality of the conductance peaks is not significantly better after illuminating the sample.

## 6.1. Linear Transport of the Quantum Dots in Weak Coupling Regime

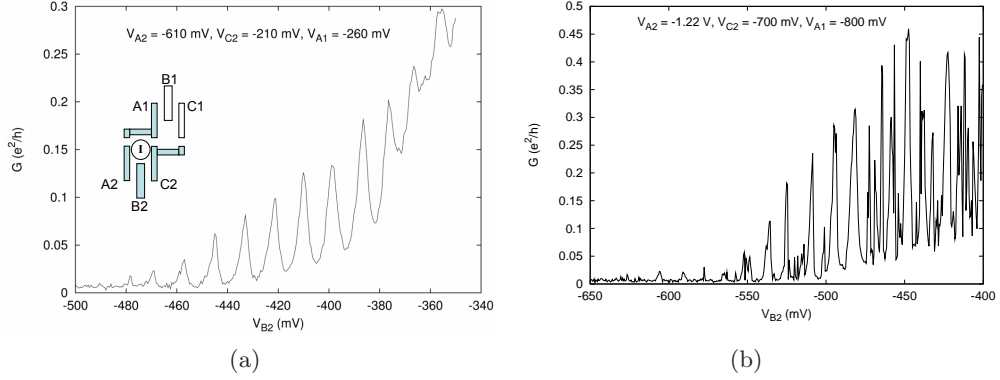


Figure 6.17.: (a) The differential conductance of dotI in the sample **PR1:d1** as a function of  $V_{B2}$ . There is the Coulomb oscillation appearing. The inset shows the schematic of another double dots structure in the sample **PR1:d1**. A quantum dot named dotI is presented and can be formed by using the shaded gates. (b) The differential conductance of dotI after illuminating the sample.

**dotI:** In the sample **PR1:d1**, we can also obtain the conductance oscillation of the dotI structure. This structure has a similar pattern as the dotIII structure, but the lithographic size of dot is smaller; 400 nm by 600 nm. The Coulomb oscillations in differential conductance of dotI are shown in Fig. 6.17(a). The schematic drawing of the dotI structure in the inset shows the shaded gates A1, A2, B2, and C2, which are used to form a small electron island in the dotI. The broad conductance peaks are shown up even though all gate voltages are set for weak coupling of the dot to the leads. The quality of the obtained peaks is not good for this dot. The spacing between peaks,  $\Delta V_{B2}$ , is approximately 12 mV. Then, the gate capacitance can be estimated of 13 aF. From the inset, because the gate C1 is broken for this structure, the dotII cannot then be performed by only three left gates (A1, C2, and B1).

In order to improve the quality of the Coulomb oscillations, we illuminated the sample and measured the differential conductance again. The measured conductance with new tuning parameters for the dotI gates is shown in Fig. 6.17(b). We were not able to obtain periodic Coulomb blockade oscillations. The conductance data fluctuates at some region during the measurement performed. The result then becomes non-stable and is not reproducible after the illumination.

In order to characterize and understand the transport in the nonlinear regime of a quantum dot with weak tunnel coupling, we perform nonlinear measurements by applying a DC-bias to source and drain contacts and measuring the differential conductance,  $G \equiv dI/dV_{sd}$ , in units of  $e^2/h$  versus the gate voltage  $V_g$  and the DC-bias source-drain voltage  $V_{sd}$ . The dot-to-lead gate voltages have been set for high tunnel barriers to obtain the sharp Coulomb conductance peaks in nearly zero DC-bias voltage.

## 6.2. Nonlinear Transport of Quantum Dots in the Sample PR1:d2

### 6.2.1. The dotII Structure

Figure 6.18 shows the nonlinear transport data of the quantum dot in the sample **PR1:d2** after un-grounding the short-circuited gate A2 to correct the conductance values. The measured differential conductance  $G$  clearly shows the pattern of Coulomb diamonds. The dark diamond-shaped areas correspond to the regions of the Coulomb blockade where  $G \approx 0$ , and the number of electrons,  $N$ , is fixed. Therefore the shape and size of the Coulomb diamonds refer to the regions where the charge,  $-eN$ , on the dot is stable. Thus it is often called a stability charge diagram. Along the  $V_{sd} \approx 0$  axis  $N$  changes to  $N + 1$  in the adjacent Coulomb diamond. For neighbouring diamonds the charge difference is equal to  $\pm e$ .

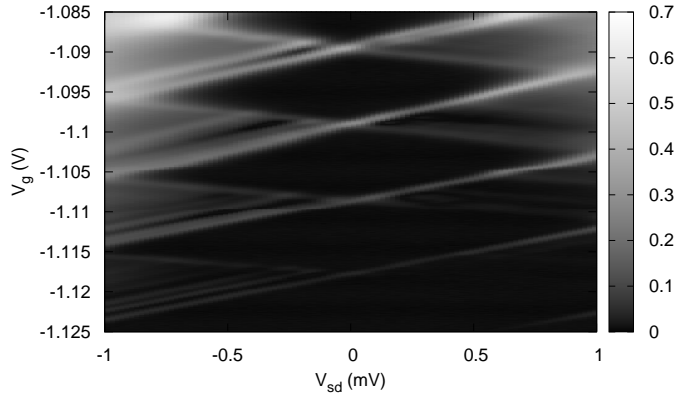


Figure 6.18.: Coulomb blockade diamonds measured on a quantum dot named dotII with  $V_{C1C2} = -345$  mV and  $V_{E1E2} = -240$  mV. The differential conductance  $G$  of the dot is showing in the grey scale.

At a fixed gate voltage  $V_g$ , an electron can tunnel through the dot when  $V_{sd}$  reaches the edge of the diamond. For an  $N$  electron diamond, the lower diamond edges correspond to the  $N$  electron ground state, and the upper edges corresponds to the  $N + 1$  electron ground state. When excited states enter into the source-drain window  $\Delta e V_{sd}$ , there are additional lines running parallel to the boundaries of the Coulomb blockade diamonds. For example, the parallel lines close to the upper edge of the  $N$  electron diamond indicate the energy of the excited states of the  $N + 1$  electron system entering into the bias window, and contributing to electron tunneling through the dot. Similarly, the lines running parallel to the lower edges indicate the energy of the excited states of the  $N - 1$  electron system. These details and analysis therefore will be discussed in the part on the excited states.

According to the constant interaction model, in the case of constant electrochemical potential level for drain reservoir  $\mu_d$ , the drain contact is grounded, all capacitances in a quantum dot system can be extracted and evaluated from the slope of the borderlines of the Coulomb

diamonds shown in Fig. 6.19 as

$$\begin{aligned}\frac{dV_g}{dV_{sd}}^+ &= \frac{C_g + C_d}{C_g}, \\ \frac{dV_g}{dV_{sd}}^- &= -\frac{C_s}{C_g},\end{aligned}\tag{6.2}$$

where  $(dV_g/dV_{sd})^+$  and  $(dV_g/dV_{sd})^-$  are the positive and negative slope of the borderlines respectively. The  $C_s$ ,  $C_d$ , and  $C_g$  are the source, drain, and gate capacitances. The total capacitance is written as  $C_\Sigma = C_s + C_d + C_g$ . The  $C_g$  is calculated from the Coulomb peak spacing  $\Delta V_g$ ;  $C_g = e/\Delta V_g$ . Therefore the proportionality factor relating a change in  $V_g$  to a shift in the energy in the dot,  $\alpha = C_g/C_\Sigma$ , and the charging energy,  $E_C = e^2/C_\Sigma = \alpha e \Delta V_g$ , can be obtained.

A quick estimate for a quantum dot can be obtained from the formula for an isolated dot of 2D metallic disk, this method is proposed by L. P. Kouwenhoven et al. [17]:

$$E_C = \frac{e^2}{C_{ii}} = \frac{e^2}{8\varepsilon_r\varepsilon_0 R},\tag{6.3}$$

where  $C_{ii}$  is a pure self-capacitance of the dot and can only be a lower bound,  $C_\Sigma > C_{ii}$ ,  $R$  is the dot radius,  $\varepsilon_r = 13$  in GaAs, and  $\varepsilon_0$  is the permittivity of free space. We can see that the size or radius of the dot is proportional to the self-capacitance  $C_{ii}$ . This clearly relates to the tunnel coupling of the dot. The energy level spacing  $\Delta E$  can be calculated by  $\Delta E = E_F/N$ , where  $E_F$  is the Fermi energy, and  $N$  is the number of electrons on the dot. We can obtain

$$\Delta E = \frac{E_F}{N} = \frac{m^*v_F^2}{2N} = \frac{\hbar^2\pi n_{2\text{DEG}}}{m^*N},\tag{6.4}$$

where  $v_F = \hbar\sqrt{2\pi n_{2\text{DEG}}}/m^*$  is the Fermi velocity in 2DEG,  $n_{2\text{DEG}}$  is the electron density of 2DEG, and  $m^* = 0.067m_e$  is the effective mass of the electron in GaAs. In case of an isolated quantum dot, the number of electrons can be estimated from  $N = n_{2\text{DEG}} \times \pi R^2$ .

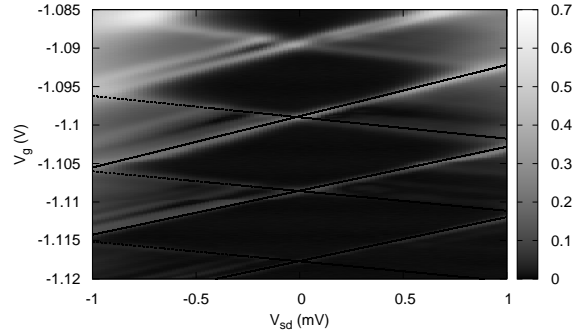
After cooling down the system, we have performed the nonlinear measurement of the dotII structure in the sample **PR1:d2** as presented in Fig. 6.19(a)-(c) for three cool down processes.<sup>1</sup> The added solid lines indicate the boundaries and shape of the Coulomb diamonds. The solid lines indicate the diamond borderlines with positive slope  $(dV_g/dV_{sd})^+$  and negative slope  $(dV_g/dV_{sd})^-$ . These measurement have been done with weak tunnel coupling by tuning the dot-lead gate voltages  $V_{C1C2}$  and  $V_{E1E2}$  to high negative values. For the first and second cooling process,  $V_{C1C2}$  and  $V_{E1E2}$  is set at -345 and -240 mV, respectively. The  $V_{C1C2} = -480$  mV and  $V_{E1E2} = -440$  mV for the third cooling process.

For the Coulomb diamonds in Fig. 6.19(a), the linear lines show the excellent fit to the boundaries of the diamonds with slope  $(dV_g/dV_{sd})^+ = 6.667$  and  $(dV_g/dV_{sd})^- = -2.778$ . There is a slight DC offset of  $V_{sd} = -15 \mu\text{V}$ . This might be due to the ground-offset of the measurement setup or instruments, i.e. current preamplifier. The Coulomb peak spacing is  $\Delta V_g = 9.6$  mV, thus the gate capacitance is  $C_g = e/\Delta V_g = 17$  aF. The parameters corresponding to these Coulomb diamonds can then be calculated that

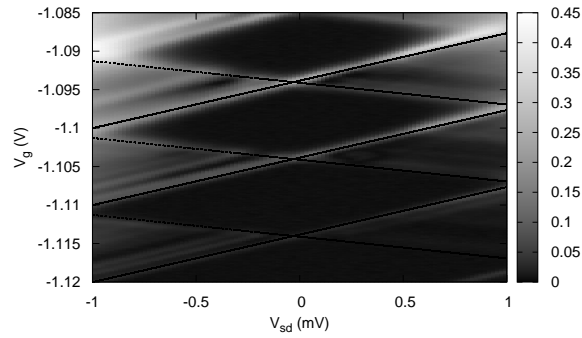
$$C_s = -C_g \frac{dV_g}{dV_{sd}}^- = 46 \text{ aF}, C_d = C_g \left( \frac{dV_g}{dV_{sd}}^+ - 1 \right) = 95 \text{ aF}.$$

<sup>1</sup>During characterization of the quantum dots system in this sample, we have got the problems about the circulation blocking of the mixture  $He^3/He^4$ , then we need to stop and repeat cooling process many times.

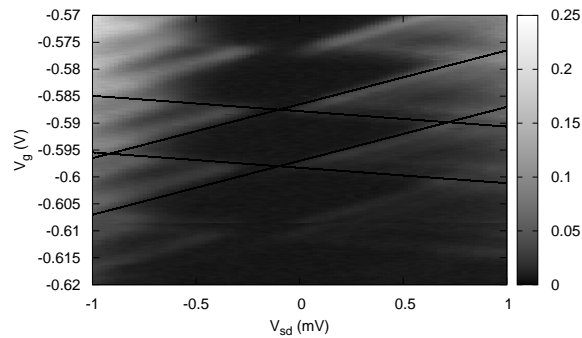
## 6. Single Quantum Dots with Weak Coupling



(a) The 1<sup>st</sup> measurement



(b) The 2<sup>nd</sup> measurement



(c) The 3<sup>rd</sup> measurement

Figure 6.19.: Comparison between the first, the second, and the third non-linear measurement. The 1<sup>st</sup> and 2<sup>nd</sup> measurement have been performed at the  $V_{C1C2} = -345$  mV and  $V_{E1E2} = -240$  mV, the 3<sup>rd</sup> has been performed at the  $V_{C1C2} = -480$  mV and  $V_{E1E2} = -440$  mV. All measurements are performed at  $T_{base} \sim 65$  mK. The solid lines indicate the border of diamonds.

Then the total capacitance is obtained as  $C_\Sigma = 158$  aF. The conversion factor  $\alpha$  and charging energy  $E_C$  are given as

$$\alpha = \frac{C_g}{C_\Sigma} = 0.106, \quad E_C = \frac{e^2}{C_\Sigma} = 1.01 \text{ meV}.$$

In weak coupling regime the capacitances are quite small values and are in order of  $\times 10^{-17}$  F. From the measurement of quantum Hall effect, the 2DEG has a electron density  $n_{2\text{DEG}} = 1.66 \times 10^{15} \text{ m}^{-2}$  at the temperature of 65 mK. According to the geometry of the dot, we can estimate the number of electrons on the dot of  $N \sim 400$ . The level spacing can then be estimated to be  $\Delta E \approx 15 \text{ } \mu\text{eV}$ .

For the second cool down, in Fig. 6.19(b), the gate voltages  $V_{C1C2}$  and  $V_{E1E2}$  are still set at the same values of -345 and -240 mV, respectively. The DC offset appearing in this figure is about  $V_{sd} = -30 \text{ } \mu\text{V}$ . The same Coulomb diamond pattern is shown that the result is reproducible, but there is a slight shift in  $V_g$  about 5 mV. From the fit lines at boundaries of the diamond,  $(dV_g/dV_{sd})^+ = 6.173$  and  $(dV_g/dV_{sd})^- = -2.825$ . All parameters extracted from both two diamonds appearing in this figure are the same values, and they can then be obtained that  $\Delta V_g = 10$  mV,  $C_g = 16$  aF,  $C_s = 45$  aF,  $C_d = 83$  aF,  $C_\Sigma = 144$  aF,  $\alpha = 0.111$ , and  $E_C = 1.11$  meV.

Figure 6.19(c) shows the Coulomb diamonds of the dotII in the third time of cool down. To reach the weak coupling regime again,  $V_{C1C2}$  and  $V_{E1E2}$  must be decreased. This might be due to the changing of 2DEG properties after repeated cool down processes. The scale of Coulomb diamonds looks quite different from (a) and (b). There are no excited states visible in the region next to blockade diamonds. From the boundaries of the diamond,  $(dV_g/dV_{sd})^+ = 10$  and  $(dV_g/dV_{sd})^- = -2.857$ . The DC offset is  $V_{sd} = -100 \text{ } \mu\text{V}$  which is higher than the offset in two previous cool down. Therefore the extracted capacitances and parameters can be obtained that  $\Delta V_g = 10.5$  mV,  $C_g = 15$  aF,  $C_s = 44$  aF,  $C_d = 137$  aF,  $C_\Sigma = 196$  aF,  $\alpha = 0.078$ , and  $E_C = 817 \text{ } \mu\text{eV}$ .

### Excited States

In the measurement of the differential conductance for dotII structure, there are additional lines clearly appearing outside the Coulomb blockade diamonds as seen already in Fig. 6.19(a) and (b). These lines run parallel to the boundaries of the diamonds. In Fig. 6.20, the differential conductance of dotII versus  $V_g$  and  $V_{sd}$  already shown in Fig. 6.19(b) has been plotted again in gray-scale in order to show the Coulomb blockade diamonds and clear lines at outside.

The black solid lines indicate the edges of the Coulomb blockade diamond shaped regions, whereas the white dashed lines represent the electron transfers. Comparing this figure with the schematic of Coulomb blockade diamonds with the excited states in Fig. 2.11(b), the dashed lines are expected to indicate the excited states. The number of electrons is also quantized in the Coulomb blockade regions. For the Coulomb diamond with  $N$  electrons in the dot, the dashed lines running parallel to the upper edges of the diamond indicate the energy of the excited states of  $N + 1$  electron system. Similarly, the excited states of  $N$  electron system are indicated by dashed lines parallel to the upper edge of the  $N - 1$  electron diamond. The dashed line beneath the lower edge of  $N$  electron diamond indicates the excited state of the  $N - 1$  electron system.

The separations in energy scale between the middle of the Coulomb diamond and the point at which the dashed lines hit the edge of the diamond are defined in Fig. 6.20. These separations correspond to the excitation energies of the electron system in the dot. When the dashed line parallel and closed to the upper edge of the  $N - 1$  electron diamond touches the solid line indicating the lower edge of the  $N$  electron diamond, the separation in energy scale from the middle of the diamond is given by  $\Delta_N \approx 136 \text{ } \mu\text{eV}$ . The  $\Delta'_N \approx 233 \text{ } \mu\text{eV}$  for the adjacent dashed

## 6. Single Quantum Dots with Weak Coupling

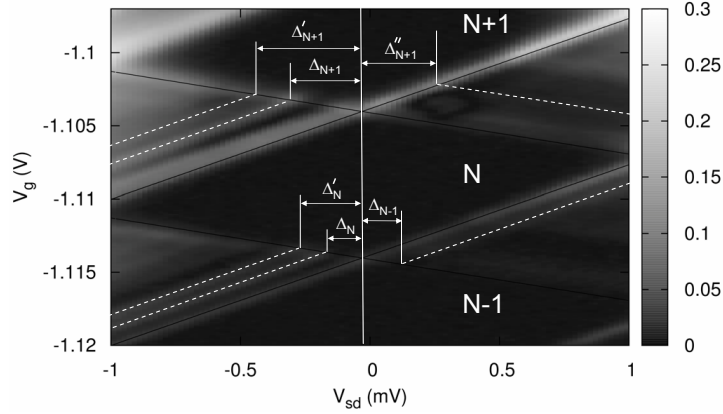


Figure 6.20.: The expansion of the second Coulomb blockade diamond in Fig. 6.19(b). Dashed lines indicate region where transport via excited states occurs.

line. At the touching point of the dashed line parallel to the lower edge of the  $N$  diamond on the the upper edge of the  $N - 1$  electron diamond, the  $\Delta_{N-1} \approx 143 \mu\text{eV}$ .

Considering the points at which dashed lines running parallel to the upper edge of  $N$  electron diamond reach the lower edge of  $N + 1$  electron diamond, the  $\Delta_{N+1} \approx 276 \mu\text{eV}$  for the dashed line with positive slope and closed to the upper edge, whereas the  $\Delta'_{N+1} \approx 434 \mu\text{eV}$  for the adjacent dashed line with positive slope. For the dashed line with negative slope, the  $\Delta''_{N+1} \approx 278 \mu\text{eV}$ . It can be seen that the  $\Delta_{N+1}$  and  $\Delta''_{N+1}$  are obtained approximately the same because they refer to the same excitation energy of  $N + 1$  electrons system.

Compared with the level spacing  $\Delta E \approx 15 \mu\text{eV}$  which is estimated earlier, we can see that the  $\Delta E$  is much smaller than the excitation energies extracted above. This infers that the electron tunneling at additional lines is contributed from the excitation of center-of-mass (CM) modes of the electron system [57]. This assumption is based on the strict separation of CM and relative motions in the parabolic confinement potential. Due to the strong correlations between electrons, most transitions involving excitations of internal degrees of freedom (internally excited states) are effectively suppressed. Since the excitation of CM modes is unaffected by the Coulomb interaction or correlations effect. These degrees of freedom can be excited easily. Therefore, channels connected to these modes dominate the excitation spectra in the transport measurement [57].

### 6.2.2. The dotI Structure

Since we have succeeded in making a quantum dot from the left gates in dotI structure, the nonlinear measurement is then performed. The gate B2 is applied with a fixed voltage. The gate A1 and QPC C (gate C1 and C2) are used to make the coupling between dotI and reservoirs, and gate voltage  $V_g \equiv V_{B1}$  is swept to observe the Coulomb oscillations in differential conductance  $G = dI/dV_{sd}$ .

Figure 6.21(a) shows the differential conductance versus gate voltage  $V_g$  and applied source-drain voltage  $V_{sd}$ . The gate voltage  $V_{B2}$  is fixed at  $-1.3 \text{ V}$ ,  $V_{A1} = -500 \text{ mV}$  and  $V_{C1C2} = -535 \text{ mV}$ . The slope of Coulomb diamond boundaries are  $(dV_g/dV_{sd})^+ = 14.286$  and  $(dV_g/dV_{sd})^- = -4.082$ , and the DC offset for  $V_{sd}$  is  $-80 \mu\text{V}$ . The Coulomb peak separation is  $\Delta V_g = 14 \text{ mV}$ , which is larger than the peak spacing measured in the dotII. The gate capacitance can then be calculated as  $C_g = e/\Delta V_g = 12 \text{ aF}$ . The other capacitances can be obtained by evaluating with the slope values that  $C_s = 47 \text{ aF}$ ,  $C_d = 154 \text{ aF}$ , and  $C_\Sigma = 213 \text{ aF}$ . The charging energy for this dot is  $E_C = 752 \mu\text{eV}$  corresponding to the conversion factor  $\alpha$  of 0.054.



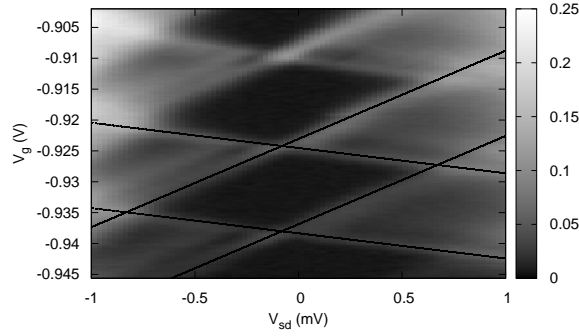
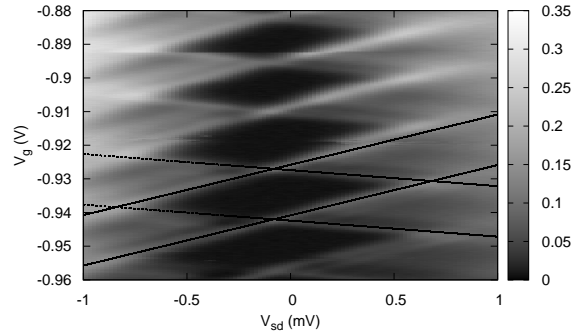

 (a)  $V_{A1} = -500$  mV and  $V_{C1C2} = -535$  mV

 (b)  $V_{A1} = -550$  mV and  $V_{C1C2} = -530$  mV

 Figure 6.21.: Measured Coulomb blockade diamonds on the dotI in the sample **PR1:d2**. (a) and (b) is set with different  $V_{A1}$  and  $V_{C1C2}$ . Both have the same  $V_{B2}$  of -1.3 V.

After re-cooling the sample, the nonlinear measurements have been performed again by applying a more negative voltage to gate A1 and QPC C in order to reach the weak coupling of the dot to leads. Then  $V_{A1} = -550$  mV and  $V_{C1C2} = -530$  mV are applied. The solid lines indicate the border lines of a Coulomb diamond in differential conductance as show in Fig. 6.21(b). The extracted parameters and capacitances are obtained that  $\Delta V_g = 15$  mV,  $C_g = 11$  aF,  $C_s = 51$  aF,  $C_d = 149$  aF,  $C_\Sigma = 210$  aF,  $E_C = 762$   $\mu$ eV, and  $\alpha = 0.051$ . It can be seen that all parameters have values very close to the values extracted from the Coulomb diamonds of the previous cool down. Furthermore, this dot is designed in the same size as the dotII structure. Hence, the number of electrons  $N$  and the level spacing  $\Delta E$  for the dotI can be estimated to be equal to values for the dotII. For comparison of the conversion factor  $\alpha$  between dotI and dotII in this sample,  $\alpha_{\text{dotI}} < \alpha_{\text{dotII}}$ . To obtain a same shift in the energy level of the dot, a change in  $V_g$  for dotI is needed more than that for dotII.

### Excited States

In Fig. 6.21(a), it can be noticed that there are slight additional lines parallel to the upper edge of each Coulomb blockade diamond, they especially appear in the negative  $V_{sd}$  region. We can use these to extract the excitation energy of the electron system directly from the separation  $\Delta_N$  between the middle of Coulomb diamond and the touching point of the line parallel to the upper edge of the  $N - 1$  electron diamond on the lower edge of the  $N$  electron diamond. Therefore,

## 6. Single Quantum Dots with Weak Coupling

$\Delta_N \approx 250 \mu\text{eV}$  for this dot system. Comparing with the level spacing estimated from the dot geometry,  $\Delta E \approx 15 \mu\text{eV}$ , the excitation energy is much larger than the level spacing. This can also be inferred that the electron tunneling via the internal excitation states contributed from the relative motion is suppressed due to strong electron correlations, whereas the center-of-mass motion still remains unaffected [57]. It can be expected that they would dominate the transport resonance. Therefore, only tunneling via the excitation of CM modes is visible as the additional conductance lines.

### 6.3. Nonlinear Transport of Quantum Dots in the Sample PR1:d1

We have performed the nonlinear measurement of the dotIII and dotIV structures in the sample **PR1:d1** to characterize their quantum dot properties. Our investigated samples are all fabricated from the same heterojunction wafer, thus we assume that all samples in this thesis have the same characteristic of 2DEG: the electron density  $n = 1.66 \times 10^{15} \text{ m}^{-2}$  and the mobility  $\mu = 63 \text{ m}^2/(\text{Vs})$  at  $T \approx 65 \text{ mK}$ .

#### The dotIII Structure

The Coulomb diamonds in Fig. 6.22(a) shows the border lines with slope of  $(dV_{E2}/dV_{sd})^+ = 16.67$  and  $(dV_{E2}/dV_{sd})^- = -6.25$ . The DC-offset in this figure is at  $-50 \mu\text{V}$ . The gate capacitance is obtained as  $C_g = 16 \text{ aF}$  corresponding to Coulomb peak spacing  $\Delta V_g \equiv \Delta V_{E2}$  of  $9.8 \text{ mV}$ . The other capacitances are  $C_s = 102 \text{ aF}$ ,  $C_d = 256 \text{ aF}$ , and  $C_\Sigma = 375 \text{ aF}$ . Then the conversion factor is  $\alpha = 0.044$  and charging energy is  $E_C = 427 \mu\text{eV}$ . From the geometry of the dotIII larger than dotI and dotII in the sample **PR1:d2**, the number of electrons is estimated to be  $N \sim 660$ . The level spacing is then estimated as  $\Delta E \approx 10 \mu\text{eV}$ .

#### The dotIV Structure

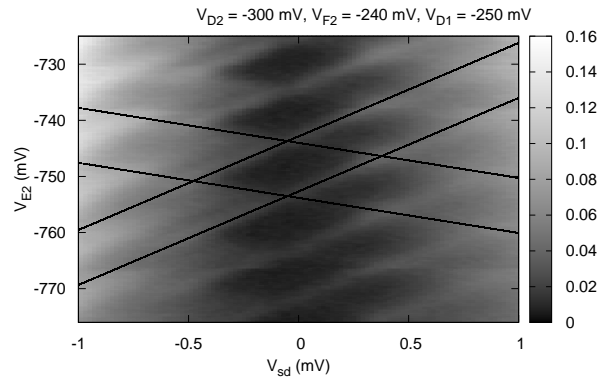
Figure 6.22(b) shows the Coulomb diamonds with identified border lines of  $(dV_{E1}/dV_{sd})^+ = 14.925$  and  $(dV_{E1}/dV_{sd})^- = -7.143$ . The DC-offset is observed at  $-60 \mu\text{V}$ . The Coulomb gap  $\Delta V_g \equiv \Delta V_{E1}$  is  $8.3 \text{ mV}$  giving the gate capacitance  $C_g = 19 \text{ aF}$ . The source and drain capacitances can be expressed that  $C_s = 138 \text{ aF}$  and  $C_d = 268.8 \text{ aF}$ . Then the total capacitance is  $C_\Sigma = 426 \text{ aF}$ . The conversion factor  $\alpha$  is obtained as  $0.045$ , and the charging energy is  $E_C = 376 \mu\text{eV}$ . The estimated number of electrons  $N$  and estimated level spacing  $\Delta E$  are the same as that of dotIII due to the same designed dot geometry.

#### The dotI Structure

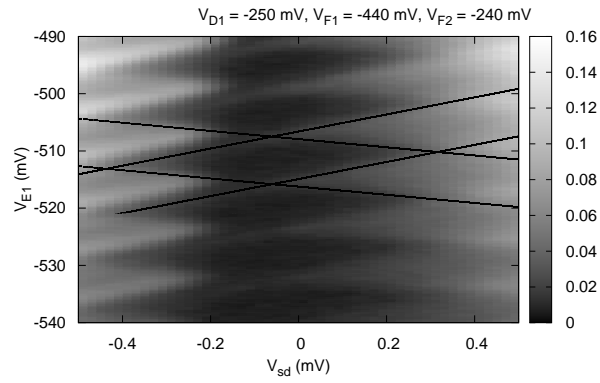
Figure 6.22(c) shows the differential conductance versus gate voltage  $V_{B2}$  and applied source-drain voltage  $V_{sd}$  of the dotI. Unfortunately, we cannot obtain nice Coulomb diamonds for this dot structure. The pattern is unstable and not reproducible. In addition it was quite different for positive and negative bias voltages  $V_{sd}$ .

For the structure of dotIII and dotIV, unfortunately, there is no additional line structure appearing outside the Coulomb blockade diamonds in Fig. 6.22(a) and (b). Thus, we cannot estimate the excitation energy of the excited states for the  $N$  electron system in both quantum dot structures.

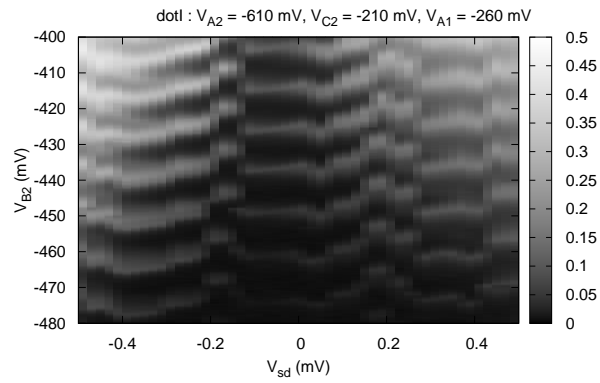
### 6.3. Nonlinear Transport of Quantum Dots in the Sample PR1:d1



(a) dotIII



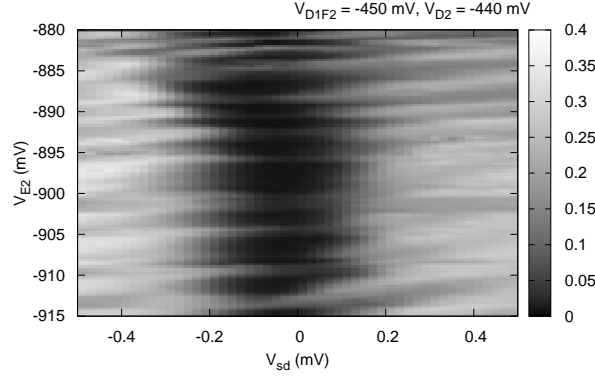
(b) dotIV



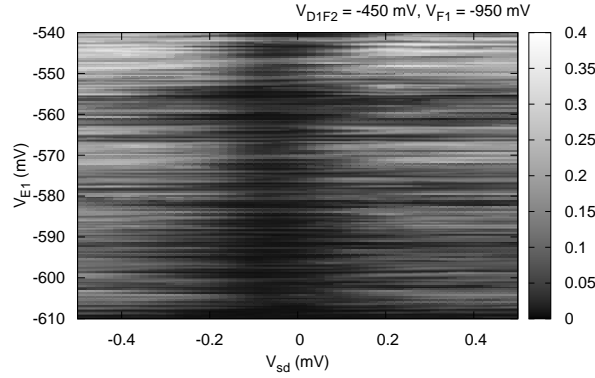
(c) dotI

Figure 6.22.: Grey-scale plot of differential conductance  $G$  as a function of  $V_g$  and  $V_{sd}$  in (a) dotIII, (b) dotIV, and (c) dotI in the sample **PR1:d1**. Solid lines indicate the boundaries of Coulomb blockade diamonds.

## 6. Single Quantum Dots with Weak Coupling



(a) dotIII:  $V_{D1F2} = -450$  mV and  $V_{D2} = -440$  mV



(b) dotIV:  $V_{D1F2} = -450$  mV and  $V_{F1} = -950$  mV

Figure 6.23.: Non-stable Coulomb blockade diamonds after illumination of (a) dotIII and (b) dotIV in the sample **PR1:d1**

### 6.3.1. After Illumination

After illuminating the sample **PR1:d1**, the differential conductance in dotIII and dotIV is measured again in nonlinear regime. The gates D1 and F2 are tuned with the same voltage. The voltage  $V_{D1F2}$  is then fixed at  $-450$  mV. Another dot-to-lead gate voltage is given as  $V_{D2} = -440$  mV for dotIII, and  $V_{F1} = -950$  mV for dotIV. The plunger gate voltage,  $V_{E2}$  for dotIII and  $V_{E1}$  for dotIV, is swept for obtain the Coulomb oscillation. The non-stable Coulomb oscillations of both dots in nonlinear transport have been shown in Fig. 6.23(a) and (b). These figures show the non-stable Coulomb diamonds in differential conductance of dotIII and dotIV. It is impossible to find a good quality Coulomb diamond to calculate the capacitances and other parameters.

## 6.4. Temperature Dependence of Coulomb Oscillations

For electron tunneling through a quantum dot in the Coulomb blockade regime, there are three important energy scales having the following order as  $\Gamma < \Delta E < U$ , where  $U = e^2/C_{\Sigma}$  is the charging energy,  $\Delta E$  is the level energy spacing, and  $\Gamma$  is the tunnel coupling of the quantum dot to the reservoirs. In the case of thermal broadening of the conductance resonance, the thermally energy will become another important energy scale, and is usually larger than  $\Gamma$ . Therefore, when

the temperature increases, the electron tunneling process changes from the quantum Coulomb blockade regime in which the tunneling occurs through a single level so called the single-level regime,  $\Gamma < k_B T \ll \Delta E < U$ , to the multilevel regime,  $\Gamma < \Delta E \ll k_B T < U$ , in which there is more than one energy level within  $k_B T$  window [22]. This clearly shows the broad resonance peaks in the Coulomb oscillation at high temperature. The multilevel regime can also be called the metallic Coulomb blockade regime.

Figure 6.24 shows the temperature dependance of the Coulomb oscillation of the dotII in the sample **PR1:d2**. The DC-offset of this data is already corrected. The conductance peaks are measured as a function of the gate voltage  $V_g$  at various temperatures. The temperature is derived from the resistance read out from the RuO<sub>2</sub> resistance thermometer contacted at the cold finger of the sample holder, and is assumed to measure also the sample temperature. For all conductance peaks, the peaks height decreases, whereas the peak width broadens with increasing temperature. The line shape fitting of an individual conductance peak is given by

$$G(V_g) = A \cdot \cosh^{-2} [B(V_g - V_{res})] + \text{offset}, \quad (6.5)$$

where  $A$  is the amplitude of the conductance peak, which decreases linearly with increasing temperature in the quantum regime and is independent of temperature in the metallic regime,  $V_{res}$  is the gate voltage at the center of the resonance peak. This equation is corrected for a background conductance offset. The factor  $B$  can be used to evaluate the full width at half-maximum (FWHM,  $V_{1/2}$ ) of the single peak as

$$V_{1/2} = 2 \cdot \frac{\text{acosh}(\sqrt{2})}{B}. \quad (6.6)$$

If the line shape is obtained by a purely thermally broadened resonance, then factor  $B = e\alpha/2k_B T$  in the quantum regime, whereas  $B = e\alpha/2.5k_B T$  in the metallic regime.

The FWHM of the conductance peaks identified as **A** and **B** in Fig. 6.24 have been plotted as a function of the temperature  $T$  in Fig. 6.25. These values of FWHM are obtained from the line shape fitting of an individual conductance peak at various temperatures<sup>2</sup>. At high temperature, the FWHM has a linear dependence on the temperature. As a function of temperature, the obtained FWHM data has been fit to the Lorentzian line width predicted by a thermally broadened Lorentzian parametrized by a full width at half-maximum of the resonance,  $\Gamma$ , in the density of state as reported in Foxman *et al.* work [21]. This is given by the convolution of a Lorentzian conductance with the negative derivative of the Fermi-Dirac distribution function at finite temperature.

This clearly shows the excellent fitting obtained with the Lorentzian line shape of the resonance peak at high temperatures, but the deviation between measured data and fitting curve occurs when temperature is reduced below  $T \approx 300$  mK for peak **A** and **B**. The fit with this model yields  $\Gamma = 101 \mu\text{eV}$  at zero temperature and  $\alpha = 0.139$  for conductance peak **A**. For conductance peak **B**,  $\Gamma = 94 \mu\text{eV}$  at zero temperature and  $\alpha = 0.112$  is yielded from the own fit as well. The  $\Gamma$  from both peaks fitting can be approximated to  $100 \mu\text{eV}$ . The  $\alpha$  factor of 0.112 yielded from peak **B** is in strong agreement with the  $\alpha$  obtained from nonlinear data.

At low sample temperature, the FWHM of the conductance peak become finite. At  $T \simeq 65$  mK, the FWHM or  $V_{1/2}$  of the conductance peak **A** and **B** are approximately 0.92 mV and 1.15 mV, respectively. We then extrapolate these values back to their own fitting curves. Therefore,

<sup>2</sup>The temperature ( $T$ ) presented in our graphs is converted from the measured resistance of the RuO<sub>2</sub> thermometer attached at the cold finger, and is approximated to the bath temperature ( $T_{bath}$ ),  $T \sim T_{bath}$ . Since our samples are glued on the cold finger with the Ag-paste. The thermal energy of the sample is transferred via Ag-paste and also gold wires connected to the chip-carrier. Thus, the sample temperature ( $T_{sample}$ ) is assumed to be approximately  $T_{bath}$  or  $T$ .

6. Single Quantum Dots with Weak Coupling

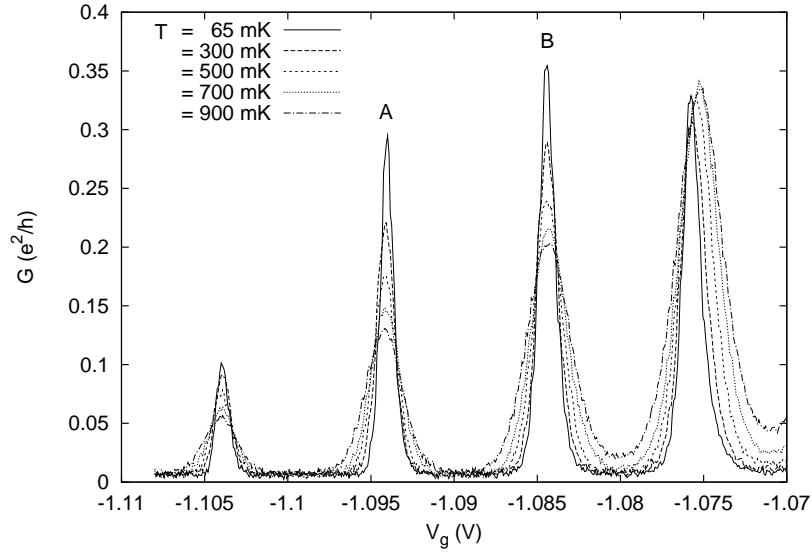


Figure 6.24.: Conductance  $G$  as a function of gate voltage  $V_g$  at various temperatures for dotII structure in the sample **PR1:d2**.

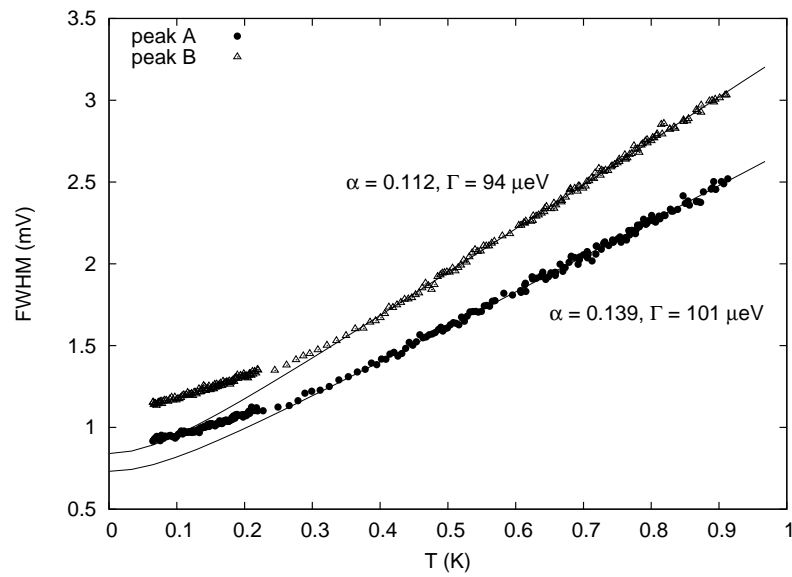


Figure 6.25.: Plot of full width at half maximum or line width of peak A and B in 6.24 as a function of temperature. Both data are fit with the curves which are generated from the thermally broadened Lorentzian parameterized by  $\Gamma$ . These curves extrapolate back to  $T = 0$  to extract  $\Gamma$ . The slope of the curve in linear temperature dependence region gives  $\alpha$  for each peak.

the electronic temperature  $T_e$  in the system can be evaluated as  $T_e \approx 160$  mK from fitting curve of the conductance peak **A**, and  $T_e \approx 190$  mK from the fitting curve of the conductance peak **B**. It can be seen that the values of  $T_e$  from extrapolating are quite close to each other.

The deviation between theory and experimental data increases as  $T \lesssim 300$  mK for both peaks. This also refers to the obtained FWHM of the conductance peak larger than expected theory value. Along the range of FWHM deviation between expected and obtained values, if we extrapolate FWHM value back to fitting curve, the obtained electronic temperature  $T_e$  below the deviation point becomes finite and is higher than the sample temperature at the cold finger. It is probably due to the result of electronic heating by residual electronic noise [56]. Above this temperature,  $T > 300$  mK, it can be assumed that the electronic temperature closely follows the sample temperature.

At the lowest sample temperature and in the quantum Coulomb blockade regime,  $\Gamma \ll k_B T \ll \Delta E$ , the electronic temperature is directly calculated from FWHM or  $V_{1/2}$  of the conductance peak by using  $T_{QM} = e\alpha V_{1/2}/[4k_B \cdot \text{acosh}(\sqrt{2})]$ . Therefore,  $T_{QM} \simeq 335$  mK for peak **A**, and  $T_{QM} \simeq 420$  mK for peak **B**. The difference between  $T_e$  and  $T_{QM}$  is around 200 mK. These difference clearly show that the electronic temperature extracted from a purely thermally broadened conductance peak is not valid, because line shape of our data is well described as a thermally broadened Lorentzian parameterized by  $\Gamma$  even at high temperature.

The peak height  $G_{Max}$  for single level conductance in the quantum regime is proportional to  $1/T$ , whereas it is temperature independent for multilevel conductance in the metallic regime [22, 58]. Figure 6.26 shows the inverse of peak height for the conductance peak **B** in Fig. 6.24 as a function of sample temperature. At  $T \lesssim 450$  mK, the slope of linearly temperature dependence of  $G_{Max}^{-1}$  is steeper than the slope at high temperature. The electron tunneling at low temperature is clearly in the single-level regime. Additionally, the transition of electron tunneling from single-level regime to multilevel regime could be expected at high temperature due to the trend of plotted data with decreasing slope which may become zero or flat at very high temperature.

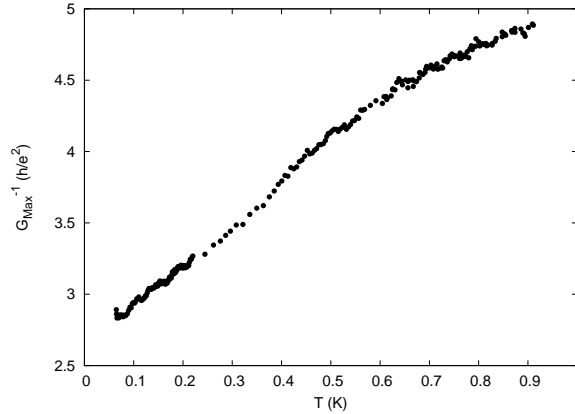


Figure 6.26.: Inverse of maximum conductance  $1/G_{Max}$  of the conductance peak **B** versus temperature for dotII structure in the sample **PR1:d2**.

Figure 6.27 shows the temperature dependence of the Coulomb oscillation of dotI in the sample **PR1:d2**. The conductance peak is broadened and the position of the peak also fluctuates with increasing temperature. It can also be noticed that the peak height increases as sample temperature is higher than base temperature of 64 mK. This strange temperature dependence of the peak height probably results from a large variation of coupling strength from one peak to another peak [59]. It is to be expected for a weakly coupled level adjacent to a strongly coupled one. When the thermal energy  $k_B T$  approaches the level spacing  $\Delta E$ , thermal excitation to the

## 6. Single Quantum Dots with Weak Coupling

strongly coupled level causes the amplitude to increase with the temperature until the multilevel regime, in which the peak height is temperature independent, is obtained. The conductance peaks can be fit quite well with Eq. 6.5 at various temperature.

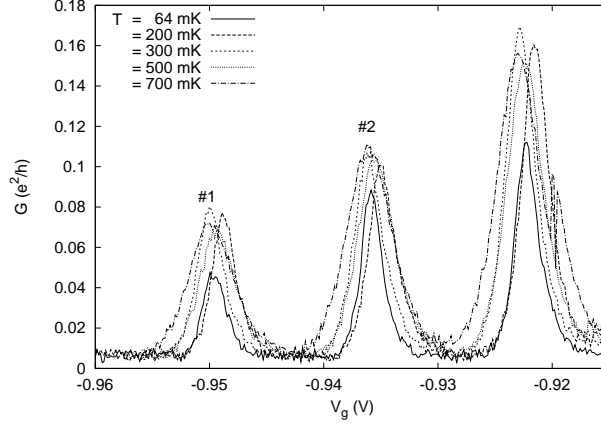


Figure 6.27.: Conductance versus the center gate voltage  $V_g$  of dot I in the sample **PR1:d2** at various temperatures.

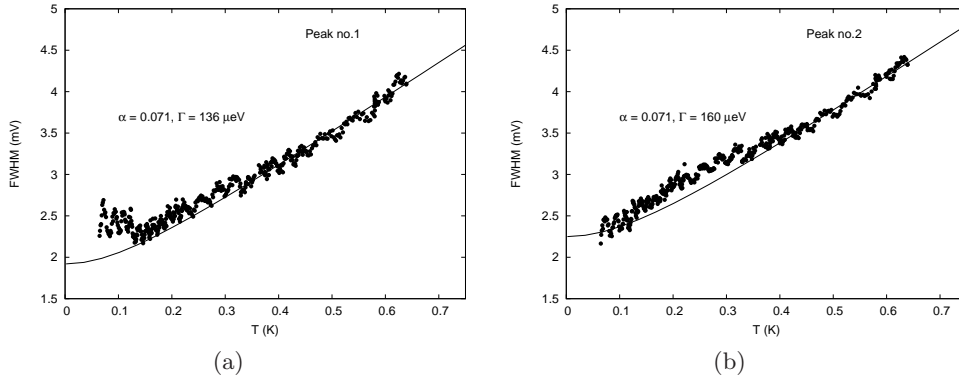


Figure 6.28.: Temperature dependence of line width of peak (a) no.1 and (b) no.2 in Fig. 6.27. Both of them are fit with the curves of temperature dependence of Lorentzian line width.

The FWHM of the conductance peak no.1 and no.2 are calculated from the line shape fitting, and plotted as a function of sample temperature as shown in Fig. 6.28(a) and 6.28(b). It clearly shows that the conductance peak is broadened with increasing temperature. The predicted line width from a thermally broadened Lorentzian line shape parameterized by  $\Gamma$  as a function of temperature is also fit to these data. This fit yields  $\Gamma = 136 \mu\text{eV}$  for peak no.1,  $\Gamma = 160 \mu\text{eV}$  for peak no.2 at zero temperature, and  $\alpha = 0.071$  for both peaks. The fit is quite good at high temperatures for both peaks, but there are some deviations occurring at lower temperatures. For peak no.1, the data begins deviating at  $T \approx 330 \text{ mK}$  and clearly deviates at  $T \approx 130 \text{ mK}$ , while the deviation occurs at  $T \approx 330 \text{ mK}$  and back to fit again at  $T \approx 130 \text{ mK}$  for peak no.2. At high temperature, the line width of both peaks are linearly temperature dependence. From the saturation of the width of peak no.1 at low temperature, we can estimate the electron temperature  $T_e$  of  $\sim 170 \text{ mK}$  by extrapolating back to fitting curve.

The conductance as a function of gate voltage of the dot III in the sample **PR1:d1** shown in Fig. 6.29. This presents the Coulomb oscillations at various temperatures. When the tempera-



#### 6.4. Temperature Dependence of Coulomb Oscillations

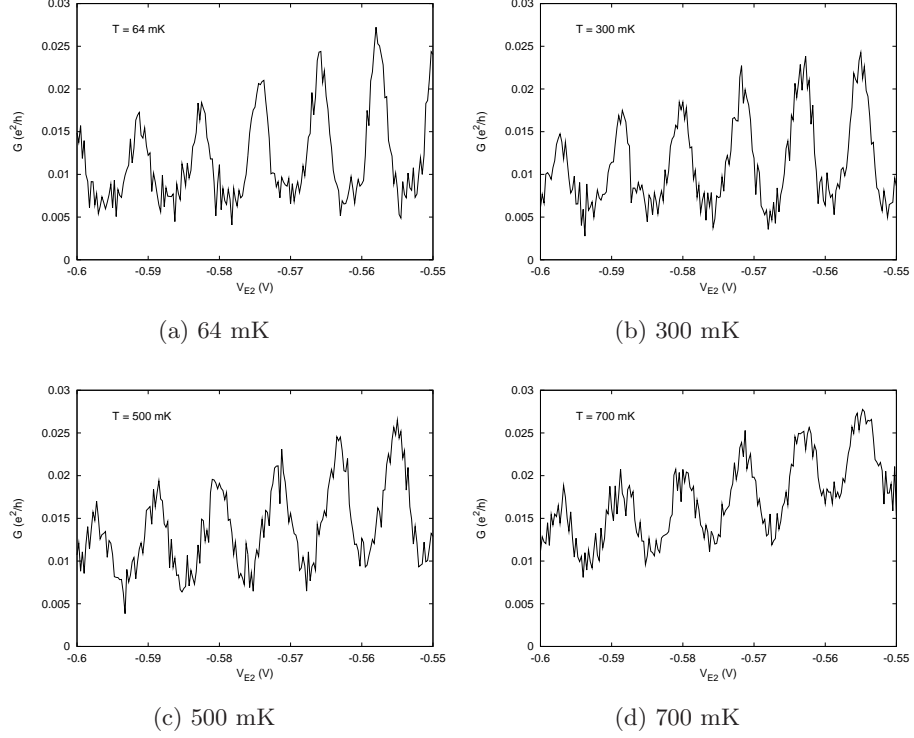


Figure 6.29.: Conductance as a function of gate voltage  $V_g$  of dotIII in the sample **PR1:d1** for various temperatures.

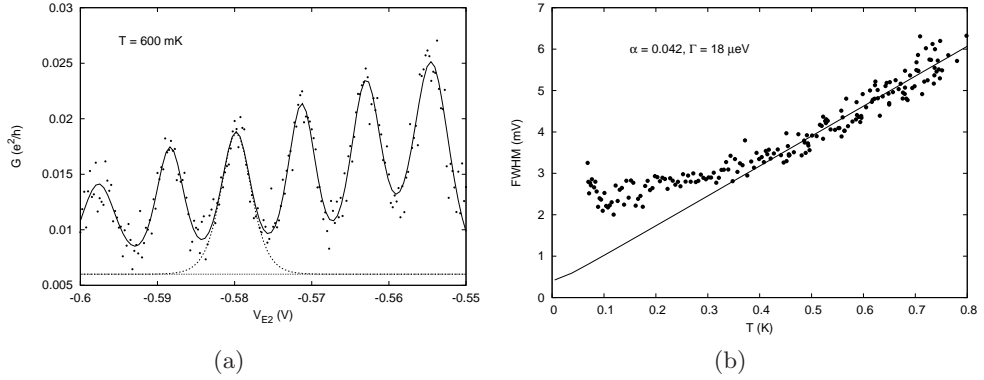


Figure 6.30.: (a) The Coulomb oscillation in conductance at  $T = 500$  mK. The data is well fit to the sum of Eq. 6.5 centered at each peak indicated by the solid line. Dashed line indicate an individual peak fitting based on the offset at lowest temperature. (b) Temperature dependence of line width of peak identified in (a) with single peak. The data is fit to the curve of thermally broadened Lorentzian line with.

## 6. Single Quantum Dots with Weak Coupling

ture increases, the conductance peaks are broadened and the valleys between two neighbouring peaks, especially in the region of high gate voltage, do not reach to the bottom which is shown at low temperature, because the the tails of adjacent peaks are overlapping. The maximum for each peak, however, does not significantly change. The Coulomb peak spacing  $\Delta V_{E2}$  is approximately 8.5 mV.

The data fit quite well, at valleys as well as peaks, to the sum of Eq. 6.5 centered at each peak, as shown in Fig. 6.30(a) at  $T = 600$  K. The dashed line show an individual line shape of the middle peak based on the offset background. The FWHM or line width taken from the data fitting is plotted as a function of temperature as presented in Fig. 6.30(b). The obtained line widths from every peaks at various temperature all repeat in same trace, and we then select the line width of the middle peak to be representative for the measurement. The data is fit to the expected line width as a function of  $T$  for thermally broadened Lorentzian peak parameterized by  $\Gamma$ . The fit is very good at high temperature. At  $T \gtrsim 360$  mK, the linearly temperature dependence is presented, and the electron temperature then follows the sample temperature at cold finger. The deviation between data and fit curve increases as  $T$  is reduced below 360 mK. The fit yields  $\alpha = 0.042$ , which is consistent with 0.044 calculated from the Coulomb diamond in the nonlinear data, and  $\Gamma = 18 \mu\text{eV}$  at zero temperature. This data shows the saturation at low temperature or  $T \lesssim 150$  mK. If we extrapolate the obtained line width at saturation back to the fit curve, the electron temperature can be estimated as  $T_e \approx 300$  mK.

### 6.5. Nonlinear Transport in a Quantum Point Contact coupled with a Single Quantum Dot

From the Coulomb oscillations appearing in the differential conductance of a standalone QPC A in the sample **PR1:d4**, we are interested to investigate the electron transport in nonlinear regime for this quantum point contact coupled with an unexpected quantum dot, which is probably caused of the impurity in the material or 2DEG. The electron micrograph of the QPC A with identified gates has been shown in Fig. 6.31. The results and discussion of the oscillatory behaviour in the differential conductance of QPC A has been presented in the section 5.2.3.

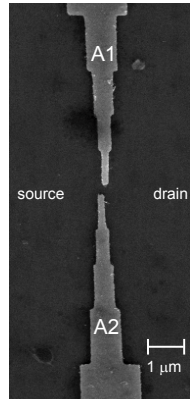


Figure 6.31.: Scanning electron micrograph of the quantum point contact A in the sample **PR1:d4**. The split gates A1 and A2 with 200 nm length are placed diagonally and vertically separated with 250 nm

The sequence of conductance peaks appears when the gate voltage  $V_{A1}$  is swept, while  $V_{A2}$  is kept as a constant value. Since this oscillation is clearly periodic, we interpret that it arises from the Coulomb blockade oscillations. The conductance traces are repeated and do not show

## 6.5. Nonlinear Transport in a Quantum Point Contact coupled with a Single Quantum Dot

any significant differences when the  $V_{A2}$  is applied below -0.4 V. Thus it is assumed that the system is in the weak coupling regime with this applied voltage  $V_{A2}$ . The gate voltage  $V_{A2}$  is then fixed at -0.4 V, and  $V_{A1}$  is swept to observe the quite stable conductance oscillations for this system. The Coulomb oscillations at  $V_{A2} = -0.4$  V has been shown in Fig. 6.32(a). The Coulomb peak spacing  $\Delta V_{A1}$  is about 4.6 mV.

Figure 6.32(b) shows the differential conductance in a logarithmic scale as a function of gate voltage  $V_{A1}$  and source-drain voltage  $V_{sd}$ . There are quite clear diamond shapes appearing in the grey-scale plot. The excited state bright lines also appear outside the diamonds. The boundaries of a Coulomb blockade diamond are indicated as lines with slope of  $(dV_{A1}/dV_{sd})^+ = 2.326$  and  $(dV_{A1}/dV_{sd})^- = -1.25$ . The DC-offset of  $V_{sd}$  is about -48  $\mu$ V. From the capacitive charging model, we can estimate the gate capacitance of a coupled dot by giving as  $C_g = e/\Delta V_g = 35$  aF. The other capacitances are extracted and given  $C_s = 44$  aF,  $C_d = 46$  aF, and  $C_\Sigma = C_g + C_s + C_d = 125$  aF. Therefore the charging energy can be evaluated that  $E_C = e^2/C_\Sigma = 1.28$  meV which is quite high and corresponds to the conversion factor  $\alpha$  of 0.28.

### 6.5.1. Excited States

Figure 6.33 shows the gray-scale plot of the logarithmic value of differential conductance  $dI/dV_{sd}$  in Fig. 6.32(b) as a function of  $V_{A1}$  and  $V_{sd}$  for clarity to investigate the additional line outside the Coulomb blockade diamonds. Few Coulomb diamonds are selected to show and defined by the number of electron. The solid lines indicate the edges of the  $N$  electron diamond, and the dashed lines outside the diamond indicate the excitation of the dot system. These additional lines appear for negative  $V_{sd}$  much more clearly than for positive  $V_{sd}$ .

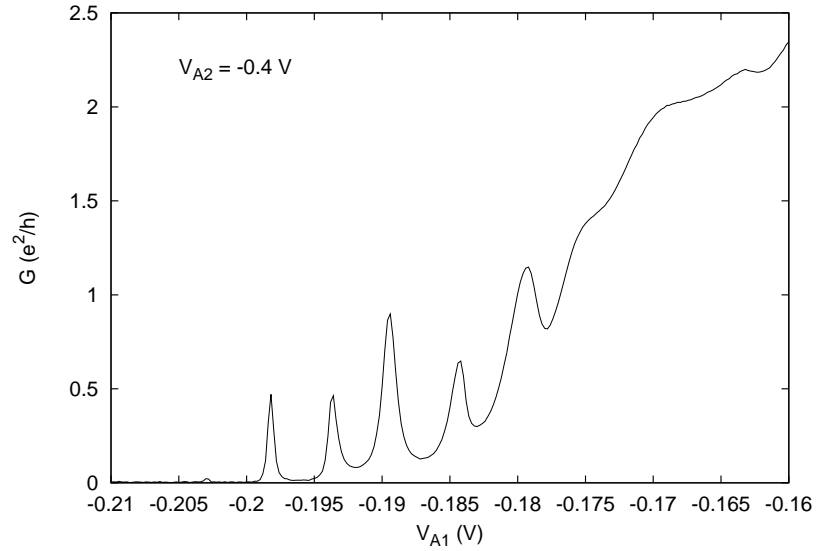
The dashed lines running parallel to the upper edge of the  $N - 1$  electron diamond hit the lower edge of the  $N$  electron diamond. The separation between this hitting point and the middle of Coulomb diamonds is given by  $\Delta_N$ , which is the excitation energy of the  $N$  electron system, whereas another dashed line parallel to the lower edge of the  $N$  electron diamond indicates the excitation energy of the  $N - 1$  electron system,  $\Delta_{N-1}$ . The excitation energy of  $N + 1$  electron system,  $\Delta_{N+1}$ , can be extracted by the separation between the point at which the dashed line running parallel to the upper edge of the  $N$  electron diamond touches the lower edge of the  $N + 1$  Coulomb diamond.

According to Fig. 6.33, it can be obtain that  $\Delta_{N-1} \approx 344 \mu\text{eV}$ ,  $\Delta_N \approx 305 \mu\text{eV}$ , and  $\Delta_{N+1} \approx 318 \mu\text{eV}$ . These excitation energies are higher than energies extracted from the Coulomb blockade diamonds of the dotI and dotII structure as presented in the section 6.2.1 and 6.2.2. The level spacing for this unexpected dot can be inferred to be smaller than these obtained excitation energies. This means that the strong correlations between electrons reduce the probability of tunneling through channels involving excitations of the internal degrees of freedom. This leads to a dominance of the center-of-mass excitations which are not affected by correlation effects [57].

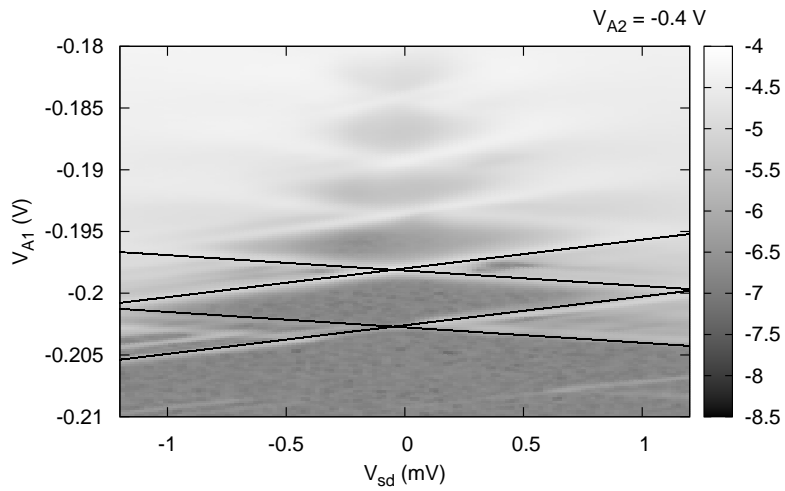
### 6.5.2. Temperature Dependence

Figure 6.34 shows the Coulomb oscillations as a function of gate voltage  $V_{A1}$  at various temperatures. The DC-offset is already corrected in this data. The conductance peaks broaden with increasing temperature. It can also be seen that the peak height, especially at  $V_{A1} < -0.188$  V, clearly decreases, while the valley between adjacent peaks increases when the temperature rises. This is due to the tail of adjacent peaks overlapping. The increasing conductance of valley at  $V_{A1} > -0.188$  V is very pronounced, and we also see the increasing of the peak height when  $T > \sim 550$  mK. This is probably due to the influence of the stronger tunnel coupling at thermal

6. Single Quantum Dots with Weak Coupling



(a)



(b)

Figure 6.32.: (a) Differential conductance as a function gate voltage  $V_{A1}$  while  $V_{A2}$  is fixed at  $-0.4$  V. (b) Grey-scale plot of logarithmic differential conductance of QPC A in the sample **PR1:d4** versus gate voltage  $V_{A1}$  and source-drain voltage  $V_{sd}$ . The solid lines indicate the boundaries of one of Coulomb blockade diamonds appearing in this plot.

## 6.5. Nonlinear Transport in a Quantum Point Contact coupled with a Single Quantum Dot

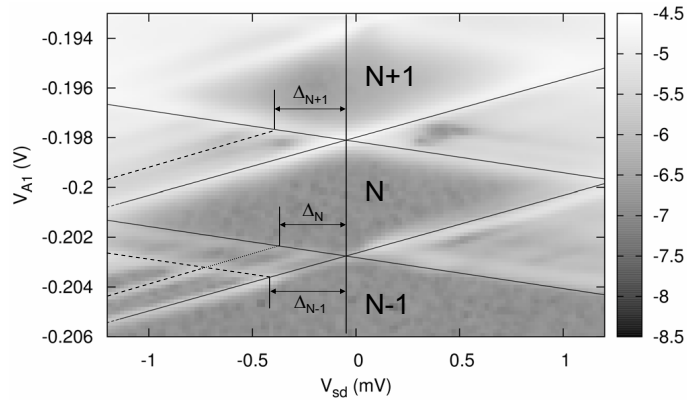


Figure 6.33.: Expansion of an indicated Coulomb blockade diamond in Fig. 6.32(b) with identified number of electrons in each diamond. The DC-offset of  $V_{sd}$  is about  $-48 \mu\text{V}$ . The gray scale represents the logarithmic value of  $dI/dV_{sd}$ . The dashed lines indicate the electron transport via the excited states.

energies comparable to energy level spacing. This leads to an increasing of conductance peak height with temperature [59].

The line shape of conductance peak at  $V_{A1} = -0.198 \text{ V}$  is well fitted to Eq. 6.5 at different temperature, as also shown in the inset of Fig. 6.35 at base temperature. The extracted line width or FWHM is plotted as a function of the sample temperature. The FWHM data is also fitted to the theoretical line width of Lorentzian peak parameterized by  $\Gamma$  at various temperature, as shown in Fig. 6.35. The fit curve yields  $\alpha = 0.344$  and  $\Gamma = 141 \mu\text{eV}$  at zero temperature. At high temperature, the data is an excellent fit to the curve. A deviation between the data and the fit curve occurs at the temperature below  $400 \text{ mK}$ . The deviation increases and converge to a finite value as  $T \lesssim 400 \text{ mK}$ . At  $T < 80 \text{ mK}$ , the electron temperature from extrapolating the almost saturated data back to the fit curve is approximately  $230 \text{ mK}$ .

6. Single Quantum Dots with Weak Coupling

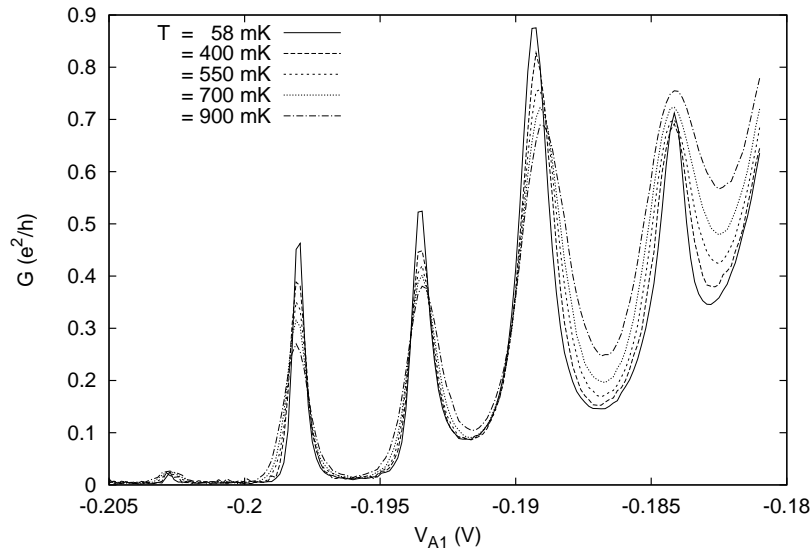


Figure 6.34.: Coulomb oscillations in the differential conductance versus gate voltage  $V_{A1}$  for different temperatures. The temperature ranges from 58 mK to 900 mK. The  $V_{A2}$  is fixed at constant of -0.4 V.

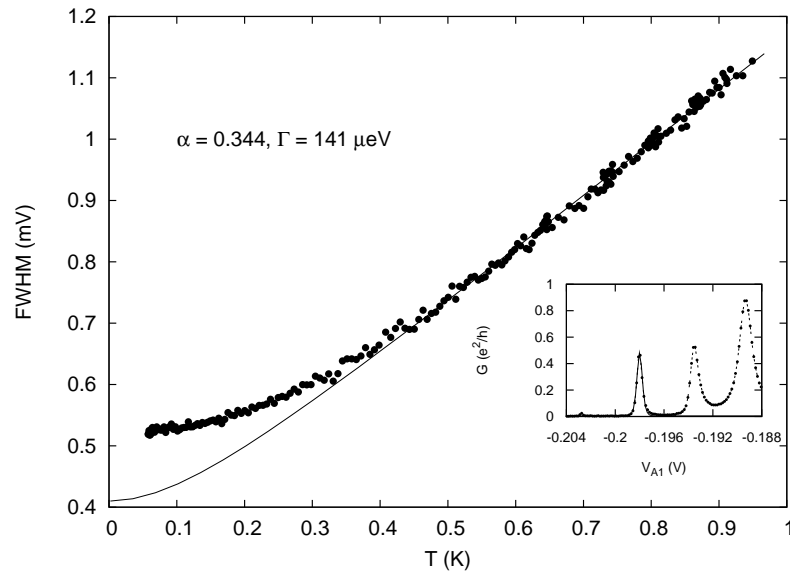


Figure 6.35.: Temperature dependence of line width of the conductance peak which is fit to the thermally broadened resonance peak as shown as solid line shape in the inset. At linear temperature dependence region, the data fits remarkably well to the curve generated from the thermally broadened Lorentzian line shape. The  $\alpha$  is then yielded from the fit curve, and  $\Gamma$  is given from extrapolating back to zero temperature.

## 7. Kondo Physics in a Single Quantum dot

The Kondo effect in a single quantum dot is usually observed in the strong coupling regime. Hence we perform the differential conductance measurement in this regime by increasing applied voltage to the left and right gate of a quantum dot coupled to the reservoirs. We found significant evidence of the Kondo effect in the dotII structure of the sample **PR1:d2** and also the point contact QPC A of the sample **PR1:d1**. Firstly, we discuss the measurement procedure and results from the conventional quantum dot in the sample **PR1:d2**, and later we show the results of the Kondo effect discovered in the conductance of a quantum point contact coupled with an unexpected quantum dot in the sample **PR1:d1**.

### 7.1. Coulomb Oscillations in Strong Coupling

In order to increase the tunnel coupling between the dotII and the reservoirs, both  $V_{C1C2} \equiv V_{\text{QPC c}}$  and  $V_{E1E2} \equiv V_{\text{QPC E}}$  are increased. Figure 7.1(a) shows the Coulomb oscillations at different gate voltages  $V_{C1C2}$  and  $V_{E1E2}$ . These two gate voltages control the coupling between the dotII and the leads. The gate voltage  $V_{E1E2}$  is changed from -235 mV in the curve A to -230 mV in the curve B. The position of the Coulomb peaks is clearly shifted to more negative values of the center gate voltage,  $V_g \equiv V_{D1D2}$ . When the gate voltage  $V_{C1C2}$  is increased from -340 mV in the curve B to -335 mV in the curve C, the Coulomb peaks are not only shifted but also broadened. The tunnel coupling can be represented by the broadening or the width of the Coulomb resonance peak  $\Gamma$ . In Fig. 7.1(b), we select gate voltages around  $V_{C1C2} = -328$  mV and  $V_{E1E2} = -218$  mV to make the strong tunnel coupling regime for the dotII structure. The Kondo effect is investigated in the region where the valleys between Coulomb peaks do not reach the zero conductance.

Figure 7.2 shows the non-linear data which corresponds to the data with the same conditions as in Fig. 7.1(b). From the Coulomb diamonds comparison between 7.2(a) and 7.2(b), the diamond pattern has been distorted due to the stronger coupling, and it can also be noticed that there is a zero bias anomaly which is most pronounced in the second and the third Coulomb diamonds from the bottom of Fig.7.2(b). The anomalous conductance peak at zero-bias in the Coulomb diamonds is referred to as the Kondo resonance in the density of states (DOS) of the quantum dot. At this condition for strong coupling, the gate voltage spacing  $\Delta V_g \simeq 10$  mV and the capacitances can be extracted that  $C_g \simeq 16$  aF,  $C_s \simeq 128$  aF,  $C_d \simeq 230$  aF,  $C_\Sigma \simeq 374$  aF, and  $\alpha \equiv C_g/C_\Sigma \simeq 0.04$ . It clearly shows that the capacitances coupled between dot and the reservoir,  $C_s$  and  $C_d$ , in strong coupling regime are much greater than that in weak coupling regime as reported in the section of nonlinear transport regime.

The Kondo effect leads to an enhanced density of states of the quantum dot at the chemical potential levels,  $\mu_L \simeq \mu_R$ , of the the electron reservoirs as shown in Fig. 7.3(a). For symmetric barriers,  $\Gamma_L = \Gamma_R$ , where  $\Gamma_{L,R}$  represent the tunnel couplings of the dot to the left and right reservoir respectively. This DOS Kondo resonance gives rise to enhanced conductance at zero bias and rapidly decreases for  $V_{sd} \neq 0$ . When a bias voltage,  $V_{sd} = (\mu_L - \mu_R)/e$ , is applied between source and drain, the Kondo peak in the DOS splits into two peaks, each pinned to one chemical potential of the reservoir, as shown in Fig. 7.3(b).

In our nonlinear measurement setup, we have obtained the result with a finite DC-offset at

## 7. Kondo Physics in a Single Quantum dot

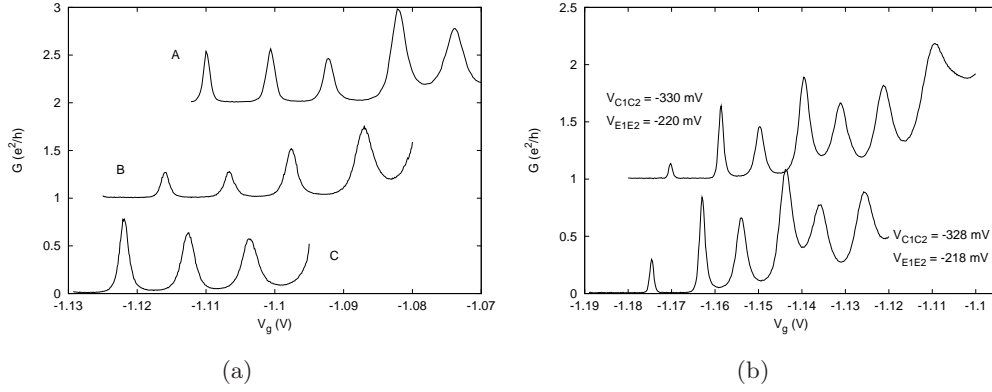
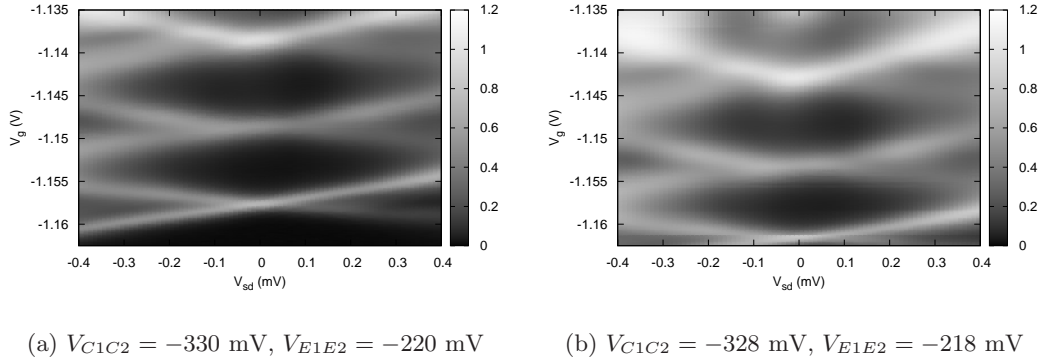


Figure 7.1.: (a) The comparison of Coulomb oscillation in three different gate voltage conditions. A:  $V_{C1C2} = -340$  mV and  $V_{E1E2} = -235$  mV, B:  $V_{C1C2} = -340$  mV and  $V_{E1E2} = -230$  mV, and C:  $V_{C1C2} = -335$  mV and  $V_{E1E2} = -230$  mV. (b) The Coulomb oscillation in strong coupling between the dotII and the reservoir. The curve is offset with  $e^2/h$  for clarity.



(a)  $V_{C1C2} = -330$  mV,  $V_{E1E2} = -220$  mV

(b)  $V_{C1C2} = -328$  mV,  $V_{E1E2} = -218$  mV

Figure 7.2.: The differential conductance of the dotII in the nonlinear measurement with strong coupling, which corresponds to Fig. 7.1(b). The coupling of the dot to the reservoirs in (b) is stronger than the coupling in (a) because both  $V_{C1C2}$  and  $V_{E1E2}$  is increased by 2 mV. More pronounced Kondo resonance appears in the second Coulomb diamond from the bottom of figure.



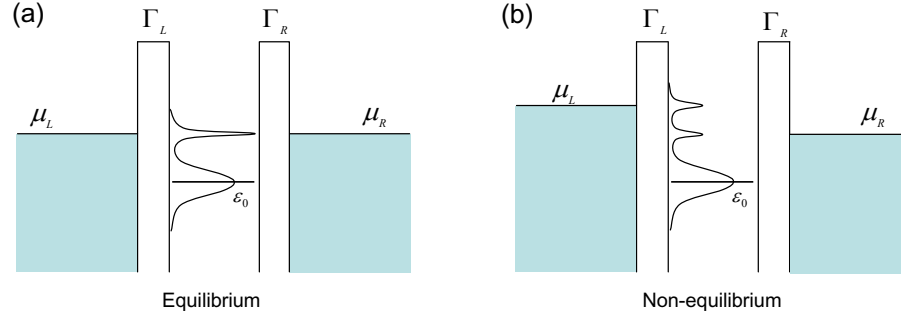


Figure 7.3.: (a) In equilibrium, the narrow Kondo resonance peak in the density of states of the dot is at chemical potential energies of the leads,  $\mu_L \simeq \mu_R$ . (b) Out of equilibrium, when a finite  $V_{sd}$  is applied, the DOS resonance peak splits into two peaks, each peak is located at each chemical potential of the leads.

zero bias which is probably due to the ground offset of the preamplifier. In Fig. 7.5, we can observe the evolution of the offset of the conductance anomaly or Kondo conductance resonance in the Coulomb blockade diamond to non-zero bias. This might be the result of asymmetric tunneling barriers of the dot,  $\Gamma_L \neq \Gamma_R$ , as shown in Fig. 7.4. The Kondo resonance in the DOS of the dot is pinned to the chemical potential of the lead with strongly coupling (the thin barrier side), this leads to the occurrence of a conductance anomaly at non-zero bias [37].

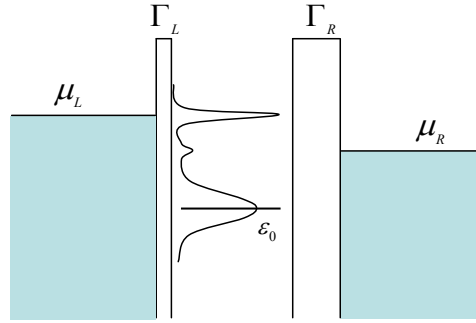


Figure 7.4.: The density of states of a quantum dot in non-equilibrium Kondo situation with asymmetric barriers. The Kondo resonance is pinned on the thin barrier side.

The shifted zero bias anomaly in Coulomb diamond of our nonlinear measurement can be seen in Fig. 7.5(a) - (g). The asymmetry in Kondo conductance resonance is probably due to the asymmetric barriers situation. It indicates that the tunneling coupling of the quantum dot is tuned into an asymmetry with varying the gate voltage  $V_{E1E2}$ , which relates to the tunneling barrier between the dot and one lead. When the gate voltage  $V_{E1E2}$  is decreased, the diamond position is shifted to higher plunger gate voltage,  $V_g \equiv V_{D1D2}$ , and the shape is also distorted. Since the higher  $V_g$  may have some influence to increase the coupling between the dot and the lead via gate voltage  $V_{C1C2}$ . Due to the higher  $V_g$  and lower  $V_{E1E2}$ , the quantum dot is tuned into stronger asymmetric coupling. Therefore the alignment of the Kondo conductance resonance peaks is obviously more tilted and is not in the middle of the Coulomb diamond.

## 7. Kondo Physics in a Single Quantum dot

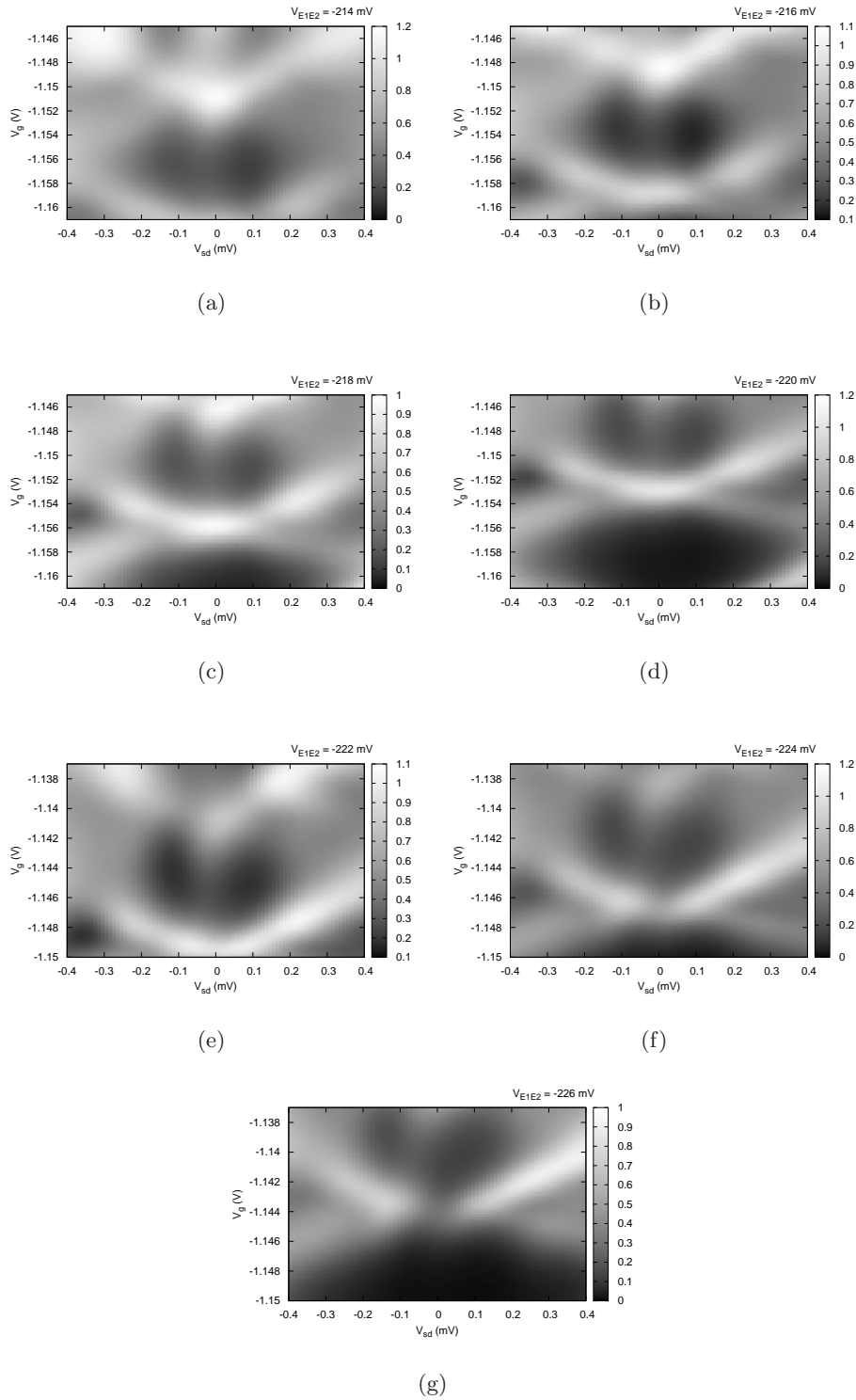


Figure 7.5.: The evolution of an asymmetric of the Kondo conductance resonance by varying gate voltage  $V_{E1E2}$  from (a) -214 mV to (g) -226 mV at  $V_{C1C2} = -325$  mV

## 7.2. Analysis of the Kondo Resonance

Figure 7.6 shows the plot of the Kondo conductance resonance peak versus the bias voltage at various gate voltages  $V_g$  as the  $V_{C1C2} = -325$  mV and  $V_{E1E2} = -220$  mV. The curves have been offset by  $0.01e^2/h$  for clarity. The topmost and bottom curves are observed at low and high negative gate voltage respectively. This data represents the Kondo resonance in the second Coulomb diamond of Fig. 7.5(d). The Kondo peaks can be seen clearly in every curve, and the position of the Kondo peak gradually shifts to more negative bias.

The measured data in each trace at fixed gate voltage  $V_g$  has been fit with the hyperbolic cosine superposed by a Lorentzian to find the width, amplitude, and peak position of the Kondo resonance peak as shown in Fig. 7.7. If there is no anomaly at the Coulomb blockade region, the conductance data in this region is very small and the trend of data is quite flat at the fixed  $V_g$ . Thus the hyperbolic cosine function is selected to fit the data without anomaly structure, whereas the Lorentzian function is selected to fit peak-shaped data for anomaly structure in the blockade region. The long-dashed line represents the Lorentzian peak and the short-dashed line represents the hyperbolic cosine curve. According to the superposed curve (solid line) and the data points, the quality of fitting is good. Therefore we use this superposed function to make Kondo peak fitting in the Coulomb diamond at different gate voltages  $V_{E1E2}$  as already presented in Fig. 7.5.

For each gate voltage  $V_{E1E2}$ , the width of the Kondo resonance peak decreases gradually with decreasing gate voltage  $V_g$ . The peak width becomes saturated and then begins rising again when the  $V_g$  is further decreased, as shown in Fig. 7.8(a). The trend of data points of the width for each different  $V_{E1E2}$  shows a parabolic behaviour. We can see that the width rises to a high value whenever the  $V_g$  moves to the region of neighbouring Coulomb peak. Figure 7.8(b) shows the dependence of the amplitude of the Kondo peak on the gate voltage  $V_g$  at different  $V_{E1E2}$ . From the fitting with superposed function, the amplitude of the Kondo peak can be calculated as the conductance at base line of Lorentzian peak subtracted from that at maximum. This amplitude data corresponds to the conductance in the valley of Coulomb oscillation where the Kondo resonance can be found. For each  $V_{E1E2}$ , the peak amplitude decreases from the conductance of the right Coulomb peak to minimum value at the Kondo valley, and then increases again to the conductance of the left Coulomb peak. This can be expressed that the amplitude of the Kondo resonance peak increases as the conductance  $G$  increases moving up the side of the Coulomb blockade peak.

In the Kondo peak fitting we assume that the width obtained is approximately the full width at half maximum (FWHM) of the peak. Since it can be defined as

$$\text{FWHM} = \frac{k_B T_K}{e}, \quad (7.1)$$

where  $k_B$  is the Boltzmann's constant and  $T_K$  is Kondo temperature, the increasing width follows the increase of  $T_K$ . As shown in Fig. 7.8(a) and 7.8(b), the Kondo resonance peak increases in both height and width when moving away from Kondo valley toward a neighboring Coulomb peak. The Kondo effect arises from the coupling between a localized electron spin and a Fermi sea of conduction electrons. The strength is characterized by the Kondo temperature  $T_K$ . The spin-coupling interactions which give rise to Kondo physics contribute significantly only for temperatures comparable to or lower than the Kondo temperature [31, 52].

According to the Anderson impurity model, the relationship of Kondo temperature as defined in Eq. 2.49:  $k_B T_K = (\sqrt{\Gamma U}/2) \exp(\pi \varepsilon_0 (\varepsilon_0 + U)/\Gamma U)$ , where  $\varepsilon_0 = \alpha e V_g + \text{constant}$ , and is the energy of the localized state measured from the Fermi energy of the leads, the  $T_K$  is proportional to the gate voltage  $V_g$ . Therefore Kondo temperature  $T_K$  increases when approaching the Coulomb blockade peaks on either side of the Kondo valley. This is the result of bringing

7. Kondo Physics in a Single Quantum dot

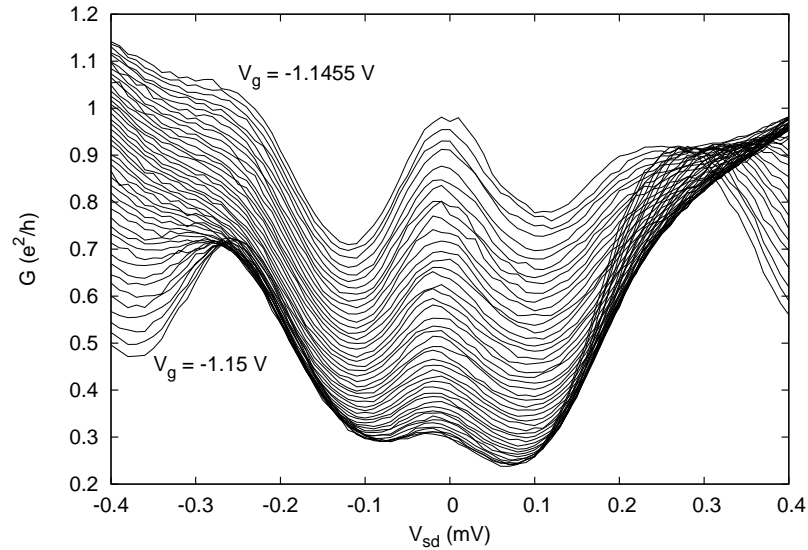


Figure 7.6.: The differential conductance  $G$  versus bias voltage  $V_{sd}$  with  $V_{C1C2} = -325$  mV and  $V_{E1E2} = -220$  mV, as referred to Fig.7.5(d). Each data trace at fixed gate voltage  $V_g$  exhibits the pronounced Kondo resonance in  $G$ . The curves have been offset with  $0.01e^2/h$  for clarity.

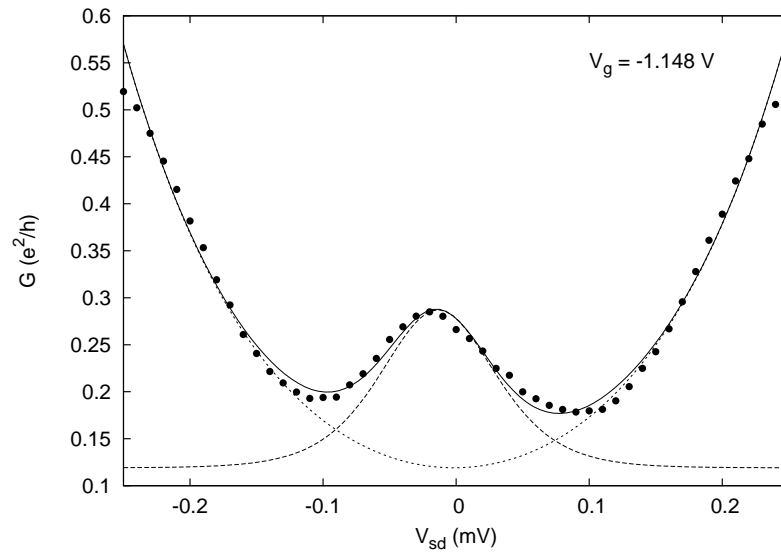
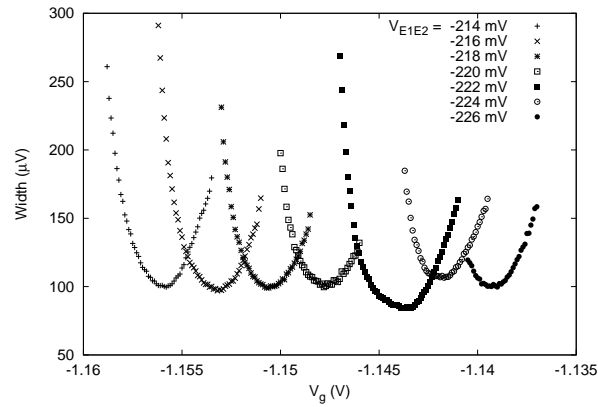
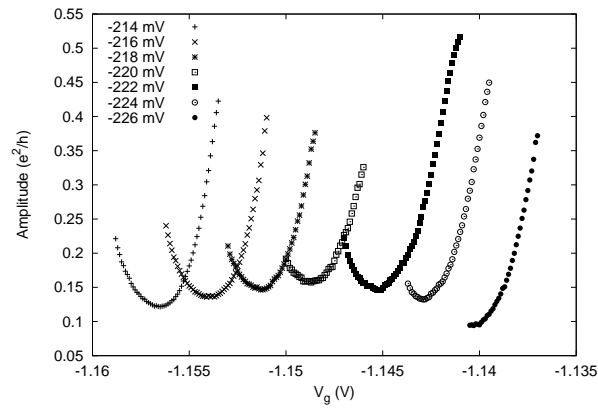


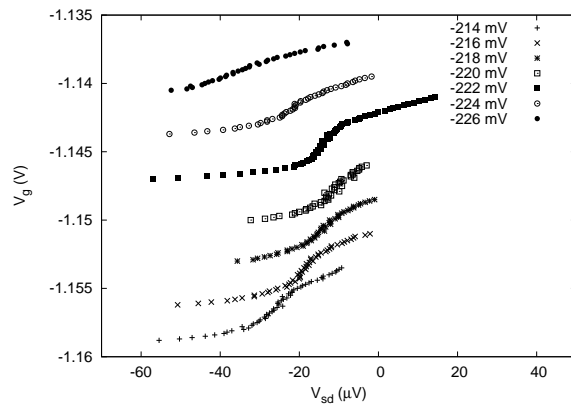
Figure 7.7.: The fit of hyperbolic cosine superposed with Lorentzian to one of data trace at  $V_g = -1.148$  V in figure above. The solid line presents an excellent fitting to the data. The dashed lines indicate the graph of hyperbolic cosine and Lorentzian peak.



(a)



(b)



(c)

Figure 7.8.: The dependence of the (a) width, (b) amplitude, and (c) the peak position of the Kondo resonance on gate voltage ( $V_g$  or  $V_{D1D2}$ ) at different  $V_{E1E2}$  varied from -214 to -226 mV corresponding to the data in Fig. 7.5. The width and amplitude at each  $V_{E1E2}$  have been clearly shown the parabolic dependence. The Kondo peak position obviously shifts when the tunnel barrier depending on  $V_{E1E2}$  is changed.

## 7. Kondo Physics in a Single Quantum dot

the energy state  $\varepsilon_0$  toward the Fermi energies  $\mu_L \cong \mu_R$  by tuning the gate voltage  $V_g$ . For example, at  $V_{E1E2} = -220$  mV, the minimum width around the middle of Kondo valley is  $\approx 100$   $\mu$ V implying  $T_K \sim 1.16$ , while the width at Kondo valley approaching one of Coulomb peak is obtained  $\approx 132$   $\mu$ V estimating  $T_K \sim 1.53$  K. It can be noticed that the minimum width referring and hence the Kondo temperature at the valley is independent of  $V_{E1E2}$ .

Figure 7.8 shows the dependence of Kondo resonance width and amplitude on the gate voltage  $V_g$  at different  $V_{E1E2}$ , which corresponds to the measured data appeared in Fig. 7.5. According to both 7.8(a) and 7.8(b), we can see clearly that the position of Kondo valley is shifted to less negative  $V_g$  as the  $V_{E1E2}$  decreases. Because the tunnel barrier is adjusted by changing  $V_{E1E2}$ , the Kondo valley is shifted under the influence of the dot-lead gate voltage  $V_{E1E2}$ . The asymmetry of the Kondo effect can be seen in Fig. 7.8(c) which shows the center of Kondo resonance peak in the Coulomb diamond for different  $V_{E1E2}$ . For each  $V_{E1E2}$ , the Kondo peak position is shifted to more negative bias when the  $V_g$  is decreased. Around the middle of the Kondo valley in (a), the Kondo peak position in (c) is slightly shifted. While the  $V_g$  is swept to neighbouring Coulomb blockade peaks, the shifting of the Kondo peak position is more clear. The slope of Kondo peak shifting in the Kondo valley is much steeper than that in the region closed to the adjacent Coulomb peaks. At  $V_{E1E2} = -224$  and  $-226$  mV, the steepest part of the Kondo peak position shifting becomes shorter. It corresponds to the region of Kondo valley getting narrower and the distortion of Coulomb diamond as seen in Fig. 7.5(f) and (g). This can be referred to the large asymmetry of the tunnel coupling of the dot at these conditions of gate voltages.

The effect of the Kondo peak position shifting is due to the influence of the asymmetry of the tunnel coupling between the dot and the electron reservoirs,  $\Gamma_L \neq \Gamma_R$ . With decreasing  $V_{E1E2}$ , the Kondo peak shifting is more pronounced and the slope for this peak changing over the Kondo valley decreases. In order to break the symmetry of the tunnel coupling of the dot to the reservoir, we adjust the voltage applied to the dot-lead gate, i.e. gate E1E2 in this case, instead of tuning the applied voltage to an additional gate close to a dot-lead gate as performed by F. Simmel et. al. [37]. The Kondo resonance in the density of states in the dot will be pinned to the electrochemical potential level of the stronger coupling of the dot to either left or right barrier. Therefore, the appearance of Kondo conductance resonance in non-zero bias can be observed even at no applied magnetic field  $B = 0$ . The shifting of enhanced conductance peaks in the Coulomb diamond also becomes more pronounced with increasing of asymmetry of the coupling by decreasing the  $V_{E1E2}$ . These asymmetry results qualitatively agree with the numerical results of density of states and differential conductance calculated from the on-dot impurity Green's function according to the Anderson Hamiltonian in the work of M. Krawiec and K. I. Wysokinski [38].

Figure 7.9(a) shows the Coulomb diamond in the Kondo regime as the tunneling gate voltage  $V_{C1C2}$  and  $V_{E1E2}$  is applied by  $-326$  mV and  $-218$ , respectively. The DC-offset in this presented data is corrected by  $30$   $\mu$ V. We will use this condition to investigate the temperature dependence of the Kondo resonance in the next section. The straight line indicates the evolution of the offset of Kondo conductance resonance with the gate voltage  $V_g$ . The slope of this line  $V_g/V_{sd}$  is about 200, which is the linear shift of the resonance with the  $V_g$ . This resonance shifting results from the influence of the  $V_g$ , which is the applied voltage to gate D1D2, to the gate C1C2 and E1E2, which is coupling of the dot to the left and right lead respectively. The shifting of the Kondo conductance resonance peak can be seen clearly in the line plot in Fig. 7.9(b) when the gate voltage  $V_g$  is swept from  $-1.1475$  V to  $-1.151$  V. Figure 7.10(a) also shows the shifting of the Kondo peak position from Fig. 7.9(a) indicated with the straight line with the same slope as described above. The effect of resonance shifting from the gate voltage  $V_g$  has also obtained before in Fig. 7.8(c) for every value of  $V_{E1E2}$ .

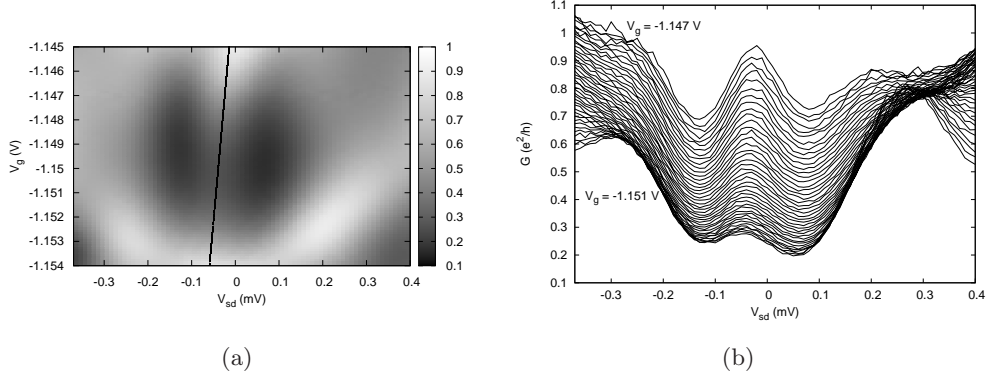


Figure 7.9.: The plot of differential conductance as a function of  $V_{sd}$  and  $V_g$  at  $V_{C1C2} = -326$  mV,  $V_{E1E2} = -218$  mV. The solid line indicates the tilting of the Kondo resonance peak offset. (b) The line shape of the Kondo peak in  $G$  is plotted from the Kondo valley in (a). The curves have been offset with  $0.01(e^2/h)$  for clarity.

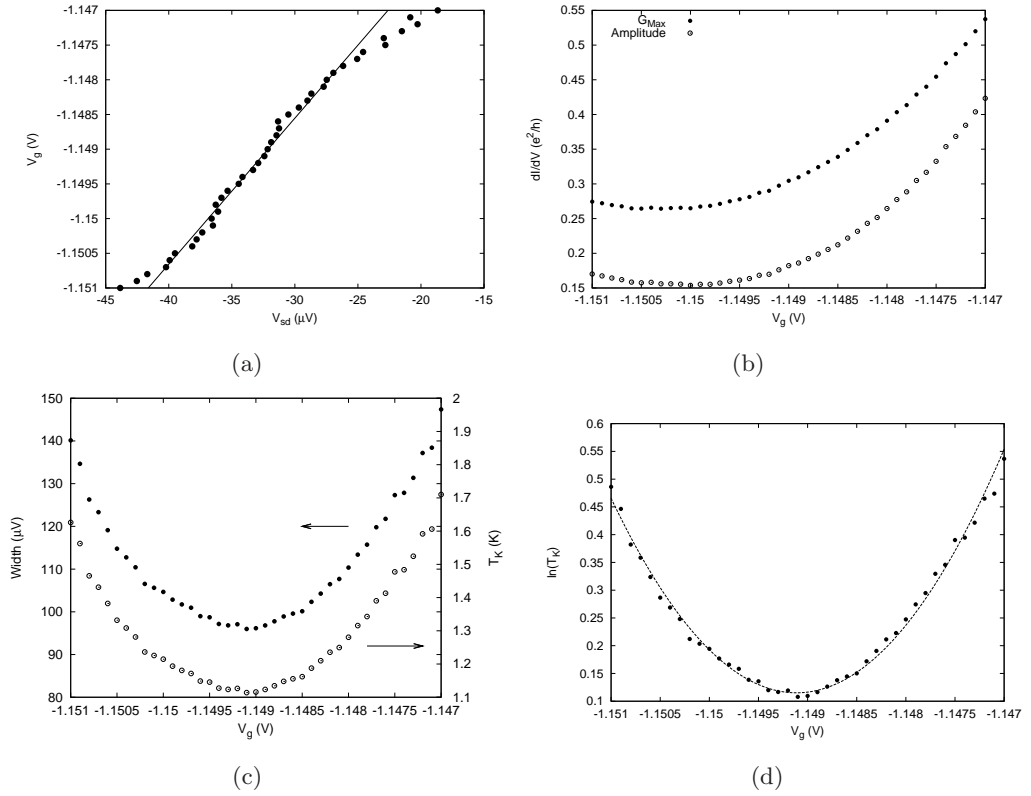


Figure 7.10.: (a) Kondo peak position, (b) maxima and amplitude of Kondo peak in differential conductance, (c) the width and depending Kondo temperature  $T_K$ , and (d) the value of  $\ln T_K$  corresponding to the data in Fig. 7.9 are presented.

## 7. Kondo Physics in a Single Quantum dot

The maximum value  $G_{Max}$  and amplitude of the Kondo peak are shown in Fig. 7.10(b), and have the same trend as the amplitude of Kondo peak in previous data. The amplitude and the width of the Kondo peak, as shown in Fig. 7.10(b) and (c), is clearly increased when moving towards the Coulomb peaks. Therefore, the Kondo temperature increases from the Kondo valley to the side of the Coulomb peak. Since the  $k_B T_K/e$  is estimated to be equal to the width of the Kondo resonance peak, the Kondo temperature  $T_K$  varies from a minimum value of  $\sim 1.1$  K in the valley to  $\sim 1.7$  K close to the Coulomb peaks, as presented in Fig. 7.10(c). The calculated Kondo temperature  $T_K$  for different gate voltage  $V_g$  has been shown and is proportional to the width of the Kondo resonance peak.

We can rewrite Eq. 2.49 as  $\ln(T_K) = \pi\varepsilon_0(\varepsilon_0 + U)/\Gamma U + \ln(\sqrt{\Gamma U}/2k_B)$  where  $\varepsilon_0 = \alpha e V_g + \text{constant}$ . This equation indicates a quadratic dependence for  $\ln(T_K)$  on the gate voltage  $V_g$ . The data set of natural logarithm values of Kondo temperature, which is derived from the width of the Kondo conductance peaks at the base temperature, is fitted to the equation above and a parabolic dependence is found, as shown in Fig. 7.10(d). From this fit, we obtain the charging energy  $U \simeq 1$  meV and the tunnel coupling to the leads  $\Gamma \simeq 550 \mu\text{eV}$ , which is much larger than  $\Gamma$  for the dot in weak coupling limit discussed in the section 6.4.

Out of equilibrium, when a finite  $V_{sd}$  is biased, the Kondo resonance appearing in the density of states of the quantum dot is split into two resonances, each pinned to one chemical potential of the respective lead. Due to the different couplings of the dot to the leads in our case, one of the resonances is enhanced whereas the other is suppressed as schematically shown in Fig 7.4. The asymmetry and energy dependence of the tunneling strengths result in an enhanced conductance in the Coulomb blockade diamond at nonzero bias [31, 37].

### 7.3. Temperature dependence of the Kondo Resonance

Figure 7.11(a) and 7.11(b) show that the differential conductance for different temperature value of the Kondo resonance peak in the Coulomb diamond in Fig. 7.9(b) at gate voltage  $V_g = -1.1475$  and  $-1.148$  V, respectively. This presented data is already corrected for the DC-offset. The pronounced peaks around  $V_{sd} \sim -30 \mu\text{V}$ , which is the shifted value from the zero-bias, reflect the Kondo resonance located at the chemical potential of the lead with strong coupling. As temperature,  $T \equiv T_{bath}$ , increases, the conductance at the Kondo resonance peak decreases whereas the conductance at the valley at both sides of Kondo peak increases. The base temperature for temperature dependence measurement is about 64 mK, whereas the electronic temperature,  $T_e$ , is about 190 mK, as indicated with the solid line for each figure.

The data is fitted quite well with a hyperbolic cosine function superposed by a Lorentzian peak as demonstrated in Fig. 7.11(c) for  $V_g = -1.1475$  V and 7.11(d) for  $V_g = -1.148$  V. The conductance at the top of the Kondo resonance peak and the peak width estimated from the full width at half maximum of the fitting Lorentzian peak can be extracted for different temperature.

The width of the Kondo resonance peaks is constant at low temperature and begin increasing at the temperature above  $\sim 150$  mK, as shown in Fig. 7.12(a) and (b). The width linearly increases at high temperature above  $\sim 250$  mK as indicated with the linear line in both figures. According to Eq. 7.1, the Kondo temperature  $T_K$  can be extracted from the constant width at the low temperature. For  $V_g = -1.1475$  V, the width is about  $129 \mu\text{V}$ , therefore the  $T_K \simeq 1.5$  K. The width of  $125 \mu\text{V}$  for  $V_g = -1.148$  V replies the  $T_K \simeq 1.45$  K. The linear fitting line at high temperature can extrapolate the width at zero temperature of  $\sim 44 \mu\text{V}$  for  $V_g = -1.1475$  V and  $\sim 38 \mu\text{V}$  for  $V_g = -1.148$  V. The slope of the linear line can be written as  $\Delta(\text{FWHM})/\Delta T = (k_B/e)(\Delta T_K/\Delta T)$ . In Fig. 7.12(a) and 7.12(b), the lines indicate a slope of  $\sim 4.5k_B/e$  and  $\sim 4.7k_B/e$ , respectively.

Figure 7.12(c) and (d) show the logarithmic temperature dependence of the conductance at the



### 7.3. Temperature dependence of the Kondo Resonance

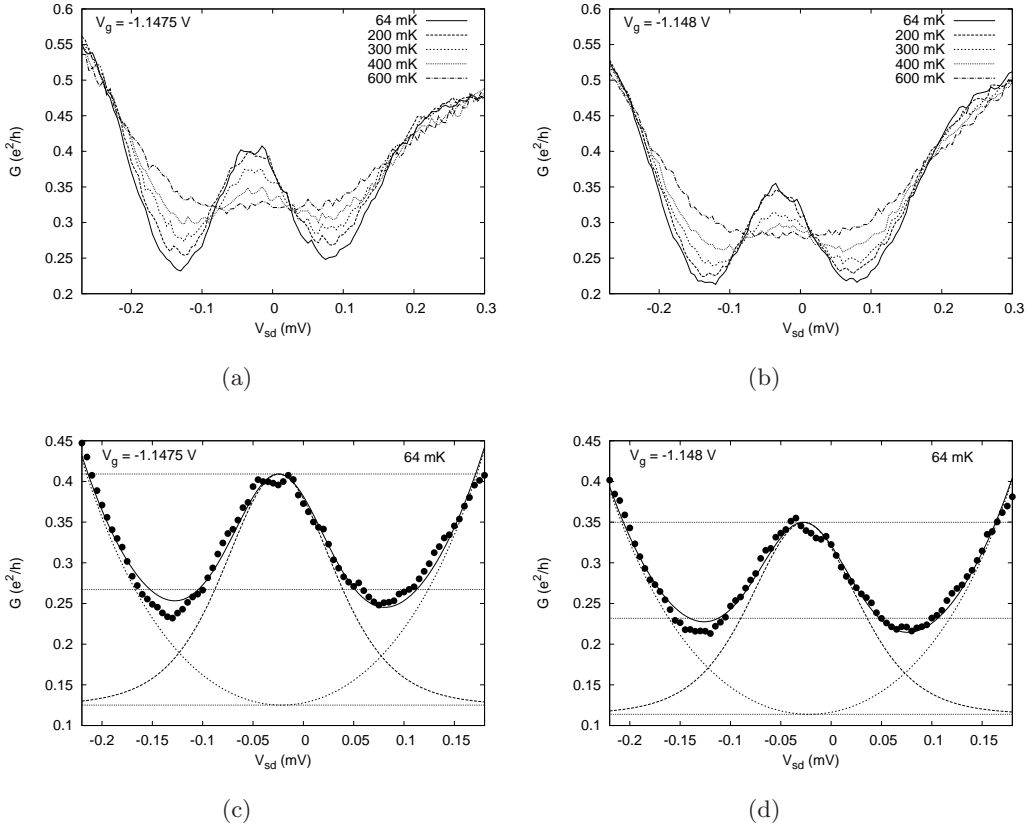


Figure 7.11.: Differential conductance  $G \equiv dI/dV_{sd}$  versus dc bias voltage between source and drain contacts  $V_{sd}$  for temperature ranging from 64 mK up to 600 mK, at  $V_g = -1.1475$  V in (a) and  $V_g = -1.148$  V in (b). Other gate voltage is set as  $V_{C1C2} = -0.326$  V,  $V_{E1E2} = -0.218$  V. (c) and (d) show the good fitting of Kondo resonance peaks corresponding to data in (a) and (b) at the base temperature.

top of the Kondo peaks. At low temperature the Kondo conductance saturates around  $0.43e^2/h$  and  $0.36e^2/h$  for  $V_g = -1.1475$  V and  $V_g = -1.148$  V, respectively. We fit the conductance  $G$  versus the temperature  $T$  for these two gate voltages to the empirical function in Eq. 2.50 as

$$G(T) = G_0 \left( \frac{T_K'^2}{T^2 + T_K'^2} \right)^s, \quad (7.2)$$

with  $T_K' = T_K/\sqrt{2^{1/s} - 1}$ , where the fit parameter  $s \approx 0.2$  for a spin-1/2 system [35]. This is an empirical fitting function to numerical renormalization group calculations (NRG) reported in work by T. A. Costi et al. [60]. The appropriate value of  $s$  is determined from the steepness of the conductance drop with increasing temperature. To compare the  $T_K$  from this method to the one extracted from the width of Kondo peak, the parameter  $s$  is fixed at 0.2 in the fit to our data. Therefore, we can obtain that the  $T_K \simeq 1.64$  K for  $V_g = -1.1475$  V, and  $T_K \simeq 1.68$  K for  $V_g = -1.148$  V. The  $T_K$  value extracted from this fitting in Fig. 7.12(c) and 7.12(d) is comparable to the previous  $T_K$  value extracted from 7.12(a) and 7.12(b).

Hence, we assume the value for  $T_K$  in Eq. 7.2 as the value extracted from the width with Eq. 7.1 (1.5 K and 1.45 K), and fit to the data in order to find the value of  $s$ . The quality of curve fitting does not change significantly. The fitting values of  $s$  are 0.22 and 0.24 for  $V_g = -1.1475$  V and  $V_g = -1.148$  V, respectively. They are quite close to expected value of

7. Kondo Physics in a Single Quantum dot

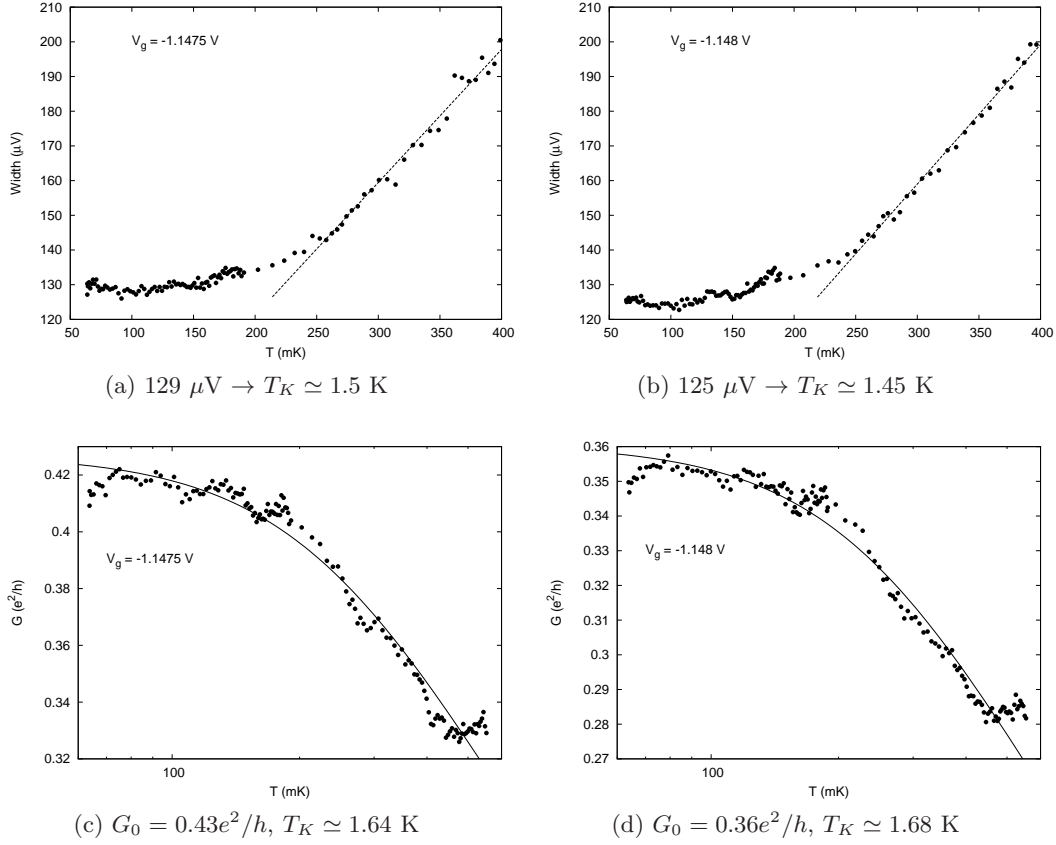


Figure 7.12.: Width ((a) and (b)) and maximum point ((c) and (d)) of Kondo peak at  $V_{C1C2} = -0.326 \text{ V}$  and  $V_{E1E2} = -0.218 \text{ V}$ . The temperature dependence have been investigated at  $V_g = -1.1475 \text{ V}$  ((a) and (c)) and  $-1.148 \text{ V}$  ((b) and (d))

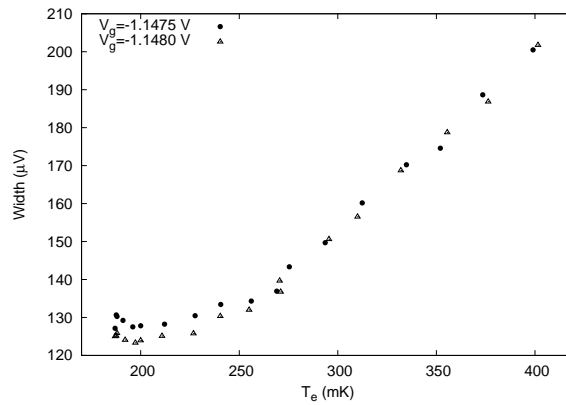


Figure 7.13.: Linewidth of Kondo conductance peaks is plotted as a function of temperature of electrons,  $T_e$ .

0.2 in Kondo regime depending on the spin of the impurity or localized electron spin. It clearly shows that the fitting with this scaling empirical function to our Kondo conductance data is acceptable and in agreement with the theory. This empirical form provides a good fit to NRG results giving the correct Kondo temperature for the Kondo regime [35, 60].

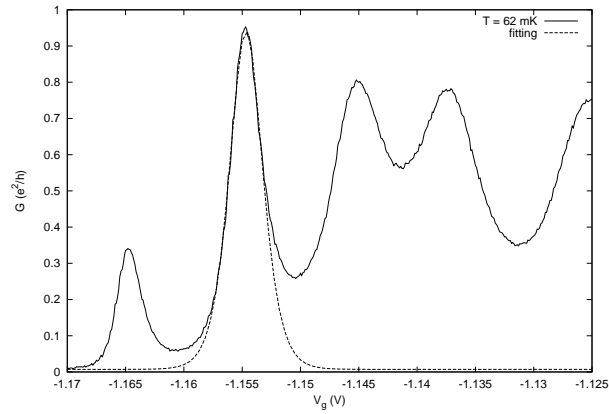
Since the saturation of Kondo linewidth is similar to the saturation in the temperature dependence of Coulomb peaks, then some of linewidth data in Fig. 7.12(a) and (b) is plotted as a function of electronic temperature  $T_e$ , as shown in Fig. 7.13. The  $T_e$  is obtained from the temperature dependence of Coulomb linewidth in Fig. 6.25 giving the correlation between bath temperature and electronic temperature. It can be seen that the width becomes saturated at  $T_e \sim 200$  mK which is comparable to the electronic temperature of  $\sim 190$  mK at base temperature of  $\sim 64$  mK. This means that the Kondo linewidth becomes saturated because the electronic temperature saturates. At  $T_e \gtrsim 250$  mK, the linear dependence of Kondo linewidth on the electronic temperature is clearly shown. At high temperature, the electron temperature  $T_e$  can be assumed to be equal to the temperature of the bath. Since  $T_K/T_e > 1$  extracted from the method above, it can be confirmed that the conductance in a quantum dot with this strong coupling condition is definitely in the Kondo regime [32].

We investigate the Coulomb oscillation in the dotII structure with strong coupling to the lead over a wide range of gate voltage  $V_g$ , as shown in Fig. 7.14(a). The fitting of the Coulomb peak in Kondo regime at the base temperature of 62 mK has also been shown. Figure 7.14(b) shows Coulomb oscillations for different temperatures. The temperature of the bath is increased from 62 to 800 mK. The conductance at the slope between the  $V_g$  of -1.15 and -1.146 V decreases with increasing temperature. This slope is the one we found the Kondo conductance peaks in the nonlinear measurement, as shown before in Fig. 7.10. The dot-lead gate voltages,  $V_{C1C2}$  and  $V_{E1E2}$ , are set at -326 and -218 mV, respectively. Comparing to the Coulomb valley between -1.163 to -1.157 V, the conductance in this valley is increased with increasing temperature.

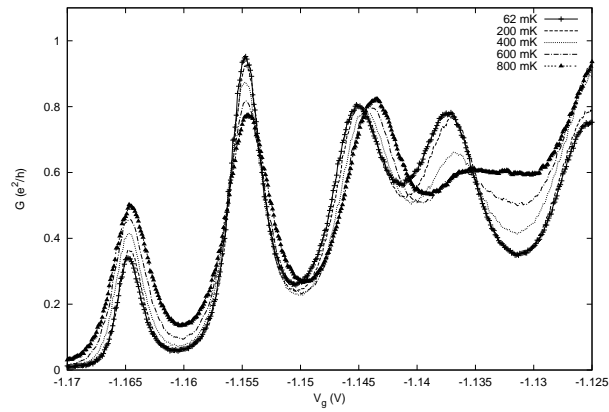
From the Coulomb peak fitting in Fig. 7.14(a) for different temperatures, we can plot the line width or full width at half maximum  $\Gamma$  of the Coulomb peak versus temperature  $T$ . The conductance peak is well described by the convolution of a Lorentzian broadening of  $\Gamma$  of the localized energy level with the derivative of the Fermi-Dirac function [21, 22]. Comparing the convolution to our temperature dependence of measured conductance peak width, we can extract  $\Gamma \approx 292 \mu\text{eV}$  from the extrapolation back to  $T = 0$  K as shown in Fig. 7.14(c). Comparing the  $\Gamma \sim 300 \mu\text{eV}$  in this section to the  $\Gamma \sim 100 \mu\text{eV}$  extracted in the weak coupling regime in the section 6.4. The  $\Gamma$  extracted at higher dot-lead gate voltage is approximately three times higher than that in the weak coupling regime. Since  $\Gamma = \Gamma_L + \Gamma_R$  reflects the tunnel coupling between the dot and the leads, we can clearly see that the electron tunneling with the dot-lead gate voltages applied in this section is definitely in the strong coupling regime giving chances to study Kondo physics in our quantum dot. The slope of the same temperature dependence gives the constant of factor  $\alpha = C_g/C_\Sigma = 0.097$ , where  $C_g$  and  $C_\Sigma$  are the gate and total capacitance, respectively. The factor  $\alpha$  is the proportionality between the localized energy level and the gate voltage  $V_g$ . At high temperature the line of the convolution function with above parameters is almost linearly decreased with decreasing temperature, and separates from our data at  $\sim 300$  mK, which corresponds to the temperature dependence of Coulomb oscillation in weak coupling or in the Coulomb regime.

Figure 7.15(a) shows the temperature dependence of the conductance  $G$  on a logarithmic scale for fixed gate voltages  $V_g$  in the Kondo regime. We fit  $G$  versus  $T$  for different gate voltages  $V_g$  to the empirical function in Eq. 7.2 to extract the Kondo temperature  $T_K$ . The gate voltage  $V_g$  is related to the localized state energy  $\varepsilon_0$  with  $\varepsilon_0 = \alpha V_g + \text{constant}$ . The normalized conductances  $G/G_0$  for the same data are replotted as a function of temperature divided by the respective Kondo temperature  $T_K$ . This yields the normalization plot, as shown in Fig. 7.15(b). In this plot

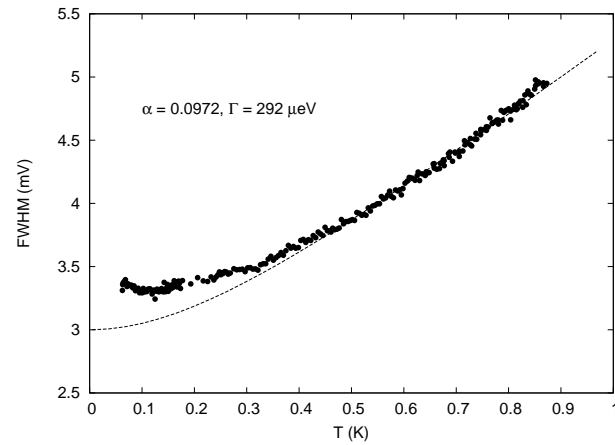
## 7. Kondo Physics in a Single Quantum dot



(a)



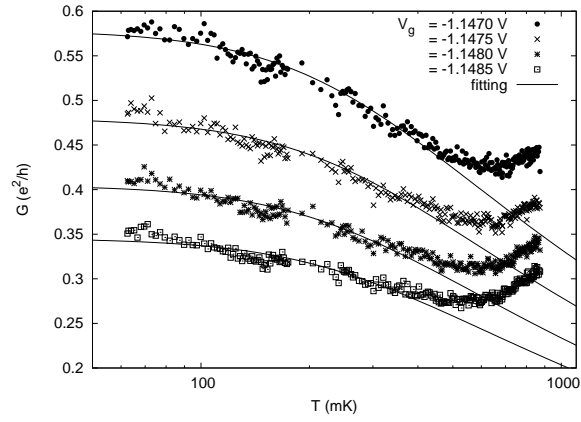
(b)



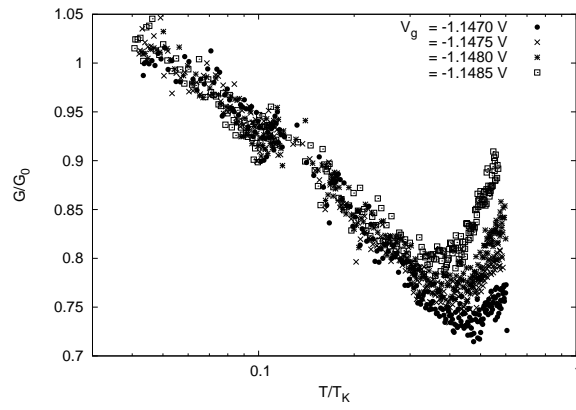
(c)

Figure 7.14.: (a) Coulomb oscillations in  $G$  versus  $V_g$  with the Coulomb peak fitting at  $V_{C1C2} = -326$  mV and  $V_{E1E2} = -218$  mV. (b) Coulomb oscillations in Kondo regime at different temperature. (c) Temperature dependence of the peak width extrapolated back to  $T = 0$  to extract  $\Gamma$ . The slope at high temperature gives  $\alpha$  value as shown in the figure.

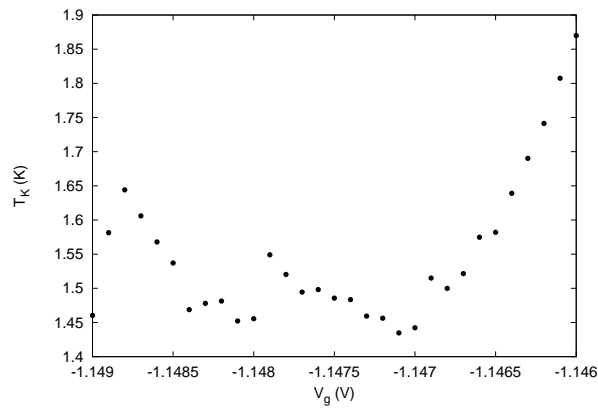
### 7.3. Temperature dependence of the Kondo Resonance



(a)



(b)



(c)

Figure 7.15.: (a) Conductance versus temperature for various values of  $V_g$ . The curves is a fit to Eq. 7.2 with a fit parameter  $s = 0.2$ . (b) The normalized conductance  $G/G_0$  versus normalized temperature  $T/T_K$  scales to a single data trace for different  $V_g$ . (c) Kondo temperature calculated from the fit in (a) at corresponding  $V_g$ .

## 7. Kondo Physics in a Single Quantum dot

the different data sets all lie on top of each other, especially at  $0.04 \lesssim T/T_K \lesssim 0.4$ . This confirms that the normalized conductance is a universal function of the normalized temperature  $T/T_K$  scaling to a single trace of data for different gate voltage  $V_g$ , and being independent of the other energy scales ( $U$ ,  $\varepsilon_0$ , and  $\Gamma$ ). The Kondo temperature  $T_K$  calculated by fitting with the empirical function for various gate voltages  $V_g$  has been shown in Fig. 7.15(c). The Kondo temperature  $T_K$  along the Kondo valley is extracted between 1.4 and 1.9 K. It shows a parabolic dependence similar to the behaviour of the Kondo temperature estimated from the width of Kondo peak, but the value of  $T_K$  obtained from fitting with empirical function is somewhat higher than that estimated from the Kondo peak width.

### 7.4. Kondo resonance in the Magnetic field

According to previous studies of the Kondo effect in an applied magnetic field [30, 31, 61], a magnetic field can split the enhanced Kondo peak in the density of states at the electrochemical potential level of the leads into two peaks with the Zeeman energy  $g\mu_B B$  above and below the potential level. This lifting of the spin degeneracy results in a splitting of the differential conductance  $G = dI/dV_{sd}$  versus  $V_{sd}$ . When a magnetic field is applied, a Kondo conductance peak splits into two peaks appearing at  $V_{sd} = \pm g\mu_B B/e$ , where  $g$  is the Lande g-factor,  $\mu_B$  is the Bohr magneton, and  $B$  is the applied magnetic field. Thus these split peaks in differential conductance are separated by twice the Zeeman energy,  $2g\mu_B B$ . In equilibrium, there is no longer a peak in the density of states at  $\mu_L = \mu_R$ , and the zero-bias conductance will be not enhanced.

In our case, we have performed the nonlinear measurements of a quantum dot in strong coupling or Kondo regime in small magnetic field. Figure 7.16(a)-(c) show the plot of our nonlinear data after corrected for the DC-offset over Kondo regime for applied magnetic field varied from 0 to 200 mT. The line shapes in the right figures have also been presented to make more clear in changing of the Kondo conductance peak. This presented Kondo region is selected around  $V_{C1C2} = -1.1425$  (topmost curve) and  $-1.146$  (bottom curve). When the applied magnetic field increases, the maximum of the Kondo peak decreases, but there is no evidence indicating a peak splitting. This might be interpreted that a slight increase in magnetic field can reduce the tunnel couplings such that a quantum dot system is turned out of the Kondo regime [37]. The applied magnetic of 200 mT is still not enough to obtain a peak separation.

The Kondo effect parameters: maximum conductance, width, and center of the resonance peak in differential conductance, are extracted and shown in Fig. 7.17(a) to (c), respectively. We can see that the maximum of the Kondo resonance decreases and the trend of the maximum conductance data points is getting flatter with increasing magnetic field, as shown in Fig. 7.17(a). This result confirms that the magnetic field might have some influence to the coupling of the dot to the leads. In Fig. 7.17(b) the width of the Kondo resonance peak in the region of  $-1.1455 < V_g < -1.1435$  slightly decreases, whereas the width outside this region approaching to the Coulomb peaks on either side increases when applied magnetic field increase.

Figure 7.17(c) shows the plot of center position of the Kondo peak in Kondo regime at different applied magnetic field. At Each value of magnetic field, the Kondo resonance peak position changes with the positive slope of  $dV_g/dV_{sd}$ . This effect might come from an asymmetric tunnel barrier of the dot as discussed above. With increasing magnetic field, the peak position at fixed gate voltage  $V_g$  changes randomly. The trend of the shifting of the peak position is nearly the same for different magnetic field.

We may apply higher magnetic fields to a quantum dot in Kondo regime with another condition of gate voltage  $V_{C1C2}$  and  $V_{E1E2}$ . Since the position and shape of the Coulomb diamond are not quite stable after we perform the measurement in applied magnetic field, we therefore have

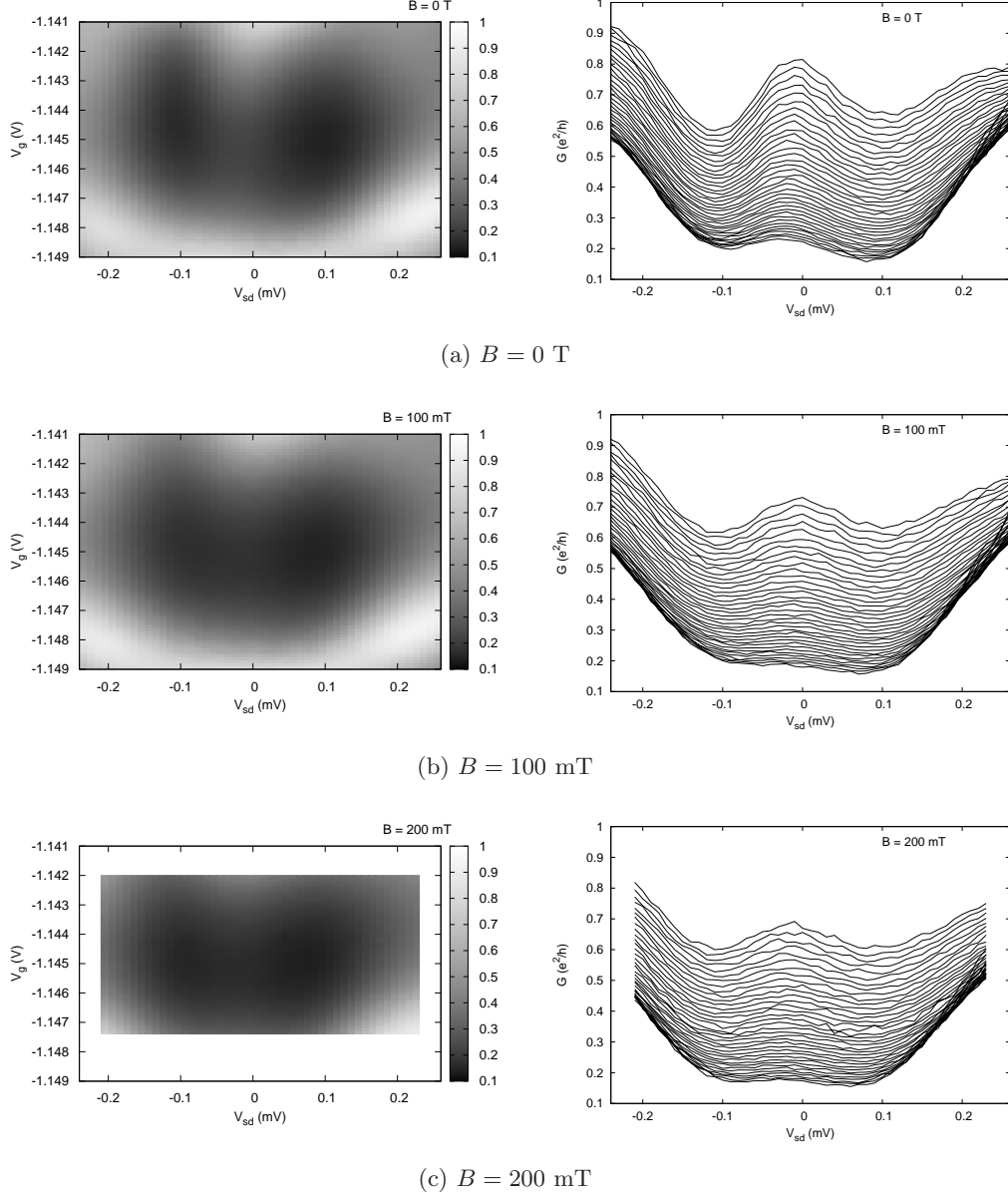


Figure 7.16.: (a)-(c) (Left) Grey-scale plot of  $G = dI/dV_{sd}$  for a quantum dot at  $V_{C1C2} = -327$  mV and  $V_{E1E2} = -220$  mV for  $B = 0$  to 200 mT, respectively. (Right) The plot of line shape of peaks in Kondo valley for depending  $B$ . The curves have been offset with  $0.01(e^2/h)$  for clarity. The topmost curve indicates  $V_g = -1.1425$  V, and  $V_g = -1.146$  V for the bottom curve.

## 7. Kondo Physics in a Single Quantum dot

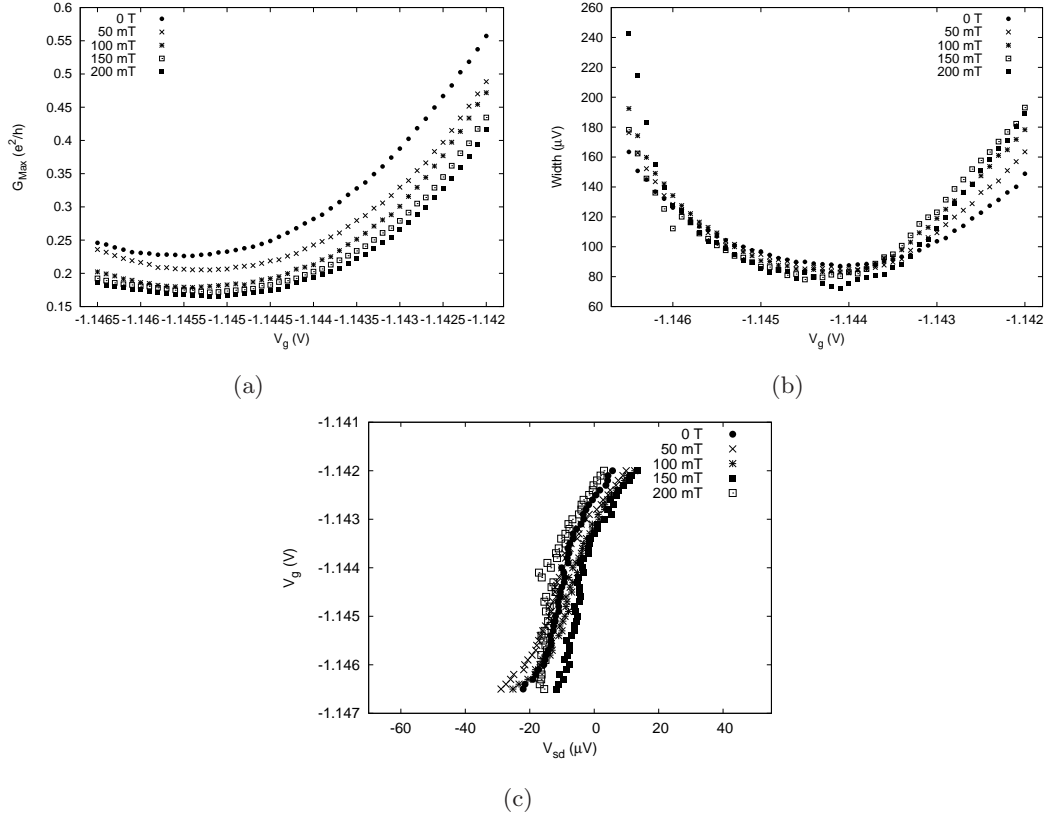


Figure 7.17.: (a) Maximum conductance  $G_{Max}$  and (b) the width of Kondo peak versus  $V_g$  for various applied magnetic field  $B$ . (c) Plot of the peak position of the Kondo resonance in  $G$  for different  $B$ . All values are extracted from the Kondo peak fit to the data in Fig 7.16. The magnetic field is applied from 0 to 200 mT.

to re-adjust  $V_{C1C2}$  and  $V_{E1E2}$  to obtain the good quality of Kondo resonance appearing in the Coulomb diamond. Figure 7.18(a) and (b) show the comparison of Kondo resonance in Coulomb diamond between no magnetic field and applied magnetic field of 250 mT. From the line shape of the Kondo peaks in both values of  $B$ , it can be seen clearly that the Kondo peak height decreases, and the regular diamond pattern for Coulomb blockade begins reappearing. At some fixed value of  $V_g$ , the Kondo peak disappears and the differential conductance in diamond region becomes flat in  $B = 250$  mT.

Figure 7.18(c) shows the maximum conductance at the top of Kondo peak at  $B = 0$  and 250 mT, which corresponds to the data in Fig. 7.18(a) and (b). The peak height at any gate voltage  $V_g$  clearly decreases as the magnetic field increases. Furthermore, the trend of data points seem to be decreased and getting flatter. The position of Kondo peak is also plotted and shown in Fig. 7.18(d). The dashed-line is the linear fit to the peak position data in no magnetic field. It is clearly seen that its slope is less than that of the dotted-line. The dotted-line is the linear fit to the peak position data in  $B = 250$  mT, and almost vertical. With  $B = 250$  mT, it improves the trend of the Kondo resonance offset by changing from tilting to vertical straight line. From these results, it is quite obvious that the magnetic field has some influence to the symmetry of the tunnel barrier of a quantum dot affecting to the symmetry of Kondo resonance and shape of Coulomb diamond. No peak splitting can be observed in this value of magnetic field.

The magnetic field might be too small to make pronounced Kondo peak splitting which can be observed. Since two splitting peaks should be separated by  $2g\mu_B B$ , one of peaks is expected



#### 7.4. Kondo resonance in the Magnetic field

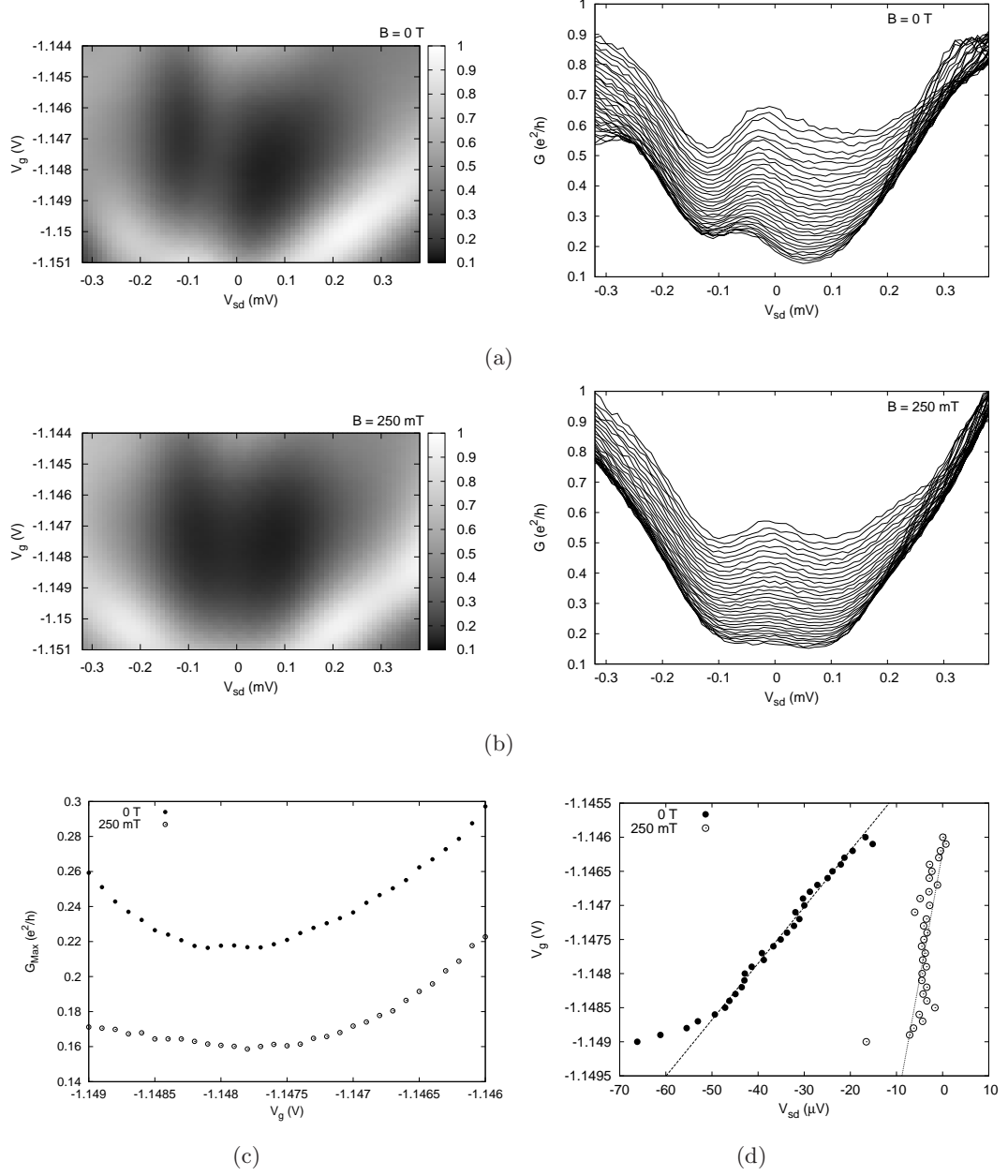


Figure 7.18.: For  $V_{C1C2} = -328$  mV and  $V_{E1E2} = -215$  mV, (a) and (b) (Left) Differential conductance on a grey scale as functions of both  $V_g$  and  $V_{sd}$  at  $T \sim 70$  mK for  $B = 0$  and 250 mT, respectively. The DC-offset is corrected for this presented data. (a) and (b) (Right) The curves of Kondo peaks at different  $V_g$  in the left have been offset with  $0.01(e^2/h)$  for clarity.  $V_g = -1.1455$  and  $-1.1485$  V are indicated at the topmost and bottom curve, respectively. (c) Conductance Maxima  $G_{Max}$  as a function of  $V_g$ , and (d) the peak position of Kondo resonance with indicated slope line as a function of  $V_g$  and  $V_{sd}$  for  $B = 0$  and 250 mT.

## 7. Kondo Physics in a Single Quantum dot

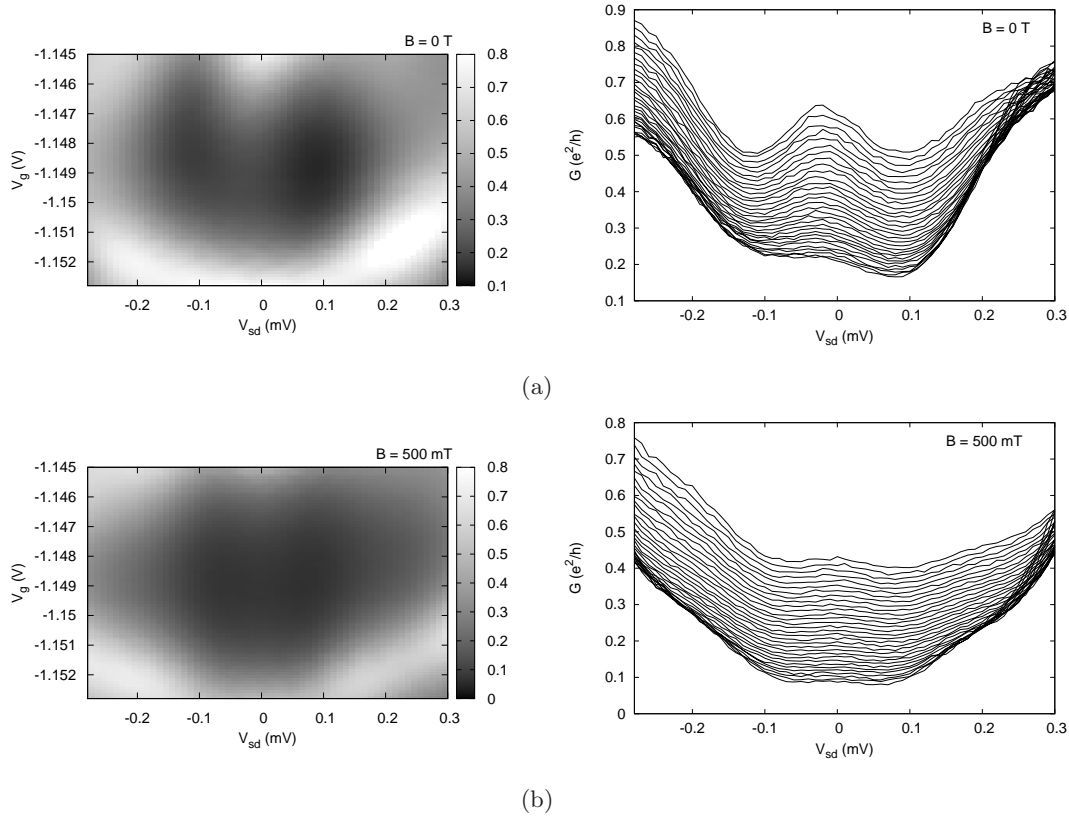


Figure 7.19.: For  $V_{C1C2} = -328$  mV,  $V_{E1E2} = -213$  mV, and  $T \sim 70$  mK, (Left) Grey-scale plot of  $dI/dV_{sd}$  as functions of  $V_g$  and  $V_{sd}$  for (a)  $B = 0$  mT and (b)  $B = 500$  mT. (Right) The plots show line shape of Kondo peaks for corresponding  $B$  in the left. The DC-offset is already corrected in this data. The curves have been offset with  $0.01(e^2/h)$  for clarity. The topmost and bottom curves indicate the gate voltage  $V_g = -1.147$  and  $-1.15$  V, respectively.

to be found at finite bias  $V_{sd} = \pm g\mu_B B/e = \pm 25 \mu\text{V}/T$ , where  $g = -0.44$  for bulk GaAs [52, 62]. For a magnetic field of  $B = 250$  mT, we expect to see the splitting peaks in the windows of  $eV_{sd} \simeq 15.8 \mu\text{eV}$  around the offset of the peaks. Unfortunately, we however swept the source-drain voltage  $V_{sd}$  in the step of  $10 \mu\text{V}$  which is bigger than  $g\mu_B B/e$ , thus we cannot observe the effect of Kondo peak splitting with small applied magnetic field. Additionally, the spin-splitting in two-dimensional electron gas might have been found to be suppressed compared with values for bulk samples [30].

We increase the tunneling coupling to the lead via QPC E by increasing  $V_{E1E2}$ . Figure 7.19 shows the results of nonlinear measurement performed in stronger coupling and higher magnetic field compared to the result in previous figures. The Kondo resonance appears in the Coulomb diamond in Fig. 7.19(a) clearly, but it almost completely disappears and the diamond pattern develops when a magnetic field of 500 mT is applied, as shown in Fig. 7.19(b). The shape of Coulomb diamond is changed completely, and the differential conductance at the middle of Kondo valley become flat. This result might be due to either the splitting of Kondo resonance in density of states around the electrochemical potential level of the leads, or the influence of magnetic field to the tunneling barrier of a quantum dot. From theory, the splitting of the Kondo peaks is expected within a window of  $V_{sd} = 2g\mu_B B/e \simeq 25 \mu\text{V}$ . Thus we are still not be able to find any evidence of the Kondo resonance splitting even for a magnetic field of 500

mT. According to data from Fig. 7.16 to 7.19, when the magnetic field is increased from zero to 500 mT, it can be noticed that the Kondo peaks are broadened. The peak height decreases and the Kondo peaks become flat at half of one tesla. The shifted Kondo resonance position and the shape of Coulomb diamond are improved with increasing magnetic field. It can be inferred that the magnetic field affects the symmetry of the tunnel coupling of the dot to leads. The symmetry of the Kondo resonance is therefore improved with increasing magnetic field.

## 7.5. Kondo Effect in a Quantum Point Contact coupled with a Single Quantum dot

In the nanostructure of the sample **PR1:d4**, Coulomb oscillations are observed in the conductance of QPC A when sweeping gate voltage  $V_{A1}$  for fixed gate voltage  $V_{A2}$ . Therefore a nonlinear measurement is performed to investigate the Kondo effect appearing in the Coulomb diamond as  $V_{A2} = -0.23$  and  $-0.24$  V. We select these values for  $V_{A2}$  because we would like to study the nonlinear data in strong coupling regime with  $V_{A2} > -0.4$  V, which is the value for stable Coulomb oscillation in the conductance of QPC A and is shown in Fig. 5.13(a).

Figure 7.20(a) shows two Coulomb diamonds of nonlinear data with  $V_{A2} = -0.23$  V. We can observe the anomaly structure indicating the Kondo conductance resonance in both diamonds. The Kondo resonance peaks occur exactly at a zero bias after the correction for DC-offset of  $\sim -40$   $\mu$ V. The line shape of the Kondo conductance peak in the top and bottom diamond is shown in Fig. 7.20(b) and Fig. 7.20(c), respectively. It can be seen that the center of the Kondo peaks is at the same position especially in the bottom diamond. It can be assumed that the unexpected dot probably has the symmetric tunnel coupling to the reservoirs. The Coulomb peak spacing is approximately 4.6 mV. The capacitances of a coupled quantum dot can be extracted from the slope of the border lines of Coulomb diamond in Fig. 7.20(a) as  $C_g \simeq 35$  aF,  $C_s \simeq 70$  aF,  $C_d \simeq 65$  aF, and  $C_\Sigma \simeq 170$  aF. We can see that the source and drain capacitances are comparable, thus the tunnel coupling to the reservoirs could be symmetric corresponding to the assumption above. The coupling factor of the gate A1 capacitance and the total capacitance is calculated as  $\alpha = C_g/C_\Sigma \simeq 0.2$ . The source-drain capacitances are obviously higher than the capacitances extracted from the diamond for  $V_{A2} = -0.4$  V as presented in the section 6.5. This may result from the stronger coupling between an unexpected quantum dot structure and the reservoir by increasing gate voltage  $V_{A2}$ .

When sweeping gate voltage  $V_{A1}$ , the conductance oscillations corrected for the source-drain offset of  $\sim -50$   $\mu$ V are shown in Fig. 7.20(d). It shows the valleys that the Kondo resonance can be found in  $-0.198$  V  $< V_{A1} < -0.194$  V and  $-0.194$  V  $< V_{A1} < -0.19$  V corresponding to two Coulomb diamonds in Fig. 7.20(a). From fitting Kondo resonance peak in Fig. 7.20(b) and 7.20(c) with hyperbolic cosine superposed by Lorentzian, the width of the resonance peaks can be calculated and is presented in Fig. 7.20(e). The Kondo temperature  $T_K$  can be estimated from the width of the resonance by using Eq. 7.1. Therefore the Kondo temperature is between  $\sim 1.7$  K and  $\sim 2.7$  K for Kondo resonance in the top Coulomb diamond, and is between  $\sim 2.1$  K and  $\sim 3.6$  for the Kondo resonance in the bottom Coulomb diamond. We find the parabolic dependence of Kondo temperature in these two regions. The parabolic dependence of Kondo line width or  $T_K$  corresponds to the conductance valley as shown in Fig. 7.20(d). Thus, we can call these valleys as Kondo valleys. The Kondo temperature increases when the distance between localized state and the Fermi energy of the leads is decreased by moving away from Kondo valley toward a neighbouring Coulomb peak.

For a decreased  $V_{A2}$  of  $-0.24$  V, Fig. 7.21(a) to (e) shows the same analysis method of the Kondo resonance as already given for  $V_{A2} = -0.23$  V. The anomaly indicating the Kondo resonance can be clearly observed in the top and bottom Coulomb diamond. After the correction of DC-offset

## 7. Kondo Physics in a Single Quantum dot

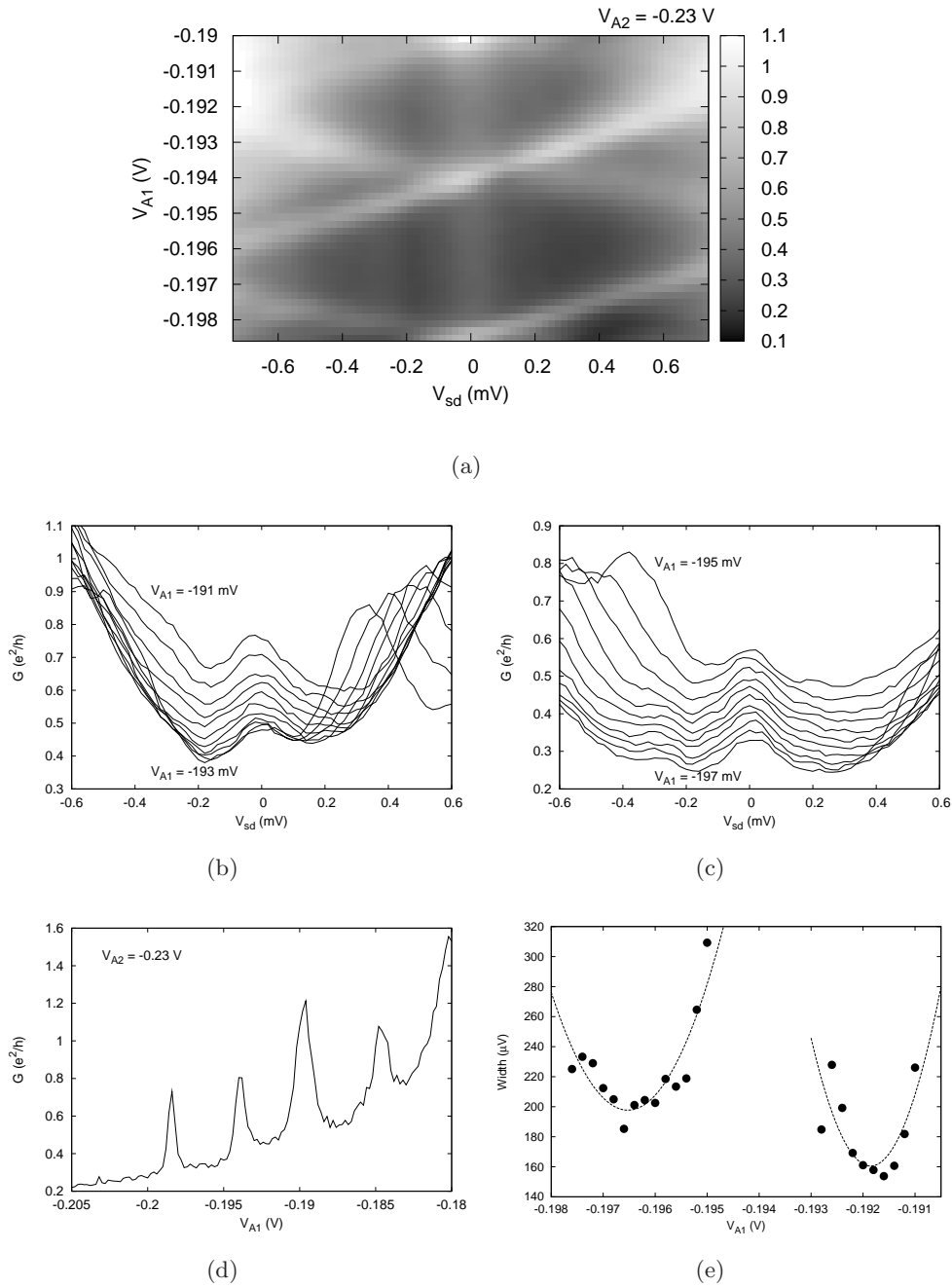


Figure 7.20.: At  $V_{A2} = -230$  mV, (a) Grey-scale plot of differential conductance  $G \equiv dI/dV_{sd}$  as a function of  $V_{A1}$  and  $V_{sd}$  shows the Kondo resonance peak in both top and bottom Coulomb diamonds. (b) and (c) Line plot of  $G$  in respective top and bottom Coulomb diamonds as a function of  $V_{sd}$ . The curves are offset with  $0.02e^2/h$  for clarity. (d) Plot of Coulomb oscillation in  $G$  versus  $V_{A1}$  with DC-offset correction of  $\sim -40 \mu\text{V}$ . (e) The Kondo peak width extracted from fitting to data in (b) and (c).

7.5. Kondo Effect in a Quantum Point Contact coupled with a Single Quantum dot

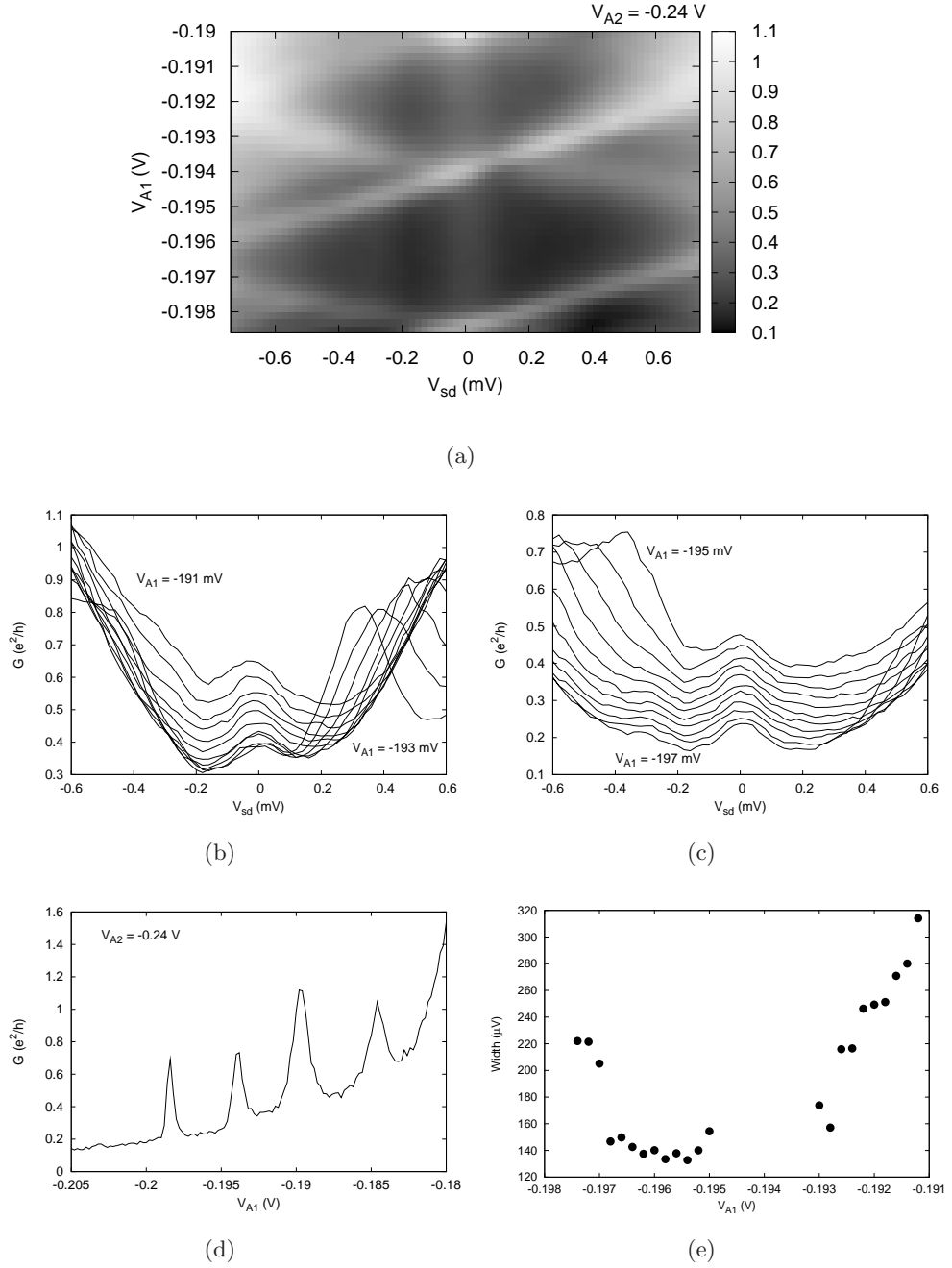


Figure 7.21.: At  $V_{A2} = -240$  mV, (a) Grey-scale plot of differential conductance  $G \equiv dI/dV_{sd}$  as a function of  $V_{A1}$  and  $V_{sd}$  shows the Kondo resonance peak in both top and bottom Coulomb diamonds. (b) and (c) Line plot of  $G$  in respective top and bottom Coulomb diamonds as a function of  $V_{sd}$ . The curves is offset with  $0.02e^2/h$  for clarity. (d) Plot of Coulomb oscillation in  $G$  versus  $V_{A1}$  with DC-offset correction of  $\sim -40 \mu$ V. (e) The Kondo peak width extracted from fitting to data in (b) and (c).

## 7. Kondo Physics in a Single Quantum dot

of  $\sim -40 \mu\text{V}$ , the line shape of Kondo peaks shows that they all are at a zero bias which is the middle of both diamonds. The Kondo temperature  $T_K$  estimated from the width of Kondo conductance peak is between  $\sim 1.8 \text{ K}$  and  $\sim 3.7 \text{ K}$  for the resonance in the top Coulomb diamond, and is between  $\sim 1.5 \text{ K}$  and  $\sim 2.5 \text{ K}$  for the resonance in the bottom Coulomb diamond. It is found that only the Kondo temperature in bottom diamond has a parabolic dependence which corresponds to the Kondo valley at  $-198 \text{ mV} \lesssim V_{A1} \lesssim -194 \text{ mV}$ . All extracted capacitances of a quantum dot and coupling factor  $\alpha$  are the same as those extracted for  $V_{A2} = -0.23 \text{ V}$ . This can be explained that the coupling of the unexpected quantum dot to the leads or reservoirs is not changed significantly, but the Kondo temperature is changed when  $V_{A2}$  is varied within the short range of  $10 \text{ mV}$ . The Kondo resonance might be sensitive to a small change of the coupling between a localized electron spin in the dot and electrons in the reservoirs. However, the Kondo temperature values between two conditions of  $V_{A2}$  for both top and bottom diamonds are still in the same order and are not too much different.

### 7.5.1. Temperature dependence

We measure the differential conductance  $G$  versus the DC bias voltage  $V_{sd}$  for different temperatures, at fixed  $V_{A1}$  and  $V_{A2}$ . Figure 7.22(a) shows the temperature dependence of the Kondo peak in the middle of both Kondo valleys in Fig. 7.20(d),  $V_{A1} = -192$  and  $-196 \text{ mV}$ , for fixed value of  $V_{A2} = -230 \text{ mV}$ . For  $V_{A2} = -240 \text{ mV}$ , the temperature dependence of Kondo conductance peak at the same position in  $V_{A1}$  is also shown in Fig. 7.22(b). The base temperature is about  $60 \text{ mK}$  for both conditions of gate voltage. When the temperature  $T$  increases, the Kondo peak in each regions broadens and the peak height decreases. The Kondo peak disappears at high temperatures.

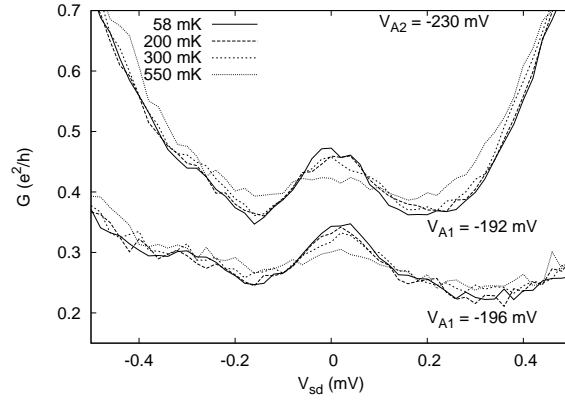
The Kondo peaks in both figures are fitted, and the width and maximum conductance of the peak can be extracted, as shown in Fig. 7.23(a) to (d). The Kondo temperature  $T_K$  can be estimated from the width of Kondo peak at base temperature by using the relationship between FWHM and  $T_K$  in Eq. 7.1. Another method to find the Kondo temperature is to use the empirical function of Eq. 7.2 fitting to the data of maximum conductance at the top of the Kondo peak. The figures of the conductance  $G$  data show the good fitting with empirical function using the fitting parameter  $s \simeq 0.2$ .

At  $V_{A2} = -230 \text{ mV}$ , the Kondo temperature  $T_K$  estimated from the peak width at base temperature shown in the left figure of 7.23(a) and 7.23(b) is  $\sim 2 \text{ K}$  at  $V_{A1} = -192 \text{ mV}$  (in the top Coulomb diamond) and  $\sim 2.7 \text{ K}$  at  $V_{A1} = -196 \text{ mV}$  (in the bottom Coulomb diamond). The Kondo temperature extracted from the good fitting in the right figure of 7.23(a) and 7.23(b) for both values of  $V_{A1}$  is approximately  $3 \text{ K}$ , which is comparable to that extracted from the Kondo line width at  $V_{A1} = -196 \text{ mV}$ .

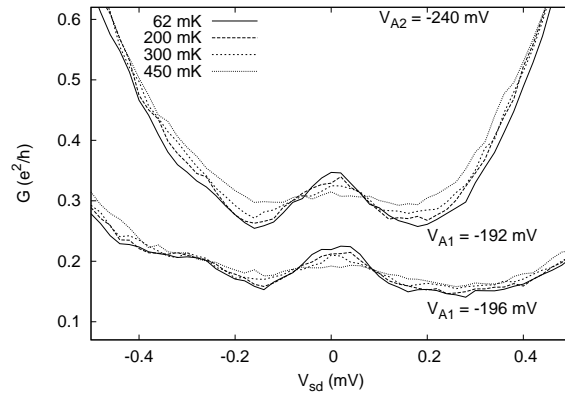
At  $V_{A2} = -240 \text{ mV}$ , the Kondo temperature  $T_K$  estimated from the peak width at base temperature shown in the left figure of 7.23(c) and 7.23(d) is  $\sim 2 \text{ K}$  for both  $V_{A1} = -192 \text{ mV}$  (in the top Coulomb diamond) and  $V_{A1} = -196 \text{ mV}$  (in the bottom Coulomb diamond). The Kondo temperature extracted from the good fitting in the right figure of 7.23(c) and 7.23(d) is  $\sim 2.3 \text{ K}$  at  $V_{A1} = -192 \text{ mV}$  and  $\sim 1.8 \text{ K}$  at  $V_{A1} = -196 \text{ mV}$ , respectively.

For all conditions of gate voltages,  $V_{A1}$  and  $V_{A2}$ , the width of Kondo peak increases linearly with higher temperature. It can be seen that the Kondo temperature  $T_K$  extracted from fitting with empirical function is a bit higher than that estimated from the width of Kondo peak at base temperature. However, they are comparable, especially at  $V_{A2} = -240 \text{ mV}$  in which  $T_K$  is obtained around  $2 \text{ K}$  in both methods. From the temperature dependence of Kondo resonance peak at two different values of  $V_{A2}$ , there is no significant difference in the physics between these two conditions of  $V_{A2}$ . Therefore we measure the conductance as a function of gate voltage  $V_{A1}$  at different temperatures only for  $V_{A2} = -230 \text{ mV}$ .

## 7.5. Kondo Effect in a Quantum Point Contact coupled with a Single Quantum dot



(a)



(b)

Figure 7.22.: Differential conductance versus  $V_{sd}$  for different temperature, at (a)  $V_{A2} = -230$  mV and (b)  $-240$  mV. The data is already corrected for the DC-offset. The gate voltage  $V_{A1}$  is set at  $-192$  and  $-196$  mV in the middle of both Kondo valleys as shown in Fig. 7.20(d) and 7.21(d).

Figure 7.24(a) shows that the conductance  $G$  versus the gate voltage  $V_{A1}$  at different temperatures. The gate voltage  $V_{A2}$  is set at  $-230$  mV, and this Coulomb oscillation is corrected for the DC-offset of  $\sim -40$   $\mu$ V. The Coulomb conductance peak is also broadened and the peak height decreases with increasing temperature. The Coulomb peak spacing  $\Delta V_{A1}$  is approximately 4.7 mV, and six conductance valleys are shown in this figure. When the temperature is increased, the conductance in the three valleys on the left hand side decreases, whereas the conductance in the next two valleys increases. The valleys around  $V_{A1} = -198$  and  $-195$  mV, and  $V_{A1} = -194$  and  $190$  mV, in which the conductance decreases with increasing  $T$ , corresponds to the Coulomb diamond region in which the Kondo resonance peak appears in Fig. 7.20(a). Hence these valleys between Coulomb peaks may be regarded as Kondo valleys.

The conductance in the center of the valleys,  $V_{A1} = -192$  and  $-196$  mV, has a logarithmic temperature dependence, as shown in Fig. 7.24(b) and (c) respectively. The fitting with empirical function in Eq. 7.2 to the data shows a good agreement with the theory. The fitting parameter is set to  $s = 0.2$ , and then the Kondo temperature  $T_K$  can be extracted as  $T_K \simeq 4$  K for  $V_{A1} = -192$  mV and  $T_K \simeq 3.2$  K for  $V_{A1} = -196$  mV. The Kondo temperature within two Kondo valleys has been shown in Fig. 7.24(d). This also shows the parabolic dependence of  $T_K$  in both valleys. We also see clearly that the Kondo temperature  $T_K$  increases when moving

## 7. Kondo Physics in a Single Quantum dot

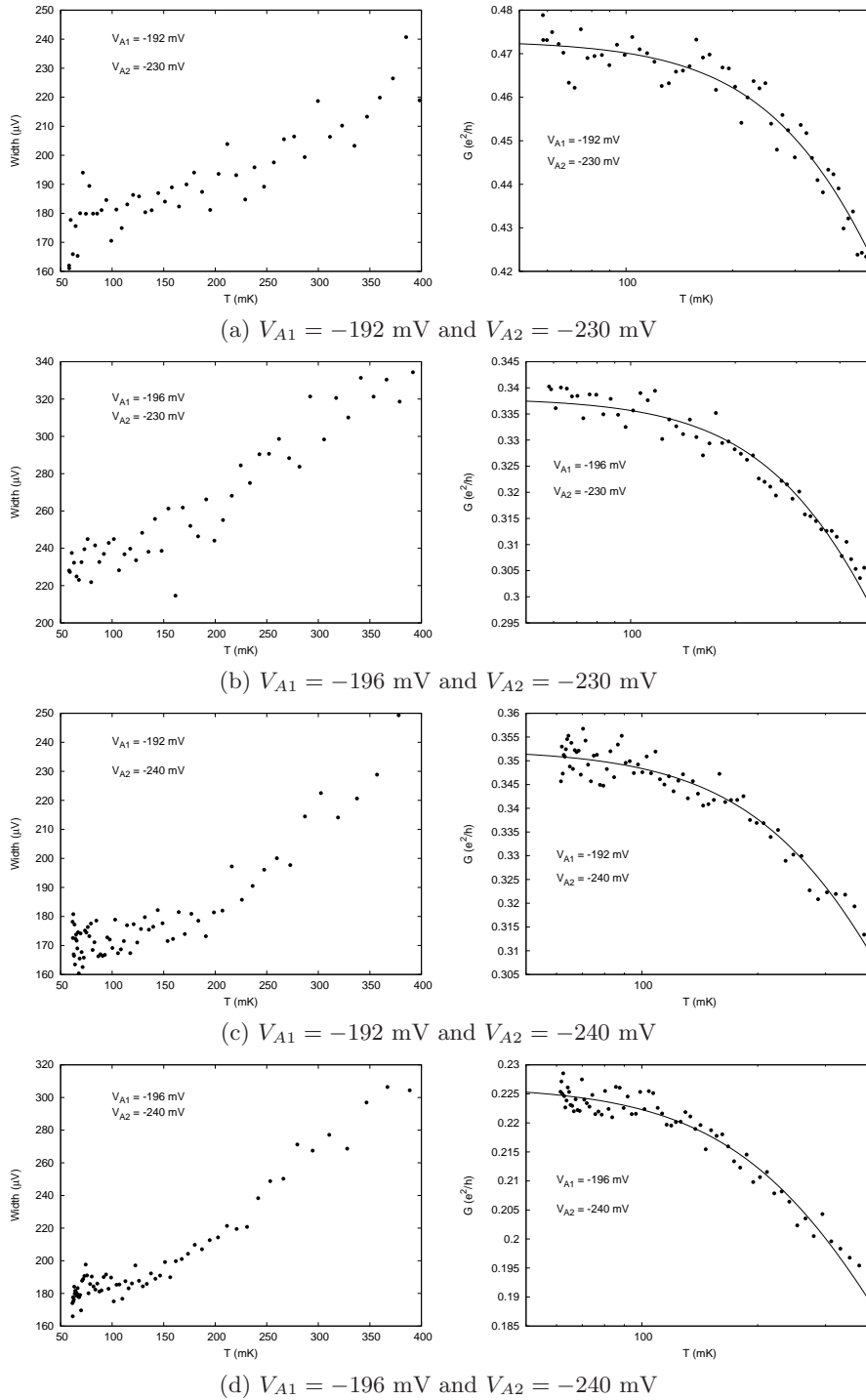


Figure 7.23.: (a)-(d) (Left) Temperature dependence of Kondo peak width at setting  $V_{A1}$  and  $V_{A2}$ . (Right) The peak maximum is logarithmic in temperature  $T$ . The curve is the fit to Eq. 7.2 with  $s \simeq 0.2$  in order to extract the Kondo temperature  $T_K$ .



7.5. Kondo Effect in a Quantum Point Contact coupled with a Single Quantum dot

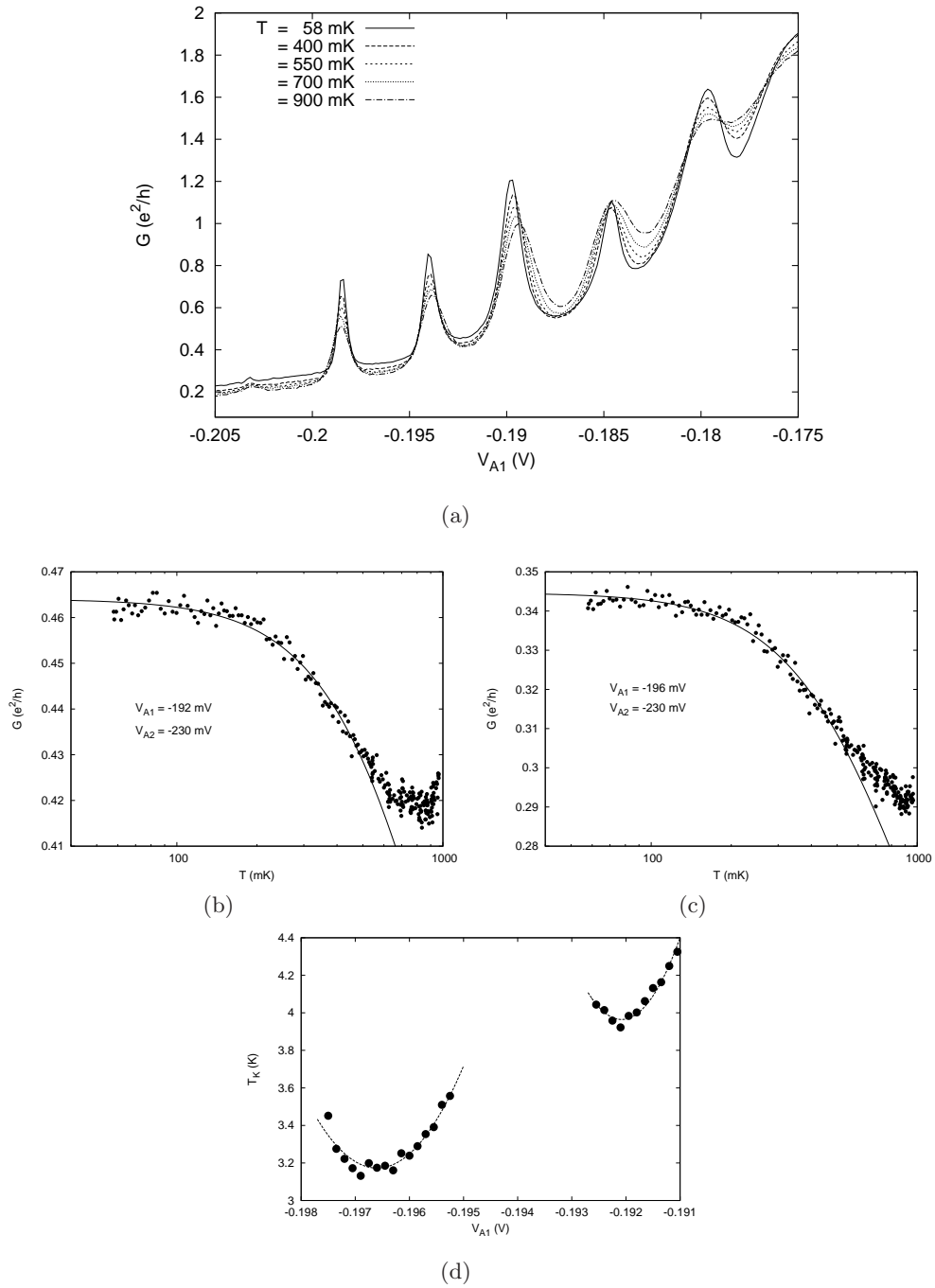


Figure 7.24.: (a) Coulomb oscillation in differential conductance at  $V_{A2} = -230$  mV for  $T$  ranging from 58 to 900 mK. (b) and (c) Logarithmic temperature dependence of Kondo peak maximum at the middle of two different Kondo valleys as indicated by  $V_{A1}$ . The curve shows a good quality of fitting with Eq. 7.2 where  $s = 0.2$ . (d) Calculated  $T_K$  at different  $V_{A1}$  along two Kondo valleys in (a)

## 7. Kondo Physics in a Single Quantum dot

close to the Coulomb peak. This corresponds to an increasing width of the Kondo peak when the separation between the localized state and the electrochemical potential in the reservoir is reduced by the influence of gate voltage  $V_{A1}$ . Furthermore, the  $T_K$  value from this method is higher than that estimated from the Kondo peak width.

## 8. Electron transport in Double Quantum Dots

### 8.1. Characterization of the Double Dot System

For the sample **PR1:d2**, the SEM micrograph and the schematic drawing of the structure of double dot system coupled in series has been shown above in Fig. 6.1. At the base temperature of  $\sim 65$  mK, we use gate B2 as an optional lower gate to define a quantum point contact with gate A1. The sequence of conductance peaks of the double dot (dotI-dotII) system shown in Fig. 8.1 is obtained by applying  $V_{A1} = V_{gateA} = -500$  mV,  $V_{C1C2} = V_{gateC} = -534$  mV,  $V_{E1E2} = V_{gateE} = -435$  mV, and  $V_{B2} = -1.3$  V. The center gate B1, D1 and D2 are connected and applied with a negative voltage  $V_g$  as in the figure below. The observed peak sequence looks like the Coulomb blockade oscillations obtained for a single dot.

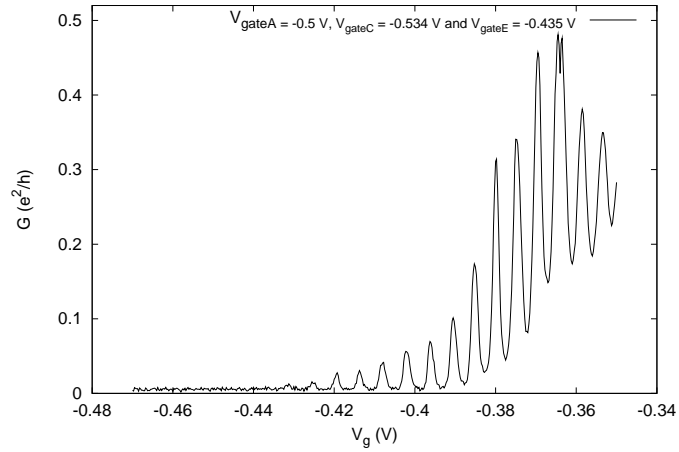


Figure 8.1.: Differential conductance of the double dots (dotI-dotII) system coupled in series in the sample **PR1:d2** as a function of  $V_g \equiv V_{B1D1D2}$ . The  $V_{B2}$  is fixed at -1.3 V.

To characterize the dotI-dotII system of the sample, the center gate B1 and gates D1D2 are varied independently and the conductance is observed as shown in Fig. 8.2. The  $V_{C1C2}$ , corresponding to the coupling between the dots, is varied from -534 to -555 mV to reduce the coupling as shown in Fig. 8.2(a)-(d). The pattern in all figures is similar but the voltage gap seems to be a little bit different. However, the pattern of charge stability diagram for double dot systems known as the honeycomb diagram does not appear, only straight a line pattern can be observed instead. It is inferred that the observed charging diagrams belong to a single dot, and that the double dot system is still not yet formed.

In order to form the double quantum dot system, we try to make the system more symmetric by connecting and applying the negative voltage to gate B2 and D2 together. Figure 8.3 (a) and (b) show the coulomb oscillation of dotI and dotII respectively when gates B2 and D2 are connected and applied with the voltage of -1.3 V. In both dot structures, the oscillations begin appearing in this range of gate voltage when the gates C1 and C2 are energized with -470 mV. For the dotII structure the oscillations are most pronounced at  $V_{C1C2} = -475$  mV. At  $V_{C1C2} = -480$  mV the gate voltage gap,  $\Delta V_g$ , is approximately 12.5 mV for the dotI and 9.6

## 8. Electron transport in Double Quantum Dots

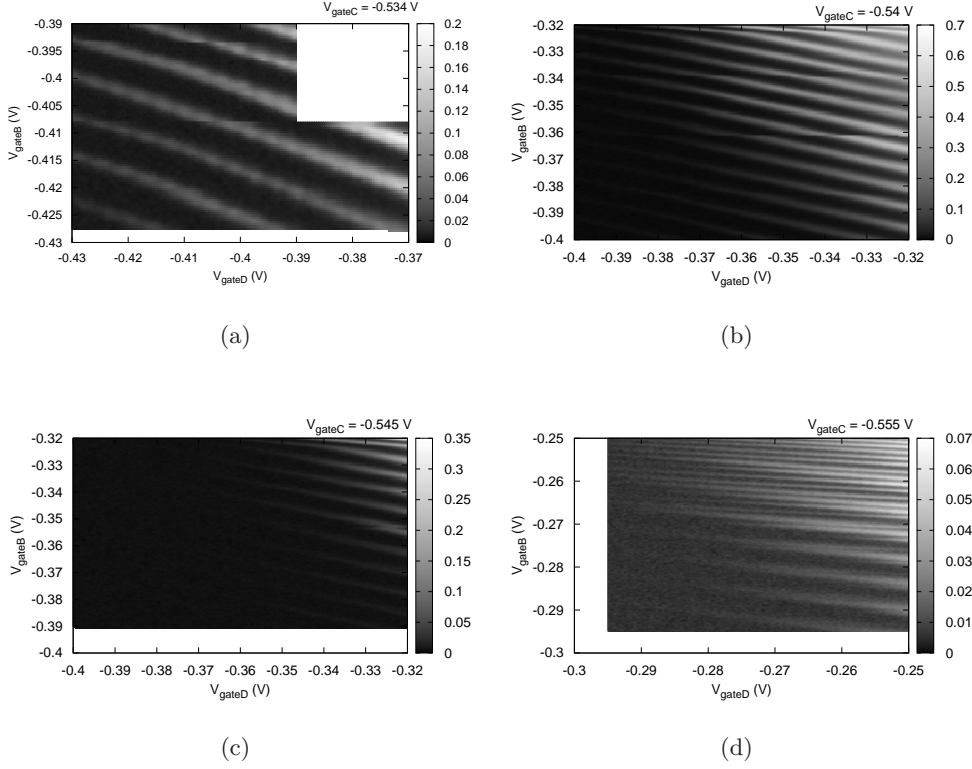


Figure 8.2.: Double dot (dotI-dotII) conductance as a function of  $V_{B1} = V_{gateB}$  and  $V_{D1D2} = V_{gateD}$ . The  $V_{C1C2}$  is varied from (a) -0.534 V to (d) -0.555 V. Each figure,  $V_{A1}$  and  $V_{E1E2}$  are fixed at -0.5 V and -0.435 V, respectively.

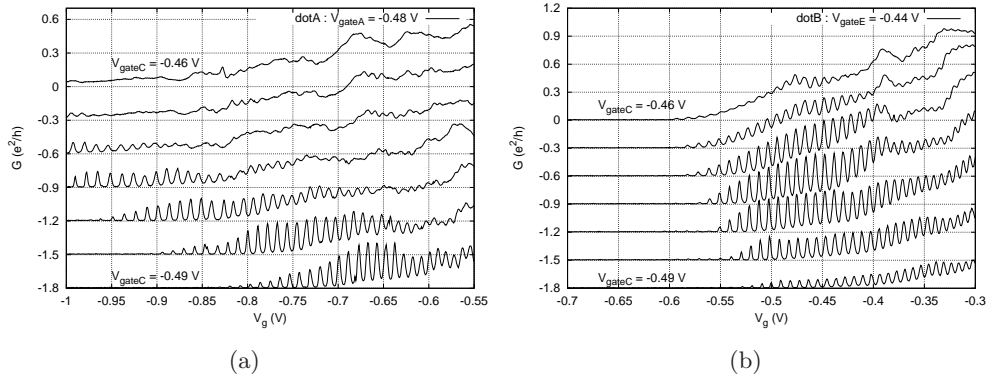


Figure 8.3.: Conductance of (a) dotI and (b) dotII as a function of their own center gate voltage  $V_g$ . The  $V_{A1} \equiv V_{gateA} = -0.48$  V for dotI, whereas  $V_{E1E2} \equiv V_{gateE} = -0.44$  V for dotII. For each dot,  $V_{C1C2} \equiv V_{gateC}$  is varied from -0.47 to -0.49 V. The gate B2 and D2 are tied together, and fixed at -1.3 V. The curves have been offset with  $0.3(e^2/h)$  for clarity.

mV for the dotII. This means that the gate capacitance,  $C_g$ , of the dotII is greater than that of the dotI in this sample. We can obtain the coulomb peaks in the range of  $-1 \text{ V} < V_g < -0.6 \text{ V}$  for the dotI and  $-0.6 \text{ V} < V_g < -0.3 \text{ V}$  for the dotII structure.

Therefore we energized every gate except gate A2 and swept the gates B1 and D1 together with gates B2 and D2 connected. The conductance peaks for the double dots are obtained and shown in Fig. 8.4. The gate C1C2 is varied from  $-470 \text{ mV}$  to  $-490 \text{ mV}$ , and the gates A1 and E1E2 have been tuned to find some evidence of double dot peaks. The gate A1 is then varied from  $-460 \text{ mV}$  to  $-480 \text{ mV}$ , and the gate E1E2 is also varied from  $-430 \text{ mV}$  to  $-445 \text{ mV}$ . The modulation of the conductance peaks, which is quite different from the oscillation of the single dot, can be obtained clearly with the gate E1E2 voltage of  $-435 \text{ mV}$  and  $-440 \text{ mV}$ . When the E1E2 gate voltage decreases to  $-445 \text{ mV}$ , the conductance modulation is not well-defined. At the fixed voltage value of gate A1 and E1E2, the amplitude of the conductance peaks decrease and the oscillations start disappearing when the voltage of the gate C1C2 decreases. The voltage conditions for gate A1 and E1E2 in Fig. 8.4(k) have been selected to perform the measurement for investigating the stability phase diagram of the double quantum dots.

Figure 8.5 shows the stability diagrams of the double quantum dots, dotI-dotII. The bright regions represent high conductance and the dark regions represent low conductance or no electron transport through the double dots. When the gate C1C2 voltage increases, the coupling between dots increases and the stability pattern evolves from the array of the conductance peaks in the weakly coupling regime, as shown in Fig. 8.5(a), to honeycomb pattern in the strongly coupling regime, as shown in Fig. 8.5(d). In the dark region for each cell the configuration of electrons in the dots,  $(n_1, n_2)$ , is constant. If we keep increasing the  $V_{C1C2}$ , the coupling between dots will increase and change the double dots to a large single dot. A pattern of straight lines will begin appearing in the stability diagram as shown in Fig. 8.5(f).

After a new cooling process<sup>1</sup>, the same measurements were repeated to investigate the stability phase diagram of this double dot system. Figure 8.6(a)-(i) shows the series of figures of the measured double dot conductance versus gate voltages  $V_{D1}$  and  $V_{B1}$  for the voltage of gate C1C2 increasing from  $-488 \text{ mV}$  to  $-455 \text{ mV}$ . The coupling between two dots increases from 8.6(a) to (i) by increasing the gate voltage  $V_{C1C2}$ . The evolution of the stability diagrams of the double dots can be observed clearly. The Coulomb blockade for the double dot system evolves from weakly coupled dots in Fig. 8.6(a) to a single large dot in Fig. 8.6(i). For weak coupling, the array of bright points indicating the conductance peaks has been predicted by Coulomb blockade theory for coupled dots as described in the section 2.4.1. Conductance through double dots in series occurs only when the number of electrons in both dots,  $n_1$  and  $n_2$  can change simultaneously, at the intersections of three stable charge configuration  $(n_1, n_2)$  regions and are known as the triple points.

In Fig. 8.6(a) and (b) the two neighboring triple points are not separately resolved. We see only that a pair of triple points is merged into one large bright point. This can be explained since there is a very small splitting of the conductance in the weak coupling regime. As shown in Fig. 8.6(a), there is no conductance boundary linking the bright points, but it occurs as the interdot coupling increases.

For stronger interdot coupling in Fig. 8.6(c) to (i), the pattern of stability diagram changes to hexagon or honeycomb pattern and is no longer described by the Coulomb blockade theory of individual dots. The quantum dot molecule regime is reached as the interdot coupling is increased. More interdot coupling corresponding to an increase of the interdot gate voltage leads to more splitting of the conductance at a pair of triple points as is shown. In this regime the electronic states are delocalized between the dots and electrons are shared by both dots. The

<sup>1</sup>In this process, the system was cooled down after the last process was stopped for two week. The base temperature was obtained at  $\sim 65 \text{ mK}$ , which is approximately the same as the cooling process before.

## 8. Electron transport in Double Quantum Dots

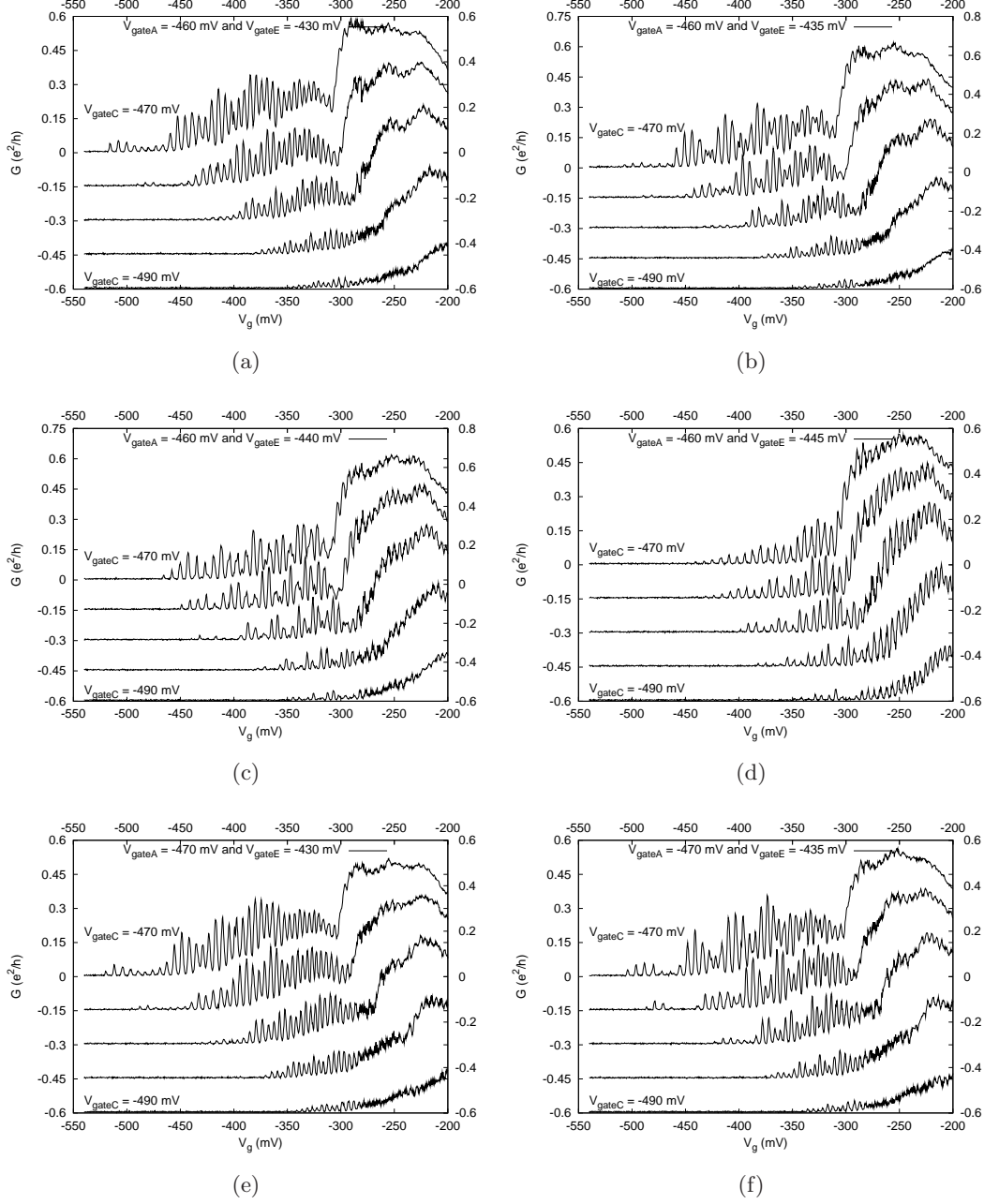


Figure 8.4.: Double dot conductance as a function of  $V_g \equiv V_{B1D1}$ . For (a) to (d),  $V_{A1} \equiv V_{gateA}$  is set at -460 mV. For (e) to (f),  $V_{A1}$  is set at -470 mV. The  $V_{C1C2} \equiv V_{gateC}$  is varied from -470 to -490 mV, and  $V_{E1E2} \equiv V_{gateE}$  is varied from -430 to -445 mV. The  $V_{B2D2}$  is fixed at -1.3 V.

## 8.1. Characterization of the Double Dot System

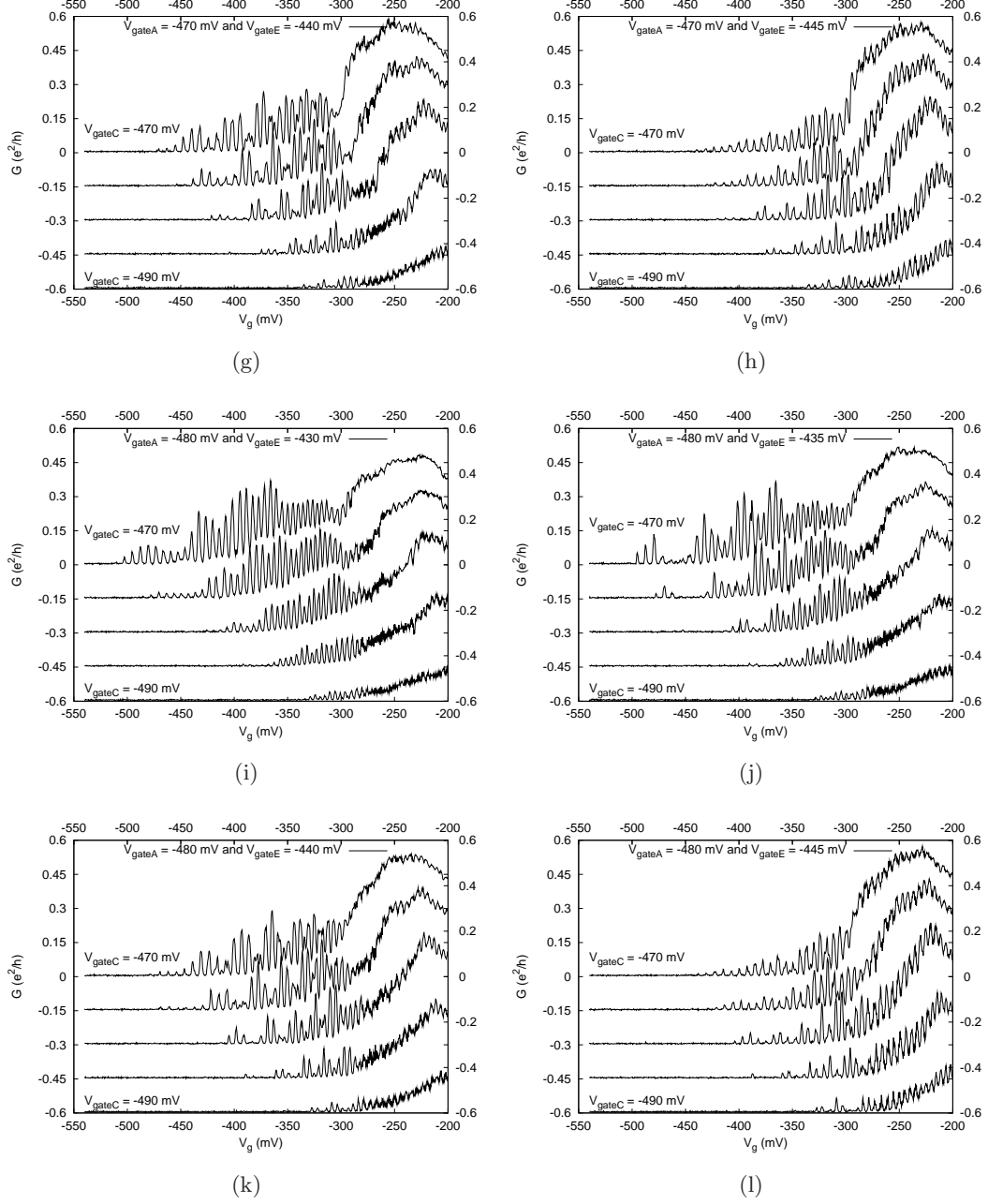


Figure 8.4.: (cont.) Double dot conductance as a function of  $V_g \equiv V_{B1D1}$ . For (g) to (h),  $V_{A1} \equiv V_{gateA}$  is set at -470 mV. For (i) to (l),  $V_{A1}$  is set at -480 mV. The  $V_{C1C2} \equiv V_{gateC}$  is varied from -470 to -490 mV, and  $V_{E1E2} \equiv V_{gateE}$  is varied from -430 to -445 mV. The  $V_{B2D2}$  is fixed at -1.3 V.

## 8. Electron transport in Double Quantum Dots

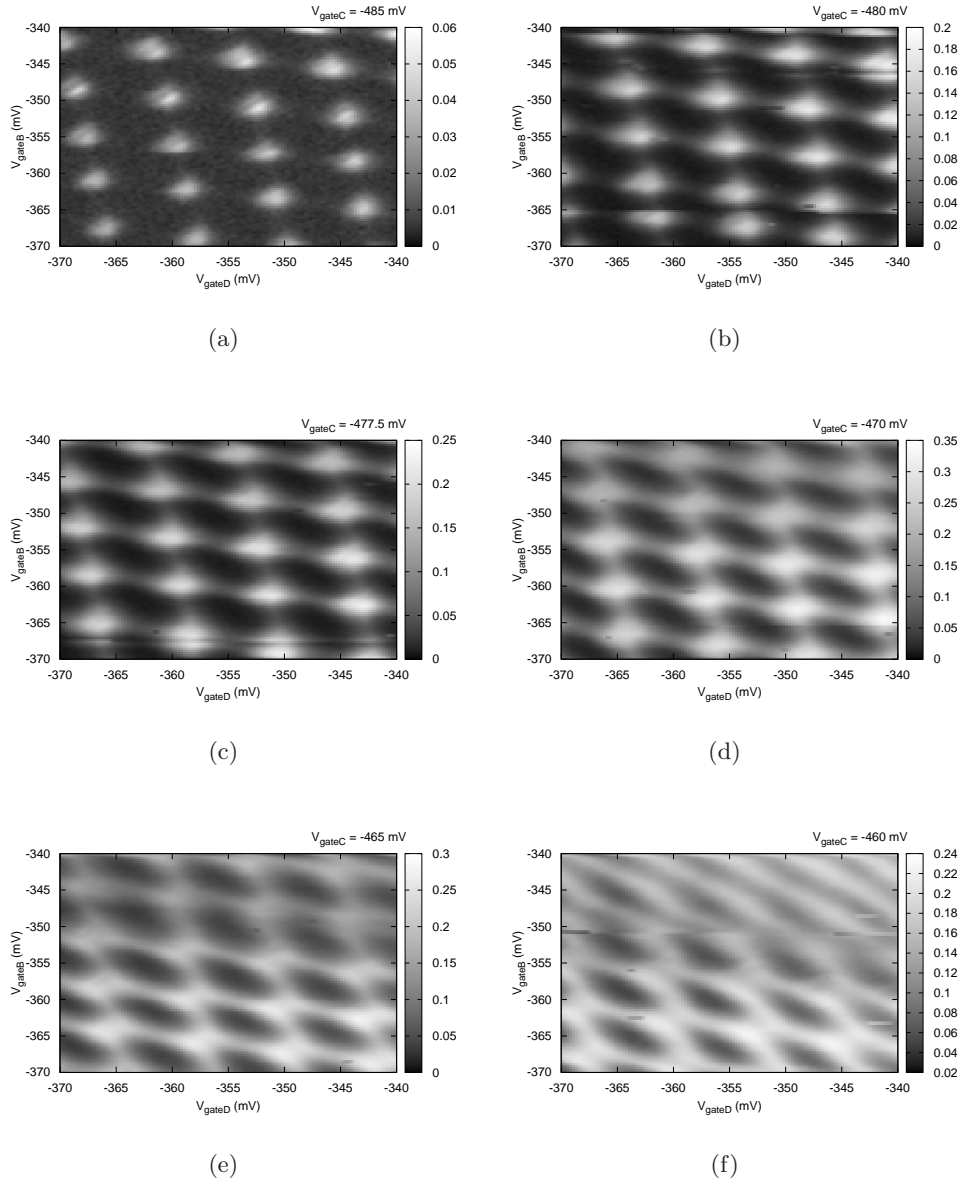


Figure 8.5.: Charge stability diagram of dotI-dotII system at  $V_{A1} \equiv V_{gateA} = -480$  mV and  $V_{E1E2} \equiv V_{gateE} = -440$  mV. Conductance is measured as a function of  $V_{B1} \equiv V_{gateB}$  and  $V_{D1} \equiv V_{gateD}$ . The  $V_{C1C2} \equiv V_{gateC}$  is varied from (a) -485 to (f) -460 mV, and  $V_{B2D2}$  is always fixed at -1.3 V.



## 8.1. Characterization of the Double Dot System

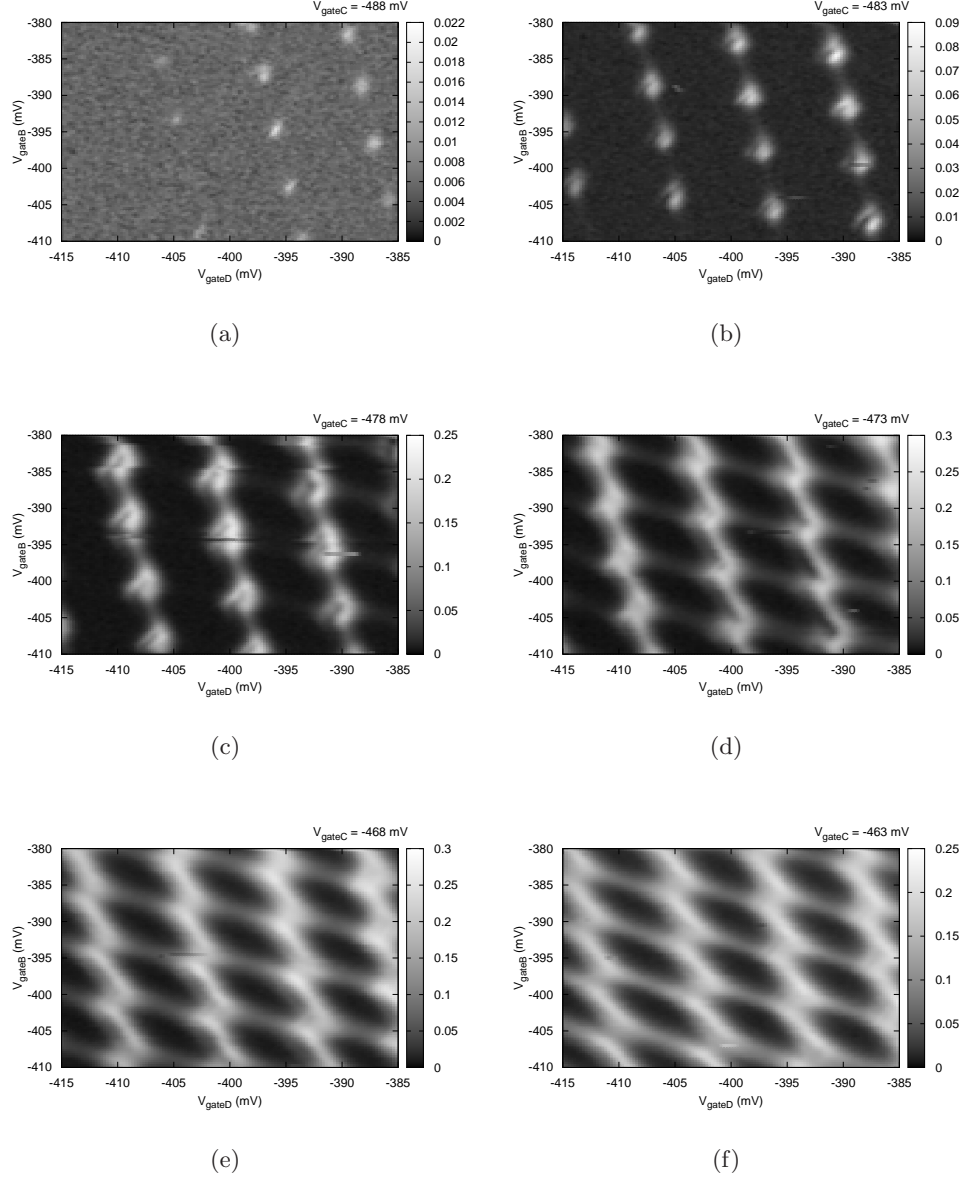


Figure 8.6.: Charge stability diagram of double dot system at  $V_{A1} \equiv V_{gateA} = -480$  mV and  $V_{E1E2} \equiv V_{gateE} = -440$  mV. Conductance is measured as a function of  $V_{B1} \equiv V_{gateB}$  and  $V_{D1} \equiv V_{gateD}$ . The  $V_{C1C2} \equiv V_{gateC}$  is varied from (a) -488 to (f) -463 mV, and  $V_{B2D2}$  is always fixed at -1.3 V.

## 8. Electron transport in Double Quantum Dots

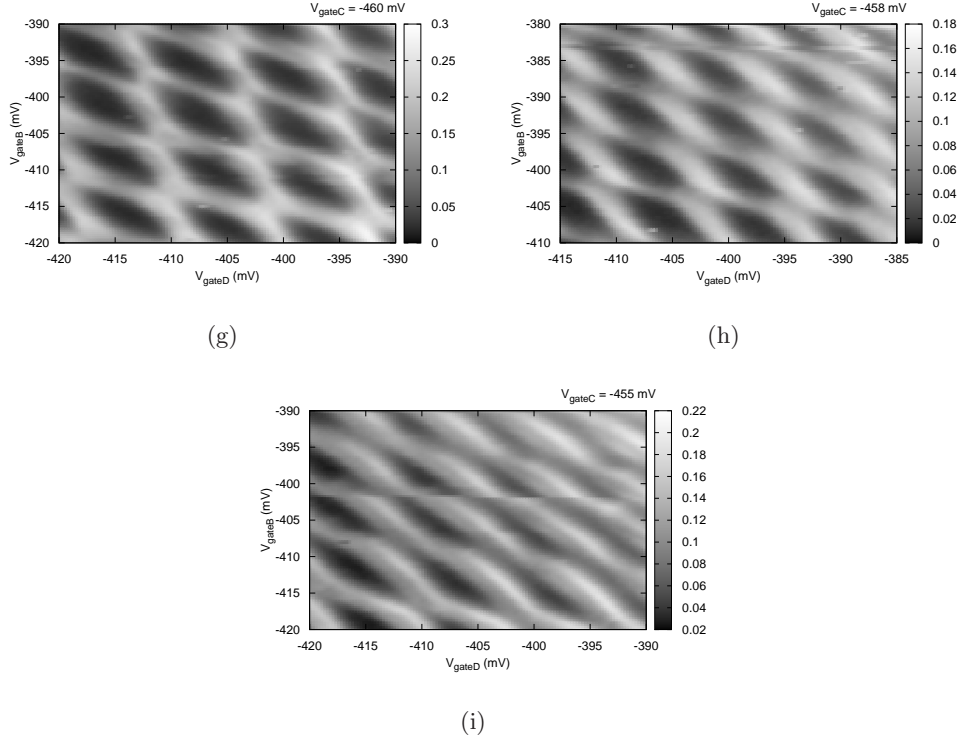


Figure 8.6.: (cont.) Charge stability diagram of double dot system at  $V_{A1} \equiv V_{gateA} = -480$  mV and  $V_{E1E2} \equiv V_{gateE} = -440$  mV. Conductance is measured as a function of  $V_{B1} \equiv V_{gateB}$  and  $V_{D1} \equiv V_{gateD}$ . The  $V_{C1C2} \equiv V_{gateC}$  is varied from (g) -460 to (i) -455 mV, and  $V_{B2D2}$  is always fixed at -1.3 V.

conductance boundary line of hexagons or honeycomb cells becomes more pronounced. This can be understood since the coupling not only between the dots but also between the dots and the leads is increased by some influence from increasing gate voltage  $V_{C1C2}$ .

The pattern is tilted and compressed along the diagonal because of the cross capacitance between each center gate and the opposite dot. In Fig. 8.6(i) the conductance pattern, especially in the range of high value of gate voltage  $V_{D1}$  and  $V_{B1}$ , becomes an array of lines corresponding to the Coulomb blockade for a single large dot. These lines separate regions defined by integer value of the total double dot charge  $n_{tot} = n_1 + n_2$ . In this case the system becomes a single Coulomb blockaded quantum dot.

According to the coupled dots in series model discussed in the theoretical background chapter, the cross capacitance is neglected when determining the double dot electrostatic energy  $U$ . However, it can be seen that the honeycomb pattern in Fig. 8.6(d) to (g) is compressed and the alignment of triple points is tilted in the direction of both center gate voltages due to the influence of the cross capacitance. Therefore the cross capacitance cannot be neglected, and has to be included to determine the total electrostatic energy. For the linear transport regime, the charge defined in Eq. 2.56 can be modified according to

$$\vec{Q} = \begin{pmatrix} Q_{dII} + C_{D1}V_{D1} + C_{B1dII}V_{B1} \\ Q_{dI} + C_{B1}V_{B1} + C_{D1dI}V_{D1} \end{pmatrix}, \quad (8.1)$$

where  $Q_{dI(II)}$  is the total charge on the dotI(II),  $C_{B1(D1)dII(I)}$  is the cross capacitance between gate B1(D1) to dotII(I),  $C_{B1(D1)}$  is the capacitance of gate B1(D1), and  $V_{B1(D1)}$  is the voltage

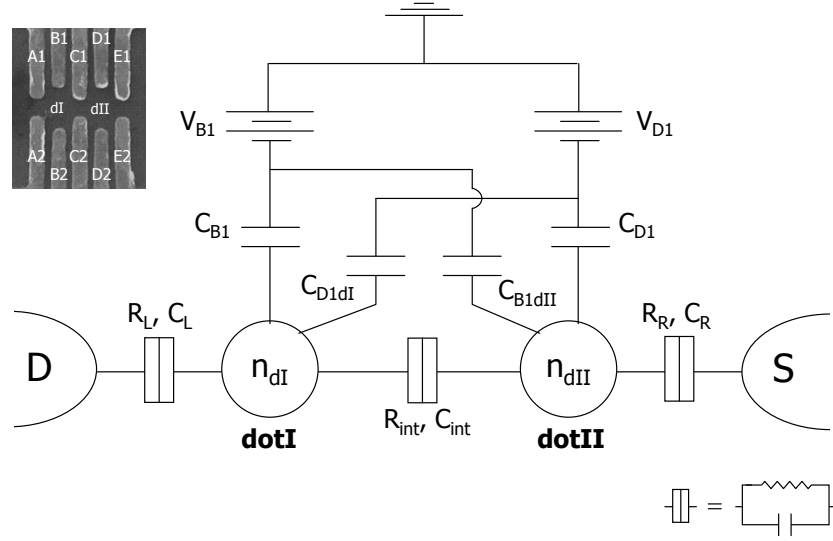


Figure 8.7.: Equivalent electronic circuit for double dot system in the sample **PR1:d2**. The cross capacitances,  $C_{D1dI}$  and  $C_{B1dII}$ , are included in this diagram.  $C_{B1(D1)}$  is the capacitance from dotI(II) to gate B1(D1),  $C_{L(R)}$  is the capacitance from dotI(II) to neighboring lead,  $C_{int}$  is the interdot capacitance, and  $V_{B1(D1)}$  is the voltage applied to the gate B1(D1). Inset: SEM micrograph of the lithographic double dot structure has been shown.

of the gate B1(D1).

We put the charge above back into Eq. 2.55 and then obtain the total electrostatic energy for the double dot system which includes a cross capacitance term:

$$\begin{aligned}
 U &= \frac{1}{2} \vec{Q}^T \begin{pmatrix} C_{dII} & -C_{int} \\ -C_{int} & C_{dI} \end{pmatrix}^{-1} \vec{Q} \\
 &= \frac{1}{C_{dI}C_{dII} - C_{int}^2} \left( \frac{1}{2} C_{dI} A^2 + \frac{1}{2} C_{dII} B^2 + C_{int} AB \right), \quad (8.2)
 \end{aligned}$$

where

$$\begin{aligned}
 A &\equiv (-en_{dII} + C_{D1}V_{D1} + C_{B1dII}V_{B1}), \\
 B &\equiv (-en_{dI} + C_{B1}V_{B1} + C_{D1dI}V_{D1}),
 \end{aligned}$$

$n_{dI(II)}$  is the number of electrons in the dotI(II), and  $C_{dI(dII)}$  is the total capacitance of dotI(II). The equivalent electronic diagram representing the double dots structure in this sample is shown in Fig. 8.7.

Therefore,  $C_{dI} = C_L + C_{B1} + C_{int} + C_{D1dI}$  and  $C_{dII} = C_R + C_{D1} + C_{int} + C_{B1dII}$ . The cross capacitance between gate D1(B1) and dotI(II) can be calculated by

$$C_{D1dI} = \frac{e}{|\Delta V_{D1}^x|} \quad \text{and} \quad C_{B1dII} = \frac{e}{|\Delta V_{B1}^x|}, \quad (8.3)$$

where  $\Delta V_{D1(B1)}^x$  is the value of gate voltage  $V_{D1(B1)}$  identified in Fig. 8.8. The value of  $V_{D1(B1)}^x$  is at the point on the  $V_{D1(B1)}$  axis intercepting with the green (red) line, which shows the tilting along  $V_{D1(B1)}$  direction. From Fig. 8.9 we can find the relationship between the capacitance and the dimension of the honeycomb diagram. According to works of F. Hofmann et al. [43, 63], the

## 8. Electron transport in Double Quantum Dots

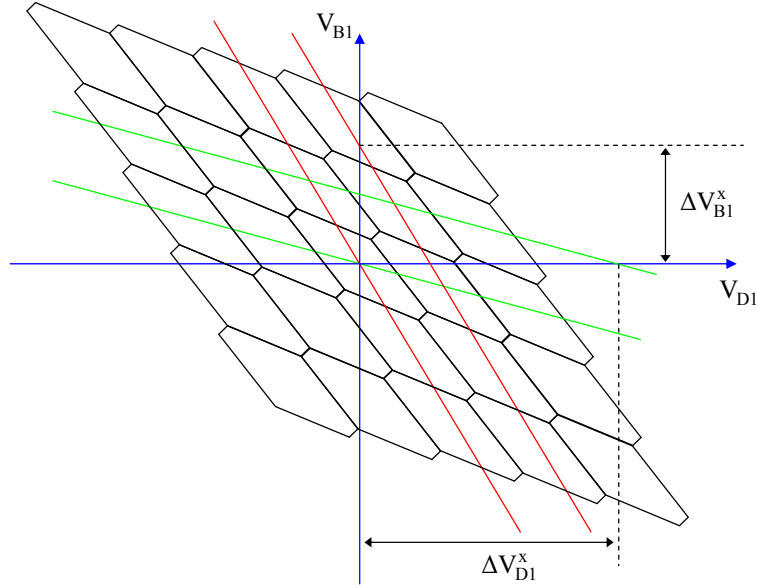


Figure 8.8.: Extracting the cross capacitance out of the honeycomb pattern in the charge stability diagram of the double dot system.

Eq. 2.72 and 2.73 are modified because of influence of the cross capacitances. The capacitance of the system can then be determined from the voltage separation in Fig. 8.9 as

$$C_{D1} = \frac{e}{\Delta V_{D1}} - C_{D1dI} \frac{\Delta V_{D1}^{int}}{\Delta V_{D1}}. \quad (8.4)$$

Similarly, we also obtain

$$C_{B1} = \frac{e}{\Delta V_{B1}} - C_{B1dII} \frac{\Delta V_{B1}^{int}}{\Delta V_{B1}}. \quad (8.5)$$

The interdot capacitance can be extracted directly from the relationship in Eq. 2.74 and 2.75 as

$$C_{int} = C_{dI} \frac{\Delta V_{D1}^{int}}{\Delta V_{D1}} \quad \text{and} \quad C_{int} = C_{dII} \frac{\Delta V_{B1}^{int}}{\Delta V_{B1}}. \quad (8.6)$$

From the data in Fig. 8.6 with  $V_{A1} = -480$  mV and  $V_{E1E2} = -440$  mV, the cross capacitance  $C_{B1dII}$  is approximately 3 aF and  $C_{D1dI}$  is approximately 5 aF. Figure 8.10(a) shows the value of gate capacitances at various interdot gate voltages. The capacitive coupling between gate B1(D1) and dot I(II),  $C_{B1(D1)}$ , over every interdot gate voltage is close to a constant, and then the average gate capacitance is  $23 \pm 5$  aF for  $C_{B1}$  and  $19 \pm 4$  for  $C_{D1}$ . Figure 8.10(b) shows the ratio between interdot capacitance and the total capacitance in each dot,  $C_{int}/C_{dI(II)}$ . The  $C_{int}/C_{dI(II)}$  increases with increasing interdot gate voltage. Thus, it is obvious that the interdot capacitance increases when the tunneling coupling between dots increases. Furthermore, the ratio  $C_{int}/C_{dII}$  is greater than  $C_{int}/C_{dI}$  at  $V_{C1C2} = -473$  and  $-468$  mV, whereas both ratios are approximately the same at higher interdot gate voltage.

From the non-linear measurement of Coulomb blockade oscillations, we can calculate the capacitive coupling between the dot and the lead according to Fig. 8.7 as  $C_L = 180 \pm 4$  aF for dot I and  $C_R = 140 \pm 4$  aF for dot II. Therefore, the interdot capacitance,  $C_{int}$ , can be extracted and increases from  $61 \pm 10$  aF to  $138 \pm 20$  aF with increasing interdot gate voltage from  $-473$

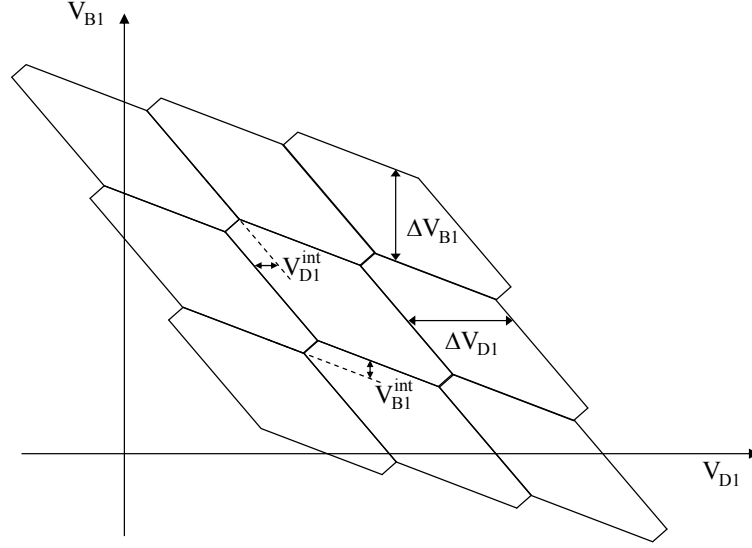


Figure 8.9.: Coulomb peak spacings in the honeycomb pattern of the charge stability diagram, which is modified from Fig. 2.21.

mV to -458 mV, as shown in Fig. 8.11(a). Figure 8.11(b) also shows that the total capacitance increases from  $268 \pm 11$  aF to  $347 \pm 21$  aF for dotI, and increases from  $223 \pm 11$  aF to  $300 \pm 21$  aF for dotII.

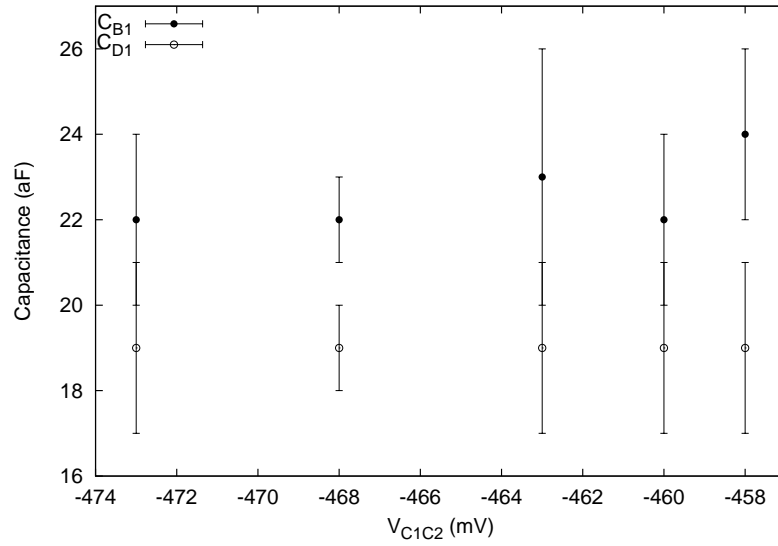
The evolution of the honeycomb pattern in Fig. 8.6 between the weak and strong tunneling coupling can also be seen in Fig. 8.12, which shows the charge stability diagram for  $V_{A1} = -520$  mV and  $V_{E1E2} = -440$  mV. The conductance at the boundary of the honeycomb cells is quite pronounced and is comparable along both directions, the gate B1 voltage and the gate D1 voltage direction. The tunneling coupling is increased with increasing interdot gate voltage,  $V_{C1C2} = -480$  mV to -460 mV, and more splitting of the triple points clearly occur. The extracted cross capacitance  $C_{B1dII}$  is approximately 3 aF, and the cross capacitance  $C_{D1dI}$  is approximately 4 aF.

From the nonlinear measurement at  $V_{C1C2} = 470$  mV, the value of  $C_L$  and  $C_R$  is estimated as  $156 \pm 4$  aF and  $141 \pm 4$  aF respectively. Therefore, we can calculate the interdot capacitance and also the total capacitance of the dot. The interdot capacitance increases from  $43 \pm 4$  aF at  $V_{C1C2} = 470$  to  $116 \pm 9$  aF at  $V_{C1C2} = -460$  mV. The average gate B1 and D1 capacitances are  $21 \pm 2$  aF and  $18 \pm 2$  aF, respectively. The total capacitance for each dot increases when the coupling between dot increases;  $C_{dI}$  increases from  $225 \pm 6$  aF to  $298 \pm 10$  aF, and  $C_{dII}$  increases from  $206 \pm 6$  aF to  $278 \pm 10$  aF. It can be seen that the total capacitance for dotI is still greater than that for dotII even though the gate voltage  $V_{A1}$  is decreased to reduce the coupling to the lead.

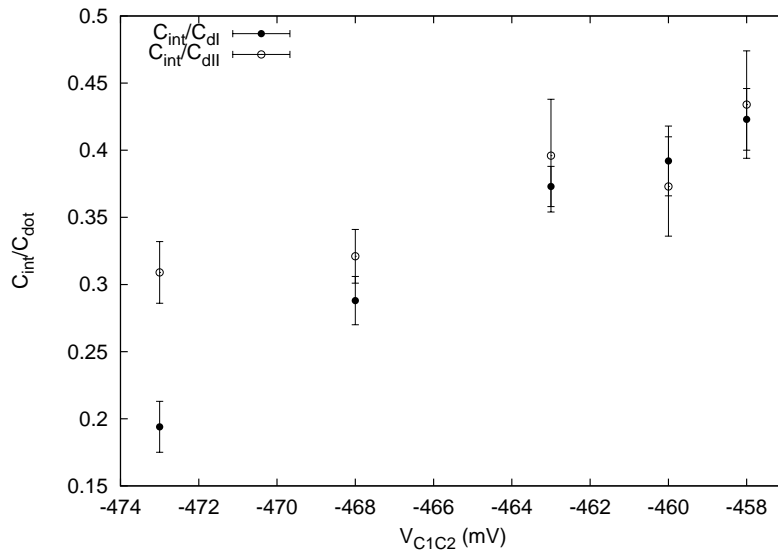
Between the two cases of extremely weak and extremely strong coupling, the observed conductance increases and extends continuously from the points in Fig. 8.6(a) and 8.12(a) along the boundaries between the charge configurations with different values of  $n_{tot}$ , as shown in Fig. 8.6(b) to (h) and 8.12(b) to (d). The shape of these boundaries changes from zigzag pattern for intermediate tunnel coupling to straight lines in Fig. 8.6(i) for extremely strong tunnel coupling regime.

Figure 8.13 shows the changing of the honeycomb pattern in the charge diagram as decreasing gate voltage  $V_{E1E2}$  and fixed interdot gate voltage  $V_{C1C2}$  at -472 mV. The honeycomb pattern in Fig. 8.13(a) changes to the pattern in Fig. 8.13(b) in which only boundaries separating different  $n_{dII}$  occur. No boundary lines separating different  $n_{dI}$  can be observed. The splitting of the

8. Electron transport in Double Quantum Dots



(a)



(b)

Figure 8.10.: (a) The gate capacitances,  $C_{B1}$  and  $C_{D1}$ , and (b) The ratio between interdot and total capacitances of dotI and dotII,  $C_{int}/C_{dI(II)}$ . Both are extracted at various interdot gate voltage  $V_{C1C2}$ . The  $V_{A1}$  and  $V_{E1E2}$  is respectively applied at -480 mV and -440 mV. The  $V_{B2D2}$  is fixed at -1.3 V.

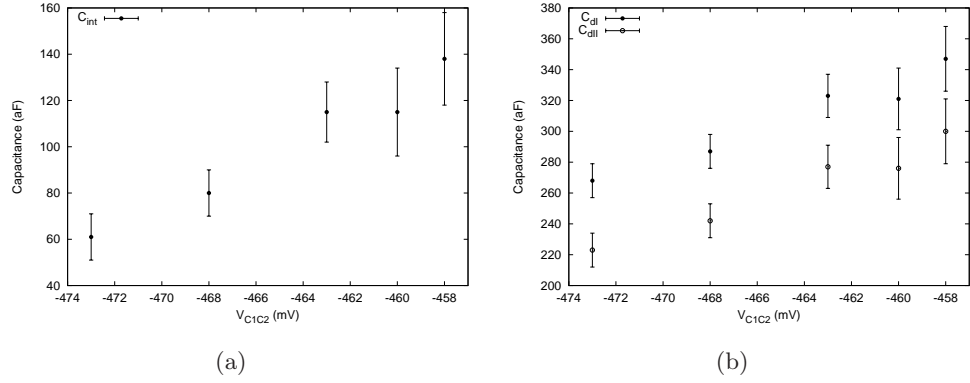


Figure 8.11.: (a) The interdot capacitances  $C_{int}$  and (b) total capacitances of dotI and dotII  $C_{dI(II)}$  are extracted at various interdot gate voltage  $V_{C1C2}$ . The  $V_{A1}$  and  $V_{E1E2}$  is applied at -480 mV and -440 mV, respectively. The  $V_{B2D2}$  is always fixed at -1.3 V.

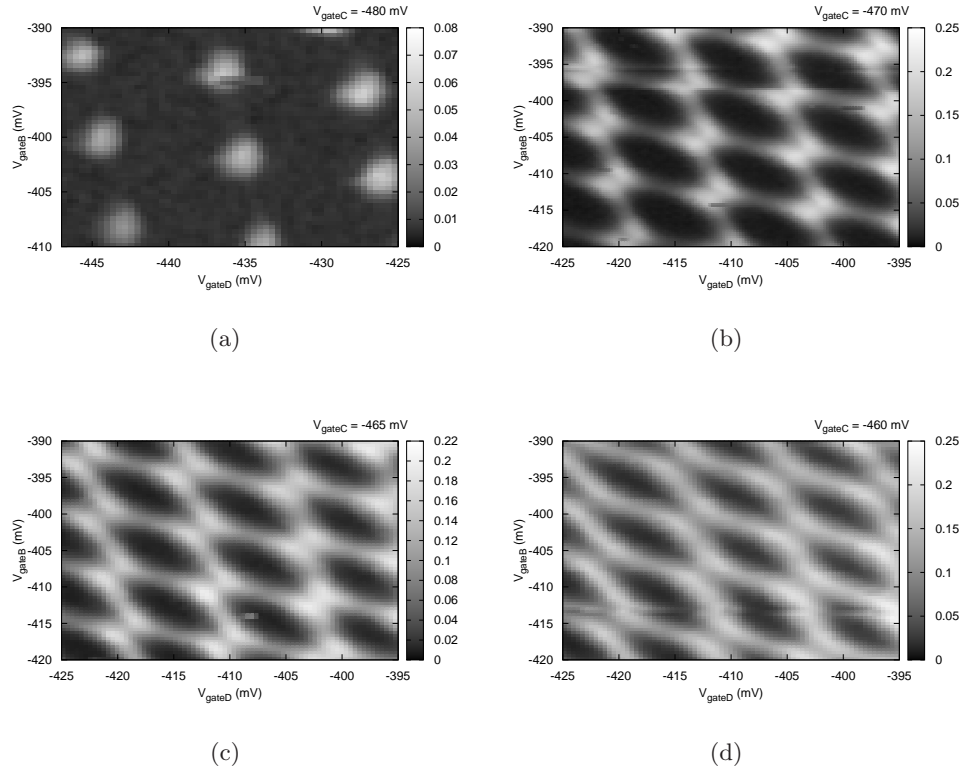


Figure 8.12.: Charge stability diagram of double dot system at  $V_{A1} \equiv V_{gateA} = -520$  mV and  $V_{E1E2} \equiv V_{gateE} = -440$  mV. The  $V_{C1C2} \equiv V_{gateC}$  is varied from (a) -480 mV to (d) -460 mV. Conductance is measured as a function of  $V_{B1} \equiv V_{gateB}$  and  $V_{D1} \equiv V_{gateD}$ . The  $V_{B2}$  is fixed at -1.3 V.

## 8. Electron transport in Double Quantum Dots

triple points however is still well defined. When  $V_{E1E2}$  is decreased, the coupling between dotII and lead is weaker, and the conductance resonances occur like the resonances in a single quantum dot of a parallel double dot system [64].

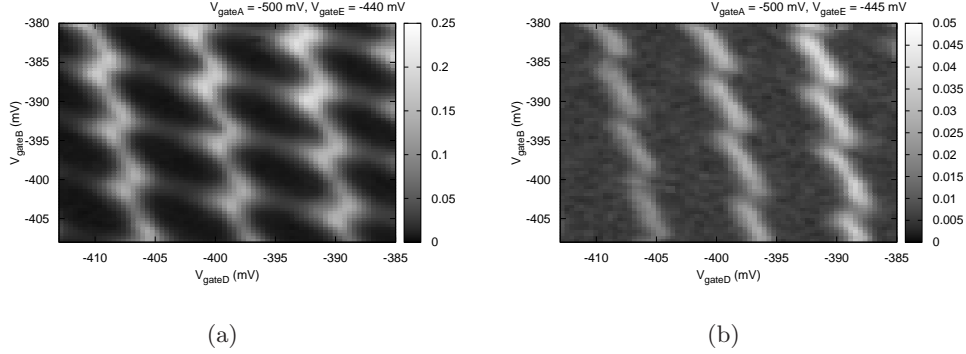


Figure 8.13.: Comparison of charge stability diagram of double dot system when  $V_{C1C2} \equiv V_{gateC}$  is set at (a) -440 mV and (b) -445 mV. For both results,  $V_{C1C2} \equiv V_{gateC}$  is kept at -472 mV and  $V_{A1} \equiv V_{gateA} = -500$  mV. Conductance is measured as a function of  $V_{B1} \equiv V_{gateB}$  and  $V_{D1} \equiv V_{gateD}$ . The  $V_{B2}$  is fixed at -1.3 V.

We also characterize and calculate the capacitances from the pattern of this figure. The gate capacitances can be extracted as  $C_{B1} = 22 \pm 2$  aF,  $C_{D1} = 19 \pm 1$  aF. The extracted cross capacitances values is not so different from the values for the previous gate voltage condition,  $C_{B1dII}$  is approximately 3 aF and  $C_{D1dI}$  is approximately 4 aF. Importantly, the interdot capacitance  $C_{int}$  for  $V_{E1E2} = -440$  mV is  $71 \pm 7$  aF, while the interdot capacitance is  $78 \pm 13$  aF for  $V_{E1E2} = -445$  mV. This means that the gates which control the coupling to the leads have some influence on the coupling between dots. However, these interdot capacitances in two different conditions for gate voltage  $V_{E1E2}$  are comparable and not so different. The total capacitances for dotII decreases from  $232 \pm 8$  aF to  $220 \pm 14$  aF because the capacitive coupling between dotII and the lead is reduced, even though the interdot coupling is slightly increased.

According to the total energy of the double dot model as expressed in Eq. 8.2, we can simulate the total electrostatic energy as a function of gate voltages ( $V_{B1}$  and  $V_{D1}$ ) and the numbers of electrons in each dot ( $n_{dI}$  and  $n_{dII}$ ). The comparison of the charge stability diagram between measured conductance data in Fig. 8.14(a) and simulated total energy data in Fig. 8.14(b). The excellent simulated total energy data has been generated from the program written by another Ph.D. student: Daniel Schefzyk [65]. By using the capacitance parameters extracted from the charge diagram of the measured conductance in Fig. 8.12(b), we obtain the total electrostatic energy in each charge configuration over the range of defined center gate voltages  $V_{B1}$  and  $V_{D1}$ . We can see clearly that the plot of simulated total energy has the same pattern and number of hexagons as the plot of the measured conductance resonance for the charge stability diagram. The slopes of borderlines as indicated as dashed lines for each honeycomb cell in Fig. 8.14(a) and the bright lines in Fig. 8.14(b) are very close. This confirms that the model used to explain the double quantum dot system is satisfied and reasonable.

To study the effect of changing the coupling between the dot and the lead to the conductance resonance, the gate voltage  $V_{A1}$  is varied from -480 to -570 mV and  $V_{E1E2}$  is varied from -435 to -440 mV, while the interdot gate voltage  $V_{C1C2}$  is fixed at -470 mV. The conductance resonances in the charge stability diagram are measured as a function of gate voltage  $V_{B1}$  and  $V_{D1}$ , and are shown in Fig. 8.15. The conductance resonance in Fig. 8.15(a) is quite pronounced in both gate voltage directions, but there is no splitting at the triple points of the honeycomb cells. There is



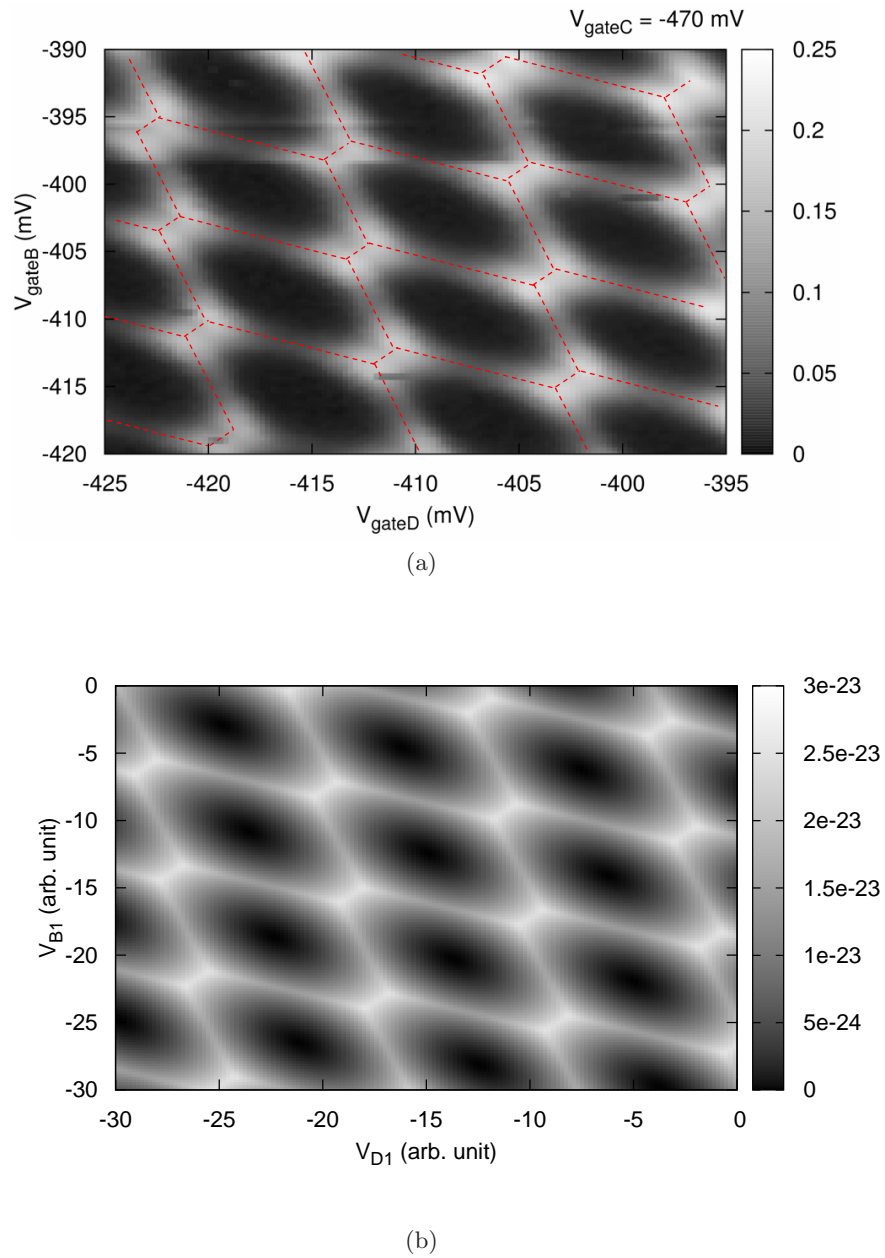


Figure 8.14.: Comparison between (a) the experimental data and (b) simulation of the charge stability diagram of double dot system. In (a), the gate voltages are set as  $V_{A1} = -520$  mV,  $V_{E1E2} = -440$  mV, and  $V_{C1C2} \equiv V_{gateC} = -470$  mV. Measured conductance as a function of  $V_{B1} \equiv V_{gateB}$  and  $V_{D1} \equiv V_{gateD}$ . Dashed lines indicate the boundaries of honeycomb cells in the diagram. In (b), the total electrostatic energy of the double dots as a function of  $V_{B1}$  and  $V_{D1}$  in arbitrary unit.

## 8. Electron transport in Double Quantum Dots

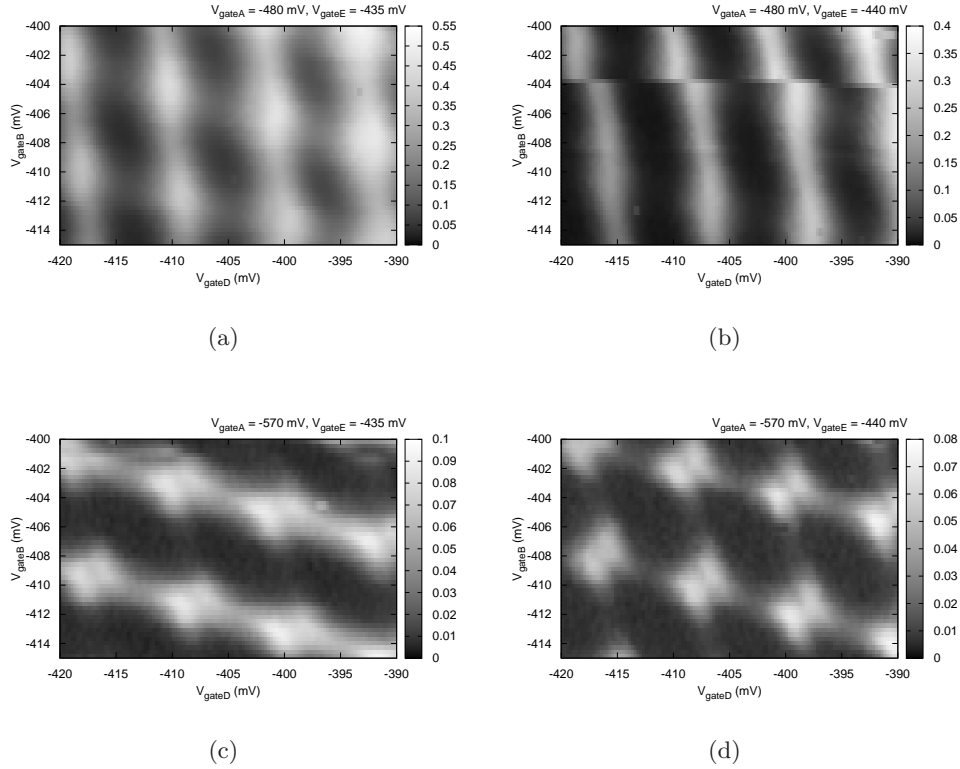


Figure 8.15.: The charging diagram of couple dot system. Measured conductance as a function of  $V_{B1} \equiv V_{gateB}$  and  $V_{D1} \equiv V_{gateD}$ . (a) and (b)  $V_{A1} \equiv V_{gateA}$  is set at -480 mV, while  $V_{A1}$  is set at -570 mV for (c) and (d). The  $V_{E1E2} \equiv V_{gateE}$  is varied between -435 mV and -440 mV. The  $V_{C1C2} \equiv V_{gateC}$  and  $V_{B2D2}$  is fixed at -470 mV and -1.3 V, respectively. The artefact in (b) is the jumping of the data during the measurement is running.

instead an array of diffuse points.

When the gate voltage  $V_{E1E2}$  is decreased, the conductance pattern changes to the same form as the result of Fig. 8.13(b). In this case, the coupling between dotII and the lead is decreased. On the other hand, if the gate voltage  $V_{A1}$  is decreased, while the other gate voltage removes fixed, the coupling between dotI and the lead is decreased. The conductance resonance only occurs along the boundaries separating different  $n_{dI}$  of the charge configuration, as shown in Fig. 8.15(c). Additionally, the triple points begin splitting and can be resolved. When the coupling between both dots in the system to neighbouring leads decreases, the interdot coupling is influenced by the tunnel coupling between double dots, as shown in Fig. 8.15(d). The splitting of the triple points is pronounced and the well defined honeycomb or hexagon pattern is seen in the charge stability diagram. Therefore, we can extract the capacitances by using this pattern at this gate voltage condition.

The cross capacitance is approximately 3 aF for  $C_{B1dI}$  and 4 aF for  $C_{D1dII}$ , which is independent of other gate voltages except the gate voltage  $V_{B1}$  and  $V_{D1}$  respectively. The gate capacitances are  $20 \pm 2$  aF for  $C_{B1}$  and  $19 \pm 1$  aF for  $C_{D1}$ . From the results presented we can see that the capacitive coupling between the center gate and any dot is almost constant and independent of the influence from interdot gate voltage or even dot-lead gate voltage. The interdot capacitance  $C_{int}$  is  $41 \pm 5$  aF, which is rather small. By reducing both gate voltage  $V_{A1}$  and  $V_{E1E2}$ , the

splitting of the conductance resonance at the triple points is clearly visible.

### 8.1.1. Honeycomb diagram in the sample PR1:d1

We now consider the double dots coupled in series fabricated in another sample. The pattern of the structure is designed to use only three pairs of split gates for forming the double dot system, and the size of this structure is also bigger than the structure in the previous sample. Figure 8.16 shows the equivalent electronic circuit for one double dot system in the sample **PR1:d1**. The dots defined as dotIII and dotIV are coupled to each other in series, and have the numbers of electrons  $n_{dIII}$  and  $n_{dIV}$  respectively. The size of the dotIII and dotIV can be adjusted by applying gate voltage  $V_{E2}$  and  $V_{E1}$  respectively. The capacitance coupled between dotIII(IV) and gate E2(E1) is defined as  $C_{E2(E1)}$ . The cross capacitances between gate E1(E2) and dot III(IV) is represented by  $C_{E1dIII(E2dIV)}$ . The interdot capacitance is defined as  $C_{int}$ , and the capacitances of the dot coupled with the lead is given by  $C_L$  and  $C_R$ .

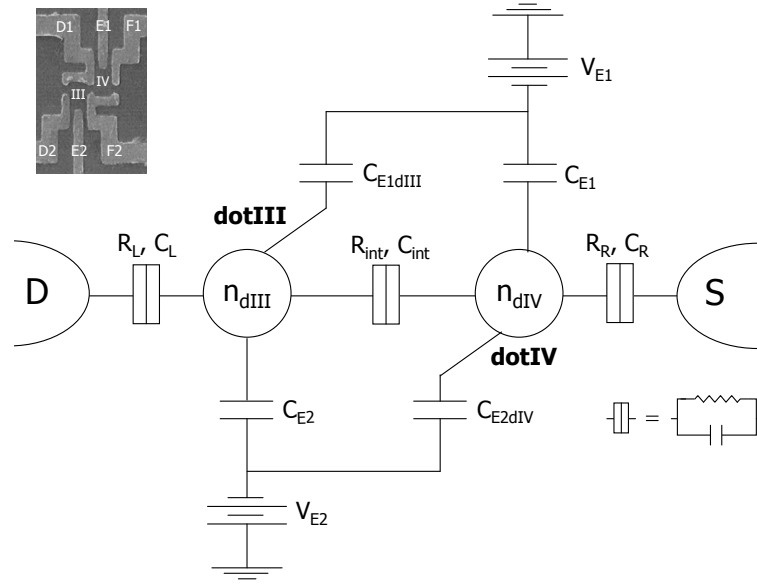


Figure 8.16.: Equivalent electronic circuit for double dot (dotIII-IV) system in the sample **PR1:d1**. The cross capacitances,  $C_{E1dIII}$  and  $C_{E2dIV}$ , are included in this diagram.  $C_{E1(E2)}$  is the capacitance from dotIV(III) to gate E1(E2),  $C_{L(R)}$  is the capacitance from dotIII(IV) to neighboring lead,  $C_{int}$  is the interdot capacitance, and  $V_{E1(E2)}$  is the voltage applied to the gate E1(E2). Inset: SEM micrograph of the lithographic double dot structure has been shown.

We measure the conductance of the double-dot system and obtain the hexagons or honeycomb pattern for the charge stability diagram. The conductance as a function of the gate voltage  $V_{E1}$  and  $V_{E2}$  at various interdot gate voltages is shown in Fig. 8.17. The interdot gate voltage  $V_{D1F2}$  is increased from -240 mV in the weak coupling to -220 mV in the strong coupling in steps of 5 mV. Figure 8.17(a) shows the conductance of double dots for weak tunnel coupling. There is an array of bright points of the unresolved pairs of triple points. In the weak tunneling regime the charges in each dot are quantized and both dots are well isolated.

The tunnel coupling between double dots increases from Fig. 8.17(a) to (d) by increasing the interdot gate voltage  $V_{D1F2}$ . The pattern of the charge stability diagram changes to a hexagonal pattern and the splitting of the triple points more pronounced, as shown in Fig. 8.17(b). If the interdot gate voltage is increased, the coupling between dots increases, the pattern will change

## 8. Electron transport in Double Quantum Dots

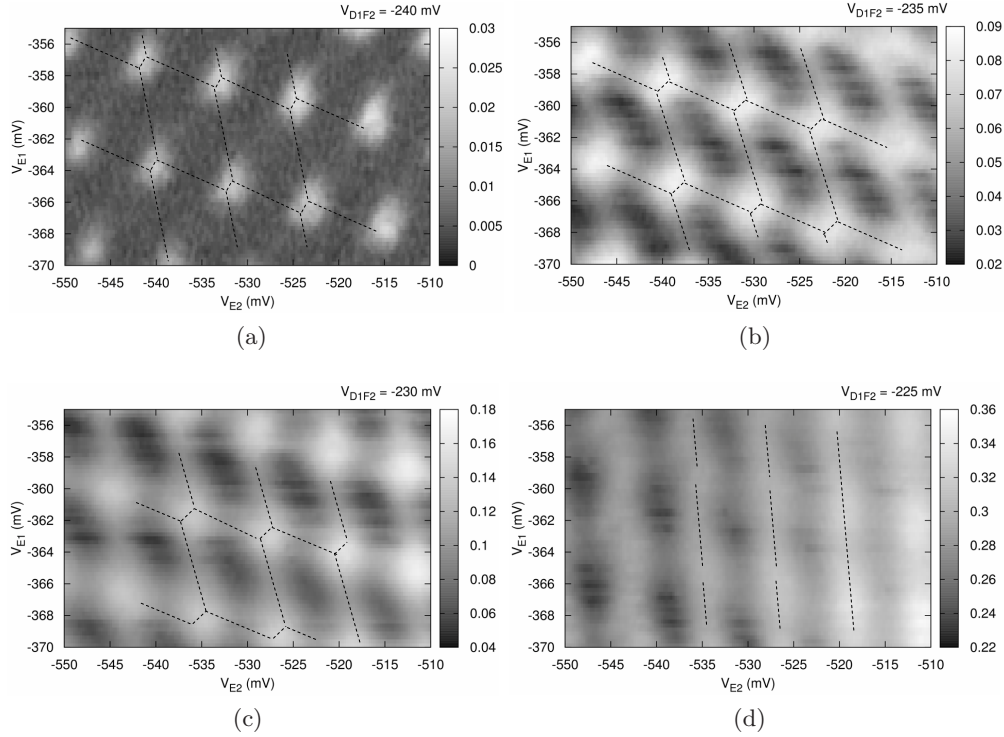


Figure 8.17.: Charge stability diagram of double dot (dotIII-dotIV) system in the sample **PR1:d1**. Conductance is measured as function of  $V_{E1}$  and  $V_{E2}$  with  $V_{D2} = -305$  mV and  $V_{F1} = -445$  mV. The interdot gate voltage  $V_{D1F2}$  is increased from (a)  $-240$  mV to (d)  $-225$  mV in the increment of  $5$  mV.

to the straight line identifying a large dot with the electron number  $n_{tot} = n_{dIII} + n_{dIV}$ , as shown in Fig. 8.17(d). The conductance measurements are not as clear for this structure as compared to the results for the structure in the previous sample, however, the evolution of the charge stability diagram shows the system changing from an isolated double-dot system to a large single dot.

In Fig. 8.17(b) - (d), we notice that the bright boundary lines are so smeared out, thus this makes the dark areas corresponding to the region of almost zero conductance in each honeycomb cell are small compared to the honeycomb diagrams of the double dot system of the sample **PR1:d2**. This means that the conductance peaks are broadened. This measurement was performed at base temperature of  $\sim 65$  mK which is the same as the measurement for previous sample. The geometry of these double dots is bigger than that of the previous sample. Thus we infer that the broadening of the boundary lines might be due to the strong coupling of double dot system to the reservoirs.

From the double dot model, we can extract the capacitances from the honeycomb pattern in Fig. 8.17(b). The gate capacitances can be calculated by determining the geometry of the hexagons or honeycomb cells and is given by  $C_{E1} = 26 \pm 4$  aF and  $C_{E2} = 20 \pm 1$  aF. The cross capacitance between gate E1 and dotIII,  $C_{E1dIII}$ , is approximately  $3$  aF and the cross capacitance between gate E2 and dotIV,  $C_{E2dIV}$ , is approximately  $4$  aF. From the non-linear measurement of the Coulomb oscillation for each dot, the interdot capacitance  $C_{int}$  is extracted as  $88 \pm 19$  aF. The total capacitance of dotIII and dotIV is  $381 \pm 19$  aF and  $388 \pm 19$  aF respectively.

As shown in the inset of Fig. 8.16, the double dots in this sample are fabricated with a special geometry. When the interdot gate voltage  $V_{D1F2}$  is adjusted, not only does the interdot coupling

change, but also the coupling between each dot to the lead. Therefore we try to characterize the influence of the interdot gate voltage to the measured conductance. All data presented in Fig. 8.18 is not obtained from the same run as data in Fig. 8.17, but the measurement is performed few days later. Thus we can see the pattern difference of charge diagram at the same condition of the gate voltages. This means that the system is not quite stable over long time scale.

Figure 8.18(a) shows the charge stability diagram of the coupled dotIII-dotIV system in the weak coupling regime. As we see in the figure of the structure, the interdot gate is tuned with the gates D1 and F2. The interdot gate voltage is set at  $-235$  mV. The gate voltage  $V_{D1}$  is increased to  $-225$  mV only and the gate voltage  $V_{F2}$  is still fixed at the same value. The interdot coupling increases as well as the coupling between dotIII and the lead, and the conductance pattern changes as seen in Fig. 8.18(b). The boundaries lines separating the different  $n_{dIV}$  are more pronounced than the lines separating different  $n_{dIII}$ . In this case the coupling of dotIV and the lead is weaker than that of dotIII and the lead.

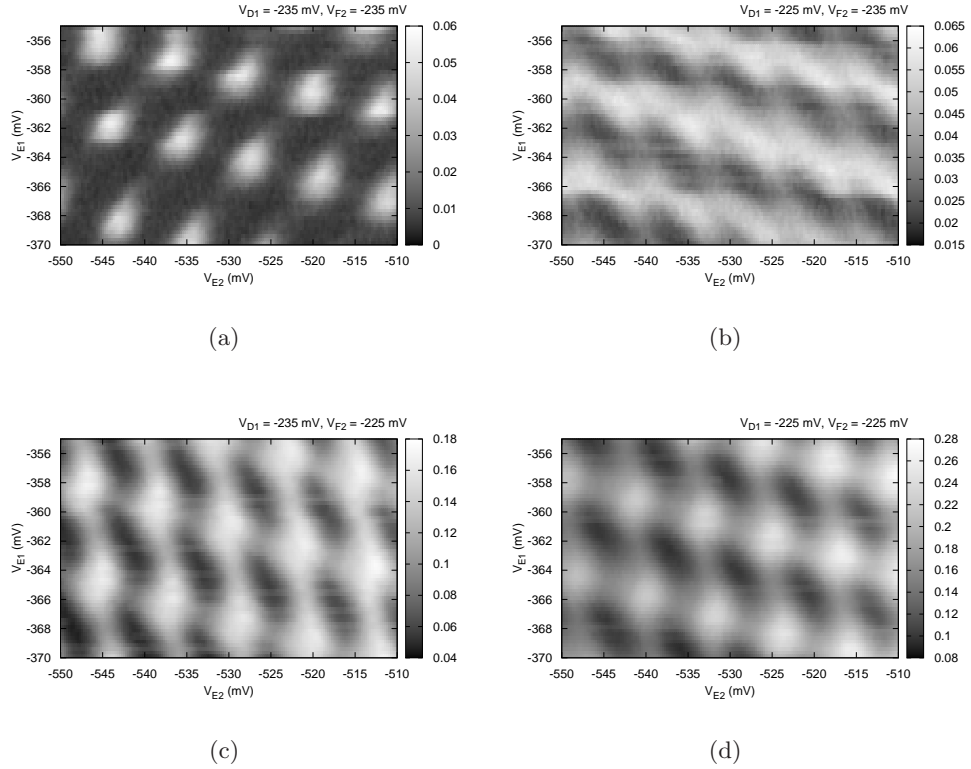


Figure 8.18.: Charge stability diagram of double dot (dotIII-dotIV) system. Conductance is measured as function of  $V_{E1}$  and  $V_{E2}$ . (a) and (b) The  $V_{F2}$  is set at  $-235$  mV, while it is set at  $-225$  mV in (c) and (d). The  $V_{D1}$  is varied between  $-235$  mV and  $-225$  mV for the same  $V_{F2}$ . The  $V_{D2}$  and  $V_{F1}$  are set at  $-305$  mV and  $-445$  mV, respectively.

On the other hand, if the gate voltage  $V_{D1}$  is fixed at  $-235$  mV and  $V_{F2}$  is increased to  $-225$  mV instead, the pattern changes to Fig. 8.18(c). The coupling between dotIII and the lead becomes weaker than that between dotIV and the lead. This also affects and increases the interdot coupling as well. The lines separating different  $n_{dIII}$  are more pronounced than boundaries lines along the other direction. Figure 8.18(d) shows the honeycomb pattern appearing in the charge

## 8. Electron transport in Double Quantum Dots

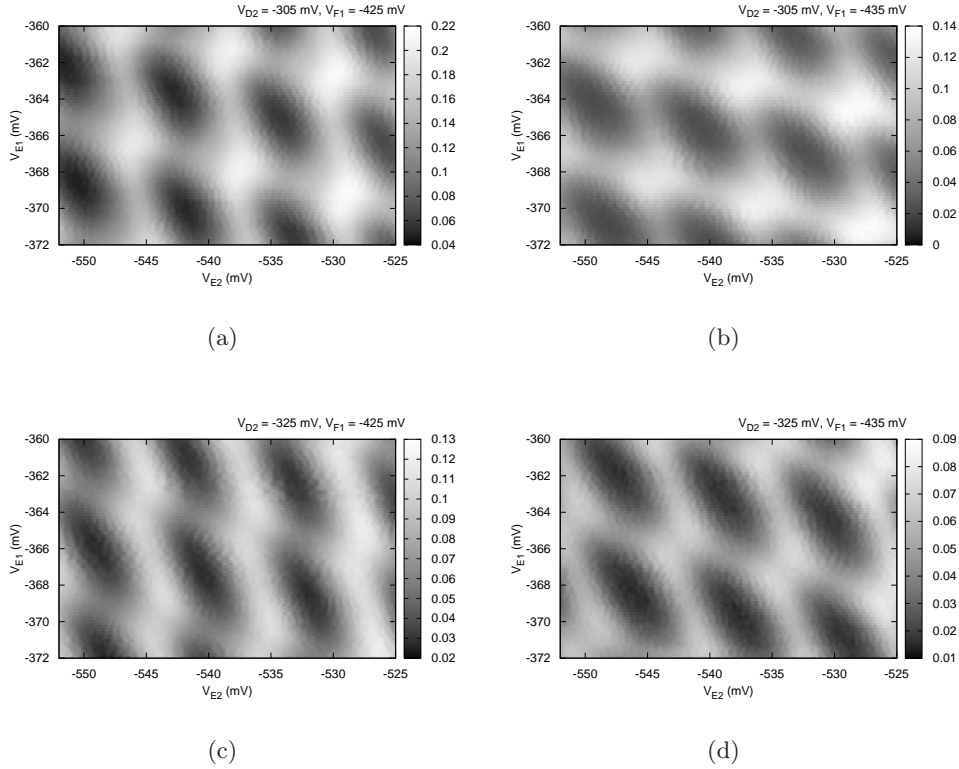


Figure 8.19.: Charge stability diagram of double dot system with interdot gate voltage  $V_{D1F2} = -230$  mV. (a) and (b)  $V_{D2}$  is set at  $-305$  mV, while it is decreased to  $-325$  mV in (c) and (d). For the same value of  $V_{D2}$ ,  $V_{F1}$  is varied between  $-425$  and  $-435$  mV. The conductance is measured as a function of gate voltages  $V_{E1}$  and  $V_{E2}$ .

diagram when both gates (gate D1 and F2) are connected together and applied with the same voltage of  $-225$  mV. This refers to the stronger coupling between two dots.

To study the dependence of conductance pattern on the coupling between the dots and the leads, we keep the interdot gate voltage  $V_{D1F2}$  constant at  $-230$  mV to obtain the honeycomb pattern in charge stability diagram in Fig. 8.19(a), and change the gate voltage  $V_{D2}$  and/or  $V_{F1}$  in Fig. 8.19(b) to (d). The gate voltage  $V_{F1}$  is decreased from  $-425$  mV to  $-435$  mV in Fig. 8.19(b) to reduce the coupling between dotIV and the lead. The boundaries lines along gate voltage  $V_{E2}$  are more pronounced than the lines along gate voltage  $V_{E1}$ . These lines separate the charge configurations with different  $n_{dIV}$ . On the other hand, we keep the gate voltage  $V_{F1}$  constant, and decrease the gate voltage  $V_{D2}$  from  $-305$  mV to  $-325$  mV in order to reduce the coupling between dotIII and the lead. Then the pattern changes quite clearly; the boundary lines along the gate voltage  $V_{E1}$  are more pronounced as be seen in Fig. 8.19(c). These lines separate charges configuration with different  $n_{dIII}$ . When both gate F1 and D2 are decreased to the values respectively defined in (b) and (c),  $V_{F1} = -435$  mV and  $V_{D2} = -325$  mV, the honeycomb pattern is well defined and the splitting of the triple points is clearly observed, as shown in Fig. 8.19(d).

We can see clearly that the coupling between each dot to the lead changes when interdot gate voltage is changed because of the special shape of the gates D1 and F2 that work in conjugation with gates D2 and F1, respectively, to define the quantum point contacts of the dot structure. To compensate this effect of the interdot gate voltage to the dot-lead gate voltage, the gate voltage

## 8.2. Conductance Peak Splitting in Double Quantum dots

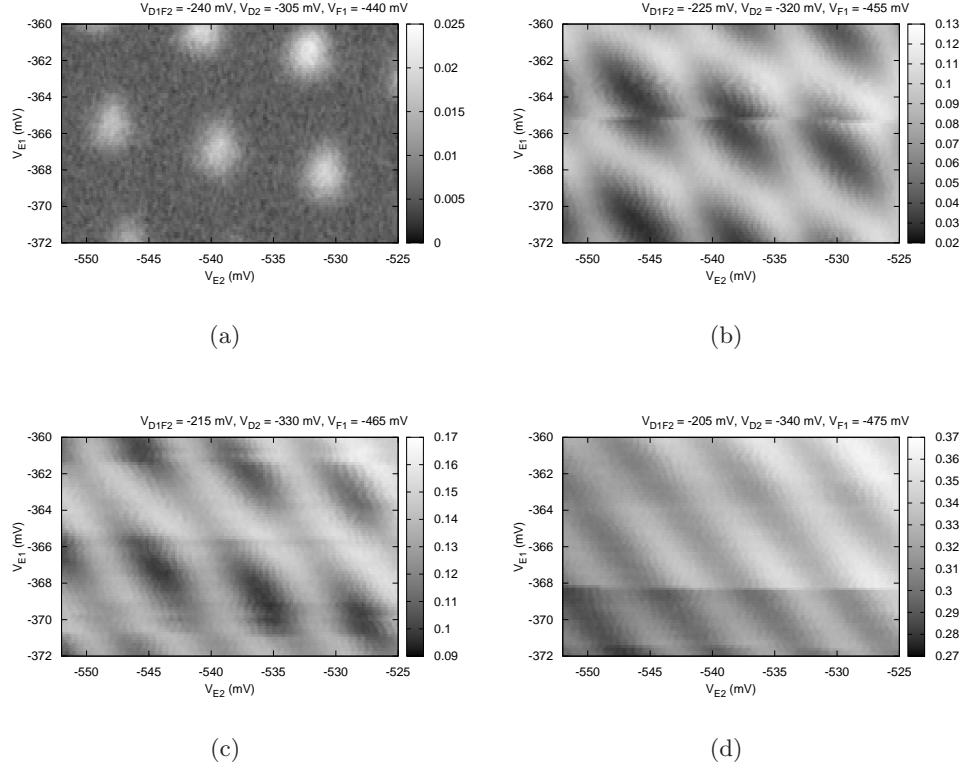


Figure 8.20.: Charge stability diagram as a function of  $V_{E1}$  and  $V_{E2}$ . The interdot gate voltage  $V_{D1F2}$  is increased from (a)  $-240$  to (d)  $-205$  mV. The side gate voltages  $V_{D2}$  and  $V_{F1}$  in (a) are reduced in order to compensate for the increasing interdot gate voltage.

$V_{D2}$  and  $V_{F1}$  is decreased whenever the interdot gate voltage  $V_{D1F2}$  increases, or vice versa. This technique is used to keep a constant coupling between dots and leads. The conductance resonance patterns measured after performing this method at various interdot gate voltage are shown in Fig. 8.20.

At the beginning, the double dot system is formed with  $V_{D1F2} = -240$  mV,  $V_{D2} = -305$  mV, and  $V_{F1} = -440$  mV. The charge stability diagram shows the double dots in the weak coupling, as shown in Fig. 8.20(a). In Fig. 8.20(b)-(d), the interdot gate voltage is increased, the dot-lead gate voltage,  $V_{D2}$  and  $V_{F1}$ , is reduced to compensate for the gate voltage  $V_{D1F2}$ . The pattern in charge stability diagram changes from the honeycomb pattern to array of the straight lines. The evolution of the double dots coupling from the weak to strong coupling can be seen clearly in this measurement.

## 8.2. Conductance Peak Splitting in Double Quantum dots

In this section we discuss the conductance peak splitting when the same voltage is applied to both center gates. First, we study the behaviour of the peak splitting of the double dot system, dotI-dotII structure, in the sample **PR1:d2**. In this measurement the pair of center gates on the same side, gate B1-D1 and gate B2-D2, are connected. The gate voltage  $V_{B2D2}$  is fixed at  $-1.3$  V. The interdot gate voltage  $V_{C1C2}$  is used to adjust the coupling between two dots as in the measurements of the previous section. The gates A1 and E1E2 are also biased with negative

## 8. Electron transport in Double Quantum Dots

voltage to couple the dot and the reservoir or lead.

The model for conductance peak splitting in double dots coupled in series has been described in details in the section 2.4.2 [45, 46]. For identical dots we can assume that total capacitance for dotI is equal to the total capacitance for dotII,  $C_{dI} = C_{dII} = C_{\Sigma}$ . The center gate capacitance of each dot  $C_{B1}$  and  $C_{D1}$  is also assumed to have the same value,  $C_{B1} = C_{D1} = C_g$ . Therefore the capacitance for dotI-lead and dotII-lead are automatically the same.

According to the peak splitting model, the relationship between the conductance peak splitting  $\Delta V_s$  along the sweeping gate voltage  $V_{B1D1}$  and the shifting  $\Delta$  in total energy for a polarized electronic configuration in double dots is defined in Eq. 2.80 as;

$$\Delta V_s = \frac{2C_{\Sigma}}{eC_g} \Delta. \quad (8.7)$$

The fractional peak splitting  $F$  for double dots is defined in Eq. 2.81,

$$F = \frac{2\Delta V_s}{\Delta V_p}, \quad (8.8)$$

where  $\Delta V_p$  is the peak separation and is equal to  $e/C_g$ . The fractional peak splitting  $F$  increases with increasing tunnel coupling of double dots,  $F = 0$  in the weak tunnel coupling and  $F = 1$  in the strong tunnel coupling. The quantities  $\Delta V_s$  and  $\Delta V_p$  are shown in Fig. 2.23(b) for double dots [45].

We perform the measurement on double dots and show how interdot tunnel coupling leads to a conductance peak splitting. Figures 8.21(a) and (b) show changes in the conductance of the double dots vs gate voltage,  $V_g = V_{B1D1}$ , with changing interdot gate voltage  $V_{C1C2}$ , which corresponds to the tunnel coupling between two dots, at two different gate voltage  $V_{E1E2}$ . In both figures, the interdot gate voltage is increased from -470 mV at the bottom curve to -440 mV at the topmost curve in steps of 3 mV. It can be seen that the peak splitting increases with increasing interdot tunnel coupling at both  $V_{E1E2} = -435$  mV and -440 mV.

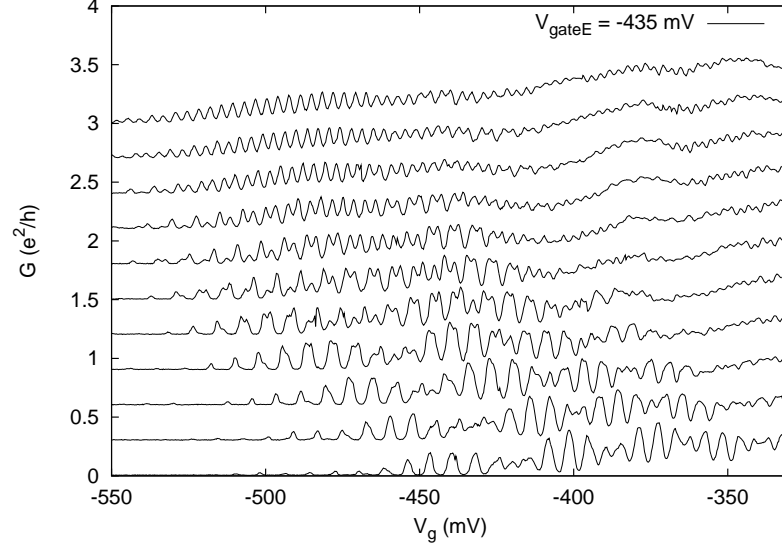
At the bottom curve of Fig. 8.21(a) and (b), interdot tunneling is weak. Each conductance peak in bottom curve corresponds to adding two electrons to the double dot, one to each dot. The double dot conductance consists of weakly split peaks when the interdot gate voltage  $V_{C1C2}$  increases from -470 to -464 mV. As increasing interdot gate voltage, each peak clearly splits into two peaks whose separation increases. Finally, for three top curves the tunnel coupling between dotI and dotII becomes very strong, the tunneling barrier between two dots is removed, and the conductance is that of a single large dot with peak separation about half that of the bottom curve. This peak splitting is similar for both values of  $V_{E1E2}$ .

The measured fractional peak splitting can be calculated from the separation of the split peaks  $\Delta V_s$  and separation of double dot peaks  $\Delta V_p$  in Fig. 8.21(a) and (b), as shown in Fig. 8.22. When the interdot gate voltage  $V_{C1C2}$  corresponding to double dots tunnel coupling increases, the interdot tunnel conductance and the fractional peak splitting increases. For strong tunnel coupling, the fractional peak splitting gradually reaches unity. The change of the fractional peak splitting for the system with different dotII-lead gate voltage shows the same trend.

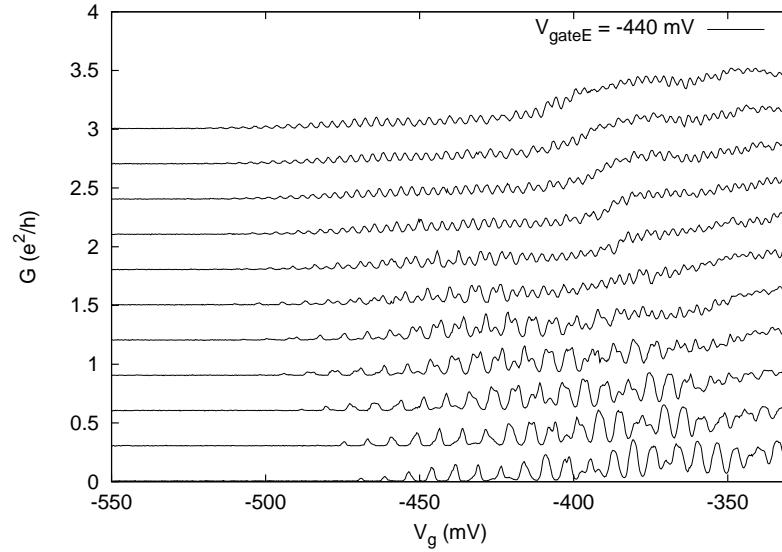
Figure 8.23(a) shows the strong correlation between peak splitting and interdot tunnel conductance. The interdot tunnel conductance  $G_{int}$  is plotted and compared to the fractional peak splitting. The  $G_{int}$  is separately measured versus interdot gate voltage  $V_{C1C2}$ . Additionally, the trace of  $G_{int}$ , which is the conductance of QPC C, is horizontally shifted with  $\Delta V_{C1C2} = 44$  mV to account for the influence of the other gates. Then the fractional peak splitting and interdot tunnel conductance track each other pretty closely.

Figure 8.23(b) plots the measured fractional peak splitting  $F$  versus the interdot tunnel conductance  $G_{int}$ . This plot of fractional peak splitting can be predicted and interpolated from





(a)



(b)

Figure 8.21.: Conductance peaks of double dots (dotI-dotII) in the sample **PR1:d2** at (a)  $V_{E1E2} \equiv V_{gateE} = -435$  mV and (b)  $V_{E1E2} = -440$  mV. Both (a) and (b) are measured at  $V_{A1} = -480$  mV. The gate B1 and D1 are connected and varied voltage together. Another gate of them are fixed at  $-1.3$  V.  $V_{C1C2}$  is varied from  $-470$  mV (bottom curve) to  $-440$  mV (top curve) in  $3$  mV increment. The curves have been offset with  $0.3(e^2/h)$  for clarity.

## 8. Electron transport in Double Quantum Dots

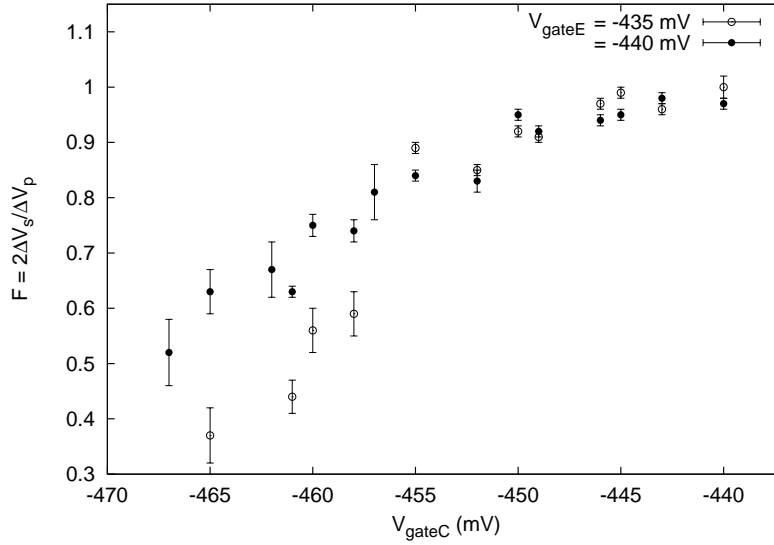


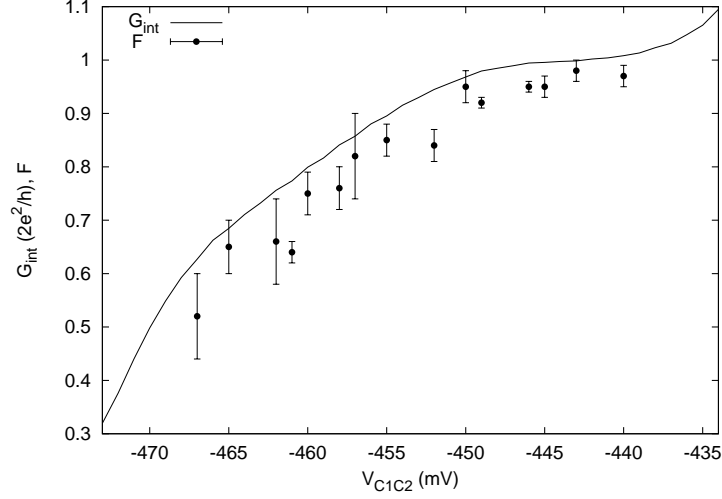
Figure 8.22.: Double dot fractional peak splitting ( $F$ ) vs interdot gate voltage  $V_{C1C2} \equiv V_{gateC}$  of double dot (dotI-dotII) system.

the theories of many body charge fluctuations developed by Matveev *et al.* and Golden *et al.* [47, 48, 49], and has no adjustable parameters in the strong tunnel coupling regime as shown in Eq. 2.83. As predicted by the theory, the measured fractional peak splitting approaches and saturates at the value of 1 for strong tunneling. As shown, the data and the many body theory, especially when  $G_{int} \rightarrow 2e^2/h$ , are in good qualitative agreement.

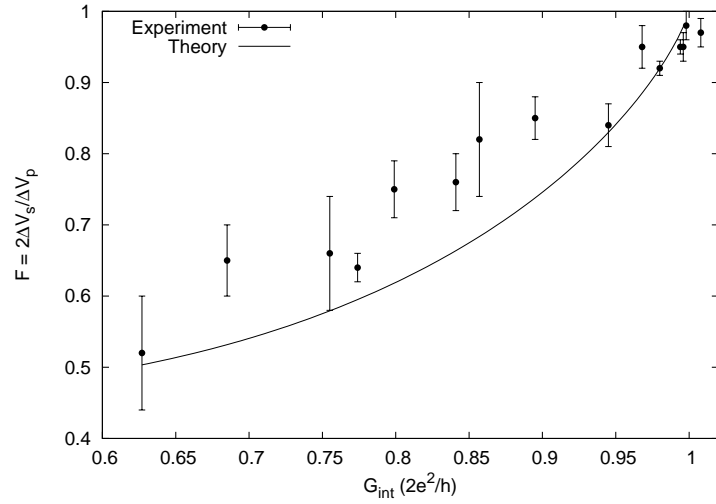
Nevertheless, only theory in the strong tunneling limit can be compared qualitatively but not quantitatively with the measured data. This error of comparison might come from two factors. The first factor is that not all gates are energized. Then the interdot point contact (QPC C) conductance has to be offset to account for the expected influence from the other gates. This procedure may not be exactly correct, and leads to a shifting of the QPC C conductance, which depends on the interdot gate voltage. To compare with the theory in Fig. 8.23(b), the  $\Delta V_{C1C2}$  of 44 mV has been selected as a offset the interdot conductance. The second factor is that both dots in our system may not be assumed to be the identical, because the gate A2 is grounded and not used to form the dot structure. The total capacitance for both dots is not exactly the same, and there is also a cross capacitances for the real system which is different from the model.

Figure 8.24 shows the nonlinear measurement of double dot differential conductance as a function of the gate voltage and the source-drain voltage  $V_{sd}$  for six different values of interdot gate voltage corresponding to the interdot tunnel conductance and coupling of two dots. In Fig. 8.24(a), the interdot gate voltage is -470 mV, the diamond shape dark regions of Coulomb blockade bounded by conductance peaks at which current begins to flow can be observed clearly. These large regions corresponds to a double dot ground state in which each dot has the same number of excess electrons, or so called unpolarized ground states [66, 67].

As interdot gate voltage increases, the primary diamonds decrease in size, width and height, and small secondary diamonds appear and grow in Fig. 8.24(b)-(e), until the size and shape of the primary and secondary diamonds is nearly identical, as shown in Fig. 8.24(f). This refers to the shifting energy  $\Delta$ , which is cost for adding an electron to the unpolarized ground stage. The interdot tunnel coupling allows the double dots to share the extra electron and then decrease the polarization. At fixed values of gate voltage, the Coulomb gap,  $\Delta V_{gap}$ , is defined as the width of the primary Coulomb blockade diamond along source-drain voltage, or the separation



(a)



(b)

Figure 8.23.: (a) Double-dot fractional peak splitting  $F = 2\Delta V_s / \Delta V_p$  and measured interdot barrier conductance  $G_{int}$  (Curve) vs gate voltage  $V_{C1C2} \equiv V_{gateC}$ . For double-dot fractional splitting measurement,  $V_{A1} = -480$  mV and  $V_{E1E2} = -440$  mV. The  $G_{int}$  is offset in  $V_{C1C2}$  direction of 44 mV because all gates except gate A2, which are energized in order to form double dot system, should have the influence to electron tunneling through the system. The value of series resistance of the sample is assumed as 800 Ohm. For strongly tunneling, (b) and (c)  $F$ , which is the tunnel peak splitting equation according to Matveev et al. and Golden and Halperin, plotted vs  $G_{int}$ .

## 8. Electron transport in Double Quantum Dots

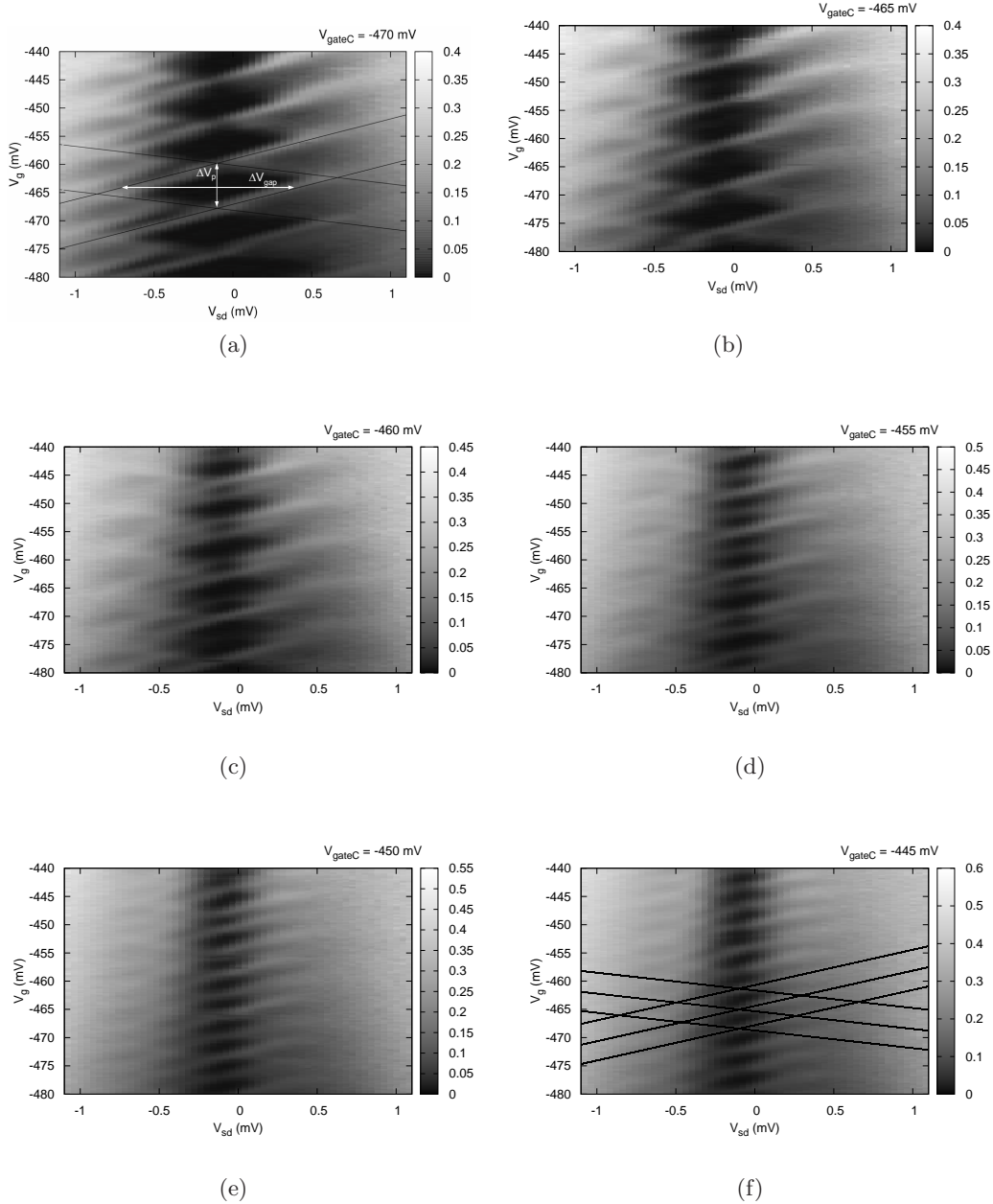


Figure 8.24.: Gray scale plot of double dot differential conductance vs center gate voltage  $V_g \equiv V_{B1D1}$  and source-drain voltage  $V_{sd}$  for interdot gate voltage  $V_{C1C2} \equiv V_{gateC}$  increased from (a) -470 mV to (f) -445 mV in 5 mV increment. Solid lines indicates the border lines of Coulomb blockade diamonds. Dark areas are regions of Coulomb blockade. The Coulomb gap  $\Delta V_{gap}$  and Coulomb peak spacing  $\Delta V_p$  are indicated in (a).  $V_{A1}$  and  $V_{E1E2}$  is respectively set at -480 mV and -440 mV. The DC-offset of  $V_{sd}$  is about -100  $\mu V$

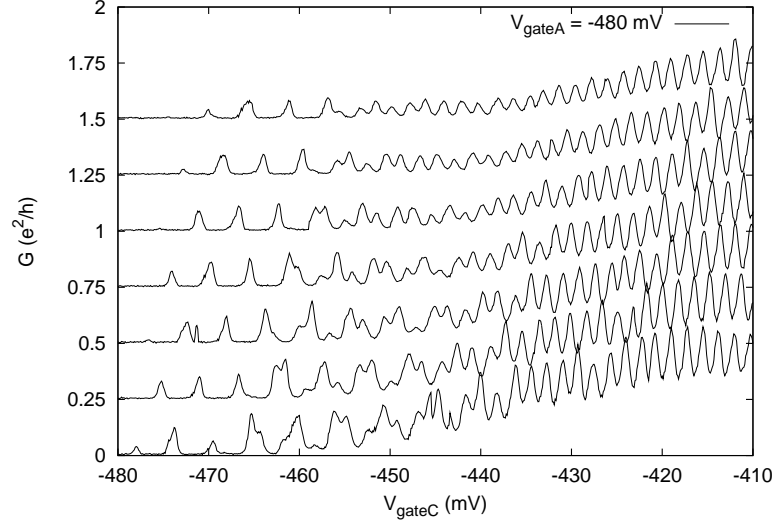


Figure 8.25.: Conductance peaks of double dot vs interdot gate voltage,  $V_{C1C2} \equiv V_{gateC}$ , for  $V_{A1} \equiv V_{gateA}$  of -480 mV at  $V_{B2D2} = -1.3$  V and  $V_{gateE} = -435$  mV.  $V_{B1D1}$  is also varied from -450 mV (bottom line) to -480 mV (top line) in 5 mV increment. The curves have been offset with  $0.25(e^2/h)$  for clarity.

between conductance peaks bounding the Coulomb blockade region.

From the data in Fig. 8.24(a) it can be extracted that  $\Delta V_p = \Delta V_g = 8$  mV,  $C_g = 20$  aF,  $C_s = 67$  aF,  $C_d = 123$  aF,  $C_\Sigma = 210$  aF, and  $\alpha = 0.095$ . Therefore the charging energy is  $E_C = e^2/C_\Sigma = \alpha e \Delta V_g \simeq 760$   $\mu$ eV. The size of diamond shape decreases with increasing  $V_{C1C2}$ . In Fig. 8.24, the  $\Delta V_{gap}$  obviously decreases from 1.12 mV at  $V_{C1C2} = -470$  mV to 540  $\mu$ eV at  $V_{C1C2} = -445$  mV. The peak separation  $\Delta V_p$  also decreases from 8 mV to 3.5 mV when interdot coupling increases from (a) to (f). In the strong tunneling limit, the size of the diamonds is half of that in the weak tunneling limit. As the interdot tunnel coupling increase from weak to strong coupling, the peak splitting  $\Delta V_s$  increases until is equal to half of the peak separation  $\Delta V_p/2$ , and the Coulomb gap  $\Delta V_{gap}$  and  $V_p$  decrease by a factor of  $\simeq 2$ . In Fig. 8.24(f) with a strong interdot coupling, two small isolated dots become a big single dot, and the capacitances extracted from a diamond are expressed as  $C_g = 46$  aF,  $C_s = 143$  aF,  $C_d = 240$  aF,  $C_\Sigma = 429$  aF. The  $\alpha$  factor is 0.107 and the charging energy is approximately 373  $\mu$ eV. It can be seen that the capacitances are much greater than those extracted from a diamond of double dots in 8.24(a).

Figure 8.25 shows the plot of double dot conductance versus interdot gate voltage  $V_{C1C2}$  for different values of fixed gate voltage  $V_{B1D1}$ . The conductance is observed at the gate voltage  $V_{A1}$  of -480 mV. For the lowest conductance curve, the transition from a single dot to a double dot with decreasing interdot tunneling clearly begins at  $V_{C1C2} \simeq -435$  mV. With changing the interdot gate voltage, the same pattern of conductance oscillations for the single-to-double quantum dot transition was also recently reported for a tunable three lead double dot with a resorcinarene spacer by M. Fleischer [68]. At  $V_{C1C2} \leq -430$  mV, neighbouring peaks begin to merge in to single broad peak with about twice the peak separation. These broad peaks with twice the separation in interdot gate voltage indicate the well isolated serial double quantum dots.

For every curve, the peak separation  $\Delta V_p$  is about 4.4 mV in double dot region and 1.8 mV in a single dot region. The influence of gate B1D1, which is used to change the size of the dot and hence the energy level separation, is shown. When the  $V_{B1D1}$  decreases, the amplitude of

## 8. Electron transport in Double Quantum Dots

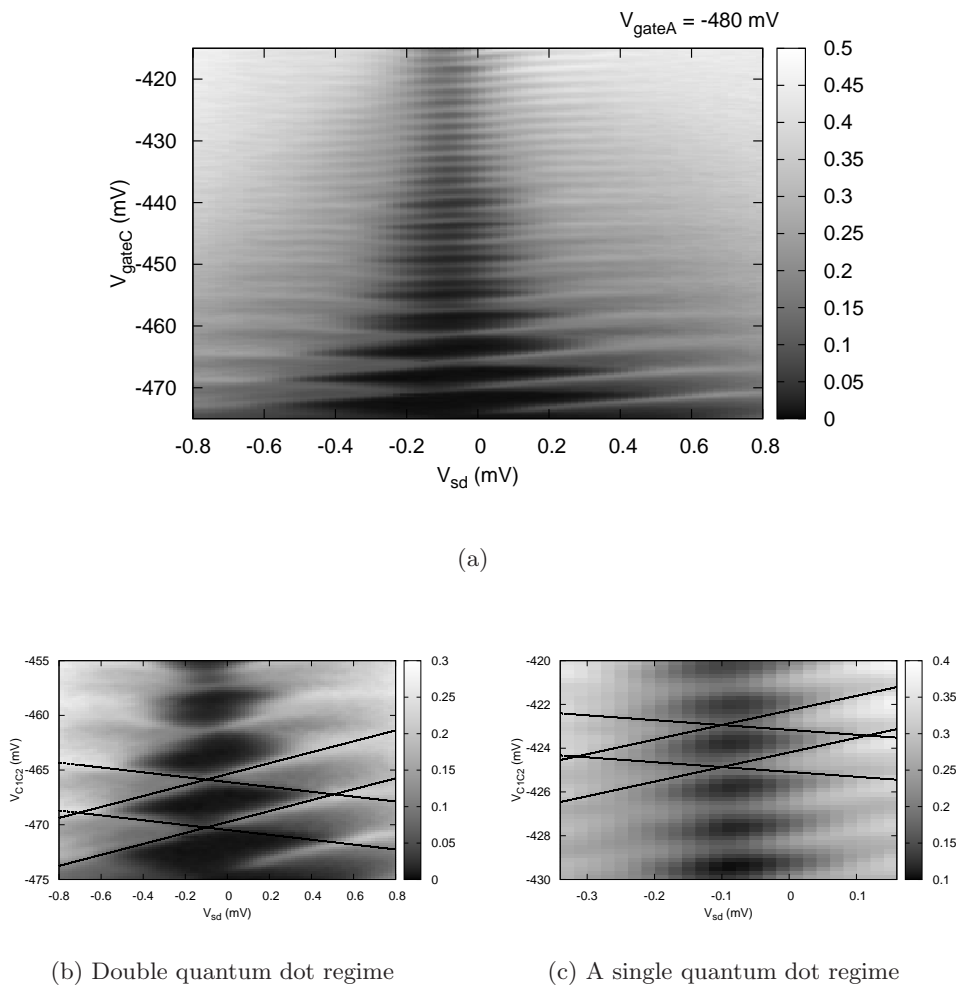


Figure 8.26.: (a) Gray scale of differential conductance of double dots as a function of interdot gate voltage  $V_{C1C2} \equiv V_{gateC}$  at  $V_{gateA} = -480$  mV,  $V_{B1D1} = -470$  mV,  $V_{B2D2} = -1.3$  V and  $V_{gateE} = -435$  mV. The DC-offset is about  $-100 \mu\text{V}$ . When  $V_{C1C2}$  is increased more negative voltage, neighbouring Coulomb diamonds start to merge into bigger diamonds with the twice period. The interdot gate voltage regime for (b) double dots and (c) a single dot have been presented. The solid lines indicate the boundaries of the Coulomb blockade diamonds.

the conductance peaks slightly decreases, but the transition can still be observed in the same region as before.

The same characteristics can be seen in the non-linear measurement. Figure 8.26(a) shows the differential conductance plotted versus source-drain voltage  $V_{sd}$  and interdot gate voltage  $V_{C1C2}$ . The neighbouring Coulomb diamonds merge into bigger diamonds when the interdot coupling decreases by reducing the interdot gate voltage, as has been previously observed in Fig. 8.24. The size of the Coulomb diamonds is indicated in Fig. 8.26(b) for the double dot region and (c) for a single dot region. The Coulomb diamond in (b) is about twice as large as in (c). The peak separation  $V_p$  is about 4.4 mV for double dot regime and 1.9 mV for a single dot regime. The Coulomb gap  $\Delta V_{\text{gap}}$  decreases from 0.86 mV in (a) to 0.29 mV in (b) when the interdot coupling increases.

### 8.2.1. Conductance peak splitting in the sample PR1:d1

The double-to-single quantum dot transition can also be observed in the double dot system in the sample **PR1:d1**. According to the pattern of double dot (dotIII-dotIV) structure, the gate E1 and E2 are connected and a negative voltage applied. The gate voltage  $V_{D2} = -310$  mV,  $V_{F1} = -445$  mV, and interdot gate voltage  $V_{D1F2} = -235$  mV are fixed while the gate voltage  $V_{E1E2}$  is swept. The measured differential conductance oscillations are shown in Fig. 8.27. The resolution of the oscillations is quite poor due to the effect of the geometry of the big double-dot system on the coupling of each dot to the leads. However, the peak splitting can be observed at this condition of tunnel coupling, which indicates the beginning of the transition from a double dot to a large single dot. It can be seen clearly that the broad peaks begin to split into two peaks.

Figure 8.28 shows the data from nonlinear measurements at various values of the interdot gate voltage. As the increased interdot gate voltage  $V_{D1F2}$  from (a) to (d), the Coulomb diamonds gap  $V_{\text{gap}}$  decreases by about half, but the Coulomb peak separation barely changes because the coupling between the dot and the lead also increases. This is due to the special geometry of the double dot system. The dot-lead gate voltage simultaneously increases with increasing interdot gate voltage. Therefore the comparison between dot-lead coupling and interdot coupling does not change significantly. The number of Coulomb diamonds is almost the same at about five diamonds. The Coulomb peak separation  $V_p$  is about 6 mV in every value of interdot gate voltage. Unfortunately we did not perform any measurements with interdot gate voltage compensation for the dot-lead gate, thus we cannot see the obvious transition of the quantum dot system in this nonlinear data.

## 8. Electron transport in Double Quantum Dots

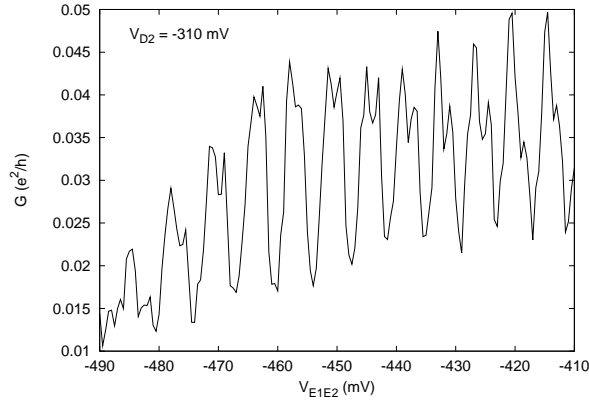


Figure 8.27.: Differential conductance of double dot (dotIII-dotIV) system in the sample **PR1:d1** as a function of tied center gate voltage  $V_{E1E2}$ . The interdot gate voltage  $V_{D1F2}$  is set at  $-235$  mV, and the dot-to-lead or side gate voltages  $V_{D2}$  and  $V_{F1}$  is respectively set at  $-310$  mV and  $-445$  mV. The splitting occurs on the conductance peaks.

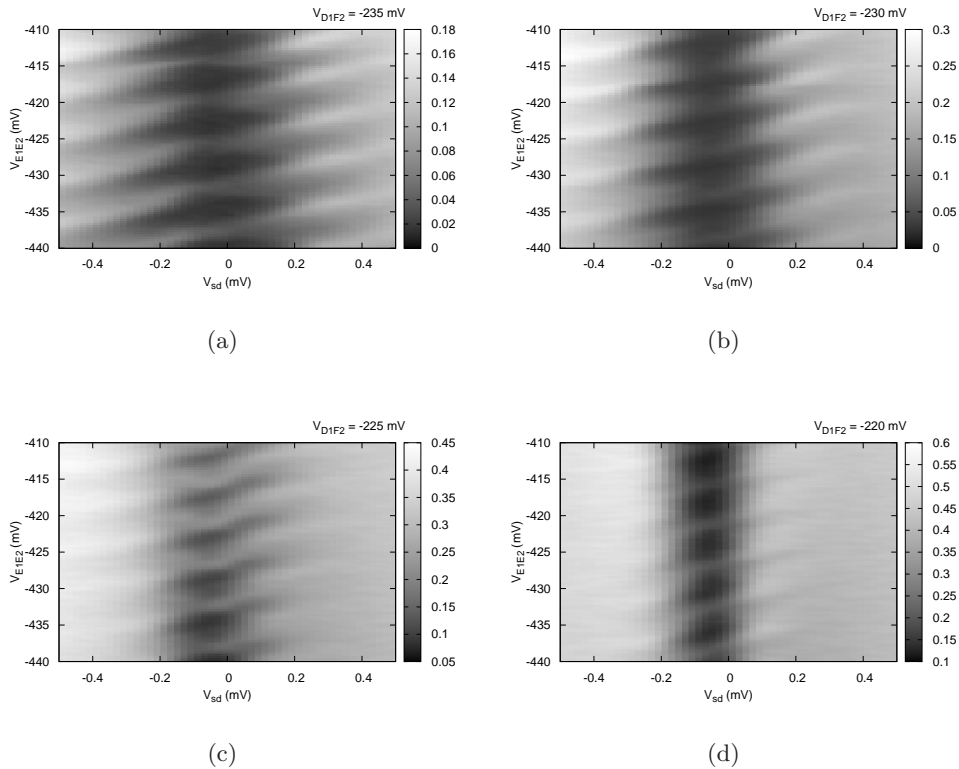


Figure 8.28.: Gray scale plot of differential conductance of double dot (dotIII-dotIV) system vs  $V_{E1E2}$  and  $V_{sd}$ . The interdot gate voltage  $V_{D1F2}$  is increased from (a)  $-235$  mV to (d)  $-220$  mV in the increment of  $5$  mV. The other gate voltage is set as  $V_{D2} = -305$  mV and  $V_{F1} = -445$  mV. The finite DC-offset also appears in this data.



## 9. Conclusions

In this thesis, a series of experiments which show the electron transport through quantum dot devices is presented. Devices are fabricated in a two-dimensional electron gas (2DEG) which is suited to investigate the effects of mesoscopic systems at low temperatures. Quantum devices on the nanometer scale or nanostructures can be fabricated by lithographic techniques, and a dilution refrigerator used to reduce the temperature down to the order of 100 millikelvin to give an opportunity to study quantum mechanical effect at very low temperatures. Quantum dots and quantum point contacts are the two types of devices considered in this work.

Quantum point contacts (QPCs), which constrict electrons tunneling through a narrow one-dimensional channel, are tuned and characterized. The quantization of differential conductance in unit of  $2e^2/h$  is clearly observed for many structures. Surprisingly, Coulomb blockade oscillations have been observed in a single QPC. It introduces new data for a single QPC and it can be inferred that there is a coupling between the QPC and an unexpected quantum dot formed in the inhomogeneous 2DEG. Due to the influence of the random impurity potential of ionized donor in the doped layer of heterostructure, the small islands of electrons or quantum dots can then be formed and coupled to a QPC.

The electron transport measurements are performed for single quantum dots with weak tunnel coupling. Many good Coulomb oscillations are observed and are clearly reproducible. The temperature dependence of Coulomb oscillations was investigated in the linear regime. The Coulomb peaks at various temperatures are well fit to the Lorentzian line shape. We can study the correlation between the electronic temperature ( $T_e$ ) and the bath temperature ( $T_{bath}$ ) of our system. At low temperatures, the evaluated  $T_e$  is higher than the  $T_{bath}$  due to electronic heating, whereas the  $T_e$  reaches and follows the  $T_{bath}$  at higher temperatures. We have used the theoretical fit to evaluate the true electronic temperature in the system. We also observe the trend of electron transport changing from single level or quantum regime to multilevel or metallic regime with increasing temperatures. The temperature dependence of Coulomb blockade oscillations in a single QPC is studied as well, and yields the same physics as that of a single quantum dot.

Nonlinear transport of single quantum dots with weak coupling was measured, and we obtained the Coulomb diamonds with good quality. The coupling parameters and the charging energy can be extracted from the geometry of these patterns, and the conversion energy factors are comparable to the values extracted from the temperature dependence. There is evidence for excited state spectroscopy which indicates the electrons transfer through the dot via excited states. The excitation energy is much larger than the level spacing estimated from the geometry of the dot. This may be due to the suppression of tunneling processes involving internally excited states resulting from the strong correlations between electrons, whereas the excitation of center-of-mass modes is unaffected by correlation effects. Therefore, the tunneling via the excitation of these modes dominate the excitation spectra in transport measurement in agreement with previous theoretical and experimental studies.

With strong coupling between dots and reservoirs, the Kondo effect can be observed in a single quantum dot. The Kondo effect is considered for the case of asymmetric tunnel coupling. Due to this asymmetry, it leads to the occurrence of a conductance anomaly in Coulomb blockade diamond at non-zero bias. The Kondo resonance in the density of states is pinned to the electrochemical potential level of the reservoir with stronger coupling or thinner tunnel barrier. The

## 9. Conclusions

Kondo temperature, which is characteristic of the coupling between electron spin in the localized state and electrons in the reservoirs, is extracted from the linewidth of the Kondo conductance peak at base temperature. According to the Anderson impurity model, the temperature dependence of the Kondo effect could be compared to theoretical predictions qualitatively, and the NRG scaling law was found to be applicable to our data. The normalized conductance is confirmed to be the universal function of the normalized temperature. The shifted Kondo resonance in non-zero bias is affected by the magnetic field. With increasing magnetic field, the position of Kondo peaks is moved toward the middle of the Coulomb diamond and the peak height is decreased. This is probably due to the improvement of symmetry of tunneling coupling influenced by the magnetic field. The Kondo resonance in our dot system disappears when magnetic field reaches 0.5 Tesla. Anomalous Kondo physics is also found in the single QPC coupled to an unexpected quantum dot. Clear Kondo conductance resonance is observed and indicates the symmetry of the tunnel coupling between dot and reservoirs.

The electron transport through double quantum dots coupled in series was also investigated. We observe the crossover from the weak interdot coupling regime in which the number of electrons in the two dots are quantized individually to the strong coupling regime in which the total numbers of electrons in both dots are quantized. The evolution of the stability charging diagram can be obtained by increasing interdot coupling. It shows the transition from isolated dots to a single large dot. The capacitances for two dots can be extracted from the geometry of the pattern in the charging diagram. When the center gate voltages of two dots are swept simultaneously, the conductance peak splitting in double dots can be study. When the interdot coupling is increased from weak to strong coupling, one conductance peak splits into two peaks with peak spacing is half as large. This indicates that the two dots combine to a large single dot with twice the gate capacitance. Qualitatively, our data agrees with the theoretical prediction of the relationship between splitting and interdot tunnel conductance for the strong tunneling limit.

For future experiments, in order to study more details of Kondo physics, the quantum dot structure should be designed such that a higher Kondo temperature can be obtained. The quantum dot of such a geometry must be much smaller than that of the dot designed to use in this thesis and should be fabricated by some modern lithographic techniques of the next generation. This dot with very small size will be able to confine few electrons inside and the level spacing will be quite large. The cooling process giving a lower sample temperature must also be improved. All these developments will yield the possibility to study interesting phenomena on quantum dot systems in both linear and nonlinear regimes.

## A. Parameters of Sample Fabrication

<b>A.1 Hallbar</b>	
<b>Surface cleaning</b>	Acetone, IPA, blow-dry with N <sub>2</sub>
<b>Photoresist coating</b>	
Surface drying	In the oven at 160 °C for 5 min or more
Adhesion chemical	HMDS 1:20, 30 s before spinning
Negative photoresist	MaN 405, 40 s with 6000 rpm (6000:5:40)
Baking	On the hot plate at 85 °C for 1 min
<b>Exposure and Developing</b>	
Exposure	UV-light for 8 s
Post baking	On the hot plate at 80 °C for 1 min
Develop	30-40 s in maD 333, stop with H <sub>2</sub> O, blow-dry with N <sub>2</sub>
<b>O<sub>2</sub> plasma</b>	0.5 mbar with 100 W for 25 s
<b>Wet etching</b>	
Hard baking	On the hot plate at 105 °C for 3 min
HCl dip	10 s in 37% HCl
Etching	70-80 s in H <sub>2</sub> O : H <sub>2</sub> SO <sub>4</sub> : H <sub>2</sub> O <sub>2</sub> ≡ 100:3:1, stop with H <sub>2</sub> O, blow-dry with N <sub>2</sub>
<b>Lift-off</b>	Acetone
<b>Cleaning</b>	Acetone, IPA, blow-dry with N <sub>2</sub>

Table A.1.: Parameters of the Hallbar fabrication.

## A. Parameters of Sample Fabrication

<b>A.2 Ohmic Contacts</b>	
<b>Surface cleaning</b>	Acetone, IPA, blow-dry with N <sub>2</sub>
<b>Photoresist coating</b>	
Positive photoresist	maP 1215, 40 s with 6000 rpm (6000:5:40)
Baking	On the hot plate at 90 °C for 3 min
<b>Exposure and Developing</b>	
Exposure	UV-light for 25 s
Develop	~ 15 s in maD 331 or MF 26A, stop with H <sub>2</sub> O, blow-dry with N <sub>2</sub>
<b>O<sub>2</sub> plasma</b>	0.5 mbar with 100 W for 25 s
<b>Evaporating</b>	
HCl dip	10 s in 37% HCl
AuGe	192 nm ≡ 1.6 g, rate ≈ 0.1 nm/s
Ni	76 nm, rate ≈ 0.05 nm/s
Au	20 nm, rate ≈ 0.1 nm/s
<b>Lift-off</b>	Acetone
<b>Cleaning</b>	Acetone, IPA, blow-dry with N <sub>2</sub>
<b>Annealing</b>	
Forming gas Process	Ar/H <sub>2</sub> = 20% with 300 mbar (i) 110 °C for 180 s with gas flow (ii) 370 °C for 120 s with no gas flow (iii) 420 °C for 50 s with no gas flow (iv) 100 °C for 2 s with gas flow

Table A.2.: Parameters of the ohmic contacts fabrication.

<b>A.3 Gate Leads and Bondpads</b>	
<b>Surface cleaning</b>	Acetone, isopropanal, blow-dry with N <sub>2</sub>
<b>Photoresist coating</b>	
Positive photoresist	maP 1215, 40 s with 6000 rpm (6000:5:40)
Baking	On the hot plate at 90 °C for 3 min
<b>Exposure and Developing</b>	
Exposure	UV-light for 25 s
Develop	~ 15 s in maD 331 or MF 26A, stop with H <sub>2</sub> O, blow-dry with N <sub>2</sub>
<b>O<sub>2</sub> plasma</b>	0.5 mbar with 100 W for 40 s
<b>Evaporating</b>	
HCl dip	10 s in 37% HCl
Cr	10 nm, rate ≈ 0.1 nm/s
Au	100 nm, rate ≈ 0.1 nm/s
<b>Lift-off</b>	Acetone
<b>Cleaning</b>	Acetone, IPA, blow-dry with N <sub>2</sub>

Table A.3.: Parameters of the gate leads and bondpads fabrication.

<b>A.4 Nanostructures</b>	
<b>Surface cleaning</b>	Acetone, isopropanal, blow-dry with N <sub>2</sub>
<b>Photoresist coating</b>	
E-beam resist Process	2% PMMA 2041 in MIBK (i) 1 s with 3000 rpm (3000:0:1) (ii) 50 s with 6000 rpm (6000:5:40)
Baking	On the hot plate at 120 °C for 5 min
Hard baking	In the oven at 160 °C for 1 hour at least
<b>Exposure</b>	
SEM Setting parameters	E-beam with 30 kV, pressure < 10 <sup>-5</sup> mbar Base dose = 160 μC/cm <sup>2</sup> Aperture and spot size at 2, blanker at 1, scan rotation at 3, magnification of 976×
<b>Developing</b>	
Develop	~ 40 s in MIBK:IPA ≡ 1:2, stop with IPA, blow-dry with N <sub>2</sub>
<b>Evaporating</b>	
Cr	10 nm, rate ≈ 0.1 nm/s
Au	30 nm, rate ≈ 0.1 nm/s
<b>Lift-off</b>	Acetone
<b>Cleaning</b>	Acetone, IPA, blow-dry with N <sub>2</sub>

Table A.4.: Parameters of the nanostructures fabrication.



# Bibliography

- [1] M. J. Kelly, *Low-dimensional Semiconductors*, Oxford Science Publications. (1995).
- [2] C. P. Poole Jr. and F. J. Owens, *Introduction to Nanotechnology*, John Wiley and Sons, (2003).
- [3] T. Heinzl, *Mesoscopic Electronics in Solid State Nanostructures*, WILEY-VCH, (2007).
- [4] S. Datta, *Electronic Transport in Mesoscopic Systems*, Cambridge University Press. (1997).
- [5] G. Snider, *1D Poisson/Schroedinger: A Band Diagram Calculator*, Department of Electrical Engineering, University of Notre Dame, (1990).
- [6] J. H. Davies, *The Physics of Low-Dimensional Semiconductors: An Introduction*, Cambridge University Press, (1998).
- [7] D.A. Wharam, T. J. Thornton, R. Newbury, M. Pepper, H. Ahmed, J. E. F. Frost, D.G. Hasko, D. C. Peacock, D. A. Ritchie, and G. A. C. Jones, *J. Phys. C, Solid State Phys.* **21**, L209 (1988).
- [8] B. J. van Wees, H. van Houten, C. W. Beenakker, J. G. Williamson, L. P. Kouwenhoven, and D. van der Marel, *Phys. Rev. Lett.* **60**, 848 (1988).
- [9] B. J. van Wees, L. P. Kouwenhoven, E. M. N. Willems, C. J. P. M. Harmans, J. E. Mooij, H. van Houten, C. W. J. Beenakker, J. G. Williamson, and C. T. Foxon, *Phys. Rev. B* **43**, 12431 (1991).
- [10] B. J. van Wees, L. P. Kouwenhoven, H. van Houten, C. W. J. Beenakker, J. E. Mooij, C. T. Foxon, and J. J. Harris, *Phys. Rev. B* **38**, 3625 (1988).
- [11] K. J. Thomas, J. T. Nicholls, M. Pepper, W. R. Tribe, M. Y. Simmons, and D. A. Ritchie, *Phys. Rev. B* **61**, R13365 (2000).
- [12] K. Berggren and M. Pepper, *New directions with fewer dimensions*, *Physics World*, October, 37 (2002).
- [13] L. P. Kouwenhoven, B. J. van Wees, C. J. P. M. Harmans, J. G. Williamson, H. van Houten, C. W. J. Beenakker, C. T. Foxon, and J. J. Harris, *Phys. Rev. B* **39**, 8040 (1989).
- [14] N. K. Patel, J. T. Nicholls, L. Martin-Moreno, M. Pepper, J. E. F. Frost, D. A. Ritchie, and G. A. C. Jones, *Phys. Rev. B* **44**, 13549 (1991).
- [15] A. Kristensen, H. Bruus, A. E. Hansen, J. B. Jensen, P. E. Lindelof, C. J. Marckmann, J. Nygard, C. B. Sorensen, F. Beuscher, A. Forchel, and M. Michel, *Phys. Rev. B* **62**, 10950 (2000).
- [16] K. S. Pyshkin, C. J. B. Ford, R. H. Harrell, M. Pepper, E. H. Linfield, and D. A. Ritchie, *Phys. Rev. B* **62**, 15842 (2000).

## Bibliography

- [17] L. P. Kouwenhoven, C. M. Marcus, P. L. McEuen, S. Tarucha, R. M. Westervelt, and N. S. Wingreen, Electron transport in quantum dots, *Mesoscopic Electron Transport*, edited by L. L. Sohn, L. P. Kouwenhoven, and G. Schoen, Series E: Applied Sciences (Kluwer Academic, Dordrecht), Vol. 345, p. 105-214 (1996).
- [18] L. P. Kouwenhoven, D. G. Austing, and S. Tarucha, *Rep. Prog. Phys.* **64**, 701 (2001).
- [19] C. W. J. Beenakker, *Phys. Rev. B* **44**, 1646 (1991).
- [20] W. G. van der Wiel, S. De Franceschi, J. M. Elzerman, T. Fujisawa, S. Tarucha, and L. P. Kouwenhoven, *Rev. Modern Physics*, **75**, (2003).
- [21] E. B. Foxman, P. L. McEuen, U. Meirav, N. S. Wingreen, Y. Meir, P. A. Belk, N. R. Belk, M. A. Kastner, and S. J. Wind, *Phys. Rev. B* **47**, 10020 (1993).
- [22] E. B. Foxman, U. Meirav, P. L. McEuen, M. A. Kastner, O. Klein, P. A. Belk, D. M. Abusch, and S. J. Wind, *Phys. Rev. B* **50**, 14193 (1994).
- [23] T. Ihn, *Electronic Quantum Transport in Mesoscopic Semiconductor Structures*, Springer Tracts in Modern Physics **192**, Springer, New York (2004).
- [24] J. Kondo, *Prog. Theor. Phys.* **32**, 37 (1964).
- [25] L. Kouwenhoven and L. I. Glazman, *Physics World*, **14**, 33 (2001).
- [26] P. W. Anderson, *Phys. Rev.* **124**, 41 (1961).
- [27] T. K. Ng and P. A. Lee, *Phys. Rev. Lett.* **61**, 1768 (1988).
- [28] Y. Meir, N. S. Wingreen, and P. A. Lee, *Phys. Rev. Lett.* **70**, 2601 (1993).
- [29] N. S. Wingreen, and Y. Meir, *Phys. Rev. B* **49**, 11040 (1994).
- [30] D. Goldhaber-Gordon, H. Shtrikman, D. Mahalu, D. Abusch-Magder, U. Meirav, and M. A. Kastner, *Nature* **391**, 156 (1998).
- [31] S. M. Cronenwett, T. H. Oosterkamp, and L. P. Kouwenhoven, *Science* **281**, 540 (1998).
- [32] S. Tarucha, D. G. Austing, S. Sasaki, T. Fujisawa, Y. Tokura, J. M. Elzerman, W. van der Wiel, S. de Franceschi, and L. P. Kouwenhoven, *Mat. Sci. Eng. B* **84**, 10 (2001).
- [33] M. A. Kastner and D. Goldhaber-Gordon, *Sol. State Comm.* **119**, 245 (2001).
- [34] S. Sasaki, S. de Franceschi, J. M. Elzerman, W. G. van der Wiel, M. Eto, S. Tarucha, and L. P. Kouwenhoven, *Nature* **405**, 764 (2000).
- [35] D. Goldhaber-Gordon, J. Goeres, M. A. Kastner, H. Shtrikman, D. Mahalu, and U. Meirav, *Phys. Rev. Lett.* **81**, 5225 (1998).
- [36] D. Goldhaber-Gordon, J. Goeres, H. Shtrikman, D. Mahalu, U. Meirav, and M. A. Kastner, *Mat. Sci. Eng. B* **84**, 17 (2001).
- [37] F. Simmel, R. H. Blick, J. P. Kotthaus, W. Wegscheider, and M. Bichler, *Phys. Rev. Lett.* **83**, 804 (1999).
- [38] M. Krawiec and K. I. Wysokinski, *Phys. Rev. B* **66**, 165408 (2002).



- [39] N. E. Bickers, D. L. Cox, and J. W. Wilkins, *Phys. Rev. Lett.* **54**, 230 (1985).
- [40] W. G. van der Wiel, S. de Franceschi, T. Fujisawa, J. M. Elzerman, S. Tarucha, and L. P. Kouwenhoven, *Science* **289**, 2105 (2000).
- [41] C. Livermore, C. H. Crouch, M. Westervelt, K. L. Campman, and A. C. Gossard, *Science* **274**, 1332 (1996).
- [42] C. Livermore, C. H. Crouch, R. M. Westervelt, K. L. Campman, and A. C. Gossard, *Superlattices and Microstructures*, **20**, 633 (1996).
- [43] F. Hofmann, T. Heinzl, D. A. Wharam, J. P. Kotthaus, G. Bohm, W. Klein, G. Trankle, and C. T. Foxon, *Phys. Rev. B* **51**, 13872 (1995).
- [44] R. H. Blick, R. J. Haug, J. Weis, D. Pfannkuche, K. v. Klitzing, and K. Eberl, *Phys. Rev. B* **53**, 7899 (1996).
- [45] F. R. Waugh, M. J. Berry, D. J. Mar, R. M. Westervelt, K. L. Campman, and A. C. Gossard, *Phys. Rev. Lett.* **75**, 705 (1995).
- [46] F. R. Waugh, M. J. Berry, C. H. Crouch, C. Livermore, D. J. Mar, R. M. Westervelt, K. L. Campman, and A. C. Gossard, *Phys. Rev. B* **53**, 1413 (1996).
- [47] K. A. Matveev, L. I. Glazman, H. U. Baranger, *Phys. Rev. B* **54**, 5637 (1996).
- [48] J. M. Golden and B. I. Halperin, *Phys. Rev. B* **53**, 3893 (1996).
- [49] J. M. Golden and B. I. Halperin, *Phys. Rev. B* **54**, 16757 (1996).
- [50] F. Pobell, *Matter and Methods at Low Temperatures*. Springer-Verlag, 1992.
- [51] Practical Cryogenics: An introduction to laboratory cryogenics. *Oxford Instruments* (1997): 35-38.
- [52] S. M. Cronenwett, *Coherence, Charging, and Spin Effects in Quantum Dots and Point Contacts*, Ph.D. Dissertation, Stanford University (2001).
- [53] K. v. Klitzing, G. Dorda, and M. Pepper, *Phys. Rev. Lett.* **45**, 494-497 (1980).
- [54] J. A. Nixon, J. H. Davies, and H. U. Baranger, *Phys. Rev. B* **43**, 12638 (1991).
- [55] M. J. Laughton, J. R. Barker, J. A. Nixon, and J. H. Davies, *Phys. Rev. B* **44**, 1150 (1991).
- [56] U. Meirav, M. A. Kastner, and S. J. Wind, *Phys. Rev. Lett.* **65**, 771 (1990).
- [57] D. Pfannkuche and S. E. Ulloa, *Phys. Rev. Lett.* **74**, 1194 (1995).
- [58] J. A. Folk, S. R. Patel, S. F. Godijn, A. G. Huibers, S. M. Cronenwett, C. M. Marcus, K. Campman, and A. C. Gossard, *Phys. Rev. Lett.* **76**, 1699 (1996).
- [59] Y. Meir, N. S. Wingreen, and P. A. Lee, *Phys. Rev. Lett.* **66**, 3048 (1991).
- [60] T. A. Costi, A. C. Hewson, and V. Zlatic, *J. Phys. Condens. Matter* **6**, 2519 (1994).
- [61] J. Schmid, J. Weis, K. Eberl, and K. v. Klitzing, *Physica B* **256**, 182 (1998).
- [62] J. D. Schmid, *The Kondo Effect in Quantum Dots*, Ph.D. Dissertation, Max-Planck-Institut fuer Festkoerperforschung Stuttgart (2000).

## Bibliography

- [63] F. Hofmann, *Transportuntersuchungen an einzelnen und gekoppelten Quantendotstrukturen*, Diplomarbeit, Ludwig-Maximilians-Universitaet Muenchen (1994).
- [64] I. H. Chan, P. Fallahi, R. M. Westervelt, K. D. Maranowski, and A.C. Gossard, *Physica E.* **17**, 584 (2003).
- [65] D. Schefzyk, Total Energy of Double Dot System Simulation Program, Faculty of Mathematics and Physics, University of Tuebingen, (2009).
- [66] C. H. Crouch, C. Livermore, R. M. Westervelt, K. L. Campman and A. C. Gossard, *Appl. Phys. Lett.* **71**, 817 (1997).
- [67] C. H. Crouch, C. Livermore, F. R. Waugh, R. M. Westervelt, K. L. Campman and A. C. Gossard, *Surf. Sci.* **361/362**, 631 (1996).
- [68] M. Fleischer, F. Panteleit, D. J. Schefzyk, D. A. Ritchie, M. Pepper and D. A. Wharam, *Semicond. Sci. Technol.* **24** (2009).

# Acknowledgements

I would like to express my sincere gratitude and appreciation to my thesis supervisor, Prof. Dr. David A. Wharam, who give me one of most important opportunity in my life to study in Germany, for his supervision, kindness suggestion and advice throughout on my doctoral work. I am also grateful to Prof. Dr. Dieter Kern serving as a second reader for my work and a committee. They have made valuable discussions and have been helpful in the production of this thesis.

I especially would like to thank to Mr. Stefan Jauerneck for his technical assistance of the measuring system and electronics stuff. I would like to thank to Mr. Daniel Schefzyk, who is skillful in the simulation programming, for contribute a lot of technical and computational assistance during the work. I also would like to thank to Dr. Monika Fleischer for helping me in many ways whether involving Physics or not. All of them are really nice and and make several helpful discussions during the period of my PhD study. I also thank to Mr. Daniel Biesinger and Mr. Matthias Kraus for a good atmosphere of working together.

I would like to acknowledge the financial support from the Development and Promotion for Science and Technology Talents Project (DPST) for the scholarship for my PhD study in Germany. I also would like to acknowledge the Institute of Applied Physics (IAP), Faculty of Mathematics and Physics, University of Tübingen for the teaching assistantship.

Many thanks to Mr. Matthias Ruoff, Mr. Dharmraj Kotekar-Patil, my friends and colleagues, whose names are not mentioned here, who have helped me in various ways. Thanks to all of my Thai friends in Tübingen for having fun together with playing a lot of strategy board games, especially Die Siedler von CATAN<sup>TM</sup>. Special thanks to Miss Danaya Raksil who is my beloved and always besides me even we were far away from each other.

Finally, a deep affectionate gratitude is acknowledged to my family, especially to my mother, for love, understanding and encouragement throughout the entire study.



# Curriculum Vitae

Kittipong Tantisantisom was born on 25 April 1980 in Rayong, Thailand.

- 1986-1992 : Primary education at Joseph Vithaya School in Chanthaburi, Thailand
- 1992-1995 : Lower secondary education at Thamai Phun Sawat Ratnukun School in Chanthaburi, Thailand
- 1995-1998 : Upper secondary education at Benchamarachuthit School in Chanthaburi, Thailand
- 1998 : A student in the special program called Development and Promotion for Science and Technology Talents Project (DPST).
- 1998-2002 : Bachelor's study at Chulalongkorn University in Bangkok, Thailand
- 2002 : Received Bachelor's degree of Science (First Class Honours) in Physics
- 2002-2005 : Master's study at Chulalongkorn University in Bangkok, Thailand
- 2005 : Received Master's degree of Science in Physics  
Topic of Master's thesis: *Preparation and Characterization of Gallium-doped Zinc Oxide Thin Films*
- 2005-2011 : PhD study at Institute of Applied Physics (IAP), Faculty of Mathematics and Physics, Eberhard-Karls-University of Tübingen, Germany  
In the group of Prof. Dr. D. A. Wharam, topic of PhD thesis: *Electron Transport in Quantum Dot Devices - Kondo Physics and Coupled Quantum Dots*